Max-Planck-Institut
für Plasmaphysik

EURATOM-Association

IPP Summer University for Plasma Physics

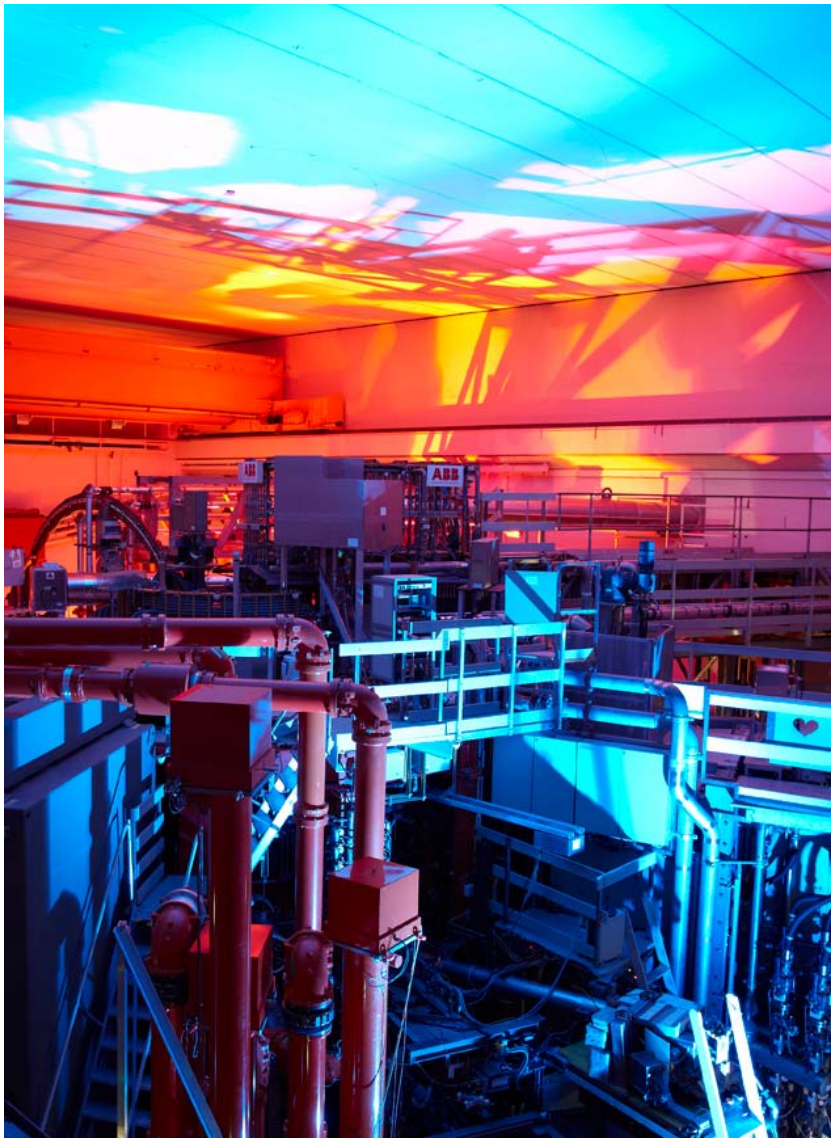

September 17 – September 21, 2012
Garching, Germany

Edited by Roberto Bilato and Ralf Kleiber

Contributions from:
R. Bilato, H.-S. Bosch, D. Breitschwerdt, R. Dux, T. Hamacher, M. Hirsch, C. Hopf, F. Jenko, R. Kleiber, H. Laqua, J. Meyer-ter-Vehn, R. Pitts, E. Poli, T. Pütterich, B.D. Scott, W. Suttrop, U. v. Toussaint

List of speakers

- Prof. Dr. Dieter Breitschwerdt — TU Berlin, Zentrum für Astronomie und Astrophysik, Hardenbergstr. 36, D-10623 Berlin
- Prof. Dr. Jürgen Meyer-ter-Vehn — Max-Planck-Institut für Quantenoptik, Abteilung für Attosekundenphysik, Hans-Kopfermann-Str. 1, D-85748 Garching
- Prof. Dr. Richard Pitts — ITER Organization, Building Headquarters, Route de Vinon - CS90046, F-13067 Saint Paul Lez Durance
- Dr. Roberto Bilato — Max-Planck-Institut für Plasmaphysik, Boltzmannstr. 2, D-85748 Garching
- Dr. Ralph Dux
- Dr. Thomas Hamacher
- Dr. Christian Hopf
- Dr. Frank Jenko
- Dr. Emanuele Poli
- Dr. Thomas Pütterich
- Dr. Bruce D. Scott
- Dr. Wolfgang Suttrop
- Dr. Udo von Toussaint
- Prof. Dr. Hartmut Zohm

- PD Dr. Hans-Stephan Bosch — Max-Planck-Institut für Plasmaphysik, Wendelsteinstr. 1, D-17491 Greifswald
- Dr. Matthias Hirsch
- Dr. Ralf Kleiber
- Dr. Heinrich Laqua

Cover page:
The experiment ASDEX-Upgrade in Garching.

Contents

Chapter 1

Basic plasma physics

Monika Bessenrodt-Weberpals,

Hugo de Blank, Axel Könies,

Emanuele Poli, Ralf Schneider

1.1 Introduction

A plasma is a hot gas consisting of charged and neutral particles which exhibit collective behaviour [1, 2, 3, 4, 5, 6, 7, 8, 9, 10, 11, 12, 13].

The name *plasma* goes back to Langmuir (1929) who discovered electromagnetic oscillations in rarefied gases which he called *plasma oscillations*.

The plasma is often referred to as the fourth state of matter (solid – liquid – gas – plasma). This concept arises from a thermodynamic description but is not completely rigorous. The variation of the basic macroscopic physical quantities like density n and temperature T determines the properties of the matter in the plasma state (see Fig. 1.1). However, the transition from the liquid, gaseous or solid state into the plasma state is not abrupt but continuous. In a gas, for example, more and more of the atoms become ionized with rising temperature and a plasma forms.

We know now that 99% of the matter in the universe is in the plasma state. Plasma can be found in the interior of the stars as well as in the interstellar space and in the core of the planets. Plasma also occurs in gas discharges (*neon light*, lightning) as part of our daily life.

The transition from weakly interacting neutral particles to charged particles which interact over the long-range Coulomb force may alter the properties of the particle system considerably. Therefore, many-body interaction plays an important role. The possible charge separation gives rise to electromagnetic oscillations or waves in a plasma.

Note that today the term plasma is understood in a very broad sense and may be applied to all systems which consist of charged particles as e.g. electrons in a solid or, even more general, systems where the bound states of the constituents are broken. The quark-gluon-plasma with its *color* charged constituents, occurring shortly after big bang or at high energy nucleus-nucleus collisions, is a famous example for this concept.

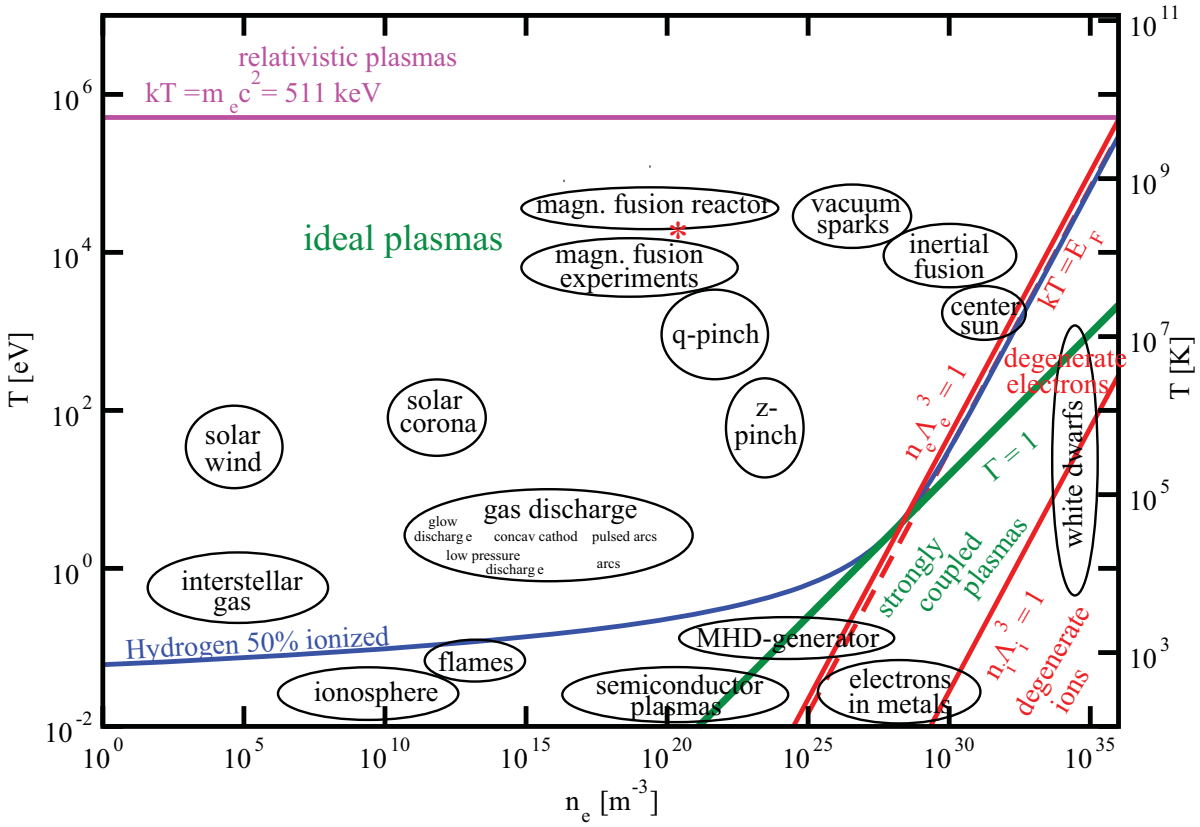

Figure 1.1: Temperatures and densities of astrophysical and laboratory plasmas. The asterisk indicates the fusion relevant parameters used in the examples: $T = 10^4$ eV, $n_e = 10^{20}$ m^{-3}, $B = 5$ T.

In the course of these lessons we will focus on plasmas made up of ions and electrons which interact over the Coulomb force and which are globally neutral. In this Chapter, we will briefly discuss the types of plasmas in the next section. Then, we go over to the plasma parameters which provide a more quantitative access to the several types of plasmas shown in Fig. 1.1. We will discuss the fundamental concepts of plasma physics, namely the Debye screening, the plasma frequency and the so-called quasi-neutrality. Further we will touch plasma collisions and we will end the lecture discussing the plasma motion in a magnetic field which is of paramount importance for plasmas in magnetic fusion devices.

Finally, appendix A reports some characteristic plasma parameters and their numerical values for typical fusion plasmas ($T = 10^4$ eV, $n_e = 10^{20}$ m^{-3}, $B = 5$ T).

1.2 Types of plasmas

1.2.1 Astrophysical plasmas

There are a variety of astrophysical plasmas in nature. They cover a wide range of densities and temperatures. Here, we will mention only a few of them.

The interior of the sun and the stars consists of a very dense and very hot plasma where light atomic nuclei fuse to heavier ones and release the excess of binding energy according to Einstein's famous formula $E = mc^2$, see chap. 2. The plasma density and the plasma temperatures

drop the closer one comes to the surface, thus the stellar atmosphere has completely different properties. The solar corona which is even more outside is a dilute magnetized plasma of several million degrees.

The sun emits an extremely dilute supersonic plasma, the solar wind, into its planet system. Near the earth the solar wind has $n_e \approx 5\,\mathrm{cm}^{-3}$ and $T_e = 10^5\,\mathrm{K}$. Because of its high temperature, the plasma has still a high conductivity, see sec. 1.6.

By interaction with the electromagnetic radiation from the sun the atoms of the upper atmosphere become partly ionized. We call this plasma which expands from about 60–2 000 km altitude the ionosphere.

A completely other type of plasmas are the degenerate plasmas within white dwarfs or neutron stars showing extremely high densities and thus behaving differently from the typical ideal plasmas we know from the majority of laboratory plasmas (ideal plasmas are defined below, sec. 1.3.4).

1.2.2 Laboratory plasmas

The tradition of laboratory plasma physics starts with the investigation of the weakly ionized plasmas of flames in the 18th century. Typical applications nowadays are plasma-aided welding and combustion for this type of plasma.

Since the plasma may carry an electric current, plasma discharges of various types are investigated in fundamental research and applied in industry. Low-pressure discharges like glow discharges carry small currents with cold electrodes. They serve for lightening, for gas lasers like the CO_2 laser or the HeNe laser, and for the wide-spread applications of plasma etching and deposition.

High-pressure discharges like arcs may carry larger currents and thereby attain higher temperature. They may also serve for lightening like the well-known high-pressure mercury lamp, for switches, and for plasma-material processing like melting, cutting, and welding.

In order to gain fusion energy in laboratories, high-temperature plasma physics has been started as a classified project around 1950. In 1958, the UN conference on the peaceful use of atomic energy has led to a declassification of fusion research, see chap. 2.

Note that free electrons in metal behave similarly to a high-density, low-temperature plasma (see Fig. 1.1).

1.3 Plasma parameters

To distinguish between different plasma states, let us look at the n-T diagram (see Fig. 1.1). The different physical behaviour is ordered by the four characteristic energies, namely the thermal energy $E_{th} = 3/2 k_B T$, the Fermi energy $E_F = (\hbar^2/2m_e) \cdot (3\pi^2 n)^{2/3}$, the electrostatic interaction energy $E_{el} = e^2/(4\pi\varepsilon_0 r)$, and the energy of Bohr's ground state $E_I = m_e e^4/(8\varepsilon_0^2 h^2)$. For simplicity, we concentrate here on hydrogen with charge $q = e$.

1.3.1 Ionization

First, with $E_{th} \approx E_I$ we can estimate the temperature T_I necessary for ionization from

$$\tfrac{3}{2} k_B T_I = m_e e^4 / (8\varepsilon_0^2 h^2)$$

we get

$$k_B T_I = \frac{m_e e^4}{8\varepsilon_0^2 h^2} \cdot 2/3 = 9 \text{ eV} . \tag{1.1}$$

Above this temperature, hydrogen plasmas are partially to fully ionized.

More exactly, the degree of ionization in a plasma in thermodynamic equilibrium is given by the Saha equation [14]

$$\frac{n_z n_e}{n_{z-1}} = 2 \frac{Z_z(T)}{Z_{z-1}(T)} \left(\frac{m_e k_B T}{2\pi\hbar^2} \right)^{3/2} \exp\left(-\frac{E_{I,z}}{k_B T} \right) \tag{1.2}$$

with n_z being the density of the z-th ionization stage and Z_z the corresponding partition function.

From Fig. 1.1, you can read the situation in a hydrogen plasma whose ionization degree is 50%. This shows that the hydrogen plasma is almost completely ionized at $k_B T > 1/10\ E_I$. The Saha equation may be applied for low ionization stages and high-density plasmas where collision processes dominate over radiative transitions and thereby determine the equilibrium. For high-ionized atoms like heavy impurities in a fusion plasma, the full set of rate equations has to be solved including both collisional and radiative transitions, see chap. 6.

1.3.2 Degeneracy and thermal wave length

The electrons which are Fermions and thus obey the Pauli principle, have actually to be described by a Fermi distribution of the energy. However, in a wide range of plasma parameters $(E_{th} \gg E_F)$ the Maxwell-distribution is an excellent approximation. This is the case for magnetic fusion plasmas, the sun, flames, gas discharges, interstellar plasmas ...

With increasing density or for low temperatures, if the Fermi energy approaches the thermal energy (see Fig. 1.1),

$$k_B T \approx E_F = \frac{\hbar^2}{2m} \left(3\pi^2 n \right)^{2/3} .$$

the electron gas becomes more and more degenerate. That means that the quantum statistical behaviour of the electrons does play a role and the Fermi distribution has to be used.

We can express the influence of the quantum character of the particles also using the ratio of the length scales of the thermal (de Broglie) wave length of the particles p

$$\Lambda_p = \frac{h}{\sqrt{2\pi m_p k_B T_p}} \tag{1.3}$$

to their average distance (also called Wigner-Seitz-Radius)

$$r_0 = \left(\frac{4\pi}{3} n \right)^{-1/3} . \tag{1.4}$$

The criterion of non-degeneracy for the particle species p is then given by

$$n_p \Lambda_p^3 \ll 1 \tag{1.5}$$

which is true if the de Broglie wave length is much less than the average particle distance.

1.3.3 Relativistic effects

If the thermal energy of the electrons is of the order of the energy corresponding to the electron rest mass

$$E_{th} \approx m_e c^2$$

at a temperature of approximately 511 keV, we have a relativistic plasma (see Fig. 1.1).

The plasma is called a relativistic degenerate plasma if the Fermi energy is of the order $m_e c^2$.

1.3.4 Ideal and non-ideal plasmas

If the thermal energy of a species of charged particles (e.g. electrons) is much larger than that of their Coulomb interaction, the plasma is called an ideal plasma.

To get a quantitative estimate, let us define the ratio of the Coulomb energy at the average interparticle distance to the thermal energy

$$\Gamma = \frac{Ze^2}{4\pi\varepsilon_0 r_0 k_B T} \,. \tag{1.6}$$

The parameter Γ allows the classification of the degree to which the Coulomb interaction determines the plasma behaviour ($\Gamma \ll 1$ almost ideal, $\Gamma < 1$ weakly non-ideal and $\Gamma > 1$ strongly non-ideal).

The Landau length λ_L is defined as the value of r_0 at which the thermal energy equals the electrostatic energy ($\Gamma = 1$):

$$\lambda_L = \frac{Ze^2}{4\pi\varepsilon_0 \, k_B T} \,. \tag{1.7}$$

This quantity will reappear in the calculation of the plasma resistivity.

A further parameter may be defined to estimate the particle-particle interaction, namely the ratio of the Landau length and the thermal de Broglie length

$$\xi_p = \sqrt{2\pi}\frac{\lambda_L}{\Lambda_p} = 2\sqrt{\frac{E_I}{k_B T}} \,. \tag{1.8}$$

If the plasma parameter ξ is of the order of one then in microscopic scattering processes the quantum mechanical interaction does play an important role and the Born series approximation cannot be applied.

1.4 Plasma fundamentals

1.4.1 Quasi-neutrality

First, let us take a closer look at the electrostatic properties of plasmas. Indeed, plasmas are usually electrically *quasi-neutral*, i.e. local concentrations of charge or external potential are shielded out at a distance which is short compared with the typical system length. A simple estimate shows that a small charge separation causes a large restoring electric field. Consider a non-zero charge density $\rho_E = e(n_i - n_e)$ caused by a small separation x of the electrons from the ions (see Fig. 1.2 left). Application of Poisson's equation $\boldsymbol{\nabla}\bullet\boldsymbol{E} = \rho_E/\varepsilon_0$ yields ($\boldsymbol{\nabla}\bullet\boldsymbol{E} \approx E/x$)

$$E \approx \frac{n_e e\, x}{\varepsilon_0}\,. \tag{1.9}$$

A fully ionized plasma at 5 eV and atmospheric pressure has an electron density of $n_e = 6 \times 10^{22}$ m^{-3}. A charge separation of $x = 1$ mm would lead to a very strong electric field $E = 1 \times 10^{12}$ V/m and an electric potential $\phi = 5 \times 10^8$ V over 1 mm. In fact, finite electric fields can be generated by very small deviations of the densities from quasi-neutrality.

1.4.2 Plasma frequency

The strong restoring electric field associated with deviations from quasi-neutrality causes a harmonic oscillation (Langmuir, 1929). In the absence of a magnetic field, electrons react to the electric field of (1.9) with

$$m_e \frac{\mathrm{d}^2 x}{\mathrm{d}t^2} = -e\,E = -\frac{n_e e^2\, x}{\varepsilon_0}\,.$$

The solution of this equation is an oscillation with the characteristic electron *plasma frequency*

$$\omega_{p,e} = \left(\frac{n_e e^2}{\varepsilon_0\, m_e}\right)^{1/2}\,. \tag{1.10}$$

The ions do not participate in these oscillations because of their high mass. The plasma frequency is temperature-independent. For typical fusion plasma densities (10^{20} m^{-3}) it is $\nu_{p,e} \approx 100$ GHz. Electromagnetic waves with frequencies below $\omega_{p,e}$ cannot propagate in plasmas since their electric fields are screened by the Debye shielding. In this case, the waves are reflected. For larger frequencies, the inertia of the electrons allows the propagation of the waves. This is the reason why metals reflect visible light but not X-rays. The picture becomes more complicated if magnetic fields are present, cf. chap. 10.3.2. Analogously, the ion plasma frequency is defined as

$$\omega_{p,i} = \left(\frac{n_i Z^2 e^2}{\varepsilon_0\, m_i}\right)^{1/2} \tag{1.11}$$

and the total plasma frequency

$$\omega_p^2 = \omega_{p,e}^2 + \omega_{p,i}^2\,. \tag{1.12}$$

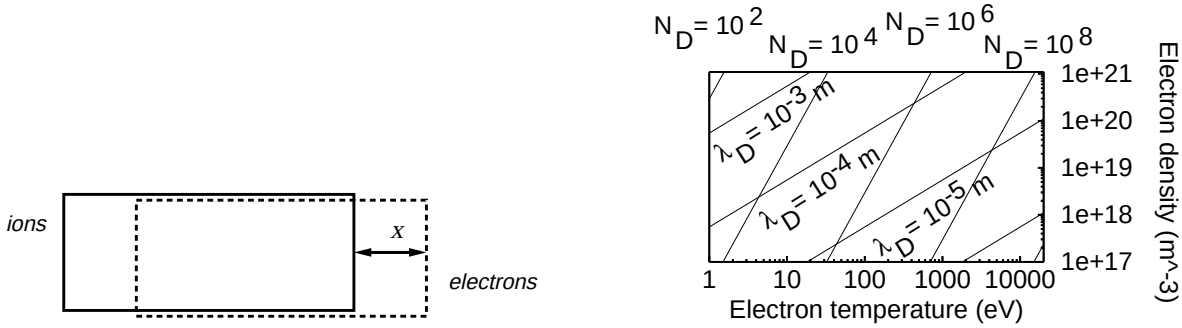

Figure 1.2: Left: Schematic illustration of charge separation in a plasma.
Right: Values of the Debye length λ_D and the plasma parameter N_D plotted against electron temperature and electron density.

1.4.3 Debye shielding

Usually, ions are surrounded by electrons which screen the ion charge. Only at small distances a deviation from charge neutrality may be observed. In the presence of an electric potential ϕ, the electron and ion densities in thermal equilibrium are modified according to Boltzmann's distribution $\sim \exp(-E/k_BT) = \exp[(-mv^2/2 - q\phi)/k_BT]$ with $q = \pm e$. Integration over all velocities yields $\tilde{n}_q = n_q \exp(-q\phi/k_BT_q)$, where n_q are the densities for $\phi = 0$. For small exponents (ideal plasmas!), this can be approximated by $\tilde{n}_q = n_q(1 - q\phi/k_BT_q)$. For singly charged ions, Poisson's equation $\nabla^2\phi = -\rho_E/\varepsilon_0$ in spherical geometry reads

$$\frac{1}{r^2}\frac{\mathrm{d}}{\mathrm{d}r}\left(r^2\,\frac{\mathrm{d}\phi}{\mathrm{d}r}\right) = \frac{e(\tilde{n}_e - \tilde{n}_i)}{\varepsilon_0} = \frac{n_e e^2}{\varepsilon_0}\,\left(\frac{1}{k_BT_e} + \frac{1}{k_BT_i}\right)\,\phi, \tag{1.13}$$

where the plasma approximation $n_e = n_i$ is used. With the definition of the *Debye length*

$$\lambda_{D,q} = \left(\frac{\varepsilon_0\, k_BT_q}{n_e e^2}\right)^{1/2}, \tag{1.14}$$

and the total Debye length

$$\lambda_D^{-2} = \lambda_{D,e}^{-2} + \lambda_{D,i}^{-2} \tag{1.15}$$

the solution of (1.13) gives the screened potential

$$\phi(r) = \frac{e}{4\pi\varepsilon_0}\,\frac{\exp(-r/\lambda_D)}{r} \tag{1.16}$$

(the constant derives from assuming that ϕ matches the usual Coulomb potential for $r \to 0$). The Debye length describes the range of an electric potential inside a plasma, which is much shorter than the range in vacuum.

A more heuristic derivation of the Debye length is the following: Small charge separations arise as a result of thermal fluctuations. In a plasma the thermal energy density of the electrons per degree of freedom is $E_f = (1/2)n_e k_B T$. The electrostatic energy density results from a separation of charge over a length x (see Fig. 1.2 left and (1.9)) as $E_e = (\varepsilon_0/2)E^2 = (\varepsilon_0/2)(n_e e x/\varepsilon_0)^2$. The comparison of E_f and E_e shows that substantial separation of charge can only occur over lengths of up to $x \approx (\varepsilon_0 k_B T/n_e e^2)^{1/2}$, which is again the Debye length λ_D given in (1.14).

Averaged over many λ_D, the electron and ion charge densities are equal, i.e. $n_e = n_i$. The thermal electron velocity $v_{th,e} = (3k_B T_e/m)^{1/2}$ is found from (1.10) and (1.14) to be

$$v_{th,e} = \sqrt{3}\,\lambda_{D,e}\,\omega_{p,e}\,.$$

Therefore, $1/\omega_{p,e}$ can be interpreted as the time that a thermal electron needs to pass the Debye length.

The definition of an ideal plasma (see sec. 1.3.4) is equivalent to the call for a large number of particles in a Debye sphere, called the *plasma parameter* N_D

$$N_D = \tfrac{4}{3}\pi\lambda_D^3\, n \gg 1\,.$$

1.5 Particle collisions

1.5.1 Coulomb collisions and Rutherford scattering

Collisions in the plasma play an important role for collective effects like e.g. resistivity in the plasma. When an electron collides with a neutral atom, no force is felt until the electron is close to the atom; these collisions are similar to billiard-ball collisions. However, when an electron collides with an ion, the electron is gradually deflected by the long-range Coulomb field of the ion. Nonetheless, an effective cross-section may be derived. We will do it in a classical picture without considering quantum mechanical or relativistic corrections.

We will consider here the scattering of an electron by an ion. Because of the large ratio of ion to electron mass we can assume the ion location in the centre of mass of the two-particle system (see Fig. 1.3 left).

In the absence of Coulomb forces, the electron would have a distance of closest approach called the *impact parameter* ρ.

For the Coulomb interaction of two charges e_1 and e_2, the potential reads $U(r) = \alpha/r$ with $\alpha = e_1 e_2/(4\pi\varepsilon_0)$.

Following textbooks of theoretical mechanics [17] we introduce cylindrical coordinates and employ the conservation of energy

$$E = \frac{m\dot{r}^2}{2} + \frac{L^2}{2mr^2} + U(r) \tag{1.17}$$

and angular momentum

$$L = mr^2\dot{\phi}\,. \tag{1.18}$$

Let us assume that the electron has the relative velocity v_∞ if it is at a very large distance from the scattering centre (ion). Then, the (conserved) energy must be equal to $E = mv_\infty^2/2$ and the (conserved) angular momentum $L = m\rho v_\infty$. For very long times the particle should again go to infinity. This allows us to calculate the angle ϕ_0 (see Fig. 1.3) as

$$\phi_0 = \int_{r_{min}}^{\infty} \frac{\rho\,\frac{\mathrm{d}r}{r^2}}{\sqrt{1 - \frac{\rho^2}{r^2} - \frac{2U}{mv_\infty^2}}}\,. \tag{1.19}$$

The distance of closest approach r_{min} is reached when $\dot{r}$ is zero, i.e. when the kinetic energy of the particle has been converted to energy in the effective potential $U(r)+L^2/(2mr^2)$ ($r = r_{min}$ is a root of the denominator in (1.19)). Integration gives

$$\rho^2 = \frac{\alpha^2}{m^2 v_\infty^4} \cot^2 \frac{\chi}{2} = \rho_0^2 \cot^2 \frac{\chi}{2}, \tag{1.20}$$

with $\chi = \pi - 2\phi_0$, cf. again Fig. 1.3. As we have usually an ensemble of particles which undergo the scattering we define the cross-section σ as

$$\mathrm{d}\sigma = \frac{\mathrm{d}N}{n}\,, \tag{1.21}$$

where N shall denote the number of particles being scattered by angles between χ and $\chi + \mathrm{d}\chi$, while n is the number of particles per area unit. Assuming a homogeneous beam, we have $\mathrm{d}N = n 2\pi\rho\mathrm{d}\rho$. Expressing this in terms of the solid angle Ω gives

$$\mathrm{d}\sigma = \frac{\rho}{\sin\chi} \left|\frac{\mathrm{d}\rho}{\mathrm{d}\chi}\right| \mathrm{d}\Omega\,. \tag{1.22}$$

Finally, the Rutherford cross-section becomes

$$\mathrm{d}\sigma = \left(\frac{\alpha}{2mv_\infty}\right)^2 \frac{\mathrm{d}\Omega}{\sin^4(\chi/2)}\,. \tag{1.23}$$

We can see that the number of collisions with small angles is larger than those of large angles. Furthermore, the value for the cross section diverges for large impact parameters ρ or small angles χ like χ^{-4} with the consequence of an infinite total cross-section. This is due to of the infinite long range of the Coulomb interaction.

From the cross section we can infer an approximate expression for the electron-ion collision time if we define the collision time as the proportionality constant between the initial parallel momentum of the electron and its change during collisions with ions at all possible impact parameters ρ

$$\frac{\mathrm{d}}{\mathrm{d}t}\left\langle \Delta p_\parallel \right\rangle = -\nu_{ei} p_\parallel\,. \tag{1.24}$$

The initial parallel momentum is $p_\parallel = p = mv_\infty$ while $p_\parallel^f = p\cos\chi$, as it can easily inferred from Fig. 1.3 left. Using trigonometric relations and (1.20) we get

$$\Delta p_\parallel = p(\cos\chi - 1) = -2p\frac{1}{1+\cot^2(\chi/2)} = -2p\frac{1}{1+(\rho/\rho_0)^2}\,. \tag{1.25}$$

In the following we will denote v_∞ by v for brevity. For the net change of momentum per time unit of the electron we have to consider all the ions that the incoming electron can encounter in this time unit

$$\frac{\mathrm{d}}{\mathrm{d}t}\langle \ldots \rangle = 2\pi n_i v \int_0^{\rho_{max}} \rho\,\mathrm{d}\rho \ldots\,. \tag{1.26}$$

The upper limit should actually be taken to be infinity. We will see, however, that the integral diverges for $\rho_{max} \to \infty$, which is the well known Coulomb divergence due to the r^{-1} dependence of the Coulomb potential. The problem can be cured considering the screening of the particle-particle interaction by the other charges in the system, resulting in the exponentially

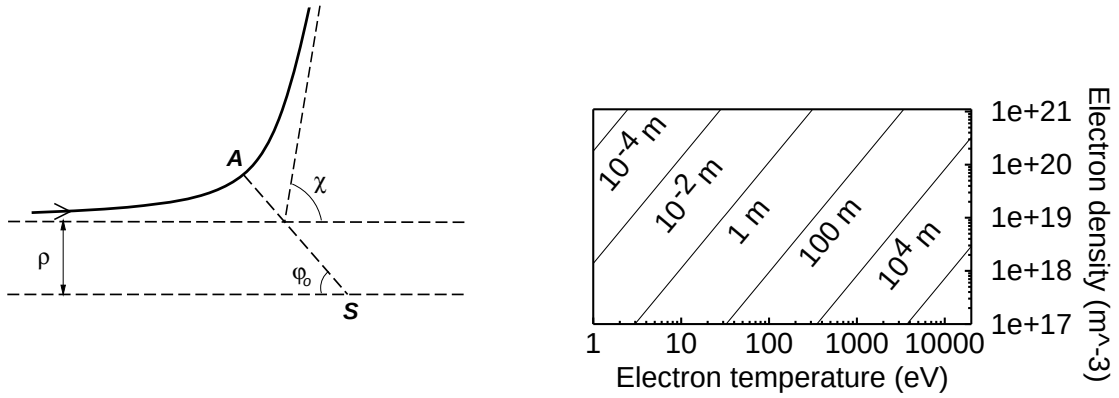

Figure 1.3: Left: Rutherford scattering; S is the centre of mass of the scattering partners. As the Coulomb force is a central force, the orbit is symmetric with respect to A and therefore $\chi = |\pi - 2\phi_0|$.
Right: Values of the mean free path of electrons λ_e plotted against electron temperature and electron density.

decaying Debye-potential we have derived in the last section. In a plasma, the typical radius of the interaction is the Debye-length. Therefore, we take this length as the upper cut-off and we obtain

$$\frac{\mathrm{d}}{\mathrm{d}t}\left\langle \Delta p_{\parallel} \right\rangle = -\frac{4\pi n_i}{mv^2}\alpha^2 \frac{1}{2}\left\{ \ln\left| 1+\left(\frac{\rho_{max}}{\rho_0}\right)^2 \right| \right\} , \tag{1.27}$$

which gives

$$\frac{\mathrm{d}}{\mathrm{d}t}\left\langle \Delta p_{\parallel} \right\rangle \approx -\frac{n_i Z_i^2 e^4}{4\pi\varepsilon_0^2 mv^2}\ln\frac{\lambda_D}{\rho_0} = -\frac{n_i Z_i^2 e^4}{4\pi\varepsilon_0^2 mv^2}\ln\Lambda , \tag{1.28}$$

if we consider that the Debye length $\rho_{max} = \lambda_D$ is much larger than ρ_0. The latter condition is true if the number of particles in a Debye sphere is large, i.e. if we have an ideal plasma, see discussion in Sec. 1.3.4. Compare ρ_0, (1.20), with the Landau length, (1.7). The expression $\ln\Lambda = \ln(\lambda_D/\rho_0)$ is called the Coulomb logarithm.

The cross sections and collision times are fundamental in order to understand the behaviour of the plasma. In the next section we will relate them to the resistivity by very simple physical arguments. Note, however, that the derivation we gave here is heuristic and not rigorous at all. An average over the velocity distribution had actually to be included in the derivation. This is shown in chap. 4.

The rigorous derivation should start from a kinetic equation. There are a lot of approaches to non-equilibrium processes which give quantum mechanical expressions for cross sections or collision times. These expressions usually include the collective effects like screening which we had to introduce artificially by the cut-off parameter. The expression we have obtained here turns out to be the first order Born approximation of a quantum mechanical cross section. This makes clear that the approximation is valid for high energies of the electron only, i.e. when the thermal energy of a particle is much larger than the Coulomb interaction. Therefore, for non-ideal plasmas the simple classical picture can not be applied and the Coulomb logarithm is a poor approximation.

The collision time for electron-electron collisions follows from comparing (1.24) and (1.28)

$$\tau_{ei} = \frac{4\pi\varepsilon_0^2}{Z^2 e^4}\frac{m_e^2 v_e^3}{n_i \ln\Lambda} . \tag{1.29}$$

From the collision time the mean free path can be calculated as $\lambda_{mfp} = \tau_{ei} v_e$. Fusion plasmas possess a mean free path of about 15 km. This is much larger than the typical laboratory plasma dimensions, leading to the term *collision-less* plasma. The mean free path for fusion reactions is still four orders of magnitude larger at this temperature.

1.6 Electric resistivity

If an electric field is applied to the plasma, the electrons and ions are accelerated in opposite directions. The electrons speed up much faster due to their lighter mass. They deliver the gained energy to the ions by Coulomb collisions, yielding a *resistance* η which, according to Ohm's law, connects the electric field $\boldsymbol{E}$ with the current density $\boldsymbol{j}$

$$\boldsymbol{E} = \eta \, \boldsymbol{j} \, . \tag{1.30}$$

The net change of electron momentum is supplied by the electric field and by the momentum loss due to collisions

$$\frac{\mathrm{d}}{\mathrm{d}t} \left\langle \Delta p_{\parallel} \right\rangle = -eE - \nu_{ei} p_{\parallel} \, . \tag{1.31}$$

Assuming an equilibrium between driving and dissipative forces, the term on the left hand side should vanish. If we further assume that the current is proportional to the relative velocity of electrons and ions $j = -en_e v = -en_e p_{\parallel}/m_e$, we obtain

$$-eE = -\frac{\nu_{ei} m_e j}{e n_e} \tag{1.32}$$

From (1.30) and (1.32) the resistivity is

$$\eta = \frac{\nu_{ei} m_e}{n_e e^2} \propto T_e^{-3/2} \, , \tag{1.33}$$

where the temperature dependence follows from the estimate $v_e \sim v_{th} \sim \sqrt{k_B T_e}$ in (1.29). The exact value of the specific resistance was derived in [15] with the help of kinetic theory and the resulting *Spitzer resistivity* is a factor of about two smaller than our first approximation. For $T_e = 1.4$ keV, the plasma resistance is comparable to copper (1.8×10^{-8} Ωm). Since η is proportional to $T_e^{-3/2}$, fusion plasmas with $T \approx 10$ keV have resistance values which are an order of magnitude smaller than that of copper. The measurement of the resistance can be used to determine plasma temperatures since it depends only very weakly on the density via $\ln\Lambda$ chap. 7. In laboratory plasmas, the effects of different ion species (impurities) on the resistivity often has to be taken into account. For plasmas in strong magnetic fields, additional corrections have to be made to the electrical resistance. The specific resistance $\eta_{\perp}$ is approximately twice the value of $\eta_{\parallel}$.

1.7 Motion of charged particles in electromagnetic fields

Both laboratory and astrophysical plasmas are often immersed in a magnetic field. The motion of a particle with electric charge q and mass m in electric and magnetic fields can be determined from the combined electrostatic and Lorentz force

$$\boldsymbol{F} = q \left(\boldsymbol{E} + \boldsymbol{v} \times \boldsymbol{B} \right) .$$

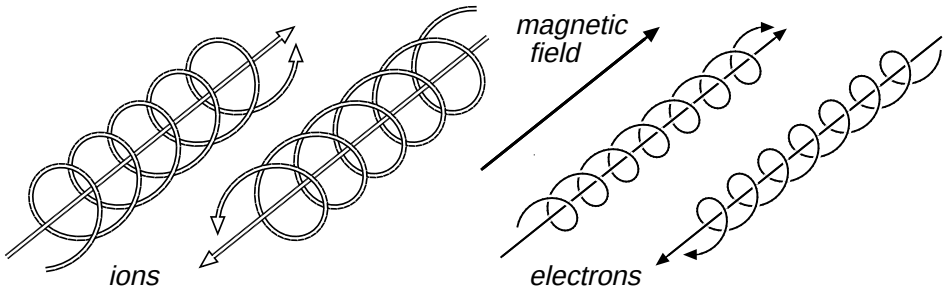

Figure 1.4: Orientation of the gyration orbits of electrons and ions in a magnetic field.

1.7.1 Homogeneous magnetic field

For $E = 0$ and a homogeneous magnetic field, the kinetic particle energy remains constant because the Lorentz force is always perpendicular to the velocity and can thus change only its direction, but not its magnitude. The motion of charged particles is then described in terms of the velocity components parallel and perpendicular to the magnetic field, $\boldsymbol{v}_\parallel$ and $\boldsymbol{v}_\perp$. Only $\boldsymbol{v}_\perp$ interacts with $\boldsymbol{B}$, leading to a circular motion perpendicular to $\boldsymbol{B}$. The superposition of this circular motion with a free streaming parallel to the magnetic field gives rise to the helical motion depicted in Fig. 1.4. The centrifugal force $mv_\perp^2/r$ balances the Lorentz force $qv_\perp B$ for a gyration radius r equal to the *Larmor radius*

$$\rho_L = \frac{mv_\perp}{|q|B} \,. \tag{1.34}$$

If $mv_\perp^2/2 = k_B T$ is taken for the two-dimensional thermal motion perpendicular to $\boldsymbol{B}$, it is

$$\rho_L = \frac{(2mk_BT)^{1/2}}{|q|B} \,.$$

In a typical fusion plasma ($T = 10$ keV, $B = 5$ T), the electrons have a Larmor radius $\rho_{L,e} = 67\ \mu$m and deuterons have $\rho_{L,i} = 4.1$ mm. The frequency of the gyration, called *cyclotron frequency* Ω_q, follows from $v_\perp = \Omega\,\rho_L$ to be

$$\Omega_q = \frac{|q|B}{m_q} \,.$$

In fusion experiments, the electron cyclotron frequency Ω_e is of the same order of magnitude as the plasma frequency $\omega_{p,e}$.

The Hall *parameter*

$$x_q = \Omega_q \tau_{qq} \tag{1.35}$$

counts the number of cyclotron revolutions between succeeding collisions. A magnetized plasma is characterized by $x_e \gg x_i \gg 1$.

The *magnetic moment* μ is defined as the product of the current I times the area A which is surrounded by the current. Thus, the magnetic moment of a single gyrating particle is

$$\mu = I \cdot A = \frac{q\Omega}{2\pi} \cdot \pi\rho_L^2 = \frac{mv_\perp^2}{2B} = \frac{\mathscr{E}_\perp}{B} \,, \tag{1.36}$$

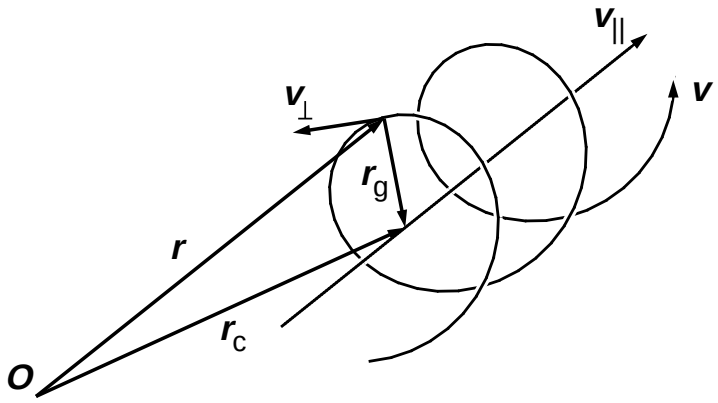

Figure 1.5: Definition of the guiding centre motion.

where $\varepsilon_\perp$ is the perpendicular fraction of the kinetic energy. The magnetic field produced by the gyrating particles counteracts the externally imposed magnetic field $\boldsymbol{B}$ (*plasma diamagnetism*).

1.7.2 Motion in a constant magnetic field due to an additional force

If, in addition to the Lorentz force, a force $\boldsymbol{F}$ acts on the charged particle, the equation of motion is

$$m\frac{\mathrm{d}\boldsymbol{v}}{\mathrm{d}t} = q\,(\boldsymbol{v}\times\boldsymbol{B}) + \boldsymbol{F}\ .$$

The motion of the particle under the influence of $\boldsymbol{F}$ can be separated from the gyration due to $\boldsymbol{B}$ by considering the *guiding centre* of the particle, as shown in Fig. 1.5. The guiding centre "c" is the centre of the gyration cycle. Its position $\boldsymbol{r}_c$ can be written as

$$\boldsymbol{r}_c = \boldsymbol{r} + \boldsymbol{r}_g\ , \tag{1.37}$$

where $\boldsymbol{r}$ is the position of the particle and $\boldsymbol{r}_g$ the gyration radius vector

$$\boldsymbol{r}_g = \frac{m}{qB^2}\,\boldsymbol{v}\times\boldsymbol{B}\ .$$

In *strongly magnetized* plasmas such as in fusion experiments, the Lorentz force dominates other forces $\boldsymbol{F}$. Then, ρ_L is often much smaller than other length scales, and Ω much higher than other frequencies. Consequently, the particle orbit is well described by the motion of the guiding centre. With the assumption of a constant B, the velocity of the guiding centre can be obtained by differentiating (1.37)

$$\boldsymbol{v}_c = \dot{\boldsymbol{r}}_c = \boldsymbol{v} + \frac{m}{qB^2}\frac{\mathrm{d}\boldsymbol{v}}{\mathrm{d}t}\times\boldsymbol{B} = \boldsymbol{v} + \frac{1}{qB^2}\left[q(\boldsymbol{v}\times\boldsymbol{B}) + \boldsymbol{F}\right]\times\boldsymbol{B}. \tag{1.38}$$

Using the vector relation

$$(\boldsymbol{v}\times\boldsymbol{B})\times\boldsymbol{B} = (\boldsymbol{v}_\perp\times\boldsymbol{B})\times\boldsymbol{B} = \boldsymbol{B}(\boldsymbol{v}_\perp\boldsymbol{\cdot}\boldsymbol{B}) - \boldsymbol{v}_\perp(\boldsymbol{B}\boldsymbol{\cdot}\boldsymbol{B}) = -\boldsymbol{v}_\perp B^2\ ,$$

the guiding centre motion follows to be

$$\boldsymbol{v}_c = \boldsymbol{v}_\parallel + \frac{\boldsymbol{F}\times\boldsymbol{B}}{qB^2}\ .$$

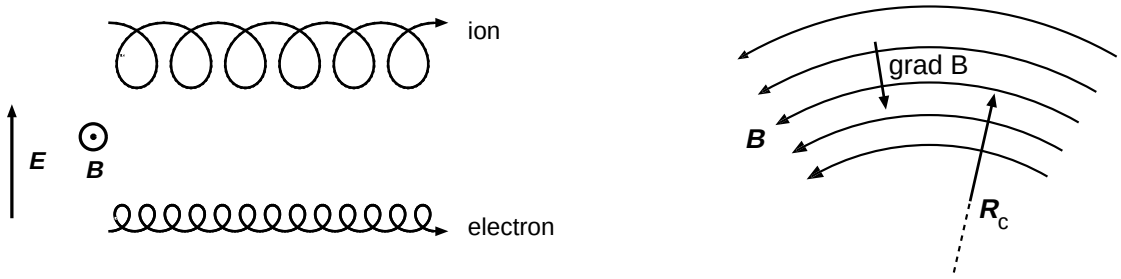

Figure 1.6: Left: $\boldsymbol{E} \times \boldsymbol{B}$ drift of ion and electron, $v_E = E/B$.
Right: Inhomogeneous magnetic field. Curvature radius and its relation to the field gradient in the absence of a plasma current ($\boldsymbol{\nabla} \times \boldsymbol{B} = 0$).

The velocity of the guiding centre can be split into components perpendicular and parallel to the magnetic field

$$\boldsymbol{v}_{c,\perp} = \frac{\boldsymbol{F}_\perp \times \boldsymbol{B}}{qB^2} , \qquad \frac{\mathrm{d}v_{c,\parallel}}{\mathrm{d}t} = \frac{F_\parallel}{m} . \tag{1.39}$$

Any force with perpendicular components to the magnetic field leads to a motion perpendicular to $\boldsymbol{B}$ and $\boldsymbol{F}$ with the velocity $\boldsymbol{v}_{c,\perp}$.

1.7.3 E × B drift, gravitational drift

The most important additional force is a constant electric force $\boldsymbol{F} = q\boldsymbol{E}$, which leads to a drift

$$\boldsymbol{v}_E = \frac{\boldsymbol{E} \times \boldsymbol{B}}{B^2} . \tag{1.40}$$

This drift velocity does not depend on the sign of the charge or the mass of the particles. Thus, the $\boldsymbol{E} \times \boldsymbol{B}$ drift leads to a macroscopic movement of a plasma. More insight into the $\boldsymbol{E} \times \boldsymbol{B}$ drift can be gained from Fig. 1.6 left. If the particle accelerates in the electric field, the Larmor radius increases. On the other hand, if it slows down its Larmor radius decreases, leading to the non-closed trajectories shown in Fig. 1.6 left. The net effect is a drift velocity perpendicular to the electric and magnetic fields.

Another drift is due to the gravitation field. If $F_g = mg$ is perpendicular to B, the drift velocity is $v_g = mg/(qB)$.

1.7.4 Particle drift in inhomogeneous magnetic fields

For spatially varying magnetic fields, (1.39) can still be applied if the relative variation of B is small along one gyration of the particle, i.e. in the case of *slowly varying* fields. One important example is the particle drift in a magnetic field with a transverse gradient. The particle orbit has a smaller radius of curvature on that part of its orbit located in the stronger magnetic field. This leads to a drift perpendicular to both the magnetic field and its gradient. Quantitatively, the force on a particle with magnetic moment μ (see (1.36)) can be written as

$$\boldsymbol{F}_{\nabla B} = -\mu \, \boldsymbol{\nabla} B ,$$

leading to

$$\boldsymbol{v}_{\nabla B} = -\frac{mv_\perp^2}{2qB^3}\,(\boldsymbol{\nabla}_\perp B)\times\boldsymbol{B}\,. \tag{1.41}$$

Let us consider a curved magnetic field in the case that the plasma current does not play a role, $\boldsymbol{\nabla}\times\boldsymbol{B}=0$ or, more generally, $\boldsymbol{\nabla}\times\boldsymbol{B}\parallel\boldsymbol{B}$. As sketched in Fig. 1.6, there is a correlation between the field gradient and the curvature radius R_c

$$\frac{\boldsymbol{R}_c}{R_c^2} = -\frac{\boldsymbol{\nabla}_\perp B}{B}\,. \tag{1.42}$$

Since the particles follow the curved magnetic field lines, a centrifugal force $\boldsymbol{F}_c = mv_\parallel^2\,\boldsymbol{R}_c/R_c^2$ is exerted, which is responsible for the drift velocity

$$\boldsymbol{v}_R = \frac{mv_\parallel^2}{qB^2}\,\frac{\boldsymbol{R}_c\times\boldsymbol{B}}{R_c^2}\,. \tag{1.43}$$

Combination of (1.41), (1.42), and (1.43), yields

$$\boldsymbol{v}_R+\boldsymbol{v}_{\nabla B} = \frac{m}{q}\,\frac{\boldsymbol{R}_c\times\boldsymbol{B}}{R_c^2}\,(v_\parallel^2+\tfrac{1}{2}v_\perp^2)\,.$$

In a very rough approximation $v_\parallel^2+1/2v_\perp^2\approx v^2$, i.e. the resulting drift is proportional to the particle energy.

As a first application of these drifts, consider the electrons and protons captured in the earth's magnetic field (trapping in a magnetic field will be discussed in the next section). Due to the gradient and curvature of the earth's magnetic field, these electrons and protons drift around the equator, the electrons from west to east and the protons in the opposite direction, producing the so-called ring currents.

1.7.5 The guiding centre equations in general geometry

In fusion plasmas the geometry of the magnetic field is usually fairly complex. Therefore, it is mandatory to derive the guiding centre equations rigorously for arbitrary geometry.

Most elegantly this was done by Littlejohn [16]. He showed that the guiding centre equations can be derived from a generalized Lagrangian. We will outline the general idea and the results only. Littlejohn has shown that there is a non-canonical transformation such that the particle motion can be expressed independently from the gyroangle α to arbitrary order in a small parameter $\varepsilon_B = |\rho_L/L_B|$ (where $L_B = B/|\nabla B|$ is the scale length of the magnetic field). This set of phase-space coordinates $(\boldsymbol{R},V_\parallel,V_\perp$, or $\boldsymbol{R},V_\parallel,\mu)$ is called guiding centre coordinates. In these coordinates, the magnetic moment constructed as

$$\mu = \frac{mV_\perp^2}{2ZeB(\boldsymbol{R})}$$

is conserved. Note, however, that the "true" $\mu = mv_\perp^2/(2ZeB)$ resulting from the velocity $v_\perp$ in the real space is not conserved in general.

To first order in ε_B and for $\mathrm{d}/(\Omega\mathrm{d}t)\ll 1$ the following results have been obtained assuming the set of independent variables to be $\mathrm{R},V_\parallel,\mu$

The time derivatives of $\boldsymbol{R}$, μ and $V_\parallel$ can be obtained from the well known Lagrangian formalism [16] with the single-particle Lagrangian

$$L = Ze\boldsymbol{A}^* \cdot \dot{\boldsymbol{R}} + \frac{1}{Ze}\mu\dot{\alpha} - \frac{1}{2}mV_\parallel^2 - \mu B - Ze\phi \tag{1.44}$$

which gives the Euler-Lagrange equations

$$\begin{aligned} Ze(\boldsymbol{E}^* + \dot{\boldsymbol{R}} \times \boldsymbol{B}^*) &= m\dot{V}_\parallel \boldsymbol{b} + \mu\boldsymbol{\nabla}B\,, & (1.45)\\ \dot{\mu} &= 0\,, & (1.46)\\ \dot{\alpha} &= \frac{ZeB}{m}\,, & (1.47)\\ \dot{\boldsymbol{R}}\cdot\boldsymbol{b} &= V_\parallel\,. & (1.48) \end{aligned}$$

The modified field quantities are defined as in Littlejohn's work [16]

$$\begin{aligned} \boldsymbol{A}^* &= \boldsymbol{A} + \frac{m}{Ze}V_\parallel \boldsymbol{b}\,, & (1.49)\\ \boldsymbol{B}^* &= \boldsymbol{B} + \frac{m}{Ze}V_\parallel \boldsymbol{\nabla}\times\boldsymbol{b}\,, & (1.50)\\ \boldsymbol{E}^* &= -\frac{\partial \boldsymbol{A}^*}{\partial t} - \boldsymbol{\nabla}\phi\,, & (1.51)\\ \boldsymbol{b} &= \frac{\boldsymbol{B}}{B}\,. & (1.52) \end{aligned}$$

Finally we are left with the following equations of motion

$$\begin{aligned} \dot{\boldsymbol{R}} &= \frac{1}{B_\parallel^*}\left[V_\parallel \boldsymbol{B}^* + \frac{1}{Ze}\boldsymbol{b}\times(\mu\boldsymbol{\nabla}B - Ze\boldsymbol{E}^*)\right]\,, & (1.53)\\ \dot{V}_\parallel &= -\frac{1}{B_\parallel^*}\boldsymbol{B}^*\cdot(\mu\boldsymbol{\nabla}B - Ze\boldsymbol{E}^*)\,, & (1.54)\\ \dot{\mu} &= 0\,, & (1.55)\\ \dot{\alpha} &= \Omega = \frac{ZeB}{m}\,. & (1.56) \end{aligned}$$

Note, in (1.54), the so-called mirror force (first term on the right-hand side) which is responsible for the *bounce* motion of a part of the particle population in regions of weaker magnetic field, as shown in Fig. 1.7 and Fig. 1.8. This phenomenon can be also understood in terms of adiabatic invariance of the magnetic moment, as explained below.

1.8 Adiabatic invariants

The gyromotion and the bounce motion seen in the previous section are two examples of quasi-periodic motion of a charged particle in a magnetic field. The word *quasi*-periodic is used because it is assumed that the trajectory changes on a time scale which is much slower than the "period" of the motion. For instance, this implies that the Larmor orbit remains nearly unchanged over many gyroperiods $2\pi/\Omega$, or that the trajectory of a trapped particle is approximately the same during many bounce times. In this case, the quantity

$$I \equiv \oint p\mathrm{d}q, \tag{1.57}$$

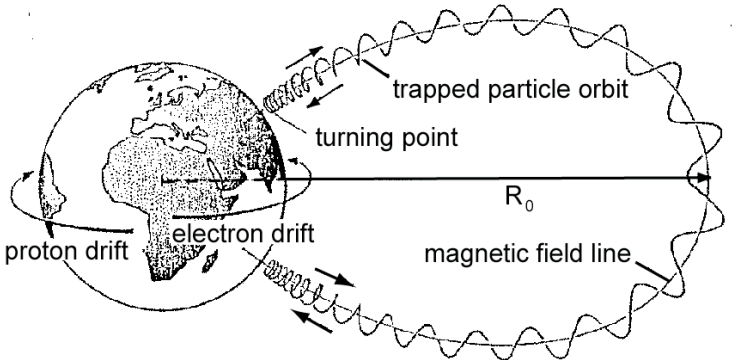

Figure 1.7: Drifts of electrons and protons in the earth's magnetic field.

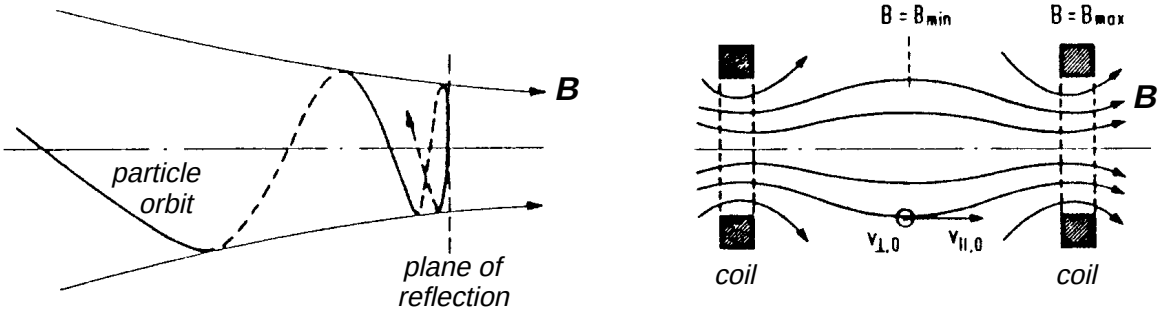

Figure 1.8: Magnetic field lines of a simple axisymmetric magnetic mirror.

where p and q are conjugate canonical variables and the integral is taken over a complete cycle in q, is called an *adiabatic invariant* of the motion. The period T can be computed directly as $T = \partial I/\partial \mathscr{E}$, where $\mathscr{E}$ is the energy of the system. Using this definition of I, we can immediately prove that the magnetic moment is an adiabatic invariant associated to the cyclotron motion. The relevant Hamiltonian is in this case $H(\boldsymbol{p},\boldsymbol{q}) = (\boldsymbol{p} - q\boldsymbol{A})^2/2m$ and the canonical momentum $\boldsymbol{p} = m\boldsymbol{v} + q\boldsymbol{A}$. (1.57) becomes then

$$I_1 = \oint m\boldsymbol{v}_\perp \cdot \mathrm{d}\boldsymbol{r}_\perp + \oint q\boldsymbol{A} \cdot \mathrm{d}\boldsymbol{r}_\perp = 2\pi\rho m v_\perp - qB\pi\rho^2 = \frac{\pi m^2 v_\perp^2}{qB} \propto \frac{m v_\perp^2}{2B} = \mu,$$

where Stokes' theorem and (1.34) have been used. This shows that the magnetic moment μ, which is proportional to I_1, is an adiabatic invariant.

We have met this adiabatic invariance in the section before and take the opportunity to recall: for a constant and homogeneous magnetic field guiding centre coordinates and real space coordinates agree what implies that μ is strictly conserved. For inhomogeneous and time dependent magnetic fields we observe that μ is conserved to a certain order in the ordering parameters ε_B and $\mathrm{d}/(\Omega \mathrm{d}t)$ only. Littlejohn's result that a phase space transform exists which finds a redefined μ as a conserved quantity can be regarded as formal expression of the term *adiabatic invariance*.

The invariance of μ is the basis for magnetic mirrors, which is schematically shown in Fig. 1.8. The parallel velocity of a particle in a (spatially or temporally) varying magnetic field is determined by $\mu = const$ and energy conservation $mv^2/2 = const$. The combination of these conditions, $mv_\parallel^2/2 + \mu B = const$, reveals that $v_\perp^2$ increases with increasing B and hence $v_\parallel$ decreases. The criterion for particle reflection ($v_\parallel = 0$) at the high field ends of the mirror machine is

Table 1.1: Characteristic times of motion for typical fusion parameters in a stellarator reactor similar to W7-X: ($B = 5$ T, large radius: 20 m, small radius 2 m, $T = 15$ keV, $n = 3 \cdot 10^{20}$ m^{-3}).

	gyration time τ_g	bounce time τ_{bounce}	drift time τ_{drift}
electrons	$\approx 7 \cdot 10^{-12}$ s	$\approx 10^{-6}$ s	$\approx 6 \cdot 10^{-2}$ s
deuterons	$\approx 3 \cdot 10^{-8}$ s	$\approx 10^{-4}$ s	$\approx 6 \cdot 10^{-2}$ s
α-particles	$\approx 3 \cdot 10^{-8}$ s	$\approx 3 \cdot 10^{-5}$ s	$\approx 10^{-4}$ s

$$\tfrac{1}{2}mv^2 = \tfrac{1}{2}mv_{\parallel,0}^2 + \mu B_{\min} \;\leq\; \mu B_{\max}\,, \tag{1.58}$$

where $v_{\parallel,0}$ is the parallel velocity in the low field region. If the mirror ratio is defined as $R = B_{\max}/B_{\min}$ and (1.58) is divided by $\mu B_{\min} = 1/2mv_{\perp,0}^2$, the velocity ratio

$$\frac{v_{\parallel,0}}{v_{\perp,0}} \leq \sqrt{R-1} \tag{1.59}$$

describes the criterion for particle confinement. The earth's magnetic field is an example of a magnetic mirror. It forms two belts of confined charged particles originating from the solar wind (see Fig. 1.7). Obviously, particles which do not meet the condition (1.59) are lost from magnetic mirrors. This so called *loss cone* in velocity space is refilled by collisions and therefore pure mirror configurations have a very poor plasma confinement.

The second or *longitudinal invariant* is

$$J = m \oint v_\parallel \, \mathrm{d}\ell \,.$$

Consider a particle between two magnetic mirrors: It bounces between them and therefore has a periodic motion at the bounce frequency. A constant of this motion is $\oint mv_\parallel \, \mathrm{d}\ell$ with ℓ being the length between two mirrors and $v_\parallel$ the longitudinal velocity. However, the motion is not exactly periodic, because the guiding centre drifts across field lines, and thus the constant of the motion becomes in general an adiabatic invariant. From this we can conclude that the particles will drift on $J = const$ contours.

If these contours are closed, the drift motion is also periodic and we observe another constant of motion – the so called third adiabatic invariant. Note, however, that to guarantee invariance the perturbations have to be even slower (see 1.8) than the drift period.

The third adiabatic invariant turns out to be the total magnetic flux Φ enclosed by the drift surface. Obviously, the particles will stay on a surface such that the total number of lines of force enclosed remains constant as $\boldsymbol{B}$ varies. This invariant has few applications because most fluctuations of $\boldsymbol{B}$ occur on a time scale short compared with the drift period.

Appendix A

1.8 summarizes characteristic plasma parameters and their numerical value for typical fusion plasmas, namely $T_e = T_i = 10^4$ eV, $Z = 1$, and $n_e = n_i = 10^{20}$ m^{-3}, $B = 5$ T for magnetically-confined experiments and $n_e = n_i = 10^{31}$ m^{-3} for inertially-confined experiments. In the table, $a = e^4 \ln\Lambda/(6\pi\varepsilon_0^2)$.

Table 1.2: Characteristic plasma parameters and their numerical value for typical fusion plasmas.

Name	Formula	Magnetic fusion	Inertial fusion
Average distance	$\overline{r} \approx (\frac{4}{3}\pi n)^{-1/3}$	$0.2\,\mu$m	3×10^{-11} m
Debye length	$\lambda_D = \sqrt{\varepsilon_0\, k_B T/(n_e e^2)}$	$75\,\mu$m	2.4×10^{-10} m
Landau length	$\lambda_L = e^2/(\pi\varepsilon_0\, k_B T)$	10^{-13} m	10^{-13} m
de Broglie length	$\Lambda_p = \hbar/(\sqrt{m_e k_B T})$	3×10^{-12} m	3×10^{-12} m
Mean free path	$\lambda_{qk} = v_{th,q}\tau_{qk}$	15 km	150 nm
Larmor radius	$\rho_{L,q} = m_q v_\perp/(\lvert q\rvert B)$	$67\,\mu$m (e), 4.1 mm (i)	
Thermal velocity	$v_{th,q} = \sqrt{3k_B T_q/m_q}$	7.3×10^7 m/s (e), 1.7×10^6 m/s (i)	7.3×10^7 m/s (e), 1.7×10^6 m/s (i)
Plasma frequency	$\omega_{p,e} = (1/2\pi)\sqrt{n_e e^2/\varepsilon_0 m_e}$	90 GHz	2×10^{17} Hz
Cyclotron frequency	$\omega_{c,q} = \lvert q\rvert B/2\pi m_q$	140 GHz (e), 40 MHz (i)	
Electron collision time	$\tau_{ee} = \frac{\sqrt{3}}{a}\sqrt{m_e}n_e^{-1}(k_B T_e)^{3/2}$	$140\,\mu$s	5.4×10^{-15} s
Ion collision time	$\tau_{ii} = \frac{\sqrt{3}}{aZ^4}\sqrt{m_i}n_i^{-1}(k_B T_i)^{3/2}$	6 ms	2.3×10^{-13} s
Electrical resistance	$\eta = m_e/(n_e e^2\tau_{ei}^E)$	$1\times10^{-9}\,\Omega$m	$3\times10^{-10}\,\Omega$m
Plasma parameter	$N_D = \frac{4}{3}\pi\, n\, \lambda_D^3$	2×10^8	500
Coulomb logarithm	$\ln\Lambda = \ln\left(\frac{9}{\sqrt{2}}N_D\right)$	17	4.4
Hall parameter	$x_q = \omega_{c,q}\tau_{qq}$	1×10^8 (e), 3×10^6 (i)	

References

[1] Y. Eliezer and S. Eliezer: *The Fourth State of Matter*, Bristol: Hilger (1989).

[2] N.A. Krall and A.W. Trivelpiece: *Principles of Plasma Physics*, New York: McGraw-Hill (1973).

[3] F.F. Chen: *Introduction to Plasma Physics*, New York: Plenum Press (1974).

[4] G. Schmidt: *Physics of High Temperature Plasmas*, New York: Academic Press (1979).

[5] R.B. White: *Theory of Tokamak Plasmas*, Amsterdam: North-Holland (1989).

[6] R.D. Hazeltine and J.D. Meiss: *Plasma Confinement*, Redwood: Addison-Wesley (1992).

[7] B.B. Kadomtsev: *Tokamak Plasma: A Complex Physical System*, Bristol: IOP Publ. (1992).

[8] P.A. Sturrock: *Plasma Physics*, Cambridge: Cambridge University Press (1994).

[9] R.J. Goldston and P.H. Rutherford: *Introduction to Plasma Physics*, Bristol: IOP Publ. (1995).

[10] J.A. Bittencourt: *Fundamentals of Plasma Physics*, Oxford: Pergamon Press (2nd ed, 1995).

[11] J.A. Wesson: *Tokamaks*, Oxford: Oxford University Press (2nd ed, 1997).

[12] K. Miyamoto: *Fundamentals of Plasma Physics and Controlled Fusion*, Tokyo: Iwanami Press (1997).

[13] K.-H. Spatschek: *High Temperature Plasmas*, Weinheim: WILEY-VCH (2012).

[14] M.N. Saha: *On a Physical Theory of Stellar Spectra*, Proc. Roy. Soc. **A99** (1921) 135.

[15] L. Spitzer, Jr., and R. Härm: *Transport Phenomena in a Completely Ionized Gas*, Phys. Rev. **89** (1953) 977.

[16] R.G. Littlejohn, J. Plasma Phys. **29**, 302 (1983).

[17] L.D. Landau, E.M. Lifshitz, Course in Theoretical Physics Vol 1: Mechanics, Butterworth-Heinemann (1982)

Chapter 2

Basic nuclear fusion

Hans-Stephan Bosch

2.1 Introduction

Any energy production from nuclear reactions is based on differences in the nuclear binding energy. Fig. 2.1 shows the nuclear binding energy per nucleon (proton or neutron). It has been derived from measurements of the masses of the nuclei, when it was observed that the masses of nuclei are always smaller than the sum of the proton and neutron masses which constitute the nucleus. This mass difference corresponds to the nuclear binding energy according to Einstein's energy-mass relation $E = \Delta m \cdot c^2$. An explanation of the structure of Fig. 2.1 was given by C.F. von Weizsäcker in 1935. Starting from the very limited range of the strong nuclear force he assumed that each nucleon just influences its nearest neighbours. The binding energy per nucleon would thus be constant. The smaller binding energies for smaller nuclei are due to the relatively large surface to volume ratio. The nucleons at the surface have missing partners and thus their contribution to the total binding energy of the nucleus is reduced. The decrease of binding energy per nucleon for nuclei beyond $A \approx 60$ is due to the repulsive coulomb force of the large amount of positive protons.

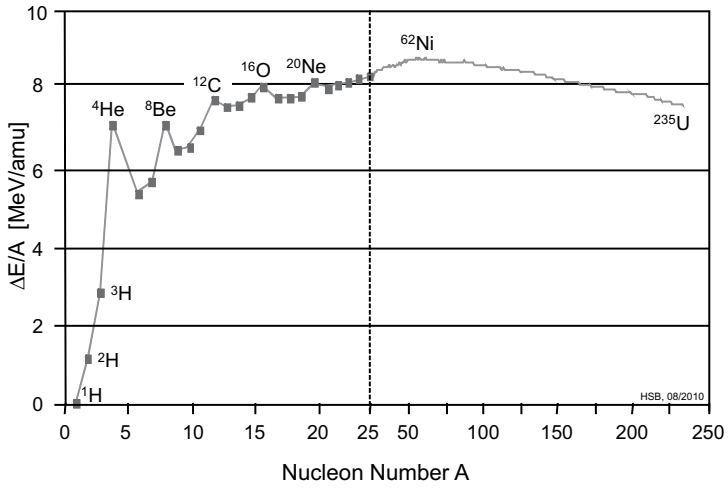

Figure 2.1: Nuclear binding energy per nucleon as a function of the nucleon number A.

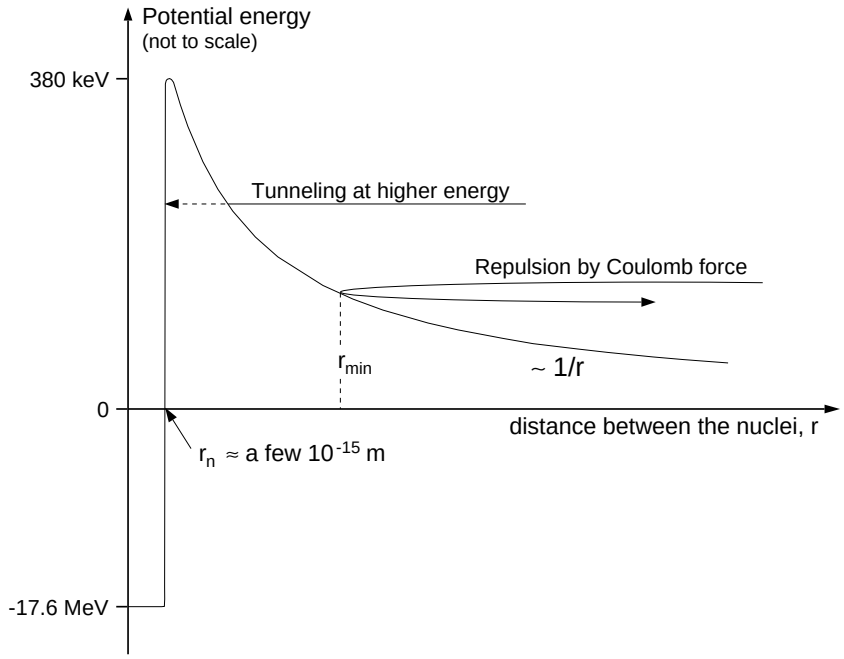

Figure 2.2: Schematic representation of the potential energy U of two nuclei as a function of their distance. The energies quoted are for a system of D (=^{2}H) and T (=^{3}H).

The finer structures in Fig. 2.1 are due to quantum mechanical effects, i.e. at certain so-called *magic* proton and neutron numbers the nucleus formed is a very stable configuration. This is roughly comparable to the stable electron configurations of the noble gases, where electron shells are completed. The first magic number is two, which is manifested as a most remarkable example of a local maximum in Fig. 2.1, i.e. the helium nucleus with two protons and two neutrons. From Fig. 2.1 it is clear that there are two ways of gaining nuclear energy:

1. By transforming heavy nuclei into medium-size nuclei: This is done by fission of uranium, which is not a topic of these lectures.

2. By fusion of light nuclei into heavier ones: In particular the fusion of hydrogen isotopes into stable helium offers the highest energy release per mass unit. Doing this in a controlled manner has been the goal of fusion research for about 40 years. Most of the following lectures are dedicated to this goal.

The energy release per nucleon is of the order of 1 MeV (= 10^6 eV) for fission reactions and in the order of a few MeV for fusion reactions. This is 6–7 orders of magnitude above typical energy releases in chemical reactions, which explains the effectiveness and attractiveness, but also the potential hazard of nuclear power.

All the nuclear reactions are mostly governed by the strong nuclear force which acts over very small distances in the order of the radius of the nuclei, but for distances above a few fermi (i.e. 10^{15} m) the repulsive Coulomb force between the positively charged nuclei becomes dominant. The potential energy of two nuclei as a function the distance between these nuclei is shown in Fig. 2.2. The depth of the deep well at small radii is determined by the binding energy, discussed before, while the barrier at a few fermi is given by the Coulomb potential of $Z_1 Z_2 e^2/4\pi\varepsilon_0 r_m$ which is much smaller, but still poses a principal problem. For alpha-particle decay (where a ^{4}He nucleus separates itself out of a positive nucleus) as well as for fusion of

lighter nuclei, this diagram demands a particle energy of the order of 500 keV, and this would make fusion processes almost impossible. However, it was known since the end of the last century, that α-particle decay occurs at room temperature, and in 1928 Gamov [1] explained this by the tunneling effect, which in turn also allows fusion reactions to occur at temperatures far below the Coulomb barrier: Due to quantum mechanical effects the minimum distance between the two nuclei is not fixed (as it is indicated by the repulsion in Fig. 2.2), but there is a finite probability for the nuclei to get closer, and eventually *tunnel* through the Coulomb barrier, as indicated by the dotted line in Fig. 2.2. In terms of wave functions, the amplitude is not zero for $r \leq r_{min}$, but it is finite and decays slowly for smaller radii. Therefore it can still be finite for $r \leq r_n$, i.e. the particles have a possibility to approach close enough for a fusion reaction to occur. This tunneling probability is a strong function of the relative velocity v of the reacting particles with charge Z_1, Z_2,

$$P_{tunneling} \sim \exp -\frac{2\pi Z_1 Z_2 e^2}{\hbar\, v} \; .$$

This equation shows that reaction partners with small mass (and charge Z) are preferred, and that the rection probability increases strongly with the relative velocity v, i.e. the temperature.

In the light of the above discussion it becomes clear why fission energy has been much more readily obtained than fusion energy: Fission is triggered by thermal neutron capture, i.e. no force prevents the neutron from entering the uranium nucleus at room temperature and causing a fission reaction.

2.2 Energy production on the sun

Though still a somewhat exotic topic on earth, nuclear fusion is *the* energy source of our universe. The light of all stars is generated by fusion reactions. On the sun the main reactions are the following

$$\begin{aligned} \mathrm{p} + \mathrm{p} &\longrightarrow \mathrm{D} + \mathrm{e}^+ + \nu_e \; , \\ \mathrm{D} + \mathrm{p} &\longrightarrow {}^3\mathrm{He} + \gamma \; , \\ {}^3\mathrm{He} + {}^3\mathrm{He} &\longrightarrow {}^4\mathrm{He} + 2\mathrm{p} \; , \end{aligned}$$

where p denotes a proton, D a deuteron, a heavy hydrogen isotope with one proton and one neutron, ^{3}He, ^{4}He are helium isotopes, γ stands for a high-energy photon, e^+ for a positron (anti-electron), and ν_e for an electron neutrino.

A very important feature of the energy production on the sun is the need for the weak interaction which transforms protons to neutrons (β^+-decay), in the first of the above listed reactions. All weak interaction processes involve the emission of neutrinos (thereby keeping the lepton number constant). As the weak interaction is very slow, it causes the long lifetime of the sun and it is an essential condition for our evolution .

Further reactions which are important at temperutures above about 1 keV, produce ${}^7_4$Be, ${}^7_3$Li, ${}^8_5$B and ${}^8_4$Be, which decays into two ${}^4_2$He nuclei. Also in these reactions neutrinos are produced, however with a higher kinetic energy than those from the pp-reactions mentioned above.

These neutrinos ignore both the strong and electromagnetic interactions and therefore it is extremely hard to detect them experimentally. Almost all neutrinos produced in the sun travel

through it without interaction and thus carry information from the reactions in the core of the sun. It was not till 1992 that the European GALLEX collaboration detected the low energy solar neutrinos from the main energy-producing reactions (pp-chain) listed above. This was the first experimental validation of our theoretical model of energy production in the stars.

For much higher temperatures ($T \geq 2\,\mathrm{keV}$), i.e. in stars which with higher mass than the sun, fusion of four protons to $^4_2$He can also occur in a catalytic process based on ^{12}C. In this so-called Bethe-Weizsäcker cycle oxygen, nitrogen and ^{13}C are involved only in intermediate stages, and the net reaction again is $4\,p \rightarrow {}^4\mathrm{He} + 2\,e^+ + 2\,\nu_e$.

2.3 Fusion on earth

The fundamentals of fusion research are well described in great detail in two (German) books by J. Raeder [4] and U. Schumacher [5].

For energy production on earth the weak interaction has to be avoided since it would lead to unacceptably small reaction rates. The sun (and all other stars) overcome this problem by their huge mass, but a fusion reactor has to be considerably smaller in size than a star.

Possible candidates for using fusion energy on earth are the following reactions (T denoting tritium, the heaviest hydrogen isotope with two neutrons)

D	+	D	$\longrightarrow$	^{3}He	+	n	+	3.27	MeV	(50 %)
			or	T	+	p	+	4.03	MeV	(50 %)
D	+	^{3}He	$\longrightarrow$	^{4}He	+	p	+	18.35	MeV	
D	+	T	$\longrightarrow$	^{4}He	+	n	+	17.59	MeV	
p	+	^{11}B	$\longrightarrow$	$3\,^4$He			+	8.7	MeV	

Because the kinetic energy of the reactants is much lower than the energy gained in the reaction, the distribution of the reaction energy onto the two product particles is inverse proportional to their mass, i.e. $E_1/E_2 = m_2/m_1$. In the DT-reaction, e.g. the α-particle has an energy of 3.54 MeV, and the neutron has 14.05 MeV. The first four reactions (for which the cross sections are shown in Fig. 2.3) can be summarized as

$$3\mathrm{D} \longrightarrow {}^4\mathrm{He} + \mathrm{p} + \mathrm{n} \quad + 21.6\,\mathrm{MeV}\,,$$

and therefore rely on deuterium as fuel only. Since the weight fraction of deuterium in water is 3.3×10^{-5}, the energy content of water is about 11.5 GJ per litre, which is about 350 times larger than the chemical energy density of gasoline. This demonstrates the huge potential afforded by nuclear fusion as an energy source.

All the reaction cross sections in Fig. 2.3 show a steep increase with the relative energy, as discussed before, but the D-T reaction

$$\mathrm{D} + \mathrm{T} \longrightarrow {}^4\mathrm{He} + \mathrm{n} \quad + 17.6\,\mathrm{MeV}$$

has by far the largest cross-section at the lowest energies. This makes the D-T fusion process the most promising candidate for an energy-producing system. The special role of D-T reactions becomes clear from the energy levels of the unstable ^{5}He nucleus shown in Fig. 2.4. It

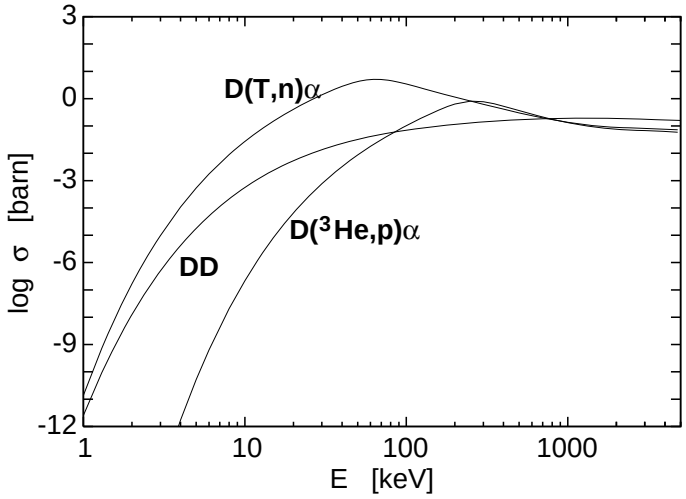

Figure 2.3: Measured cross-sections for different fusion reactions as a function of the center of mass energy [3]. The curve labeleld DD shows the sum of the cross sections for both branches of this reaction. Reaction cross sections are usually measured in barn, where 1 barn = 10^{-28} m^2.

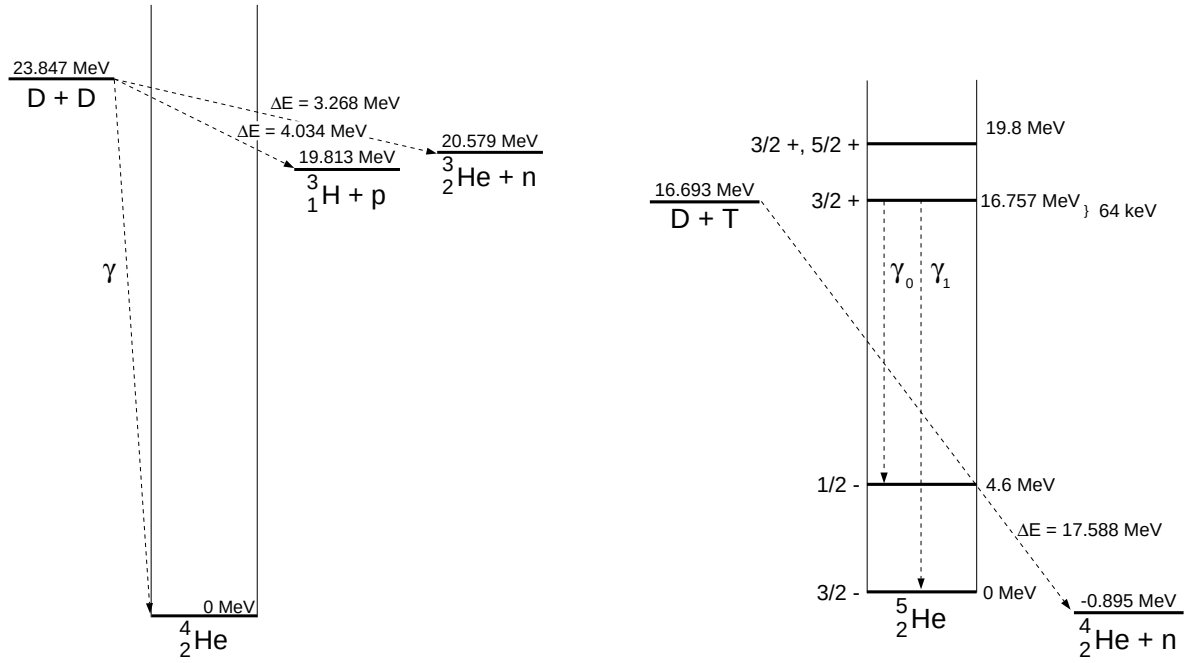

Figure 2.4: Left: Energy diagram of the ^{4}He nucleus and
Right: Of the unstable ^{5}He nucleus (right), where the resonance at 16.76 MeV dominates the reaction cross section. The numbers left of the level scheme indicate the J-value and parity of the respective level.

has an excited state just 64 keV above the sum of the masses of deuterium and tritium. The D-T fusion cross-section therefore reaches its maximum at this energy difference, due to the resonance-like reaction mechanism. The DD reactions (see Fig. 2.4, left part) show no such resonances, and their cross sections are solely governed by the tunneling probability, showing a smooth increase without any maximum, while the D^{3}He reaction also has a resonance at about 270 keV in the ^{5}Li system, not shown here.

To be a candidate for an energy-producing system, the fusion fuel has to be sufficiently abun-

Table 2.1: Estimated world energy resources. The figures are only indicative, being dependent on prices and subject to uncertainty because of incomplete exploration.

Present world annual primary energy consumption	3×10^{11} gigajoules	
Resources		
Coal	10^{14}	300 years
Oil	1.2×10^{13}	40 years
Natural Gas	1.4×10^{13}	50 years
^{235}U (fission reactors)	10^{13}	30 years
^{238}U and ^{232}Th (breader reactors)	10^{16}	30000 years
Lithium (D-T fusion reactors):		
Land	10^{16}	30000 years
Oceans	10^{19}	3×10^{7} years

dant. As mentioned earlier, deuterium occurs with a weight fraction of 3.3×10^{-5} in water. Given the water of the oceans, the static energy range is larger than the time the sun will continue to burn (a few billion years).

Tritium is an unstable radioactive isotope. It decays to

$$\mathrm{T} \longrightarrow {}^{3}\mathrm{He} + \mathrm{e}^{-} + \bar{\nu}_e$$

with a half-life of 12.3 years. Note the previously mentioned neutrino production of this β^- decay. Owing to the unstable character of tritium no significant amounts exist, but tritium can be produced with nuclear reactions of the neutrons from the D-T reaction and lithium

$$\begin{aligned} n + {}^{6}\mathrm{Li} &\longrightarrow {}^{4}\mathrm{He} + \mathrm{T} \quad +4.8\,\mathrm{MeV}\,, \\ n + {}^{7}\mathrm{Li} &\longrightarrow {}^{4}\mathrm{He} + \mathrm{T} + \mathrm{n}' \quad -2.5\,\mathrm{MeV}\,. \end{aligned}$$

The reaction with ^{7}Li is particularly important because it does not consume a neutron and opens the possibility for self-sufficient tritium production in a fusion reactor, i.e. each fusion neutron will produce at least one new tritium nucleus.

The ultimate fusion fuel will thus be deuterium and lithium. The latter is also very abundant and widespread in the earth's crust and even ocean water contains an average concentration of about 0.15 ppm (1 ppm = parts per million). Tab. 2.3 summarizes the estimated world energy resources.

2.4 Thermonuclear fusion

As discussed before, for a fusion reaction to occur, the two nuclei have to *touch* each other since the range of the nuclear force is of the order of the dimensions of the nuclei. The repulsive

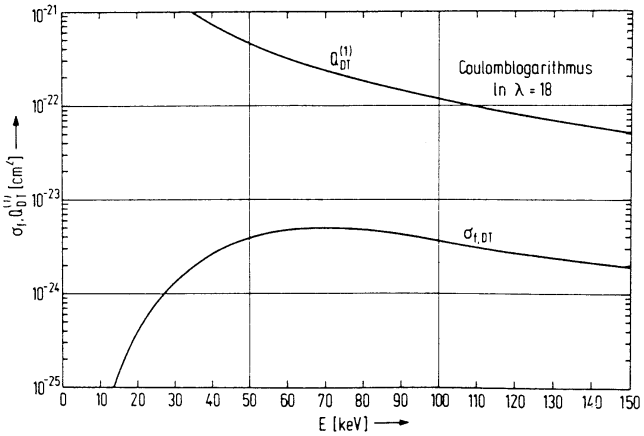

Figure 2.5: Comparison of the D-T fusion cross-section $\sigma_{f,DT}$ and the cross-section for momentum exchange by Coulomb scattering Q_{DT} in a fusion relevant plasma.

Coulomb force counteracts all attempts to bring them close together. This is what the difficult research on nuclear fusion is all about: How can the two reaction partners be brought into contact?

The simplest approach to realize the fusion reactions would be to accelerate the reactants to about 100 keV and bring them to collision. This does not lead to a positive energy balance, since the elastic Coulomb scattering as another reaction type has a much larger cross-section, as shown in Fig. 2.5. Thus the two particle beams would just scatter and diverge after one interaction.

A way of overcoming this problem is to confine a thermalized mixture of deuterium and tritium particles at energies of about 10 keV. Since the average energy of particles at a certain temperature is about kT, where k is the Boltzmann constant, temperatures are often given in electron volt units (1 eV $\hat{=}$ 1.16×10^4 °C). At energies of 10 keV the hydrogen atoms are completely ionized and form a plasma of charged ions and electrons. The basic physics of plasmas are discussed in chap. 1. For now it should suffice to observe that in a plasma the particles thermalize as a result of many Coulomb scattering processes and thus entail a Maxwellian velocity distribution

$$f(v) = n \left(\frac{m}{2\pi kT} \right)^{3/2} \cdot \exp\left(-\frac{mv^2}{2\,kT} \right) ,$$

where f is the number of particles in the velocity interval between v and $v+dv$, n is the density of particles, m is their mass, and kT is their temperature.

The reaction rate per unit volume R can be written as

$$R = n_D \cdot n_T \cdot \langle \sigma\, v \rangle$$

with v now being the relative particle velocity and $\langle \sigma\, v \rangle$ being the reaction parameter, i.e. the average of the product of cross-section times velocity.

Calculation of the reaction parameter requires integration over the distribution function of deuterium and tritium. After some numerical transformations one obtains

$$\langle \sigma\, v \rangle = \frac{4}{(2\pi m_r)^{1/2} (kT)^{3/2}} \int \sigma(\varepsilon_r) \cdot \varepsilon_r \cdot \exp\left(-\frac{\varepsilon_r}{kT} \right) \, d\varepsilon_r ,$$

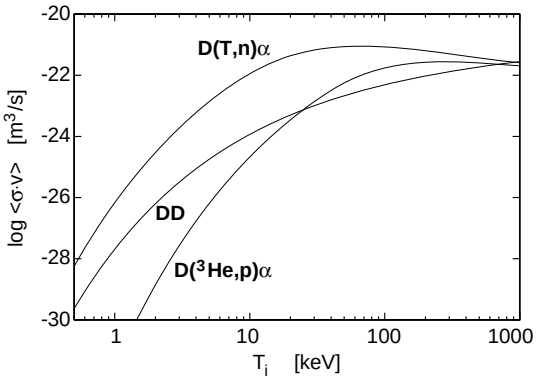

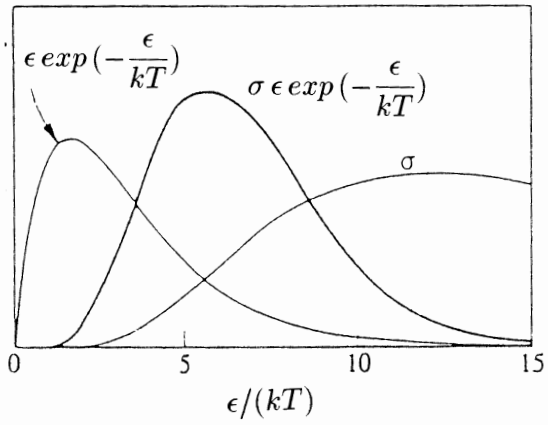

Figure 2.6: Left: Reaction parameter $\langle \sigma\, v \rangle$ as a function of ion temperature T_i for different fusion reactions [3].
Right: Graph of integrand of the reaction parameter equation and of its two factors $\sigma(\varepsilon)$ and $\varepsilon \cdot \exp(-\varepsilon/kT)$ versus the normalized energy ε/T for a D-T plasma at T = 10 keV.

where m_r is the reduced mass, and ε_r the relative kinetic energy.

Fig. 2.6 left shows the reaction parameter for some important fusion reactions. At temperatures of interest the nuclear reactions come predominantly from the tail of the distribution. This is illustrated in Fig. 2.6 right, where the integrand of the last equation is plotted versus ε_r/T together with the two factors $\sigma(\varepsilon)$ and $\varepsilon \cdot \exp(-\varepsilon/kT)$ for a D-T plasma at a temperature of 10 keV.

Thermalization is thus not just a way of handling the large cross-sections for elastic Coulomb scattering, it also considerably increases the reaction rate considerably in relation to beam experiments with single particle energies.

2.5 Ignition

In the following the condition which a thermalized D-T plasma has to satisfy to serve as an energy producing system is investigated. Historically, in 1957 John D. Lawson deduced a criterion for a positive energy balance using quantities such as the thermal cycle efficiency η of power reactors [2]. Today the approach has changed slightly to a more physics oriented condition: The aim is an ignited plasma where all energy losses are compensated by the α-particles from the fusion reactions, which transfer their energy of 3.5 MeV to the plasma while slowing down. The neutrons cannot be confined and leave the plasma without interaction.

Transport processes such as diffusion, convection, charge exchange and others are empirically described by an energy confinement time τ_E leading to the power loss term $3nkT/\tau_E$ with $3nkT$ as the inner thermal plasma energy (n is the electron density). Note that this is twice the ideal gas value since every hydrogen atom is split into two particles (electron and nucleus). Another loss mechanism is the bremsstrahlung, which becomes particularly important at high temperatures and impurity concentrations. The power loss due to bremsstrahlung can be written as

$$P_{bremsstrahlung} = c_1 \cdot n^2 \cdot Z_{eff} \cdot (kT)^{1/2}$$

with c_1 being the bremsstrahlungs constant ($c_1 = 5.4 \times 10^{-37}\,\mathrm{Wm^3keV^{-1/2}}$), and Z_{eff} the effective charge of the plasma, including all (impurity) species: $Z_{eff} = \Sigma_z n_z Z^2/n$.

The energy balance now reads

$$\left(\frac{n}{2}\right)^2 \langle\sigma v\rangle \cdot \varepsilon_\alpha = 3nkT/\tau_E + c_1 n^2 Z_{eff}(kT)^{1/2}$$

and this can be rewritten to the ignition condition

$$n\tau_E = \frac{12\,kT}{\langle\sigma v\rangle\varepsilon_\alpha - 4c_1 Z_{eff}(kT)^{1/2}}\,,$$

where ε_α is the energy of the α-particle, 3.54 MeV. This equation shows that the product of the particle density and energy confinement time is only a function of the plasma temperature, with a minimum at about 13 keV. In the range of 10 keV the reaction parameter $\langle\sigma v\rangle$ is roughly proportional to T^2, which motivated the definition of the so-called fusion product

$$n\tau T = \frac{12\,kT^2}{\langle\sigma v\rangle\varepsilon_\alpha - 4c_1 Z_{eff}(kT)^{1/2}}$$

which has a flat minimum of about $35 \times 10^{20}\,\mathrm{s/m^3keV}$ around 10 keV. The fusion product dictates the strategy for developing fusion power as an energy producing system: One has to attain temperatures of around 10 keV (about 100 million °C) and achieve the required density and energy confinement time simultaneously. There are two distinct approaches

1. The hot plasma is confined by strong magnetic fields leading to maximum densities of about $1.5 \times 10^{20}\,\mathrm{m^{-3}}$, which is 2×10^5 times smaller than the atom density of a gas under normal conditions. With these densities, the energy confinement time required is in the range of 2–4 seconds. This approach, which is the main line in fusion research, will be covered by most of the following lectures, and is introduced in the next section.

2. The other extreme is to maximize the density. This can be done by strong, symmetric heating of a small D-T pellet. The heating can be done with lasers or particle beams and leads to ablation of some material causing implosion due to momentum conservation. It is clear that the energy confinement time is extremely short in this concept: it is the time required for the particles to leave the hot implosion center. Since it is the mass inertia which causes the finiteness of this time, this approach to fusion is often called *inertial fusion*. The density required is about 1 000 times the density of liquid D-T; the pressure in the implosion center reaches (at temperatures of 10 keV) that in the center of the sun. A detailed description of the actual status in this area can be found in references [7] and [8].

Fig. 2.7 left illustrates the progress of nuclear fusion research in approaching the required $n\tau T$ condition. Today a factor seven is missing for ignition, whereas in the mid-sixties the best experiments fell short of the required conditions by more than five orders of magnitude. However, it has to be kept in mind that achieving ignited plasmas is not sufficient for building fusion reactors. In addition, this plasma state has to be maintained for very long times to allow continuous energy production. One of the most difficult problems will be the interaction of the edge plasma with the surrounding structures and the removal of helium ash. Consequently, edge plasmas constitute an increasingly important research topic.

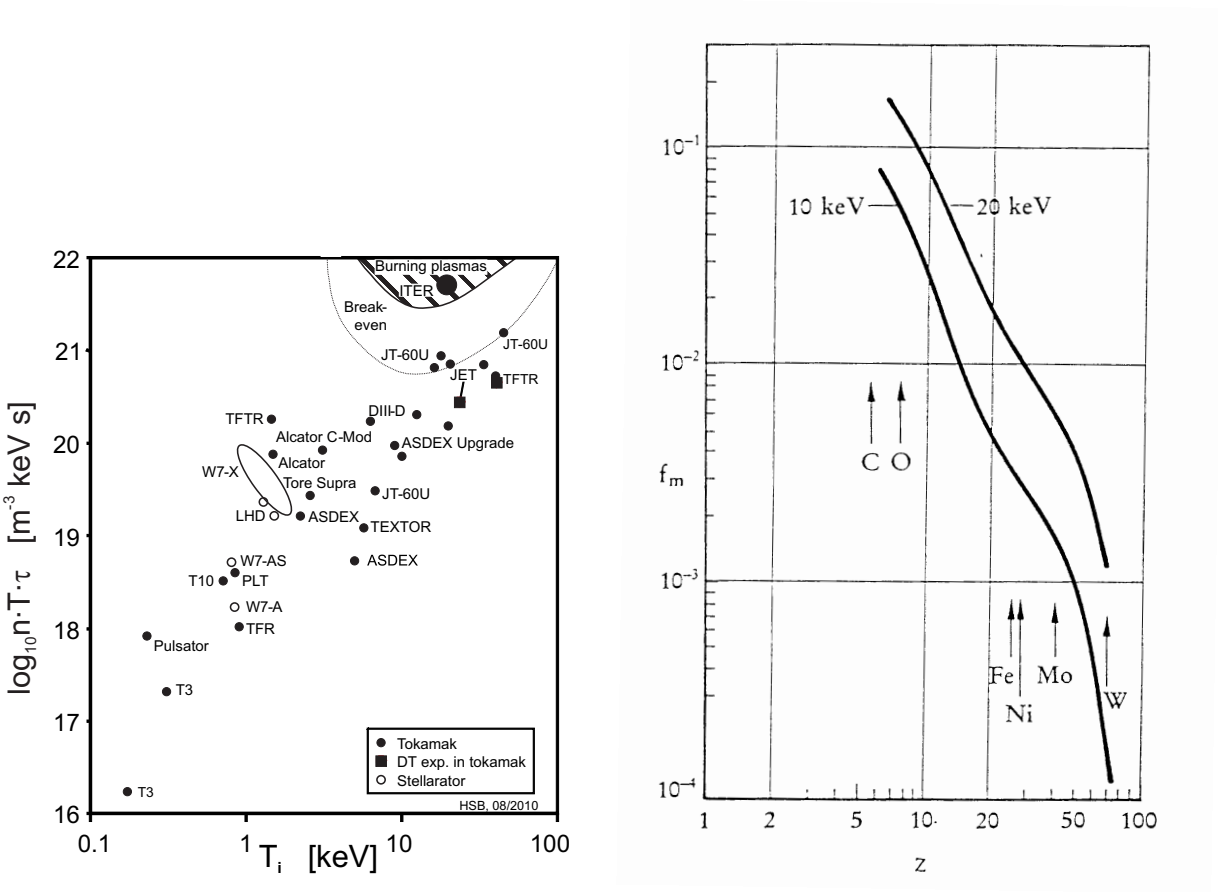

Figure 2.7: Left: Diagram of $nT\tau$ values versus T obtained in different experiments.
Right: Maximum tolerable impurity concentrations in a plasma to reach ignition.

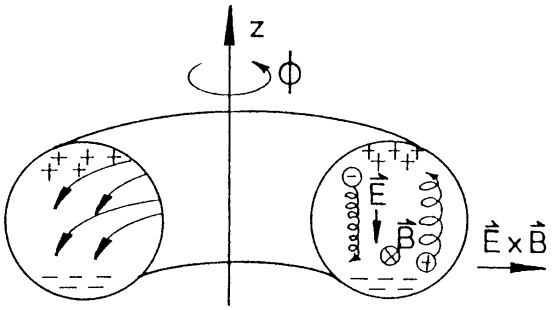

Figure 2.8: Vertical drifts and associated E × B in a toroidal field.

Impurities from the walls worsen the ignition condition in two ways. They dilute the fuel concentration and even in small amounts they can significantly enhance the radiation losses. Fig. 2.7 right shows the maximum tolerable impurity concentration to reach ignition. Depending on the charge it ranges from a few % for light atoms to the few 10^{-4} level for high Z materials.

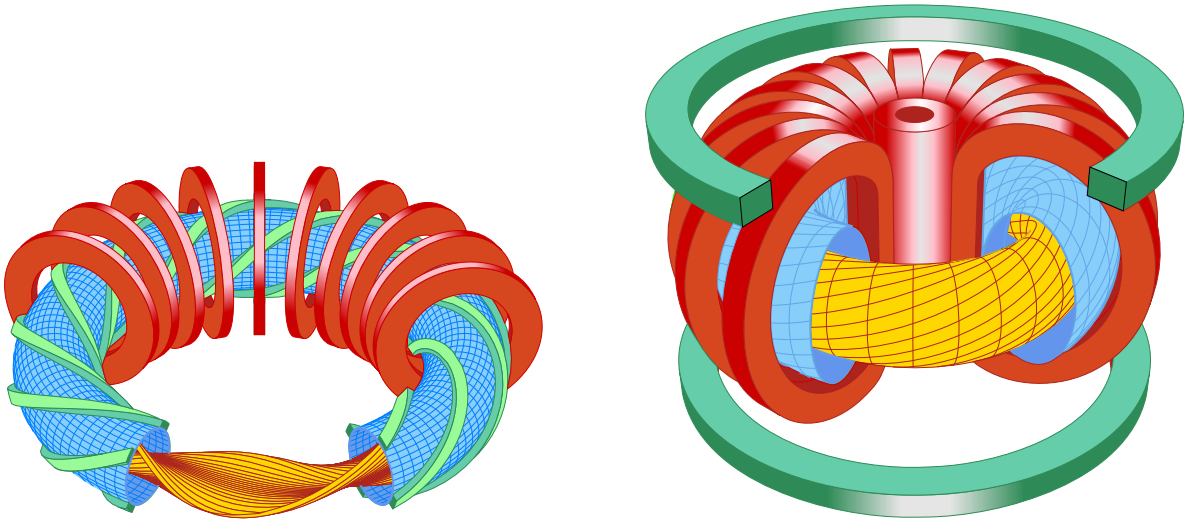

Figure 2.9: Left: Schematic view of a stellarator with four helical coils wound onto the vacuum vessel.
Right: Tokamak concept. The innermost cylindrical coil is the transformer coil for inducing a plasma current. The toroidal coils above and below the machine create a vertical field for plasma shaping and position control.

2.6 Magnetic confinement

As discussed in chap. 1, plasmas can be confined by magnetic fields, but in linear configurations the end losses are by far too large to reach the necessary energy confinement time τ_E of the order of some seconds. These end losses can be completely avoided in a toroidal system, but in a simple toroidal system with purely toroidal magnetic field, the magnetic field curvature and gradient (approximately as in Fig. 2.8) result in a vertical drift which is in opposite directions for ions and electrons. The resulting electric field causes an outward $\mathrm{E} \times \mathrm{B}$ drift of the whole plasma, and therefore such a simple magnetic field configuration will be unstable. To avoid this charge separation, it is necessary to twist the magnetic field lines by additional magnetic field components. Then, single field lines map out so-called flux surfaces. On these flux surfaces, plasma transport is fast, as it is always parallel to B, and therefore plasma parameters usually are constant on a given flux surface. Perpendicular to the flux surfaces, transport is hindered because particle motion perpendicular to B is restricted by the Lorentz force, and therefore plasma parameters can vary strongly in this direction.

Two different principles for twisting the magnetic field lines have been invented in the 50's, and are under investigation worldwide.

2.6.1 The stellarator

The stellarator was invented in 1951 by Lyman Spitzer, Jr. in Princeton. In a stellarator the twist of the field lines is created by external coils wound around the plasma torus, as shown in Fig. 2.9 left. Due to these external currents the plasma shape is not circular, but shows some indentation. In this case, with four coils (neighbouring coils carry opposite current), the plasma has an oval shape.

These external coils have the advantage that the current can be controlled from outside, and can flow continously, but the configuration shown in Fig. 2.9 left, is very difficult from the engineering point of view, due to the interlinked magnetic coil systems. Also, these *classical* stellarators have shown a rather poor confinement of particles and energy. A solution for both problems has been found by means of numerical optimization of stellarator configurations. Following these studies, *classical* stellarators nowadays have been replaced by *modular* stellarators, where the planar toroidal coils and the helical coils have been replaced by one complex, but modular system of non-planar coils, as will be discussed in chap. 12 and chap. 13.

2.6.2 The tokamak

The second approach is the tokamak proposed by the two Russian physicists I. Tamm and A.D. Sakharov, in the year 1952 and realized by L.A. Artsimovich. The word *tokamak* itself is derived from the Russian words for toroidal chamber with magnetic field. The tokamak concept is outlined in Fig. 2.9 right. The toroidal magnetic field is provided by simple magnets and the necessary twist is produced by the plasma itself, by means of an electric current in the plasma which gives rise to the poloidal component of the twisted magnetic field. The current also serves for plasma build-up and heating. This current is produced by induction, the plasma acting as the secondary winding of a transformer. Tokamaks have proved to be very successful in improving the desired fusion plasma conditions and the today's best experiments are based on the tokamak principle. Of course, a transformer can induce the (dc-) plasma current only during a finite time, while, as mentioned before, a stellarator may principally run steady-state. For truely continuous tokamak operation, alternative current drive methods are being developed. Another disadvantage of the required large plasma current is the potential danger of so-called disruptions: Uncontrolled very fast (~ 10 ms) plasma current decays which can give rise to large forces on the machine.

More details on tomaka physics are described in chap. 8 and chap. 7 and a review on the status of tokamak research is given in [6].

2.6.3 The fusion reactor

The basic geometry of fusion reactors will be a torus (ring) for magnetically confined plasmas. A schematic cross-section of such a reactor is shown in Fig. 2.10. The hot plasma is surrounded by the first wall and blanket. The latter is filled with lithium to produce the tritium, as discussed before, and the majority of thermal energy of the plant is delivered here by neutron moderation. A shield is provided behind the blanket to stop the neutrons not captured by the blanket in order to reduce the heat and radiation loads to the cold structures of the superconducting magnets. The application of superconduction is mandatory for fusion reactors to obtain a positive energy balance.

2.7 Muon-catalyzed fusion

The real issue in achieving nuclear fusion is to overcome the repulsive Coulomb forces of light nuclei. The *conventional* approach is strong heating to reach the ignition conditions described above. Another, more exotic, way is to screen the electric charge by replacing the electron in

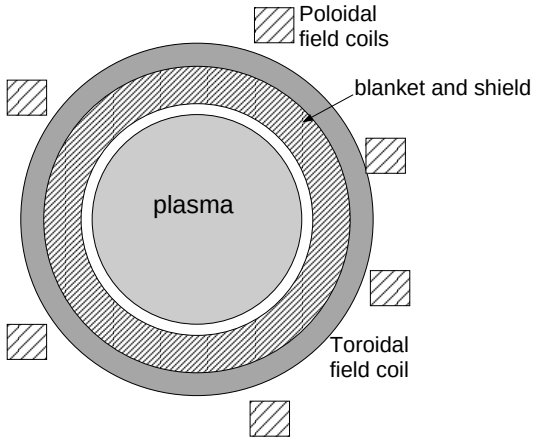

Figure 2.10: Layout of principal components in a conceptual fusion reactor.

the hydrogen atom with a muon [9]. This idea was first proposed by A.D. Sakharov in 1948. A muon is an elementary particle, a so-called lepton (*light* particle). This muon has the same properties as an electron, the only difference being that its mass is 200 times larger. Due to its larger mass the muon decays with a half-life of 1.5×10^{-6} seconds

$$\mu^- \longrightarrow e^- + \overline{\nu}_e + \nu_\mu \ .$$

Muons can be produced in accelerators which provide collisions between accelerated protons and some other material. In these collisions many pions are produced. A pion is the lightest elementary particle participating in the strong interaction (so-called hadrons). The three types of pions (π^-, π^+ and π^0) are produced in equal amounts. A negative muon is formed from the decay of a negative pion

$$\pi^- \longrightarrow \mu^- + \overline{\nu}_\mu \ .$$

In a D-T mixture the muon slows down very fast ($\approx 10^{-9}$ s) and forms a $D\mu$ or $T\mu$ atom with a small Bohr radius of

$$a_\mu = a_e \cdot m_e/m_\mu \approx 2.5 \cdot 10^{-13}\,\mathrm{m} \ .$$

This reduced atomic radius is the key point for possible catalyzed nuclear fusion: If a $D\mu T$ molecule is formed, it takes just 10^{-12} s until quantum mechanical tunnelling triggers a fusion reaction

$$\mathrm{D}\mu T \longrightarrow^4 \mathrm{He} + \mathrm{n} + \mu^- \quad + \ 17.6\,\mathrm{MeV} \ .$$

There are two limiting factors in this approach: the first is the time needed to form a DμT molecule. This time can be influenced by some resonance mechanisms. The second limitation comes from the 0.6% probability that the muon will stick to the helium atom after the fusion reaction and will thus be lost for catalyzing more fusion reactions during its lifetime. Recently, experiments obtained fusion rates of more than 100 reactions per muon. For a pure energy producing system this rate is not sufficient, since about 3 GeV ($= 3 \times 10^9$ eV) is needed to produce one negative muon.

References

[1] G. Gamov; *Zur Quantentheorie des Atomkernes*, Zeitschrift für Physik **51** (1928), p. 204–212.

[2] J.D. Lawson; *Some Criteria for a Power Producing Thermonuclear Reactor*, Proceedings of the Physical Society **B70** (1967), p.6.

[3] H.-S. Bosch, G.M. Hale; *Improved Formulas for Fusion Cross-Sections and Thermal Reactivities*, Nuclear Fusion **32** (1992), p. 611–631.

[4] J. Raeder et al.; *Kontrollierte Kernfusion*,
Teubner Verlag, Stuttgart (1981).

[5] U. Schumacher; *Fusionsforschung*,
Wissenschaftliche Buchgesellschaft, Darmstadt (1993).

[6] J.G. Cordey, R.J. Goldston, R.R. Parker;
Progress toward a Tokamak Fusion Reactor, Physics Today, January 1992, p. 22–42.

[7] J.D. Lindl, R.L. McCrory, E.M. Campbell;
Progress Toward Ignition and Burn Propagation in Inertial Confinement Fusion, Physics Today, September 1992, p. 32–40.

[8] W.J. Hogan, R. Bangerter, G.L. Kulcinski;
Energy from Inertial Fusion, Physics Today, September 1992, p. 42–50.

[9] S.E. Jones; *Muon-Catalysed Fusion Revisited*, Nature **231** (1986), p. 127–133.

Chapter 3

An introduction to MHD, or magnetic fluid dynamics

Bruce D. Scott

3.1 What MHD is

Magneto-hydro-dynamics (MHD) means magnetic fluid dynamics. It is a model system designed to treat macroscopic dynamics of an electrically neutral fluid which is nevertheless made up of moving charged particles, and hence reacts to magnetic fields. Because the magnetic field is in turn produced by electric currents – here, a relative drift between the two fluids of opposite charge density which permeate each other – the resulting dynamical system is rich in nonlinear character.

This is a heuristic introduction to the ideas of fluid dynamics and MHD. Each fluid – they may be termed electrons and ions – is separately treated as a perfect fluid which reacts in a dissipation-free way to the electric and magnetic fields. By perfect fluid, the concept of thermodynamic equilibrium is implied: The effects of dissipation in all forms are taken to be negligible. These include resistivity, thermal conductivity, and viscosity. The two fluids interact only through the electric and magnetic fields they induce. These fields in turn react to changes in the distribution of sources, which are the charge densities and currents represented by the two fluids. Externally imposed fields may also be present. An infinitesimal element of each fluid is assumed to contain an arbitrarily large number of charged particles of the corresponding species, but to be small compared to the spatial scale over which macroscopic thermodynamic or field quantity varies. The picture is a meaningful one if this scale is large compared to the mean-free path between particle collisions, and the radius of gyration of each particle about magnetic field lines is negligibly small. This is the *ideal two-fluid model* of plasma dynamics.

Then, because the mass of an individual electron is so much smaller than that of an individual ion, the contribution of the electrons to fluid inertia may be neglected. With a few additional assumptions which in effect define a parameter regime, the system is treated as a single fluid which responds to a magnetic force of the Lorentz type, except that the plasma current enters instead of the fluid velocity. The magnetic field, responding to the electric field as usual, is actually advected by the velocity field, since the latter is related in a constitutive way to the electric field. This is the *ideal MHD model* of plasma dynamics, a subset of the two-fluid model.

3.2 The ideas of fluid dynamics

A fluid is in essence a continuous medium. Rather than an ensemble of particles, each individually treated, *populations* of particles are treated. The system is described in terms of a velocity flow field, a density field, and a few thermodynamic state variables. In the simplest picture, the fluid is an ideal gas, in which all state variables are simple relations of the density and temperature.

3.2.1 The density in a changing flow field – conservation of particles

We are first interested in how the density of the fluid evolves, when the flow field is known. This involves the deformation of volumes by the flow. Consider first a volume V, which is fixed in space. The conservation of particles follows simply from counting: The change of the number of particles N, in V is given by the number of particles entering V, less those that leave V. Consider that V is bounded by a surface S, an element of which is ΔS with unit normal $\hat{\mathrm{e}}_S$. For each area element, the number of particles which cross it in a time interval Δt, is given by

$$\delta N = n\,\Delta x\,\Delta S\,, \qquad\qquad \Delta x = v\cos\theta\,\Delta t = \mathrm{v}\cdot\hat{\mathrm{e}}_S\,\Delta t\,,$$

where $n = N/V$ is the density of particles per unit volume, θ is the angle between the velocity vector and the unit normal, and Δx gives the thickness of the region containing particles which cross ΔS during Δt (a note on signs: The unit normal points outward, so a positive δN, indicating particles leaving V, contributes negatively to the change in the total number of particles ΔN).

Since S is a closed surface, we may add up all the contributions from the ΔS's by performing a surface integral

$$\Delta N = -\oint_S \Delta S\, n\mathrm{v}\cdot\hat{\mathrm{e}}_S\,\Delta t\,.$$

Since V is fixed, a change in N affects the density

$$\Delta N = \oint_V dV\,\Delta n\,,$$

so upon setting these two expressions equal, we have

$$\oint_V dV\,\Delta n = -\oint_S \mathrm{dS}\cdot(n\mathrm{v})\,\Delta t\,,$$

where ΔS and $\hat{\mathrm{e}}_S$ have been combined into dS. Note now that since S is the surface which encloses V, we may apply the Gaussian divergence theorem:

> For any volume V enclosed by surface S, with directional element dS, any continuously differentiable vector F satisfies
>
> $$\oint_V dV\,\nabla\cdot\mathrm{F} = \oint_S \mathrm{dS}\cdot\mathrm{F}\,.$$

Therefore, we may write

$$\oint_V dV\,\Delta n = -\Delta t\oint_V dV\,\nabla\cdot n\mathrm{v}\,.$$

This is valid for arbitrary V; specifically, it is valid for an infinitesimal volume about any point. This means the integrands must themselves be equal, since in general they do not vanish. Further taking $\Delta t \to 0$, we obtain

$$\frac{\partial n}{\partial t} = -\nabla \cdot n\mathrm{v}$$

as a statement of conservation of particles of number density n, advected by velocity v. It holds for a *fixed* reference frame. The partial time derivative refers to the fact that V is fixed in space.

So what is meant by divergence?

Suppose now that we take the same flow and particle distribution, but now let the boundary surface elements of the volume move with the fluid. Note now that no particles enter or leave V

$$\Delta N = 0 \, .$$

The volume does, however, change with time: since the density is given by $n = N/V$, its change is inverse to that in V

$$\frac{\Delta n}{n} = -\frac{\Delta V}{V} \, .$$

At each point, the boundary element moves with the velocity

$$\Delta \mathrm{x} = \mathrm{v}\Delta t \, .$$

The separation of points changes according to spatial variations in the velocity

$$\Delta \mathrm{x}_2 - \Delta \mathrm{x}_1 = (\mathrm{v}_2 - \mathrm{v}_1)\Delta t \, .$$

A volume may be expanded in a combination of two ways: Spreading or stretching. If the direction of a surface element dS is taken as the z-direction at some point, spreading is due to the expansion perpendicular to the element: $\partial v_x/\partial x + \partial v_y/\partial y$. Stretching is due to longitudinal variation: $\partial v_z/\partial z$. The sum of these is called the *divergence*, and the divergence of a velocity means the same thing as the expansion of the advected volume

$$\Delta V = V\nabla \cdot (\Delta \mathrm{x}) \, ,$$

or, including Δt, which commutes with spatial derivatives

$$\frac{\Delta V}{\Delta t} = V\nabla \cdot \frac{\Delta \mathrm{x}}{\Delta t} = V\nabla \cdot \mathrm{v} \, .$$

With this for the volume change, the density change is given by

$$\frac{\Delta n}{\Delta t} = -\frac{n}{V}\frac{\Delta V}{\Delta t} = -n\nabla \cdot \mathrm{v} \, ,$$

or

$$\frac{dn}{dt} = -n\nabla \cdot \mathrm{v} \, ,$$

as a statement of conservation of particles of number density n, advected by velocity v. It holds for the *co-moving* reference frame. Note that the total time derivative d/dt, gives changes in the frame moving with the fluid at each point, hence the name co-moving.

One final note: A common name for the equation for the conservation of particles is often called the *continuity equation*, since the fact that n and v are continuously differentiable field quantities has been implicitly used to get it.

3.2.2 The advective derivative and the co-moving reference frame

We now have two statements of the general conservation of particles in terms of the density, n, and the velocity with which they are advected v. One is in the fixed reference frame

$$\frac{\partial n}{\partial t} = -\nabla \cdot n\mathrm{v} \, .$$

The other is in the co-moving reference frame

$$\frac{dn}{dt} = -n\nabla \cdot \mathrm{v} \, .$$

These are actually the same statement in two different coordinate systems. Let the fixed system be denoted as (t,x,y,z) and the co-moving frame as (t',x',y',z'). The transformation between them, which is a *local* transformation, may be written

$$dx' = dx - v_x dt \, , \qquad dy' = dy - v_y dt \, , \qquad dz' = dz - v_z dt \, .$$

The time derivative transforms as

$$\begin{aligned} \frac{d}{dt} &= \frac{\partial}{\partial t} + \frac{dx}{dt}\frac{\partial}{\partial x} + \frac{dy}{dt}\frac{\partial}{\partial y} + \frac{dz}{dt}\frac{\partial}{\partial z} \\ &= \frac{\partial}{\partial t} + v_x\frac{\partial}{\partial x} + v_y\frac{\partial}{\partial y} + v_z\frac{\partial}{\partial z} \, , \end{aligned}$$

where the velocity components are not differentiated because the transformation is local. In general form

$$\frac{d}{dt} = \frac{\partial}{\partial t} + \mathrm{v} \cdot \nabla \, .$$

This is the time derivative in the co-moving frame, written in terms of the time derivative in the fixed frame and the local, instantaneous velocity. It is also known as the *advective derivative*, or in some texts the substantiative derivative. Its usefulness is that the laws governing the motion or constitutive change of fluid elements are often most easily formulated in the co-moving frame (or the fluid element's rest frame) and then transformed into the fixed frame. One can readily see that the two equations for the fluid density are equivalent.

3.2.3 Forces on the fluid – how the velocity changes

We now allow the velocity to change, and see how it is caused to change. We examine the forces on the fluid element in the co-moving frame, and then transform to the fixed frame. We consider only fluid pressure and electromagnetic (Lorentz) forces, neglecting such others as gravitation or the effects of moving boundaries.

Consider first the fluid pressure p. Each of the fluid particles is moving with a velocity w, in the co-moving frame, and the average of w over all the particles in a fluid element is zero. Nevertheless, the fluid exerts pressure on any surface, according to the rate at which momentum is transferred by the random particle motion. If p is prescribed, we may compute the net force F, on any fluid element by adding up the forces ΔF, on each surface element dS:

$$\Delta\mathrm{F} = p\,\mathrm{dS} \, .$$

Summing all the force elements over a closed surface gives an area integral

$$\mathrm{F} = \oint_S \mathrm{dS}\, p \,.$$

Since the force is exerted on the enclosed volume, V, we may apply another vector theorem

> For any volume V enclosed by surface S, with directional element dS, any continuously differentiable scalar ζ satisfies
>
> $$\oint_V dV\, \nabla\zeta = \oint_S \mathrm{dS}\, \zeta \,.$$

It is important to get the correct sign: The force is exerted against the surface from the surrounding fluid; hence the signs in the above should all be negative (except for the theorem). Considering a cubical fluid element, oriented such that the pressure on the right is higher than that on the left: The forces on the top and bottom are equal and opposite, the forces on the front and back are equal and opposite, but the force from the right towards the left is greater than the force from the left toward the right. There is a net force from right to left, given by the pressure difference $\Delta p = p_{\mathrm{right}} - p_{\mathrm{left}}$, times the surface area ΔS. If the coordinates are set up such that z increases towards the right, we can see that the force from right to left is *opposite* to the directional gradient in the pressure. Since the size of the element is Δz, then the force is given by

$$\mathrm{F} = -\Delta p\, \Delta S\, \hat{\mathrm{e}}_z = -\Delta z\, \Delta S\, (\Delta p/\Delta z) \hat{\mathrm{e}}_z = -\Delta V\, \nabla p \to -\oint_V dV\, \nabla p \,.$$

This force acts to accelerate the fluid element. The mass in the element is given by the mass of each particle m, times the number of particles N, in the volume V. The element accelerates according to

$$Nm\frac{d\mathrm{v}}{dt} = \mathrm{F} \,,$$

or taking the volume to zero about a given point, the velocity change can be taken inside the integral

$$\oint_V dV\, nm\frac{d\mathrm{v}}{dt} = -\oint_V dV\, \nabla p \,.$$

Dispensing with the volumes as before, we obtain

$$nm\frac{d\mathrm{v}}{dt} = -\nabla p \,,$$

in the co-moving frame, and

$$nm\left(\frac{\partial}{\partial t} + \mathrm{v}\cdot\nabla\right)\mathrm{v} = -\nabla p \,,$$

in the fixed frame.

This is the force law which determines how the fluid velocity field changes in reaction to gradients in its pressure. Standing alone, it is the force law for a neutral fluid.

Adding the Lorentz force is straightforward, since the force is a body force, one which acts on the element as a whole and not through the surface. The force on N particles of charge q in the fixed frame is

$$\mathrm{F} = Nq\left(\mathrm{E} + \frac{\mathrm{v}}{c}\times\mathrm{B}\right) = \oint_V dV\, nq\left(\mathrm{E} + \frac{\mathrm{v}}{c}\times\mathrm{B}\right) \,,$$

so that the integrand is added to the neutral fluid force law to obtain the force law for a charged fluid

$$nm\left(\frac{\partial}{\partial t}+\mathrm{v}\cdot\nabla\right)\mathrm{v}=-\nabla p+nq\left(\mathrm{E}+\frac{\mathrm{v}}{c}\times\mathrm{B}\right)\ .$$

Note that one could just as easily derive the Lorentz force term in the co-moving frame as well, with v zero, and then transform to the fixed frame via the Lorentz transformation (the low-velocity form of which is the transformation used in sec. 3.2.2.

We now have equations describing the evolution of the density and velocity of a fluid in general, so we could build up the two-fluid system consisting of one set of these for each species, and then close the system with Maxwell's equations for the electric and magnetic fields. This would only be complete for an isothermal system, though, so we do need to discuss how the pressure changes.

3.2.4 Thermodynamics of an ideal fluid – how the temperature changes

The simplest system is the ideal fluid: One which evolves quasi-statically through successive states of local thermodynamic equilibrium. Changes are expected to be slow enough such that equilibrium is maintained, but fast enough so that fluid elements do not exchange entropy.

In thermodynamic equilibrium with only isentropic changes considered, the first law reads

$$\Delta E+p\Delta V=\Delta Q\rightarrow 0\ .$$

E is the internal energy of a given fluid element of N particles. For the ideal gas law

$$E=\frac{3}{2}NkT\ .$$

V is the volume occupied by the N particles. Over infinitesimal time intervals

$$\frac{dE}{dt}+p\frac{dV}{dt}=0\ ,$$

in the co-moving frame.

We already know how the volume changes

$$\frac{dV}{dt}=V\nabla\cdot\mathrm{v}\ .$$

Given that the number of particles is kept fixed

$$\frac{3}{2}Nk\frac{dT}{dt}+pV\nabla\cdot\mathrm{v}=0\ ,$$

and since the density is $n=N/V$,

$$\frac{3}{2}nk\frac{dT}{dt}+p\nabla\cdot\mathrm{v}=0\ .$$

Now, transforming to the fixed frame, we have the relation governing the change of the fluid's temperature given the flow field and all the thermodynamic state variables

$$\frac{3}{2}nk\left(\frac{\partial T}{\partial t}+\mathrm{v}\cdot\nabla T\right)+p\nabla\cdot\mathrm{v}=0\ .$$

3.2.5 The composite fluid plasma system

Under the preceding conditions: Perfect fluid with an ideal gas law, no reactions that create or destroy particles of any species, maintenance of local thermodynamic equilibrium...

The system of several fluids each made up of charged particles of species α evolves according to

$$\begin{aligned}
\frac{\partial n_\alpha}{\partial t} + \nabla \cdot n_\alpha \mathrm{v}_\alpha &= 0 \,, \\
n_\alpha m_\alpha \left(\frac{\partial}{\partial t} + \mathrm{v}_\alpha \cdot \nabla \right) \mathrm{v}_\alpha &= -\nabla p_\alpha + n_\alpha q_\alpha \left(\mathrm{E} + \frac{\mathrm{v}_\alpha}{c} \times \mathrm{B} \right) \,, \\
\frac{3}{2} n_\alpha k \left(\frac{\partial T_\alpha}{\partial t} + \mathrm{v}_\alpha \cdot \nabla T_\alpha \right) &+ p_\alpha \nabla \cdot \mathrm{v}_\alpha = 0 \,,
\end{aligned}$$

while the electric and magnetic fields evolve according to Maxwell's equations

$$\begin{aligned}
\nabla \cdot \mathrm{E} &= 4\pi \sum_\alpha n_\alpha q_\alpha \,, \\
\frac{1}{c} \frac{\partial \mathrm{E}}{\partial t} &= \nabla \times \mathrm{B} - \frac{4\pi}{c} \sum_\alpha n_\alpha q_\alpha \mathrm{v}_\alpha \,, \\
\nabla \cdot \mathrm{B} &= 0 \,, \\
\frac{1}{c} \frac{\partial \mathrm{B}}{\partial t} &= -\nabla \times \mathrm{E} \,.
\end{aligned}$$

Note that the charge density and the current have been specified in terms of the fluid variables

$$\rho_{ch} = \sum_\alpha n_\alpha q_\alpha \,, \qquad \mathrm{J} = \sum_\alpha n_\alpha q_\alpha \mathrm{v}_\alpha \,,$$

The above constitutes a closed system governing the evolution of several charged ideal fluids and the electric and magnetic fields they induce. Note that external fields may also be imposed.

3.3 From many to one – the MHD system

In many cases, the regime of parameters in which the plasma finds itself allows considerable simplification of the multi-fluid system. The fact that the electron mass is so much smaller than that of any ion allows one to neglect the electron inertia in comparison to that of the ions, with the result that the electron force equation becomes a relation for the electric field in terms of the velocity and magnetic field.

For purposes of illustration it is useful to consider that there is only one ion species.

The following assumptions are made:

1. The *displacement current*, which is the term involving the time derivative of E, is negligible because the time for a light wave to cross the system is much shorter than any relevant dynamical scale.

2. The electron mass is sufficiently small that parallel force balance on the electrons is maintained at all times. This allows the neglect of electron inertia. For the ideal MHD system we assume that the parallel electron dynamics are generally negligible; this means the components of both ∇p_e and E parallel to the magnetic field.

3. The drift velocity of the electrons relative to the ions due to the current is small compared to the ion velocity. This allows one to assume that all species move with the same velocity, when specifying velocities.

4. Pressure forces are negligible compared to Lorentz forces on all the fluids.

5. The system is approximately neutral, such that the total charge density is negligible compared to that of any constituent.

Note that this does not mean that $\mathrm{E} \to 0$, but that the spatial scale of any variation is large compared to the Debye length of the plasma, and that the plasma frequency is faster than any rate of change. This means, however, that we can use the relation of zero charge density as a good approximation for the electron density in terms of the ions. For one ion species with charge Ze, this means

$$n_e \approx Z n_i \ .$$

These assumptions will be checked once we explore the dynamical scales of the MHD system.

3.3.1 The MHD force equation

The electron and ion force equations appear as

$$\begin{aligned} n_i M_i \left(\frac{\partial}{\partial t} + \mathrm{v}_i \cdot \nabla \right) \mathrm{v}_i &= -\nabla p_i + n_i Z e \left(\mathrm{E} + \frac{\mathrm{v}_i}{c} \times \mathrm{B} \right) \ , \\ 0 &= -\nabla p_e - n_e e \left(\mathrm{E} + \frac{\mathrm{v}_e}{c} \times \mathrm{B} \right) \ , \end{aligned}$$

Adding these and using the charge neutrality relation, we obtain

$$\rho \left(\frac{\partial}{\partial t} + \mathrm{v} \cdot \nabla \right) \mathrm{v} = -\nabla p + \frac{1}{c} \mathrm{J} \times \mathrm{B} \ .$$

This is the MHD force equation. To get it, we have written p for the total pressure $p = p_e + p_i$, and $\rho = n_i M_i$ for the mass density. We have further dropped the subscript on the ion velocity, using this as the bulk fluid velocity. The electron velocity is obtainable from v and J. Note that the current is

$$\mathrm{J} = n_i Z e \mathrm{v}_i - n_e e \mathrm{v}_e \ .$$

The electrons have two roles:

1. They provide pressure, and can be dominant in doing so (but only if the temperatures are allowed to be unequal).

2. They keep the system quasi-neutral through their ability to move arbitrarily fast along the magnetic field lines.

3.3.2 Treating several ion species

One can easily generalise the MHD force equation to a system of several ion species by defining the total velocity as the velocity of the *center of mass*

$$\rho \mathrm{v} = \sum_i n_i M_i \mathrm{v}_i \ ,$$

where the sum is over all the ion species. The mass density evolves according to the continuity equations for all ion species

$$\frac{\partial \rho}{\partial t} + \nabla \cdot \rho \mathrm{v} = 0 \ .$$

Provided all the temperatures are equal, this can be done for the energy equation as well

$$C_v \left(\frac{\partial}{\partial t} + \mathrm{v} \cdot \nabla \right) T + p \nabla \cdot \mathrm{v} = 0 \ ,$$

where the specific heat at constant volume is

$$C_v = \frac{3}{2} k \sum_\alpha n_\alpha \ ,$$

and the sum is over all species, including the electrons. Alternatively, this may be combined with the continuity equation to reflect the fact that p/ρ^γ, with $\gamma = 5/3$, is conserved in the dynamics, even for several species (see below).

One very important note: The system can be treated as ideal either if the heat exchange among the particle populations is (1) negligible or (2) so fast that the temperatures are all kept equal. In laboratory plasmas the first of these limits is usually well-satisfied for dynamics, and the second is usually valid for quasi-static equilibria.

3.3.3 The MHD kinematic equation

We need now only determine how the magnetic field evolves, and since the current is given by

$$\mathrm{J} = \frac{c}{4\pi} \nabla \times \mathrm{B} \ ,$$

that will be enough to close the system.

The magnetic field evolves according to

$$\frac{1}{c} \frac{\partial \mathrm{B}}{\partial t} = -\nabla \times \mathrm{E} \ ,$$

and from the electron force equation we have

$$\mathrm{E} + \frac{\mathrm{v}_e}{c} \times \mathrm{B} = -\frac{1}{n_e e} \nabla p_e \ .$$

For the dynamical scales of interest, it will become clear that the pressure gradient is negligibly small in this equation (recall we are neglecting parallel electron dynamics). This is assumption (4) above. We have already assumed that J is small enough that the electron and ion velocities

are equal to high accuracy (assumption 3). This implies that the component of the fluid velocity across the magnetic field is given by the *E×B velocity*

$$\mathrm{v} = \frac{c}{B^2}\mathrm{E}\times\mathrm{B}\ ,$$

which means that all the particles E×B drift together across the magnetic field lines, preventing any significant charge build-up. Substituting for E in the equation for B, we obtain

$$\frac{\partial \mathrm{B}}{\partial t} = \nabla\times(\mathrm{v}\times\mathrm{B})\ .$$

This is the MHD kinematic equation. Whether or not the magnetic field has important effect on the dynamics, it describes how the magnetic field is advected by the flow velocity. Much of the character of MHD springs from this equation, especially its most important consequence: Flux conservation. We will see what this is and what it means in a moment.

3.3.4 MHD at a glance

The complete ideal MHD system is collected here for clarity.

The continuity equation

$$\frac{\partial \rho}{\partial t} + \nabla\cdot\rho\mathrm{v} = 0\ .$$

The MHD force equation

$$\rho\left(\frac{\partial}{\partial t} + \mathrm{v}\cdot\nabla\right)\mathrm{v} = -\nabla p + \frac{1}{c}\mathrm{J}\times\mathrm{B}\ .$$

The adiabatic pressure equation

$$\left(\frac{\partial}{\partial t} + \mathrm{v}\cdot\nabla\right)p + \frac{5}{3}p\nabla\cdot\mathrm{v} = 0\ .$$

The MHD kinematic equation

$$\frac{\partial \mathrm{B}}{\partial t} = \nabla\times(\mathrm{v}\times\mathrm{B})\ .$$

Ampere's law

$$\mathrm{J} = \frac{c}{4\pi}\nabla\times\mathrm{B}\ .$$

3.4 The flux conservation theorem of ideal MHD

There is an important result that arises immediately from the MHD kinematic equation. This is that the magnetic flux through any surface element advected by the fluid remains constant no matter what the flow field. Closely related is that the flux through the surface defined by any closed curve within the fluid is also conserved. The result gives rise to the concept of the magnetic flux tube.

3.4.1 Proving flux conservation

Consider an arbitrary, infinitesimal surface defined by a triangle of infinitesimal sides. Three points, x_0, x_1, x_2, are given, and the surface element is

$$\mathrm{dS} = \frac{1}{2}(\mathrm{x}_1 - \mathrm{x}_0)\times(\mathrm{x}_2 - \mathrm{x}_1) \; .$$

The magnetic flux through the surface is given by $\mathrm{B}\cdot\mathrm{dS}$, and it changes according to

$$\frac{d}{dt}\mathrm{B}\cdot\mathrm{dS} = \frac{d\mathrm{B}}{dt}\cdot\mathrm{dS} + \mathrm{B}\cdot\frac{d}{dt}\mathrm{dS} \; .$$

Remembering that the surface and magnetic field are advected by the fluid

$$\frac{d\mathrm{B}}{dt} = \frac{\partial \mathrm{B}}{\partial t} + \mathrm{v}\cdot\nabla\mathrm{B} \; .$$

Now find how the surface element changes

$$\frac{d}{dt}\mathrm{dS} = (\mathrm{x}_1 - \mathrm{x}_0)\times\frac{1}{2}(\mathrm{v}_2 - \mathrm{v}_1) + \frac{1}{2}(\mathrm{v}_1 - \mathrm{v}_0)\times(\mathrm{x}_2 - \mathrm{x}_1) \; ,$$

noting that $d\mathrm{x}/dt = \mathrm{v}$. Reform this in terms of contributions to $\Delta\mathrm{x}\times\mathrm{v}$

$$\begin{aligned}
\frac{d}{dt}\mathrm{dS} &= -(\mathrm{x}_1 - \mathrm{x}_0)\times\frac{1}{2}(\mathrm{v}_1 + \mathrm{v}_0) - (\mathrm{x}_2 - \mathrm{x}_1)\times\frac{1}{2}(\mathrm{v}_2 + \mathrm{v}_1) \\
&\qquad - (\mathrm{x}_0 - \mathrm{x}_2)\times\frac{1}{2}(\mathrm{v}_0 + \mathrm{v}_2) \\
&= -\sum_j \Delta\mathrm{x}_j\times\mathrm{v}_j \; ,
\end{aligned}$$

where j tracks the midpoint of each line segment. Employ a vector identity to replace this expression by

$$\frac{d}{dt}\mathrm{dS} = -(\mathrm{dS}\times\nabla)\times\mathrm{v} \; .$$

We require to further re-form this; using the component-index representation of the right side, we have

$$\begin{aligned}
[(\mathrm{dS}\times\nabla)\times\mathrm{v}]_i &= \varepsilon_{ipq}(\varepsilon_{plm}\Delta S_l\,\partial_m)\,v_q \\
&= \varepsilon_{pqi}(\varepsilon_{plm}\Delta S_l\,\partial_m)\,v_q \\
&= \Delta S_q\,\partial_i v_q - \Delta S_i\,\partial_q v_q \; ,
\end{aligned}$$

which may be written in vector form as

$$\frac{d}{dt}\mathrm{dS} = \mathrm{dS}(\nabla\cdot\mathrm{v}) - (\nabla\mathrm{v})\cdot\mathrm{dS} \; .$$

Inserting this back into the original expression for the flux evolution, we obtain

$$\begin{aligned}
\frac{d}{dt}\mathrm{B}\cdot\mathrm{dS} &= \left(\frac{\partial\mathrm{B}}{\partial t} + \mathrm{v}\cdot\nabla\mathrm{B}\right)\cdot\mathrm{dS} + \mathrm{B}\cdot\left[\mathrm{dS}(\nabla\cdot\mathrm{v}) - (\nabla\mathrm{v})\cdot\mathrm{dS}\right] \\
&= \mathrm{dS}\cdot\left(\frac{\partial\mathrm{B}}{\partial t} + \mathrm{v}\cdot\nabla\mathrm{B} - \mathrm{B}\cdot\nabla\mathrm{v} + \mathrm{B}\nabla\cdot\mathrm{v}\right) \\
&= \mathrm{dS}\cdot\left(\frac{\partial\mathrm{B}}{\partial t} - \nabla\times\mathrm{v}\times\mathrm{B}\right) = 0 \; ,
\end{aligned}$$

since the expression in parentheses vanishes according to the MHD kinematic equation.

This proves the flux conservation theorem for an infinitesimal surface element advected by the fluid. It follows that the flux through any *surface* advected by the fluid is also conserved; simply add up all the surface elements.

3.4.2 Magnetic flux tubes

As a result of the fact that the magnetic flux through any surface advected by the fluid is conserved, we may find a group of field lines which serve as the boundary for a definite volume. Define a closed curve which is the boundary for a small but finite surface, the magnetic flux through which is not zero. Follow each field line an arbitrary distance away from the original curve, and define another curve which intersects the same field lines. This is a *magnetic flux tube*. Note that the magnetic flux through the sides of the tube is zero, and because the flux is conserved it stays zero.

Under advection of a flow which deforms the flux tube, the identity of the flux tube is maintained, even though the flux tube may be very greatly twisted and tangled with several other flux tubes. The consequence of this is that the field line topology is not allowed to change.

Consider two flux tubes which may be defined in a sheared magnetic field. Shear in the magnetic field may be thought of as follows: Consider a horizontal plane in which parallel lines are drawn. Now consider a plane immediately above or below the first one, in which parallel lines are also drawn. If the orientation of each set of parallel lines changes from plane to plane, then the field represented by the drawn lines is said to be *sheared*, and the shear can be quantified by giving the rate of change of this angle of orientation with perpendicular distance. Label two very narrow flux tubes, one lying in one such plane and another lying initially in a plane immediately below the first one, “a” and “b”, respectively. Due to the shear, when the flux tubes are brought together by a flow field, they cross. Propose that they might pass through each other as they are forced together. Before the interaction, the magnetic flux through the sides of both tubes is zero. If they are allowed to pass through each other, the field lines due to tube “a” would intersect the sides of tube “b”, and vice versa. The magnetic flux through the sides of the tubes would no longer be zero. This is in obvious contradiction to the flux conservation theorem, so the conclusion is that the flux tubes are never allowed to cross. Note that this conclusion holds as well for flux tubes of infinitesimal cross-section, and hence for individual field lines.

> In ideal MHD, magnetic flux tubes and field lines cannot be advected through each other, because of the magnetic flux conservation theorem.

Below, we will explore how this constraint is relaxed by a finite plasma resistivity.

3.5 Dynamics, or the wires-in-Molasses picture of MHD

Note that the magnetic force term in the MHD force equation can be split into two pieces using an elementary vector identity

$$\frac{1}{c}\mathrm{J}\times\mathrm{B} = \frac{1}{c}\left(\frac{c}{4\pi}\nabla\times\mathrm{B}\right)\times\mathrm{B} = -\nabla\frac{B^2}{8\pi} + \frac{\mathrm{B}\cdot\nabla\mathrm{B}}{4\pi}\,.$$

These two contributions denote *magnetic pressure* and *magnetic tension*, respectively. Magnetic pressure may be combined with gas pressure

$$\rho\left(\frac{\partial}{\partial t}+\mathrm{v}\cdot\nabla\right)\mathrm{v}=-\nabla\left(p+\frac{B^2}{8\pi}\right)+\frac{\mathrm{B}\cdot\nabla\mathrm{B}}{4\pi}\,,$$

where one notes that it behaves like an energy density with two degrees of freedom (for which the pressure and energy density are equal).

The other contribution is magnetic tension. It is part of what gives MHD its unique character (flux conservation, or the advection of magnetic field lines is the other part). To see why it is called tension, consider the magnetic field due to a wire carrying current, surrounded by a vacuum. The field lines are described by loops centered upon the wire, and the forces are obviously zero because it is a vacuum. A cylindrical coordinate system may be defined, with z in the direction of the wire and r perpendicular to it. The only nonzero component of $\mathrm{B}\cdot\nabla\mathrm{B}$ is

$$\mathrm{B}\cdot\nabla\mathrm{B}=-\frac{B^2}{r}\,\hat{\mathrm{e}}_r\,.$$

This shows that magnetic tension is a force which acts in the direction of the curvature vector (towards the loop's center), a general result for a curved field line. Since the current outside the wire vanishes, the tension and pressure forces must be in balance: since $B\sim I/r$,

$$-\nabla\frac{B^2}{8\pi}=2\frac{B^2}{8\pi}\frac{1}{r}\hat{\mathrm{e}}_r=\frac{B^2}{4\pi r}\hat{\mathrm{e}}_r=-\mathrm{B}\cdot\nabla\mathrm{B}\,.$$

In such a situation, which can also exist in a plasma where the current is not zero, magnetic pressure and tension are in balance, and the configuration is termed *force-free*.

3.5.1 Magnetic pressure waves

Consider a compression in a magnetised plasma in equilibrium, perpendicular to the magnetic field. The velocity depends only on the direction perpendicular to the field, and it is itself directed perpendicular to the field. In this situation

$$\mathrm{B}\cdot\nabla\mathrm{B}=0\,,$$

since B is compressed perpendicular to its direction. The field lines are compressed together with the fluid, according to the MHD kinematic equation

$$\frac{\partial\mathrm{B}}{\partial t}=-\mathrm{v}\cdot\nabla\mathrm{B}-\mathrm{B}\nabla\cdot\mathrm{v}\,,$$

where the third piece, $\mathrm{B}\cdot\nabla v$, vanishes due to the geometry. This equation states that B reacts exactly as would a density

$$\frac{\partial\mathrm{B}}{\partial t}+\nabla\cdot\mathrm{vB}=0\,.$$

With the vanishing magnetic tension, the force equation reads

$$\rho\left(\frac{\partial}{\partial t}+\mathrm{v}\cdot\nabla\right)\mathrm{v}=-\nabla\left(p+\frac{B^2}{8\pi}\right)\,.$$

The result is exactly analogous to sound waves, since both the pressure and magnetic field are perturbed in the same way. Consider small perturbations of short wavelength, on which scale the equilibrium pressure and magnetic field is homogeneous. We *linearise* the equations by retaining terms only to first order in the perturbations, which are denoted by a tilde symbol. For example, B^2 becomes $B^2 + 2\mathrm{B}\cdot\widetilde{\mathrm{B}}$, with the term quadratic in $\widetilde{\mathrm{B}}$ neglected. The velocity requires no symbol, since it is understood to belong to the perturbations. Both pressure and magnetic perturbations are induced by compression in the velocity

$$\frac{1}{\gamma p}\frac{\partial \widetilde{p}}{\partial t} = \frac{1}{B}\frac{\partial \widetilde{\mathrm{B}}}{\partial t} = -\nabla\cdot\mathrm{v}\,,$$

with $\gamma = 5/3$. The perturbed force equation reads

$$\rho\frac{\partial \mathrm{v}}{\partial t} = -\nabla\left(\widetilde{p} + \frac{B\widetilde{\mathrm{B}}}{4\pi}\right)\,,$$

and note the factor of two arising from perturbing B^2. These may be combined into a wave equation

$$\frac{\partial^2 \widetilde{\mathrm{B}}}{\partial t^2} - \left(\frac{B^2}{4\pi\rho} + \frac{\gamma p}{\rho}\right)\nabla_\perp^2 \widetilde{\mathrm{B}} = 0\,,$$

where it is noted that the derivatives are all perpendicular to B.

The second term in the parentheses will be recognised as the square of the adiabatic sound velocity v_s. The first term introduces the characteristic velocity of MHD in general, and the velocity of propagation of small magnetic disturbances in particular. It is the square of the *Alfvén velocity*

$$v_A^2 = \frac{B^2}{4\pi\rho}\,,$$

after Hannes Alfvén, who is recognised as the founder of the MHD description of plasma fluid dynamics. Magnetic pressure waves, like sound waves, are longitudinal waves, but unlike sound waves they are in their pure form only when the disturbance propagates perpendicular to the magnetic field. In general, when both gas pressure and magnetic pressure are present, they both contribute to the actual wave speed: $v^2 = v_s^2 + v_A^2$. More on the ratio of gas to magnetic pressure shortly.

3.5.2 Alfvén waves: magnetic tension waves

Because the magnetic field also exhibits tension, transverse waves similar to waves on a taut string also occur in MHD. Assume now that there is a divergence-free perturbation of a magnetised plasma in equilibrium, still perpendicular to the magnetic field. The velocity now depends only on the direction parallel to the field, although it is itself directed perpendicular to the field. In this situation

$$\nabla\cdot\mathrm{v} = \widetilde{p} = \mathrm{B}\cdot\widetilde{\mathrm{B}} = 0\,,$$

since the disturbance is a transverse-shear perturbation. The field lines are not compressed, but are bent, according to the MHD kinematic equation

$$\frac{\partial \mathrm{B}}{\partial t} = -\mathrm{v}\cdot\nabla\mathrm{B} + \mathrm{B}\cdot\nabla\mathrm{v}\,,$$

where the divergence piece, $\mathrm{B}\nabla\cdot\mathrm{v}$, vanishes due to the geometry. Field line bending becomes clearer when this expression is re-cast in the co-moving frame

$$\frac{d\mathrm{B}}{dt} = \mathrm{B}\cdot\nabla\mathrm{v}\,.$$

The single contribution arises due to the fact that the field line is moved in alternate directions according to position along it.

This is a new situation, in which the pressure is unperturbed, and the magnetic field is perturbed only through the component perpendicular to the equilibrium field. For homogeneous perturbations

$$\begin{aligned}\frac{\partial\widetilde{B}_\perp}{\partial t} &= \mathrm{B}\cdot\nabla\widetilde{v}_\perp\,,\\ \rho\frac{\partial\widetilde{v}_\perp}{\partial t} &= \frac{\mathrm{B}\cdot\nabla\widetilde{B}_\perp}{4\pi}\,,\end{aligned}$$

where there is no factor of two since the perturbed field component is perpendicular. These may be combined into a wave equation

$$\frac{\partial^2\widetilde{B}_\perp}{\partial t^2} - \frac{B^2}{4\pi\rho}\frac{(\mathrm{B}\cdot\nabla)^2}{B^2}\widetilde{B}_\perp = 0\,,$$

where note now that the derivatives are all parallel to B.

This type of disturbance propagates parallel to B, and it is a transverse wave. It is called an *Alfvén wave*, since it is the type of propagating wave which exists in MHD but not in neutral fluid dynamics. Its propagation speed is purely the Alfvén velocity. The detection of Alfvén waves in the solar wind by spacecraft in the 1960s gave evidence that MHD phenomena do occur in nature and are not a theoretical artifice.

The concept of field line tension is now clear, since the behavior of the field line in MHD is the same as that of a taut string: *Pluck it, and transverse waves run down the line*. The concept of *field line bending* is closely related: curvature of a field line gives rise to the magnetic tension force. However, field line bending should not be considered as a force in itself, but a cause of one.

> A general description of MHD can be that of *molasses threaded by wires*. The wires are magnetic field lines, which exert force on the fluid and which are advected by the fluid as it moves. Additions to this are that the wires exert pressure as well as tension, tending to repel each other, and that in the ideal limit the fluid is not viscous.

One final note: The attractive force between two wires is due to magnetic tension overcoming magnetic pressure.

3.6 The validity of MHD

The Alfvén velocity as just introduced determines the natural time scale of any MHD phenomena of a confined system. With this in hand, we are in a position to judge the validity of MHD by providing *a posteriori* checks on its fundamental assumptions. The Alfvén times are discussed first, and then the checks are made.

3.6.1 Characteristic time scales of MHD

Although they were derived for small disturbances on a homogeneous background, the wave velocities for propagation perpendicular and parallel to the magnetic field indicate the characteristic time scales for adjustment to equilibrium for general perturbations of any confined MHD system. This is much the same as the way the time it takes for a sound wave to cross a neutral fluid in hydrostatic equilibrium under gravity gives the characteristic adjustment time for that fluid. The reason is that a global free oscillation is nothing more than the longest-wavelength limit of the appropriate wave. Examples of the neutral fluid case would be an ocean layer, the Earth's atmosphere, or the Sun. In that case, for a scale length a, the sound-wave transit time is

$$\tau_s = a/c_s \ ,$$

which is also the inverse of the frequency of the fundamental global mode of oscillation (cf. the five-minute oscillation observed on the Sun).

For a confined plasma in equilibrium the sound speed is replaced by the Alfvén velocity, v_A. It must be noted, though, that the geometry of the confined system is important, since different types of waves propagate parallel to and perpendicular to the magnetic field. With characteristic scale lengths $L_\perp$ perpendicular to the field and $L_\parallel$ parallel to the field, two time scales are of interest. Due to the propagation of magnetic pressure waves, we have the *fast Alfvén*, or compressional Alfvén time: $\tau_A = L_\perp/v_A$. From the propagation of magnetic tension waves (Alfvén waves) we have the *slow Alfvén*, or shear Alfvén time: $\tau_A = L_\parallel/v_A$.

Both of these are usually written as τ_A in the literature, and one has to extract the meaning from the context. The name *shear Alfvén time* originates from the fact that parallel length scales for many laboratory plasma instabilities arise from the existence of magnetic shear in the equilibrium configuration.

These time scales and characteristic velocities can be deduced directly from the MHD force and kinematic equations by *scaling* them. Assuming that the spatial scale is a, the kinematic equation yields

$$\frac{\partial \mathrm{B}}{\partial t} = \nabla\times(\mathrm{v}\times\mathrm{B}) \qquad \rightarrow \qquad \frac{B}{\tau} \sim \frac{Bv}{a} \ ,$$

and the force equation yields

$$\rho\frac{d\mathrm{v}}{dt} = -\nabla p + \frac{1}{c}\mathrm{J}\times\mathrm{B} \qquad \rightarrow \qquad \rho\frac{v}{\tau} \sim \frac{B^2}{4\pi a} \ ,$$

if the gas pressure is negligible. These similarity relations may be solved for v and τ, given B and a, and the result is $v \sim v_A$ with $\tau \sim a/v_A$.

3.6.2 Checking the assumptions

With a as a representative spatial scale and τ_A as the corresponding time scale, we may now examine the MHD assumptions listed in sec. 3.3, a little out of order.

1. The displacement current is neglected because $v_A \ll c$. This is easily satisfied for laboratory and space plasmas.

5. Quasineutrality depends additionally on both $\tau_A \omega_{pe} \gg 1$ and $\rho_i \gg \lambda_D$. The latter three parameters in this list are the electron plasma frequency ($\omega_{pe}^2 = 4\pi n e^2/m_e$), the ion Larmor gyroradius ($\rho_i^2 = c^2 M_i T_i / e^2 B^2$), and the Debye screening length ($\lambda_D^2 = T/4\pi n e^2$). The former inequality is needed to neglect the parallel electric field, as the time scale for the electrons to equilibrate charge is ω_{pe}. The latter is needed in order to use the Lorentz force in the fluid description, since the Lorentz force has the gyroradius as its implicit length scale and the particles are not supposed to individually interact.

3. Fluid elements of all species move with velocity v, with the relative drift implied by J negligible. This requires $J \ll n e v_A$, or using Ampere's law to express J in terms of B (as magnitudes), we find

$$\frac{\rho_i^2}{a^2} \equiv (\text{drift parameter})^2 \ll \text{plasma beta} = \beta \equiv \frac{8\pi p}{B^2} \, .$$

(The plasma beta is discussed below.) Neglecting ion inertia as a correction to the E×B velocity for ions depends on the same limit, since $\tau_A \Omega_i \gg 1$ is an equivalent statement ($\Omega_i = eB/M_i c$ is the ion gyrofrequency). The statement that the drift parameter be smaller than some limit is a requirement on how strongly the plasma is magnetised, and that it must be smaller than $\beta^{1/2}$ is usually well-satisfied in any fusion or space plasma application.

2. Electron inertia is negligible because $m_e \ll M_i$ in general. It is negligible compared to the pressure gradient if $n m_e v_A/\tau \ll p/a$, which implies $\beta \gg m_e/M_i$. This has no impact on the MHD kinematic equation, since ∇p is negligible to that anyway. But this serves as a check that electron inertia is negligible even when ion inertia is very strong compared to pressure corrections, which is why a limit on β makes sense (see below).

4. That ∇p is negligible compared to the Lorentz force term is implied as well by (3), since J×B/c is comparable to ∇p and $J \ll n e v_A$. If $\beta \ll 1$, then this is even more so.

3.6.3 A comment on the plasma beta

The *plasma beta*, defined by

$$\frac{\text{gas pressure}}{\text{magnetic pressure}} = \frac{8\pi p}{B^2} \equiv \beta \, ,$$

is very important in plasma fluid dynamics. It gives the relative importance of the gas pressure to the magnetic field as the restoring force to any disturbance. If $\beta \gg 1$, then the magnetic force has a negligible effect on the dynamics, but the magnetic field is still advected by the flow. This is called *MHD kinematics*. It is important in studies of the generation of a magnetic field by a conducting fluid undergoing motion forced by other means, such as convection in a gravitational field. The generation of a large-scale magnetic field by convective turbulence is called the *dynamo effect*, and it is thought to be the most likely scenario for the origin of planetary and stellar magnetic fields. (A note: Some treatments define β with 4π instead of 8π.)

In the opposite limit, $\beta \ll 1$, the gas pressure drops out of the MHD force equation to lowest order in β, but it remains as a slight correction to the geometry of any equilibrium. For such a *low-beta* plasma, the gas pressure is still important because it can break the tendency of

magnetic pressure and tension to cancel. A consequence is that a finite gas pressure prevents the establishment of a force-free equilibrium, to which the plasma tends to relax in many important configurations, even in a situation with a nonzero current density. In addition, the gas pressure can cause instability in an equilibrium which would otherwise be stable to MHD perturbations (*MHD-stable*). In the tokamak configuration for a fusion plasma, for example, this fact is responsible for limiting the plasma beta to quite low values.

The tendency of magnetic pressure and tension to cancel is ultimately the reason that assumptions (3) and (5) have to be separately checked.

3.7 Parallel dynamics and resistivity, or relaxing the ideal assumption

One limit which was not examined above is the role of parallel dynamics: The general case of flows parallel to the magnetic field. If we compare the drift velocity implied by J not to v_A but to v_s, we get a different limit: $\beta \gg \rho_i/a$ (the reader is invited to check this). The drop of one power of the drift parameter places a rather strict limit on how low the beta can be allowed to go. In solar plasmas the drift parameter is really very small, so this point can be ignored. In fusion plasmas, especially tokamak and stellarator plasmas in which β is quite limited by effects arising from the gas pressure, the limit can be violated, and it is nearly always violated in the boundary regions of the plasma. It is important to realise that a perturbation compressing the gas purely parallel to the magnetic field involves no disturbance of the field. A small disturbance of this type merely leads to longitudinal sound waves propagating parallel to the field lines. Such parallel effects may be neglected for any disturbance of the general equilibrium or violent instability, since these evolve on Alfvén time scales. However, transport phenomena may give rise to force imbalances along the field lines, and these would relax on the parallel sound transit time scale. If phenomena on this scale are of global importance, then the kinematic MHD equation will be affected since although these effects are parallel, the forces they cause may have a nonzero perpendicular curl. When this is the case, studies of the consequences must treat the electron and ion fluids separately, on an equal footing. Further inquiry along these lines is beyond the scope of this introduction to MHD.

A simpler effect which breaks the ideal MHD constraints but still allows treatment of the system as MHD and as a single fluid is electrical resistivity. Resistivity means an exchange of momentum between electrons and ions as their respective fluids drift past each other. The details of the electron-ion collision process are complex, due to the fact that the angle through which an electron is scattered upon close approach to an ion depends strongly on the relative velocity. Nevertheless, by the inclusion of a simple momentum exchange term loosely based on a collision frequency, a qualitative picture of the most important consequence can be given: Magnetic field line diffusion, or how those flux tubes tangled together at arbitrarily small scale eventually relax. MHD with electrical resistivity is called *resistive MHD*.

Consider a plasma with a single ion species of charge e, and allow the ions and electrons to exchange momentum. The continuity and energy equations are unaffected, but the electrons lose momentum to the ions on a time scale given by a collision frequency ν_{ei}

$$0 = -\nabla p_e - n_e e\left(\mathrm{E} + \frac{\mathrm{v}_e}{c}\times\mathrm{B}\right) - n_e m_e \nu_{ei}(\mathrm{v}_e - \mathrm{v}_i)\ ,$$

in which inertia is still neglected. To conserve momentum, the same term appears with opposite sign in the ion momentum equation

$$n_i M_i \frac{d\mathrm{v}_i}{dt} = -\nabla p_i + n_i e\left(\mathrm{E} + \frac{\mathrm{v}_i}{c}\times\mathrm{B}\right) + n_e m_e \nu_{ei}(\mathrm{v}_e - \mathrm{v}_i) \; .$$

We now add these two to obtain the resistive MHD force equation

$$\rho\left(\frac{\partial}{\partial t} + \mathrm{v}\cdot\nabla\right)\mathrm{v} = -\nabla p + \frac{1}{c}\mathrm{J}\times\mathrm{B} \; .$$

Note that since the MHD force equation is one for *total* momentum, the addition of resistivity does not alter its form.

Now consider the MHD kinematics. Solving the electron momentum equation for E, obtain

$$\mathrm{E} + \frac{\mathrm{v}_e}{c}\times\mathrm{B} = -\frac{\nabla p_e}{n_e e} - \frac{m_e \nu_{ei}}{n_e e^2} n_e e(\mathrm{v}_e - \mathrm{v}_i) \; .$$

As before, we neglect the pressure force and assume that v_e is v. Note as well that $n_e e(\mathrm{v}_e - \mathrm{v}_i) = \mathrm{J}$. (The astute reader will note the slight complications that arise when the charge state of the ions differs from $+1$; let this be left as an exercise.)

The electron force balance, modified by resistivity, now reads

$$\mathrm{E} + \frac{\mathrm{v}}{c}\times\mathrm{B} = \eta\mathrm{J} \; ,$$

where $\eta = m_e\nu_{ei}/n_e e^2$ is the resistivity. Inserting this relation into the MHD kinematic equation, we find

$$\frac{\partial \mathrm{B}}{\partial t} = \nabla\times(\mathrm{v}\times\mathrm{B}) - \nabla\times\frac{\eta c^2}{4\pi}\nabla\times\mathrm{B} \; .$$

Assuming for the moment that η is homogeneous, the double-curl operation may be reduced, re-casting the kinematic equation as

$$\frac{\partial \mathrm{B}}{\partial t} = \nabla\times(\mathrm{v}\times\mathrm{B}) + \frac{\eta c^2}{4\pi}\nabla^2\mathrm{B} \; .$$

This has the form of a diffusion, which is the role that resistivity plays. The eventual fate of tangled magnetic flux tubes is now apparent. Supposing that

$$\frac{v_A}{a} \gg \frac{\eta c^2}{4\pi}\frac{1}{a^2} \; ,$$

or in terms of the *Lundquist number S* and *resistive decay time* τ_R

$$S \equiv \frac{\tau_A}{\tau_R} \gg 1 \; , \qquad\qquad \tau_R = \frac{a^2}{\eta c^2/4\pi} \; ,$$

the system evolves according to ideal MHD on large scales. When flux tubes are tangled on ever-smaller scales, however, some scale, λ, is reached at which $S(a\to\lambda)\sim 1$. At that scale the magnetic field lines lose their identity through diffusion and *re-connection*, and the tangles are smoothed out.

3.8 Towards multi-fluid MHD

Further relaxing the assumptions of MHD brings one eventually to the necessity of treating all the constituent fluids on an equal footing, especially when further *collisional* phenomena become important. This is in any case beyond the goal of this study, which is to introduce the ideas of MHD. Interested readers will no doubt find it stimulating both to explore MHD phenomena further, and to consider in more depth the different effects one finds in two- or more-fluid dynamics. For this purpose a set of references is provided.

References

A good MHD text, both for an introduction to MHD and for further study of the basic phenomena (it is the very best book containing reconnection and MHD turbulence): *Nonlinear Magnetohydrodynamics*, by D. Biskamp (Cambridge, 1993). It cites all of the references below.

A perhaps more introductory text which is less like a review is *Ideal Magnetohydrodynamics*, by J.P. Freidberg (Plenum Press, New York, 1987).

The standard text for astrophysical MHD applications is *Cosmical Magnetic Fields*, by E.N. Parker (Clarendon Press, Oxford, 1979). Convection of magnetic flux tubes and dynamo theory form the centerpiece of this book.

A tokamak-oriented text which includes the basic MHD problems as well as the more complicated phenomena one encounters is *Theory of Tokamak Plasmas,* by R.B. White (North Holland, Amsterdam, 1989).

The best source on two-fluid dynamics is still the review article by S.I. Braginskii, in *Reviews of Plasma Physics*, M.A. Leontovich, ed. (Consultants Bureau, New York, 1965), Vol. 1, p. 205. It contains a systematic derivation of the equations from kinetic theory as well as a clear introduction to the effects represented by the individual terms (and why they appear). One obtains a good understanding of the dependence of both the two-fluid and MHD models on the kinetic theory of plasmas, and their range of validity.

Chapter 4

Kinetic theory

Emanuele Poli

4.1 Introduction

The most complete description of a plasma composed by N particles would rely on the solution of the $3N$ equations of motion $\boldsymbol{F}_i = m_i \boldsymbol{a}_i$, where in the calculation of the force acting on the i-th particle one has to take into account the influence of all the particles in the system. The solution of this formidable set of coupled differential equations for realistic parameters is of course prohibitive from a computational point of view and would, moreover, require the knowledge of the $6N$ initial values of position and velocity of each particle. But perhaps even more important than this is the fact that a complete solution of Newton's equations would simply yield a tremendous amount of unnecessary information, since we will never perform an experiment aiming at determining the *microscopic* behaviour of each particle in the plasma. What we are going to measure are *macroscopic* quantities like density, temperature, currents and so on. To connect these two levels, a statistical approach, in the sense that will be specified in the next section, is required. This is the scope of kinetic theory.

The importance of kinetic theory is twofold. First of all, it constitutes a theoretical foundation for the macroscopic descriptions of a plasma, like fluid theory and magnetohydrodynamics. Moreover, processes whose treatment requires the knowledge of the velocity distribution of the particles in the plasma must be examined in the framework of kinetic theory. In these notes, the first point is not addressed. The focus will be rather on the second aspect. After sketching the derivation of the kinetic equation (see sec. 4.2) and of the Fokker-Planck term (see sec. 4.3), we will consider two of the most known applications of kinetic plasma theory, namely the Landau damping (see sec. 4.4) and the Coulomb collision operator (see sec. 4.5).

In order to be able to fit the content of this lecture in roughly fifteen pages, the standard derivation of the Landau damping, which can easily be found in standard textbooks, has been omitted. A short list of references is given at the end.

4.2 The kinetic equation for a plasma

The fundamental quantity in kinetic theory is the *distribution function*. It expresses the particle density in a six-dimensional phase space $\{\boldsymbol{r}, \boldsymbol{v}\}$, in a way which can be easily understood if we

first introduce the so-called Klimontovitch distribution function

$$f_K(\boldsymbol{r},\boldsymbol{v},t) \equiv \sum_{i=1}^{N} \delta^{(3)}\left(\boldsymbol{r}-\boldsymbol{r}_i(t)\right)\delta^{(3)}\left(\boldsymbol{v}-\boldsymbol{v}_i(t)\right) , \tag{4.1}$$

where the sum runs on the position and velocity of the N plasma particles. As stated in the introduction, we do not want to be bound to the knowledge of position and velocity of each particle. Hence, we can introduce a smoother distribution function by averaging f_K over a volume $\Delta\boldsymbol{r}\Delta\boldsymbol{v}$ in phase space,

$$f(\boldsymbol{r},\boldsymbol{v},t) \equiv \frac{1}{\Delta\boldsymbol{r}\Delta\boldsymbol{v}} \int_{\Delta\boldsymbol{r}} \mathrm{d}^3\boldsymbol{r} \int_{\Delta\boldsymbol{v}} \mathrm{d}^3\boldsymbol{v}\; f_K = \frac{N_p}{\Delta\boldsymbol{r}\Delta\boldsymbol{v}} . \tag{4.2}$$

Here, N_p is the number of particles in the volume $\Delta\boldsymbol{r}\Delta\boldsymbol{v}$, which is taken to be large enough to contain a large number of particles (so that the averaging procedure implied by (4.2) is meaningful in a statistical sense); at the same time, this volume should be small compared to the macroscopic scale of the system, in such a way that the coordinates $\boldsymbol{r}$ and $\boldsymbol{v}$ can be still be thought as *local*. According to these considerations, we can denote the level of description expressed by the distribution function $f(\boldsymbol{r},\boldsymbol{v},t)$ as *mesoscopic*. Since the distribution function has the meaning of a phase-space density, its integral over the whole phase space gives the total number of particles in the system, $\int \mathrm{d}^3\boldsymbol{r}\mathrm{d}^3\boldsymbol{v} f = N$. Alternatively, the distribution function can be normalised as $\int \mathrm{d}^3\boldsymbol{r}\mathrm{d}^3\boldsymbol{v} f = 1$, in which case $f\Delta\boldsymbol{r}\Delta\boldsymbol{v}$ should be interpreted as the *probability* of finding a particle in the volume $\Delta\boldsymbol{r}\Delta\boldsymbol{v}$.

We turn now to the problem of determining an evolution equation for the distribution function. Being a particle density in phase space, f must satisfy a continuity equation, expressing the fact that the total number of particles must be conserved. Such an equation reads

$$\frac{\partial f}{\partial t} + \nabla_{\boldsymbol{r},\boldsymbol{v}} \cdot [(\boldsymbol{v},\boldsymbol{a}) f] = 0 ,$$

where $\nabla_{\boldsymbol{r},\boldsymbol{v}}\cdot$ is the divergence in the six-dimensional space. Writing $\boldsymbol{a} = \boldsymbol{F}/m$, the previous equation becomes

$$\frac{\partial f}{\partial t} + f\frac{\partial}{\partial \boldsymbol{r}}\cdot\boldsymbol{v} + \boldsymbol{v}\cdot\frac{\partial f}{\partial \boldsymbol{r}} + f\frac{\partial}{\partial \boldsymbol{v}}\cdot\frac{\boldsymbol{F}}{m} + \frac{\boldsymbol{F}}{m}\cdot\frac{\partial f}{\partial \boldsymbol{v}} = 0 . \tag{4.3}$$

At this point, we write the force $\boldsymbol{F}$ as $\boldsymbol{F}^{\mathrm{ext}} + \boldsymbol{F}^{\mathrm{int}}$, i.e. we separate the forces *external* to the volume $\Delta\boldsymbol{r}\Delta\boldsymbol{v}$ (those acting equally on each particle in this volume), from the *internal* forces arising from the particle interaction (*collisions*) inside $\Delta\boldsymbol{r}\Delta\boldsymbol{v}$ (for these internal forces the point-like nature of the plasma is still important). Let us first neglect the contribution of the internal forces and suppose that, at the each *mesoscopic* point of the system, the Hamiltonian equations of motion $\boldsymbol{v} = \partial H/\partial \boldsymbol{p}$ and $\boldsymbol{F}^{\mathrm{ext}} = \dot{\boldsymbol{p}} = -\partial H/\partial \boldsymbol{r}$ (with $\boldsymbol{p} = m\boldsymbol{v}$) are satisfied. It is then immediate to see that (4.3) simplifies to

$$\frac{\partial f}{\partial t} + \boldsymbol{v}\cdot\frac{\partial f}{\partial \boldsymbol{r}} + \frac{\boldsymbol{F}}{m}\cdot\frac{\partial f}{\partial \boldsymbol{v}} = 0 \tag{4.4}$$

(the apex $^{\mathrm{ext}}$ will be omitted from now on). This is the collisonless kinetic equation, also called the *Vlasov equation*. Introducing the total time derivative in phase space as $\mathrm{d}/\mathrm{d}t \equiv \partial/\partial t + \boldsymbol{v}\cdot\partial/\partial\boldsymbol{r} + (\boldsymbol{F}/m)\cdot\partial/\partial\boldsymbol{v}$, we see immediately that (4.4) can be written simply as $\mathrm{d}f/\mathrm{d}t = 0$. This means that f is constant along trajectories (*characteristics*) satisfying the Hamiltonian equations of motion. Moreover, it conserves entropy.

The influence of the internal forces can be modelled simply by introducing on the right-hand side of (4.4) a collision term, which will be calculated explicitly later (cf. sec. 4.3 and sec. 4.5). The kinetic equation becomes then

$$\frac{\partial f}{\partial t} + \boldsymbol{v}\cdot\frac{\partial f}{\partial \boldsymbol{r}} + \frac{\boldsymbol{F}}{m}\cdot\frac{\partial f}{\partial \boldsymbol{v}} = \left.\frac{\partial f}{\partial t}\right|_{\text{coll}} . \tag{4.5}$$

In this form, the kinetic equation is also called the *Boltzmann equation*. It exhibits the following important properties, which are reported here without proof. First of all, Boltzmann's H-theorem holds, i.e. the time derivative of the quantity $H \equiv \int f \ln f \mathrm{d}^3\boldsymbol{v}$ is never positive. It can be easily shown that H is (except for a constant term) proportional to $-s$, where s is the entropy density of the system. Moreover, at thermal equilibrium, the distribution function is a Maxwellian, which hence corresponds to the state with maximum entropy. Due to its importance, we report here its explicit form[1]

$$f_M = n\left(\frac{m}{2\pi k_B T}\right)^{3/2} \exp(-mv^2/2k_B T) , \tag{4.6}$$

where n is the density and T is the temperature. An important quantity connected with the exponent of f_M is the *thermal velocity*

$$v_{\text{th}} \equiv \sqrt{\frac{2k_B T}{m}} . \tag{4.7}$$

Despite their rather compact form, (4.4), (4.5) are by no means easy to solve. This is essentially due to the fact that the forces acting on the system can depend in some complicated way on the distribution function itself. This makes these equations, in general, nonlinear integro-differential equations. An explicit solution of the Vlasov equation is considered in sec. 4.4.

4.3 Markovian processes and the Fokker-Planck equation

In this section, we obtain an equation for the evolution of the distribution function under the influence of the microscopic (internal) forces. In the approach presented here, the effect of these forces is modelled as a stochastic process introducing a probabilty $\psi(\boldsymbol{Z},\Delta\boldsymbol{Z})$ that the position $\boldsymbol{Z}$ of a particle in *phase space* changes by an amount $\Delta\boldsymbol{Z}$ in a time Δt. This probability function does not depend explicitly on the time t, i.e. each transition is independent of the previous history of the particle. Such a process is called *Markovian*. The perhaps best-known example of Markovian process is the Brownian motion. Clearly, the function ψ must be normalised in such a way that its integral over all possible displacements $\Delta\boldsymbol{Z}$ is equal to one, $\int \mathrm{d}(\Delta\boldsymbol{Z})\,\psi = 1$.

The distribution function at a given position $\boldsymbol{Z}$ and time t is supposed to be related to the distribution function at $\boldsymbol{Z}-\Delta\boldsymbol{Z}$ and $t-\Delta t$ by the Chapman-Kolmogorov equation

$$f(\boldsymbol{Z},t) = \int \mathrm{d}(\Delta\boldsymbol{Z})\; f(\boldsymbol{Z}-\Delta\boldsymbol{Z}, t-\Delta t)\,\psi(\boldsymbol{Z}-\Delta\boldsymbol{Z},\Delta\boldsymbol{Z}) , \tag{4.8}$$

which represents a *sum* over all possible displacements $\Delta\boldsymbol{Z}$ leading to a given position $\boldsymbol{Z}$, each term of the *sum* being weighted with its probability ψ. If the changes $\Delta\boldsymbol{Z}$ are small compared to the size of the system, $|\Delta\boldsymbol{Z}| \ll |\boldsymbol{Z}|$, the right-hand side of (4.8) can expanded as follows

$$f(\boldsymbol{Z},t) = \int \mathrm{d}(\Delta\boldsymbol{Z})\left[f\psi - \Delta\boldsymbol{Z}\cdot\frac{\partial}{\partial\boldsymbol{Z}}(f\psi) - \Delta t\frac{\partial f}{\partial t}\psi + \frac{1}{2}\Delta\boldsymbol{Z}\Delta\boldsymbol{Z} : \frac{\partial^2(f\psi)}{\partial\boldsymbol{Z}\partial\boldsymbol{Z}}\right] , \tag{4.9}$$

[1] The form reported in (4.6) corresponds to the normalisation $\int \mathrm{d}^3\boldsymbol{r}\mathrm{d}^3\boldsymbol{v} f = N$.

where all quantities are evaluated at the position $\boldsymbol{Z}$ and the dyadic notation has been used in the last term on the right-hand side of (4.9). In this expansion, it has been taken explicitly into account that ψ does not depend on time. Moreover, the expansion is performed up to the second order in $\boldsymbol{Z}$ but only to the first order in t. This is consistent with the fact that, in a random walk ansatz, the mean square displacement is found to scale linearly with time.

Let us introduce the average changes in $\Delta\boldsymbol{Z}$ (*friction* coefficient) and $\Delta\boldsymbol{Z}\Delta\boldsymbol{Z}$ (*diffusion* coefficient) during the time Δt as

$$\langle \Delta\boldsymbol{Z} \rangle \equiv \frac{1}{\Delta t} \int \mathrm{d}(\Delta\boldsymbol{Z})\, \Delta\boldsymbol{Z}\, \psi(\boldsymbol{Z}, \Delta\boldsymbol{Z}) \,, \tag{4.10}$$

$$\langle \Delta\boldsymbol{Z}\Delta\boldsymbol{Z} \rangle \equiv \frac{1}{\Delta t} \int \mathrm{d}(\Delta\boldsymbol{Z})\, \Delta\boldsymbol{Z}\Delta\boldsymbol{Z}\, \psi(\boldsymbol{Z}, \Delta\boldsymbol{Z}) \,. \tag{4.11}$$

With these definitions, dividing both sides of (4.9) by Δt and recalling the normalisation condition for ψ (and that f is not a function of $\Delta\boldsymbol{Z}$) we obtain finally

$$\frac{\partial f}{\partial t} = -\frac{\partial}{\partial \boldsymbol{Z}} \cdot (\langle \Delta\boldsymbol{Z} \rangle f) + \frac{1}{2} \frac{\partial^2}{\partial \boldsymbol{Z} \partial \boldsymbol{Z}} : (\langle \Delta\boldsymbol{Z}\Delta\boldsymbol{Z} \rangle f) \,. \tag{4.12}$$

This is the Fokker-Planck equation[2], which we will use in the following section to obtain a physical picture of Landau damping and in sec. 4.5 to calculate an explicit form for the collision operator.

4.4 Landau damping

The basic difference between a gas and a plasma is the fact that the plasma is composed by charged particles, which react to electromagnetic forces. As mentioned above, this makes the solution of the kinetic equation very complicated even in the collisionless limit, because the electromagnetic fields that determine these forces are functions of the charge and current distributions in the plasma, and hence of the distribution function itself.

As an example, we consider here the propagation of an electrostatic wave in a collisionless electron plasma (the ions will be supposed to give simply a neutralising static background). For these waves (which do not exist in vacuum, but can propagate in a plasma), the oscillating magnetic field is zero and the electric field is parallel to the wave vector, as can be deduced from the Maxwell equation for the curl of the electric field in the electrostatic limit, $\nabla \times \boldsymbol{E} = 0$, which yields in Fourier space $\boldsymbol{k} \times \boldsymbol{E} = 0$. To account for the interaction between this wave and the plasma, we need then the Vlasov equation (4.4), where the force $\boldsymbol{F} = -e\boldsymbol{E}$ must be calculated from

$$\nabla \cdot \boldsymbol{E} = \frac{\rho_{\mathrm{ch}}}{\varepsilon_0} = -\frac{e}{\varepsilon_0} \int f \mathrm{d}^3\boldsymbol{v} \,. \tag{4.13}$$

In the last step, the charge density ρ_{ch} has been expressed as an integral over velocity space of the distribution function. If we substitute (4.13) into the Vlasov equation, we see imediately that it becomes a nonlinear equation for f. However, if we suppose that the influence of the wave is just to produce a small perturbation of the background plasma, we can write the distribution function as $f = f_0 + f_1$, with $|f_1/f_0| \ll 1$, where f_1 represents the effect of the

[2] This name is also used for the equation resulting from substituting (4.12) into the right-hand side of the Boltzmann equation (4.5).

wave. Retaining then only the first-order terms in f_1 (i.e. in a *linear* picture), the coupled Vlasov-Maxwell set of equations becomes

$$\begin{aligned} &\frac{\partial f_1}{\partial t} + \boldsymbol{v} \cdot \frac{\partial f_1}{\partial \boldsymbol{r}} - \frac{e\boldsymbol{E}}{m} \cdot \frac{\partial f_0}{\partial \boldsymbol{v}} = 0 \,, \\ &\nabla \cdot \boldsymbol{E} = -\frac{e}{\varepsilon_0} \int f_1 \mathrm{d}^3 \boldsymbol{v} \,. \end{aligned} \tag{4.14}$$

The solution derived by Landau (1946) for these equations can be found in many textbooks and is not reported here.

An instructive physical interpretation of the Landau damping can be obtained from a direct calculation of change in the velocity of an electron in the presence of an electrostatic wave and is discussed in the remainder of this section. Since the problem is one-dimensional, we simply write the wave field as

$$\boldsymbol{E} = E_0 \hat{\boldsymbol{x}} \cos(kx - \omega t) \,,$$

where again the field amplitude is supposed to be small enough that it leads just to a small perturbation of the electron orbit. If this is the case, we can integrate the equation of motion

$$m \frac{\mathrm{d}v}{\mathrm{d}t} = -eE_0 \cos(kx - \omega t) \tag{4.15}$$

along the unperturbed orbit $x = x_0 + v_0 t$, to obtain

$$\begin{aligned} \Delta v &= -\frac{eE_0}{m} \int_0^t \mathrm{d}t' \cos\left[kx_0 + (kv_0 - \omega)t'\right] \\ &= -\frac{eE_0}{m} \frac{1}{kv_0 - \omega} \left(\sin\left[kx_0 + (kv_0 - \omega)t\right] - \sin(kx_0)\right) \,. \end{aligned} \tag{4.16}$$

The resonant denominator appearing in (4.16) indicates that the energy exchange between wave and particle is particularly effective if the velocity of the particle is close to the phase velocity of the wave, $v_0 \approx \omega/k$, because in this case the particle does not experience a rapidly oscillating field (with a vanishing average effect), but rather a constant one. Whether Δv is then positive or negative depends on the relative phase kx_0 between wave and particle (in other words, it depends on whether the particle travels in phase with a positive or negative electric field).

At this point, we assume that it is possible to treat the wave-particle interaction as a Markovian process. This amounts to say that we suppose that there is some random process (e.g. binary collisions) running in the background that destroys the phase coherence between particles and wave on a typical time scale τ. We can then calculate the average values of Δv and $(\Delta v)^2$ using (4.10) and (4.11), assuming $\Delta t = \tau$ and that the values of the phase between wave and particle are uniformly distributed (i.e., that the probability ψ is constant). The integral over all the possible *displacements* Δv for a given electron is equivalent to an integral over all the initial phases between the wave and the electron. We obtain immediately

$$\langle \Delta v \rangle = \frac{1}{2\pi\tau} \int_0^{2\pi} \mathrm{d}(kx_0)\, \Delta v|_{t=\tau} = 0$$

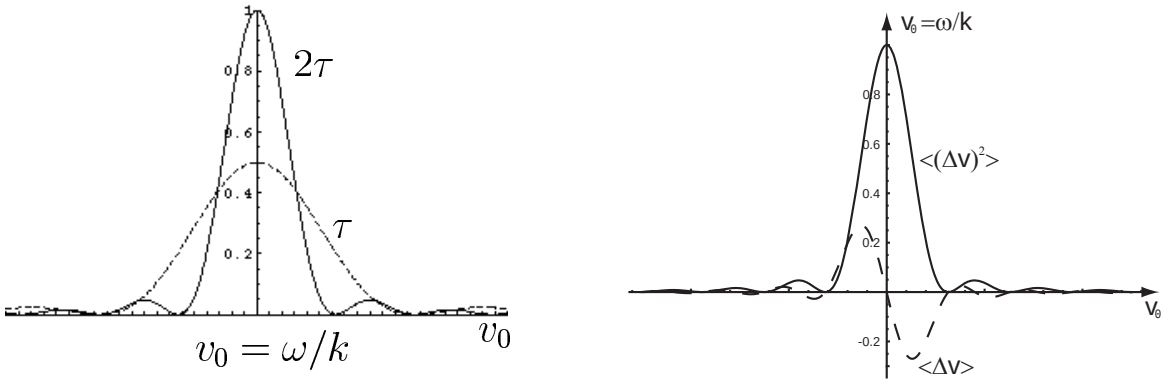

Figure 4.1: Left: The quantity $\langle(\Delta v)^2\rangle$ as a function of v_0.
Right: The quantities $\langle\Delta v\rangle$ and $\langle(\Delta v)^2\rangle$ as functions of v_0.

and, employing the trigonometric relation $\sin\alpha - \sin\beta = 2\cos[(\alpha+\beta)/2]\sin[(\alpha-\beta)/2]$ in (4.16),

$$\langle(\Delta v)^2\rangle = \frac{1}{2\pi\tau}\int_0^{2\pi} \mathrm{d}(kx_0)\,(\Delta v)^2\big|_{t=\tau} = \frac{e^2E_0^2}{m^2}\frac{2}{(kv_0-\omega)^2\tau}\sin^2\left[\frac{(kv_0-\omega)\tau}{2}\right] . \tag{4.17}$$

As we see, $\langle(\Delta v)^2\rangle$ is proportional to E_0^2. If we want to use (4.12) to determine the change in the distribution function due to the wave-particle interaction, we need for consistency to calculate $\langle\Delta v\rangle$ also to the second order in E_0. This can be achieved by integrating the equation of motion, (4.15), along the orbit perturbation Δx given by

$$\Delta x = \int_0^t \Delta v(t')\mathrm{d}t' = -\frac{eE_0}{m}\frac{1}{kv_0-\omega}\left[\frac{-\cos[kx_0+(kv_0-\omega)t]+\cos(kx_0)}{kv_0-\omega} - t\sin(kx_0)\right] ,$$

where Δv has been taken from (4.16). In calculating the second-order expression for Δv we make the further assumption that $k\Delta x(\tau) < 1$, which implies that the electric field in the equation of motion can be expressed as $E \approx (\partial E/\partial x)\Delta x$. The result is then

$$\begin{aligned}\Delta v = -\frac{e}{m}\,\Delta x\int_0^t \mathrm{d}t'\frac{\partial E}{\partial x} &= \frac{e^2E_0^2}{m^2}\frac{k}{(kv_0-\omega)^2} \\ &\times\left[\frac{-\cos[kx_0+(kv_0-\omega)t]+\cos(kx_0)}{kv_0-\omega} - t\sin(kx_0)\right] \\ &[\cos[kx_0+(kv_0-\omega)t]-\cos(kx_0)] ,\end{aligned} \tag{4.18}$$

which allows us to obtain finally

$$\langle\Delta v\rangle = \frac{1}{\tau}\frac{e^2E_0^2}{m^2}\frac{k}{(kv_0-\omega)^2}\left[\frac{-1+\cos[(kv_0-\omega)\tau]}{kv_0-\omega} + \frac{\tau}{2}\sin[(kv_0-\omega)\tau]\right] . \tag{4.19}$$

We can now make some comments on these results. First of all, we notice that $\langle(\Delta v)^2\rangle$ is peaked around $v_0 = \omega/k$, as shown in Fig. 4.1 left for two different values of the parameter τ. The fact that the peak value of $\langle(\Delta v)^2\rangle$ increases with τ but its width decreases can be explained as follows. When the interaction time becomes longer, more energy can be exchanged between

the electron and the wave, but only if the velocity of the particle is closer to the resonance condition, because otherwise it will be kicked away from the resonance by the wave field. For this reason, the net energy exchange turns out to be independent of τ. In the limit $\tau \to \infty$ we have[3] $\langle(\Delta v)^2\rangle \to \pi(eE_0/m)^2\delta(kv_0-\omega)$ i.e. only particles which exactly satisfy the resonance condition contribute to the energy exchange, according to the standard result for Landau damping.

Before turning to the Fokker-Planck equation to determine the variation of the kinetic energy of the electrons interacting with the wave, we point out that the following relation holds

$$\langle \Delta v\rangle = \frac{1}{2}\frac{\partial}{\partial v_0}\left[\langle(\Delta v)^2\rangle\right] , \tag{4.20}$$

as can be verified from a direct differentiation of (4.17) employing the trigonometric identity $\sin^2(\alpha/2) = (1-\cos\alpha)/2$. The dependence of $\langle\Delta v\rangle$ and $\langle(\Delta v)^2\rangle$ on v_0 is shown in Fig. 4.1 right.

The $\langle\Delta v\rangle$ term, which has been computed going up to the second order in the evaluation of wave-particle interaction, has also a simple meaning. Consider first the particles which are (slightly) slower than the wave: Those which have a phase such that they are accelerated by the wave field are brought into resonance and exchange energy for a longer time than those which are decelerated by the wave. On average, hence, slower particles are accelerated. Similarly, particles which are faster than the wave will, on average, loose energy while interacting with the wave.

Using (4.12) we can now determine the energy gained (or lost) by an electron distribution interacting with an electrostatic wave. In the picture given here, the distribution function f determines the distribution of the initial velocities v_0. Let us now drop the subscript from v_0 for simplicity. The time derivative of the kinetic energy $\mathscr{E}$ of the plasma is

$$\frac{\partial\mathscr{E}}{\partial t} = \int \mathrm{d}v\, \frac{mv^2}{2}\frac{\partial f}{\partial t} = \int \mathrm{d}v \left[mv\langle\Delta v\rangle + \frac{1}{2}m\langle(\Delta v)^2\rangle\right] f , \tag{4.21}$$

where the first term on the right-hand side of (4.12) has been integrated once by parts and the second term twice.

We can now discuss the different mechanisms that contribute to the change in the particle energy.

1. The energy is quadratic in the velocity. Random changes in v lead to a non-vanishing change in the energy $m\langle(\Delta v)^2\rangle/2$.

2. The average $\langle\Delta v\rangle$ is odd in v around ω/k. However, $\int v\langle\Delta v\rangle \mathrm{d}v < 0$. If f is not a function of v then the first term on the right-hand side of (4.21) will give a negative contribution. It turns out that in this case the negative contribution exactly cancels the positive contribution of $m\langle(\Delta v)^2\rangle/2$. This can be immediately seen if we substitute (4.20) into the first term on the right-hand side of (4.21) and then integrate this first term by parts to obtain $\partial\mathscr{E}/\partial t = -(m/2)\int \mathrm{d}v\langle(\Delta v)^2\rangle\, v\,\partial f/\partial v$, which is clearly zero is f is independent of v.

3. If f is a function of velocity such that there are more particles for which $v < \omega/k$ than for $v > \omega/k$ (which usually the case), there is a net increase in particle energy, i.e. an absorption of energy from the wave.

[3] We recall the representation of the δ-function as $\delta(x) = \lim_{a\to 0}(a/\pi x^2)\sin^2(x/a)$.

Summarising, there will be a net absorption of wave energy if the gradient of the distribution function at $v = \omega/k$ is negative, as we know from the standard picture of Landau damping. That the absorption is proportional to the gradient of the distribution function can also be seen by combining (4.12) with (4.20) to obtain

$$\frac{\partial f}{\partial t} = \frac{1}{2}\frac{\partial}{\partial v}\left[\langle(\Delta v)^2\rangle \frac{\partial f}{\partial v}\right] \tag{4.22}$$

i.e. by writing the Fokker-Planck equation as a diffusion equation in velocity space. If the gradient of the distribution function is zero, no diffusion takes place and f is constant in time. If the gradient of the distribution function is positive, then the particles give energy to the wave. This will lead to an instability in which the wave amplitude is exponentially increasing.

Finally, let us briefly discuss the limits of applicability of our description of Landau damping. If the coherence time τ becomes too long, particles can make multiple bounces in the potential of the wave, i.e. they are trapped in this potential, making our (quasi-)linear ansatz invalid. Indeed, we decided to ignore such a process when we have assumed that $k\Delta x(\tau) < 1$. The absorption in the case of multiple bounces goes down. Another point deserves particular attention. The mechanism of Landau damping does not rely explicitly on collisions. However, there has to be some random process which destroys the coherence between the particles and the wave on a short enough time scale. As mentioned before, in a plasma this role is usually played by collisions. Since the amount of energy absorption is independent of the coherence time (if it is not too long), the collision frequency can determine the coherence time without appearing explicitly in the expression for the amount of damping of the wave.

4.5 The Fokker-Planck collision operator

As mentioned in sec. 4.2, the discreteness of the particles reveals itself through the appearence of *internal* forces, i.e. of collisions. Coulomb collisions can be regarded as a Markovian process leading to a change of the particle velocity, if we suppose that each collision event can be regarded as independent of the previous ones. So, we want to employ (4.12) to determine the right-hand side of (4.5). Before calculating the average changes in the particle velocity for a single electron according to (4.10) and (4.11), let us briefly recall some basic features of Coulomb scattering.

A Coulomb interaction between two particles labeled one and two leads to a scattering over an angle θ in the center of mass frame as sketched in Fig. 4.2 left. This angle is determined by the impact parameter b through the equation

$$\tan\frac{\theta}{2} = \frac{b_0}{b}\,, \tag{4.23}$$

where b_0 is the impact parameter for 90° angle scattering

$$b_0 = \left|\frac{e_1 e_2 (m_1 + m_2)}{4\pi\varepsilon_0 m_1 m_2 |\boldsymbol{g}|^2}\right|\,, \tag{4.24}$$

where the relative velocity $\boldsymbol{g} \equiv \boldsymbol{v}_1 - \boldsymbol{v}_2$ has been introduced. In the following, we will denote with $\boldsymbol{v}_1$ the velocity of particle one before the collision and with $\boldsymbol{v}_1'$ its velocity after it.

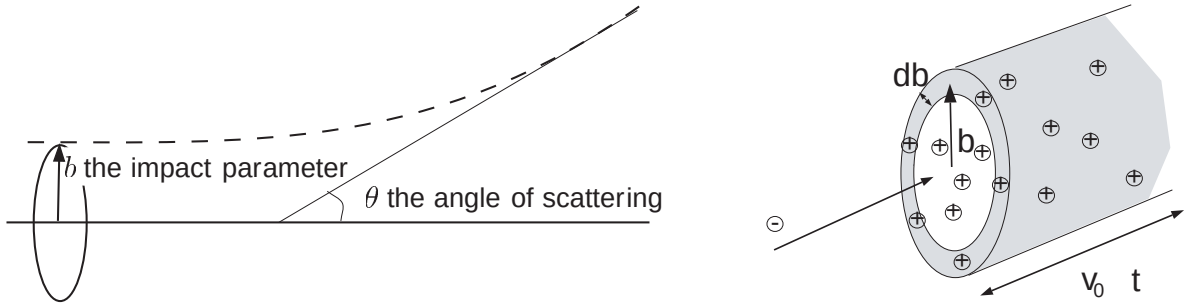

Figure 4.2: Left: Scattering of the particle in the center of mass frame.
Right: Scattering of an electron by ions as the electron travels for a time Δt.

What we want to calculate is the average value of $\Delta \boldsymbol{v}_1 \equiv \boldsymbol{v}_1' - \boldsymbol{v}_1$. Introducing the centre-of-mass velocity $\boldsymbol{v}_{cm} \equiv (m_1\boldsymbol{v}_1 + m_2\boldsymbol{v}_2)/(m_1+m_2)$, and recalling that in the absence of external forces (neglected on the time scale of the collision process) $\boldsymbol{v}_{cm} = \boldsymbol{v}_{cm}'$, it is easy to show that

$$\Delta \boldsymbol{v}_1 = \frac{m_2}{m_1+m_2}\Delta \boldsymbol{g} = \frac{m_2}{m_1+m_2}\, g(\sin\theta\cos\phi, \sin\theta\sin\phi, \cos\theta - 1)\ .$$

In the last step, we have chosen the reference frame in such a way that $\boldsymbol{g}$ is in the direction of the z-axis, $\boldsymbol{g} = (0,0,g)$ and we have employed cylindrical coordinates. As expressed by (4.23), there is a one-to-one correspondence between θ and b, so that an average in θ can be substituted by an average over b. In fact, the probability that particle one is scattered by particle two between an angle θ and an angle $\theta + \mathrm{d}\theta$ during the time Δt is given by the probability of finding particle two inside a cylindrical cell of radius between b and $b + \mathrm{d}b$ and of length $|\boldsymbol{v}_1 - \boldsymbol{v}_2|\Delta t = |\boldsymbol{g}|\Delta t$ (see Fig. 4.2 right for the case of an electron scattered by an ion population). We can hence write

$$\langle \Delta \boldsymbol{v}_1 \rangle = \frac{m_2}{m_1+m_2}\int \mathrm{d}\phi \int b\mathrm{d}b \int \mathrm{d}^3\boldsymbol{v}_2 |\boldsymbol{g}|\ f(\boldsymbol{v}_2)\ \Delta \boldsymbol{g}\ . \tag{4.25}$$

Before proceeding with the calculation of this integral, it is important to understand whether 90°-scattering processes are likely to occur, or if small-angle diffusion dominates. To this aim, we can calculate the mean value of b_0 over the velocity distribution, for instance in the case of a Maxwellian distribution (4.6). We can then compare this value with the typical distance between particles in the plasma, to know whether they come close enough to experience 90°-degree scattering. In general, the mean value of a quantity $A(v)$ over the distribution function is obtained from

$$\overline{A} \equiv \frac{\int A(v)\, f_M(v)\mathrm{d}^3\boldsymbol{v}}{\int f_M(v)\mathrm{d}^3\boldsymbol{v}}\ .$$

In order to calculate $\overline{b_0}$, according to (4.24) we have to evaluate the average distribution of the initial inverse squared velocities $1/v_0^2$

$$\overline{1/v_0^2} = \int \frac{f_M(v_0)}{v_0^2}\mathrm{d}^3\boldsymbol{v}_0 = 4\pi \int_0^\infty \frac{f_M(v_0)}{v_0^2} v_0^2 \mathrm{d}v_0 = \frac{m}{k_B T}\ ,$$

where the integral over the polar angles has been performed in the first step and the formula $\int_0^\infty \exp[-x^2]\mathrm{d}x = \pi^{1/2}/2$ has been used in the second. This yields

$$\overline{b_0} = \frac{e_1 e_2}{4\pi\varepsilon_0 k_B T} \equiv \lambda_L\ ,$$

which is the definition of the *Landau length* λ_L. This quantity must be compared with the average distance of the plasma particles. This can be easily done by evaluating the number of particles within a sphere of radius λ_L, taking $e_1 = e_2 = e$. Recalling the definition of the Debye length $\lambda_D^2 = \varepsilon_0 k_B T/e^2 n$ one obtains immediately

$$\frac{4\pi}{3}\lambda_L^3 n = \frac{1}{3}\left(\frac{1}{4\pi\lambda_D^3 n}\right)^2 = \frac{1}{27N_D^2} \ll 1 ,$$

$N_D \equiv (4\pi/3)\lambda_D^3 n \gg 1$ being the number of particles inside the Debye sphere. This result shows that the particles are usually not close enough in order for large-angle scattering to occur, so that the plasma is dominated by small-angle collisions. In other words, the Coulomb potential is usually much smaller than the mean kinetic energy of the particles.

It follows from these considerations that the integral over b in (4.25) can safely be performed taking b_0 as the lower integration bound, because below this value no scattering process occurs. In the opposite limit, it is known that for distances larger than the Debye length the potential of a charged particle is screened by the others, so that also for $b > \lambda_D$ no scattering takes place. Moreover, since small-angle collisions dominate, we can approximate $\sin\theta \approx \theta$ and $\cos\theta \approx 1 - \theta^2/2$. (4.25) becomes then

$$\begin{aligned}\langle \Delta \boldsymbol{v}_1 \rangle &= \frac{m_2}{m_1+m_2}\int_0^{2\pi} \mathrm{d}\phi \int_{b_0}^{\lambda_D} b\mathrm{d}b \int \mathrm{d}^3\boldsymbol{v}_2 f(\boldsymbol{v}_2)\, g^2 \left(\theta\cos\phi, \theta\sin\phi, -\frac{\theta^2}{2}\right) \\ &= -\frac{2\pi m_2}{m_1+m_2}\int_{b_0}^{\lambda_D} b\mathrm{d}b \int \mathrm{d}^3\boldsymbol{v}_2\, g\boldsymbol{g}\frac{\theta^2}{2}\end{aligned}$$

(remember that $\boldsymbol{g}$ points by definition in the z-direction). Since from (4.23) it is $\theta^2/2 \simeq 2b_0^2/b^2$, using the definition of b_0 (4.24) we arrive finally at

$$\langle \Delta \boldsymbol{v}_1 \rangle = -\frac{e_1^2 e_2^2 \ln\Lambda}{4\pi\varepsilon_0^2 m_1^2}\frac{m_1+m_2}{m_2}\int \mathrm{d}^3\boldsymbol{v}_2 f(\boldsymbol{v}_2)\,\frac{\boldsymbol{g}}{g^3} , \tag{4.26}$$

where we have introduced the *Coulomb logarithm* $\ln\Lambda \equiv \ln(\lambda_D/b_0) \gg 1$.

The same exercise can be performed for $\langle \Delta\boldsymbol{v}_1 \Delta\boldsymbol{v}_1 \rangle$. First of all, let us write down the elements of the symmetric matrix $\{\Delta g_i \Delta g_j\}$

$$\begin{aligned}&\Delta g_1\Delta g_1 = g^2\theta^2\cos^2\phi , \qquad \Delta g_2\Delta g_2 = g^2\theta^2\sin^2\phi , \quad \Delta g_3\Delta g_3 = g^2\tfrac{\theta^4}{4} , \\ &\Delta g_1\Delta g_2 = g^2\theta^2\cos\phi\sin\phi , \quad \Delta g_1\Delta g_3 = -g^2\tfrac{\theta^3}{2}\cos\phi , \quad \Delta g_2\Delta g_3 = -g^2\tfrac{\theta^3}{2}\sin\phi .\end{aligned}$$

The only non-vanishing elements after the integration over ϕ are the elements "11" and "22" (neglecting terms of order θ^4), for which we have

$$\int_0^{2\pi}\mathrm{d}\phi\Delta g_1\Delta g_1 = \int_0^{2\pi}\mathrm{d}\phi\Delta g_2\Delta g_2 = \pi g^2\theta^2 , \tag{4.27}$$

where again we can approximate $\theta^2 = 4b_0^2/b^2$. This yields

$$\begin{aligned}\langle \Delta v_{1i}\Delta v_{1j}\rangle &= \left(\frac{m_2}{m_1+m_2}\right)^2 \int_0^{2\pi}\mathrm{d}\phi\int_{b_0}^{\lambda_D} b\mathrm{d}b\int \mathrm{d}^3\boldsymbol{v}_2 f(\boldsymbol{v}_2)\, g\Delta g_i\Delta g_j \\ &= \frac{e_1^2e_2^2\ln\Lambda}{4\pi\varepsilon_0^2m_1^2}\int \mathrm{d}^3\boldsymbol{v}_2 f(\boldsymbol{v}_2)\frac{g^2\delta_{ij}-g_ig_j}{g^3} ,\end{aligned} \tag{4.28}$$

where the last expression derives from the fact that $g_1 = g_2 = 0$, $g_3 = g$. The two following identities, which can be checked employing the definition of $\boldsymbol{g}$

$$-\frac{\boldsymbol{g}}{g^3} = \frac{\partial}{\partial \boldsymbol{v}_1}\left(\frac{1}{g}\right) \qquad\qquad \frac{g^2\delta_{ij} - g_i g_j}{g^3} = \frac{\partial^2 g}{\partial v_{1i}\partial v_{1j}} \tag{4.29}$$

help us put the previous expressions in a more compact form

$$\langle \Delta \boldsymbol{v}_1 \rangle = \gamma \frac{\partial H}{\partial \boldsymbol{v}_1}\,, \tag{4.30}$$

$$\langle \Delta v_{1i} \Delta v_{1j} \rangle = \gamma \frac{\partial^2 G}{\partial v_{1i}\partial v_{1j}}\,, \tag{4.31}$$

where $\gamma \equiv e_1^2 e_2^2 \ln\Lambda / 4\pi\varepsilon_0^2 m_1^2$ and

$$H(\boldsymbol{v}_1) \equiv \frac{m_1 + m_2}{m_2}\int \mathrm{d}^3\boldsymbol{v}_2 \frac{f(\boldsymbol{v}_2)}{|\boldsymbol{v}_1 - \boldsymbol{v}_2|} \qquad\qquad G(\boldsymbol{v}_1) \equiv \int \mathrm{d}^3\boldsymbol{v}_2\, f(\boldsymbol{v}_2)|\boldsymbol{v}_1 - \boldsymbol{v}_2| \tag{4.32}$$

are the *Rosenbluth potentials*. Substituting (4.30) and (4.31) into the Fokker-Planck equation we obtain the following form for the Coulomb collision term

$$\left.\frac{\partial f}{\partial t}\right|_{\mathrm{coll}} = -\gamma \frac{\partial}{\partial \boldsymbol{v}_1}\cdot\left(f(\boldsymbol{v}_1)\frac{\partial H}{\partial \boldsymbol{v}_1}\right) + \frac{\gamma}{2}\frac{\partial^2}{\partial \boldsymbol{v}_1 \partial \boldsymbol{v}_1} : \left(f(\boldsymbol{v}_1)\frac{\partial^2 G}{\partial \boldsymbol{v}_1 \partial \boldsymbol{v}_1}\right)\,. \tag{4.33}$$

The collision operator is local, i.e. all quantities are evaluated at the same position. Moreover, it is nonlinear in the distribution function, which appears once explicitly and once implicitly in the Rosenbluth potentials.

Before applying (4.33) to the case of a *test particle* in a uniform plasma in thermal equilibrium, we observe that the collision operator conserves particle number, momentum and energy. Furthermore, as stated in sec. 4.2, it satisfies Boltzmann's H-theorem.

Consider now the simple case in which a single particle with velocity $\boldsymbol{V}(t)$ collides with a thermal background, for which the distribution of the velocities $\boldsymbol{v}_2$ is Maxwellian

$$f(\boldsymbol{v}_2) = \frac{n}{\pi^{3/2} v_{\mathrm{th}}^3}\, e^{-v_2^2/v_{\mathrm{th}}^2} \tag{4.34}$$

with $v_{\mathrm{th}}^2 \equiv 2k_B T/m$, see (4.7). The distribution function for the colliding particle is simply

$$f(\boldsymbol{v}_1) = \delta^{(3)}[\boldsymbol{v}_1 - \boldsymbol{V}(t)]\,. \tag{4.35}$$

The moments of (4.33) can be calculated to obtain expressions for the rate of change of velocity, energy, etc. as shown below. Let first multiply (4.33) by $\boldsymbol{v}_1$ and integrate over $\mathrm{d}^3\boldsymbol{v}_1$. On integrating twice by parts, the last term on the right-hand side of (4.33) vanishes. The other term can be integrated once by parts. The result is an evolution equation for the velocity of the test particle

$$\frac{\partial \boldsymbol{V}}{\partial t} = \gamma \frac{\partial H}{\partial \boldsymbol{V}}\,. \tag{4.36}$$

This confirms the interpretation of the first term on the right-hand side of the Fokker-Planck equation (4.12) as a dynamical friction decelerating the particle. Using (4.34), the Rosenbluth potential H and its derivative can be computed analytically as

$$H(\boldsymbol{v}) = \left(\frac{m_1 + m_2}{m_2}\right)\frac{n}{v}\phi\left(\frac{v}{v_{\mathrm{th}}}\right)\,,$$

where the index one has been dropped for simplicty and

$$\phi(x) \equiv \frac{2}{\sqrt{\pi}} \int_0^x \mathrm{d}t\, e^{-t^2} \tag{4.37}$$

is the error function. Noting that H is in our case an isotropic function, we can write (4.36) as

$$\frac{\partial V}{\partial t} = \gamma \frac{\partial H(V)}{\partial V} \equiv -\nu_f(V) V \,, \tag{4.38}$$

which defines the frictional coefficient ν_f. Computing explicitly the derivative of H we have

$$\nu_f = \frac{2\gamma}{V} \left(\frac{m_1 + m_2}{m_2} \right) \frac{n}{v_{\rm th}^2} \psi \left(\frac{V}{v_{\rm th}} \right) \,, \tag{4.39}$$

where

$$\psi(x) \equiv \frac{\phi(x) - x\phi'(x)}{2x^2} \tag{4.40}$$

is the Chandrasekhar function. The functions ϕ and ψ have the following limits

$$\begin{aligned} \lim_{x\to 0} \phi(x) &= \tfrac{2x}{\sqrt{\pi}} \,, \quad & \lim_{x\to\infty} \phi(x) &= 1 \,, \\ \lim_{x\to 0} \psi(x) &= \tfrac{2x}{3\sqrt{\pi}} \,, \quad & \lim_{x\to\infty} \psi(x) &= \tfrac{1}{2x^2} \end{aligned}$$

and they are constants of order one for $x = 1$.

From (4.39) we see that the frictional coefficient is proportional to density and inversely proportional to temperaure. For very fast test particles, $V/v_{\rm th} \to \infty$, ν_f is proportional to $1/V^3$, while it is independent of V at low speeds, $V/v_{\rm th} \to 0$. Eq. (4.38) then implies that the frictional force increases with V at small speeds, but decreases as V increases in the opposite limit. This means that a current in a plasma is usually carried by fast electrons in the tail of the distribution function. Another interesting consequence is the phenomenon of the so-called *runaway electrons*, for which the friction becomes too small to balance a constant accelerating force, like for instance a constant electric field.

As a second example, we multiply (4.33) by $v_{1\perp}^2$ and integrate over $\mathrm{d}^3\boldsymbol{v}_1$, assuming again that the distribution functions for the colliding particles are given by (4.34) and (4.35). Here, $v_{1\perp}^2$ is the sum of the squares of the components of $\boldsymbol{v}_1$ perpendicular to $\boldsymbol{V}(0)$. In this case, only the second term on the right-hand side of (4.33) is found to contribute and we obtain

$$\frac{\partial V_\perp^2}{\partial t} = \frac{2\gamma}{V} \frac{\partial G}{\partial V} \,. \tag{4.41}$$

For a Maxwellian plasma, the Rosenbluth potential G and its derivative can again be computed analytically. A *collision frequency* ν can be defined by imposing the right-hand side of (4.41) to equal to νV^2, with the result

$$\nu = \frac{2\gamma}{V^3}\, n \left[\phi\left(\frac{V}{v_{\rm th}} \right) - \psi\left(\frac{V}{v_{\rm th}} \right) \right] \,. \tag{4.42}$$

In order to evaluate the collision frequency, (4.42), we will assume that a test electron travels at a speed $V = v_{{\rm th},e}$ and a test ion at $V = v_{{\rm th},i}$.

For the case of electron-electron and ion-ion scattering we take then $\phi(1)-\psi(1)\approx 1$ and recalling the definition of γ we get (taking the ion charge equal to absolute value of the electron charge)

$$\nu_{ee} = \frac{ne^4 \ln\Lambda}{2\pi\varepsilon_0^2 m_e^2 v_{\mathrm{th},e}^3} ,$$
$$\nu_{ii} = \frac{ne^4 \ln\Lambda}{2\pi\varepsilon_0^2 m_i^2 v_{\mathrm{th},i}^3} .$$

For the case of an electron scattered by ions and of an ion scattered by electrons we have to take in ϕ and ψ the limit for $x\to\infty$ and $x\to 0$, respectively

$$\nu_{ei} = \frac{ne^4 \ln\Lambda}{2\pi\varepsilon_0^2 m_e^2 v_{\mathrm{th},e}^3}\left[1-\frac{1}{2(v_{\mathrm{th},e}/v_{\mathrm{th},i})^2}\right] \propto \frac{1}{m_e^2 v_{\mathrm{th},e}^3} ,$$
$$\nu_{ie} = \frac{ne^4 \ln\Lambda}{2\pi\varepsilon_0^2 m_i^2 v_{\mathrm{th},i}^3}\frac{4}{3\sqrt{\pi}}\frac{v_{\mathrm{th},i}}{v_{\mathrm{th},e}} \propto \frac{1}{m_i^2 v_{\mathrm{th},e} v_{\mathrm{th},i}^2} .$$

For nearly equal electron and ion temperatures, $T_e\approx T_i$, we have $v_{\mathrm{th},i}\approx v_{\mathrm{th},e}(m_e/m_i)^{1/2}$. The resulting ordering of these collision frequncies is then

$$\nu_{ee} : \nu_{ii} : \nu_{ei} : \nu_{ie} = 1 : \left(\frac{m_e}{m_i}\right)^{1/2} : 1 : \left(\frac{m_e}{m_i}\right) . \tag{4.43}$$

The ions have a smaller (by a factor $(m_e/m_i)^{1/2}$) thermal velocity need more time than the electrons to meet and be deflected by each other. An even longer time is needed for a heavy ion to be deflected by the much lighter electrons.

As a last application of (4.33), we derive the so-called energy exchange times, which are related to the typical time scale required for a particle population to relax to a Maxwellian. Indicating by $\mathscr{E}$ the kinetic energy of the test particle, we can write $\Delta\mathscr{E} = m\left[v_1^2 - V(0)^2\right]/2$. Following again the procedure outlined before, i.e. multiplying both sides of (4.33) by $(\Delta\mathscr{E})^2$ and integrating over $\boldsymbol{v}_1$, it is possible to derive an equation for the evolution of $\Delta\mathscr{E}$ in the form

$$\frac{\partial(\Delta\mathscr{E})^2}{\partial t} = \nu^E\left(\frac{mV^2}{2}\right)^2 ,$$

where the energy exchange frequency defined in the previous equation is found to be

$$\nu^E = \frac{8\gamma}{V^3}\, n\, \psi\left(\frac{V}{v_{\mathrm{th}}}\right) . \tag{4.44}$$

Assuming again v_1 of the order of the thermal speed, we first see that $\nu_{ee}^E\sim\nu_{ee}$ and $\nu_{ii}^E\sim\nu_{ii}$. Moreover, in analogy with (4.43), we can write an ordering of these frequencies for different species

$$\nu_{ee}^E : \nu_{ii}^E : \nu_{ei}^E\ (\sim\nu_{ie}^E) = 1 : \left(\frac{m_e}{m_i}\right)^{1/2} : \left(\frac{m_e}{m_i}\right) . \tag{4.45}$$

In other words, thermal equilibration is reached first by electrons (on the electron-electron collision time scale), then by ions (on the ion-ion collision time), whereas equilibration between these two species takes place after a time which is longer than the electron thermalisation time by a factor m_i/m_e.

Acknowledgments

I wish to thank Dr. R. Bilato and Dr. A. G. Peeters for making available the scripts of their previous lectures on this subject.

References

Most of the material of this lecture is exhaustively covered in Chapters 7 and 8 of T.J.M. Boyd and J.J. Sanderson, *The Physics of Plasmas*, Cambridge University Press, and for Landau damping in Chapter 8 of T.H. Stix, *Waves in Plasmas*, AIP (1992). The physics of Coulomb scattering is described in H. Goldstein, *Classical Mechanics* (2nd edition), Addison-Wesley, 1980.

For a more advanced reading on the derivation of the collision operator the review article of Trubnikov in *Reviews of Plasma Physics*, Ed. M.A. Leontovich, Consultants Bureau, NY, 1965, Vol. 1 is still an undying masterpiece.

For insatiable readers, we recommend the seminal (original) papers of Landau on Coulomb interactions in Plasmas, Zh. Eksper. Theor. Fiz. **t**, p. 203 (1937), and on Landau Damping, J. Phys (Moscow) **10**, p. 25 (1946): They are examples of rare clarity and rigorous logic.

Chapter 5

Plasma heating

Dirk Hartmann

5.1 Introduction

In a fusion reactor that exploits the reaction D+T $\rightarrow$ ^{4}He $+n+17.6\,$MeV the plasma temperature is sustained by the heating done by the created and confined α-particles, i.e. ^{4}He. The cross-section of this reaction is temperature dependent, in particular, it almost vanishes at low temperatures. Thus a temperature of about 20 keV is required for a fusion reactor to ignite. This temperature is much higher than what occurs during plasma start-up in tokamaks and stellarators. Therefore some additional heating is required to raise the plasma temperature until the fusion reaction commences to a sufficient extent and supplies the necessary heating.

Heating of the plasma means that the kinetic energy of the electrons and ions is increased. The heating schemes employed usually do not heat the different plasma species by the same amount. Rather only a fraction of the plasma particles is given kicks in velocity. Furthermore, this velocity increase is not isotropic. Subsequent collisions between the heated fraction and the bulk plasma, however, lead to randomization and equipartition of the additional energy. Generally, this energy causes enhanced radiation losses and particle losses to the walls. Eventually, the plasma reaches a new steady-state where the energy input per time balances the energy losses. This power flow is schematically shown in Fig. 5.1. There the conversion efficiency of the electric power into heating power (up to 50% in some cases) and the loss in the process of coupling the heating power to the plasma have been included.

Different heating methods have been developed and are successfully applied to plasmas:

- Ohmic heating (OH) assumes a singular role. It is the Joule dissipation of the toroidal plasma current that is driven in a tokamak. By itself this heating does not suffice to drive the plasma to reactor relevant temperatures. It is not usable for stellarators since it would unduly modify the magnetic field structure.
- Neutral beam injection heating (NBI) consists of injecting a beam of neutral fuel atoms at high energy that can cross the magnetic field lines into the plasma. By prudent choice of beam energy and plasma density one can achieve that the beam becomes ionized and therefore confined in the plasma center. Through collisions the beam ions transfer their energy to the bulk plasma.

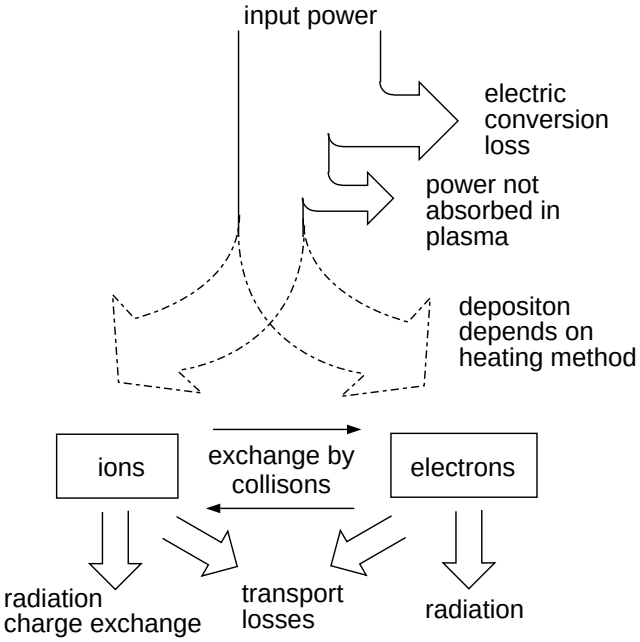

Figure 5.1: Principle of power flow for plasma heating.

- Radiofrequency heating (RF) consists of launching high power electromagnetic waves into the plasma. Depending on the choice of frequency, plasma density and composition different constituents of the plasma can be heated. RF heating is predominantly applied in the range of low frequency Alfvén waves (1–10 MHz), ion cyclotron frequencies (30–100 MHz), lower hybrid frequencies (1–10 GHz) and electron cyclotron frequencies (50–150 GHz).
- α-particle heating, finally, sustains the plasma temperature in a fusion reactor. Initially the α-particles carry 20% of the fusion energy, i.e. 3.5 MeV. But they need to be confined sufficiently long so that they can impart their energy onto the other constituents while thermalizing. Control of the current profile, then solely determined by the bootstrap current, might still require additional ohmic or non-inductive current.

If a neutral beam is injected at an oblique angle or if waves are launched predominantly in one direction with respect to main magnetic field then the current profile is also change due to the heating. This so called *non-inductive current drive* is desirable for tokamaks in order to extend the pulse duration and to access operation regimes of superior confinement which often depend on the current profile. Using non-inductive current drive is one of the advanced tokamak concepts. Current drive might also be necessary for stellarators in order to compensate for the bootstrap current.

5.2 Ohmic heating

A current flows in the plasma if an electric field is applied in the direction of the magnetic field. This current is predominantly carried by electrons since the ions are basically immobile. Due to the finite resistivity of the plasma the current is dissipated by Joule heating.

In the electric field E the electrons are accelerated up to a drift velocity at which the force due to the field is balanced by a frictional force due to collisions with the ions and other

electrons. Ohm's law applies and the plasma resistivity is defined by $E = \eta j$, where j is the parallel current density. The plasma resistivity was calculated in an earlier chapter. It decreases with plasma temperature as $T_e^{-3/2}$. The local ohmic power density, p, then is given by $p(r) = \eta(r) j^2(r)$. Usually the current profile is peaked in the center where the electron temperature is highest. The total heating power is calculated by integration to be

$$P = 2\pi R \cdot 2\pi \int_0^a \eta(r) j^2(r) r dr \, .$$

Even though the resistivity decreases with temperature, this in itself does not rule out the use of ohmic heating to raise the plasma temperature till ignition. The plasma current, however, cannot be arbitrarily increased since it has been found, that magnetohydrodynamic stability requires the q-value at the plasma edge q_a to be greater than two. Thus with $q_a = aB_\phi / RB_\theta > 2$ and $B_\phi = \langle j \rangle \pi a^2 \mu_0 / 2\pi a$ one obtains for the average current density

$$\langle j \rangle < \frac{1}{\mu_0} \frac{B_\theta}{R} \, .$$

In ASDEX Upgrade this limits the plasma current to 1.6 MA. The central current could be higher, but this would also increase the MHD-activity (sawtooths).

The maximum achievable temperature can be estimated from power balance: $\eta j^2 = 3nT/\tau_E$, where τ_E is the energy confinement time which is dependent on plasma parameters. The empirical knowledge of many experiments and of different operating regimes has been condensed into statistical scaling laws for τ_E. For tokamak discharges it has been found that τ_E does not depend on plasma current, thus it is independent of heating power, whereas for other heating methods in tokamaks and stellarators alike it was found that $\tau_E \propto P_{tot}^{-0.5}$, where P_{tot} is the total auxiliary heating power. The proportionality factor and the details of the scaling depend on confinement regimes of stellarators and tokamaks, but even though the maximum expected temperatures of 3–4 keV are still too small for ignition.

Technically the toroidal electric field is induced in the tokamak by changing the magnetic flux ϕ through the center of the torus. This has been shown illustrated earlier when the tokamak concept was introduced. The torus itself is the single winding of a transformer on its secondary side. The flux through the center is changed by ramping the current on the primary side.

5.3 Neutral beam injection heating

A beam of plasma fuel atoms (H, D, T) at high velocities ($\geq$ 50 keV) is injected into the plasma since only neutrals can cross the magnetic field lines. In the plasma the beam atoms are ionized through ionization by electrons (important only for low electron temperatures of 1 keV), charge exchange (dominant process below 90 keV for deuterium beam), and ionization by ions (dominant process above 90 keV for deuterium beam).In total these different processes lead to an approximately exponential decay of the beam neutral density along its path. In a reactorgrade plasma a 100 keV deuterium beam has a decay length of about 0.3 m. This would entail edge heating. Therefore it is desirable to go to higher injection velocities in order to penetrate deeper into the plasma.

The beam ions are slowed down by collisions with plasma ions and electrons. For typical values of $T_i = T_e = 5\,\mathrm{keV}$ and 100 keV deuterium beam the velocities are ordered as $v_i^{th} \ll v_i^b \ll v_e^{th}$. At high beam energies collisions with electrons are the most frequent. This causes the beam to be slowed down without much change of the direction of propagation and causes the electrons to be dragged along. After the beam energy has become smaller than a critical energy E_c given by

$$E_c = 14.8 \frac{A_b}{{A_i}^{2/3}} T_e \,,$$

where A_b, A_i are the charge states of the beam ions and plasma ions respectively, collisions with plasma ions become dominant. These lead to a change in velocity perpendicular to the initial beam velocity. Together, the decrease of the beam energy E_b is given by

$$\frac{dE_b}{dt} = -2\frac{E_b}{\tau_s}\left[1 + \left(\frac{E_c}{E_b}\right)^{3/2}\right] \,,$$

where τ_s is the slowing down time of an ion by an electron with faster velocity. The first term describes the slowing down on electrons and the second term describes the slowing down on ions. The total energy imparted on ions during the slowing down process of a beam with initial energy E_{b0} can be calculated by integrating the second part of the equation. The result is shown in Fig. 5.2 left. Nowadays many experiments have beam energies comparable to the critical energy, thus NBI equally heats ions and electrons. At ASDEX Upgrade the injection energy is 55 keV for deuterium and the critical energy of a 3 keV deuterium plasma is $E_c = 57\,\mathrm{keV}$.

Injecting the neutral beam perpendicular to the magnetic field lines, toroidal and helical ripple losses become important. In smaller devices there is also the problem that the beam is not completely absorbed by the plasma and impinges on the opposite wall causing sputtering and releasing impurities. Injection the neutral beam at an acute angle to the magnetic field lines is technologically more difficult because of the limited space between magnetic coils, but is essential in order to drive a plasma current.

The basic elements of a neutral beam injection system are shown in 5.2 right. It is necessary that particles are charged that need to be accelerated. These particles, say D^+, are generated in an RF or hot tungsten wire discharge. The ions are extracted through a grid and accelerated in an electric field of up to several hundred keV. The shape of the extraction grid allows some steering of the beamlets. By passing the beam through a gas target at low density the beam is partially neutralized through charge exchange processes. A magnet after the neutralizer separates out the unwanted fraction of still unneutralized ions and electrons and steers them onto a dump. The left over neutrals propagate into the plasma. Strong vacuum pumps are required to keep the pressure low in the beam duct. Usually the ion source also creates D_2^+ and D_3^+. These molecules have a lower velocity corresponding to their higher mass and get ionized closer to the plasma edge. The initial beam ion energyiesin the plasma then are at $E_{b0}, E_{b0}/2$ and $E_{b0}/3$.

Beams with energies higher than 100 keV are necessary to penetrate deeper into the plasma. The neutralization efficiency of the gas target decreases rapidly with beam energy. It has its maximum of 60% at 19 keV. The neutralization efficiency of negative ions, D^-, depends less on the beam energy because the affinity of the additional electron to the deuterium is weak. However, extracting large beam currents of negative ions out of an ion source is difficult,

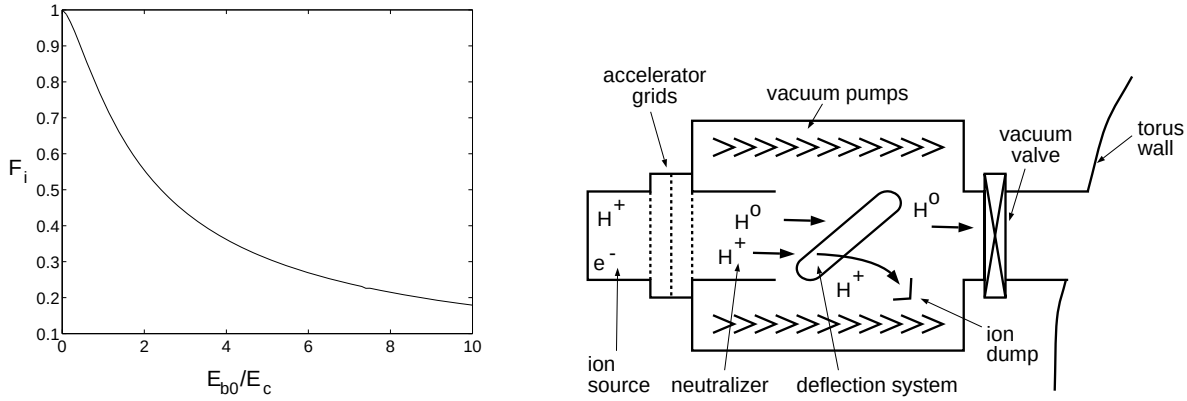

Figure 5.2: Left: Fraction F_i of the initial beam energy E_{b0} going to ions during the slow down process.
Right: Principle of neutral beam injection line.

even though it can be improved by adding cesium to the source plasma. A large fraction of electrons leaves the ion source together with the ions. The goal is to extract 40 A of ion current and accelerate it to 1 MeV. The neutralization efficiency is then about 50% and thus three beam injectors would suffice to couple 50 MW to ITER.

Neutral beam injection has proven very reliable on a number of fusion experiments. Some of its advantages are that the injectors can be tested separately on test-beds, the power deposition can be calculated to good accuracy and injecting neutrals into the center of the plasma is a means of particle refueling. Disadvantages are that the injectors have to be in the immediate vicinity of the torus thus being subjected to high neutron fluxes and tritium contamination. Present research on NBI focuses on the further development of injectors based on negative ion acceleration, new neutralizers based on plasma discharges or lasers, with the goal of high efficiency and continuous operation.

5.4 Radiofrequency heating

RF heating has been used successfully on many devices employing different schemes. In all cases low loss transmission lines exist that make it possible to transmit power from a remote generator to an antenna in the vessel, from which the power is radiated into the plasma. Even though the charged particles are accelerated and decelerated by the electric RF field the dissipation is usually very small because the RF frequency is much higher than the collision frequency of the particles. An exception are resonances that will be discussed at length.

In typical magnetic fusion plasmas the propagation of the RF waves is well described by the cold plasma dispersion relation derived in a preceding chapter, because the plasma pressure is much smaller than the magnetic pressure. The finite size of the plasma bounded by a conducting wall and the shape of the antenna imposes boundary conditions. In particular, the antenna typically fixes the values of $k_\parallel$ of the launched waves, i.e. their $k_\parallel$-spectrum, for a given frequency, ω, of the RF generator. This together with the values of the plasma density and magnetic field determine the corresponding values of $n_\perp \equiv ck_\perp/\omega$ of the plasma waves. The extrema where $n_\perp = 0$ (cutoff) or $n_\perp = \infty$ (perpendicular wave resonance) are of particular interrest. Cutoffs mark regions of the plasma where the wave cannot propagate and resonances mark regions where the phase and group velocity go to zero, thus where the wave energy is

bound to pile up unless *something happens*. In the latter region the phase velocity becomes smaller than the thermal velocity of the plasma particles and the cold plasma dispersion relation is no longer sufficient to describe the plasma properly. Then thermal effects need to be included. This can be done in an orderly fashion though a finite Larmor radius (FLR) expansion where the smallness parameter is the ratio of the Larmor radius to the perpendicular wavelength. This increases the order of the dispersion relation and leads to the *apperance of new waves* that were not present in the solution of the cold plasma dispersion relation. At the former resonances coupling to the new waves occurs. The dispersion relation also predicts damping of the waves. This does not come as a surprise since the Kramers-Kronig relations state (based on causality) that resonances in the real part of the dispersion relation are connected with a non-vanishing imaginary part (usually predicting damping).

The damping process of the wave can be understood on a kinematic level. If a charged particle moves in the same direction and with about the same speed as the phase velocity of a wave, the wave electric field in the moving frame of the particle stays constant and the particle is accelerated or decelerated depending on its position with respect to the wave. If there are more particles that are decelerated than there are particles that are accelerated then there is net energy transfer from the wave to these resonant particles. The wave is damped and the average velocity of the particles is increased. For a Maxwellian velocity distribution wave damping can become significant for waves with phase velocities between one and three times the thermal velocity. Since collisions only partially restore the distribution function such an absorption process leads to a local deviation in velocity space.

With the addition of a static magnetic field the situation becomes slightly more complicated. The motion along the magnetic field still separates out and a wave-particle resonance is possible if the wave has an electric field component along the magnetic field and its phase velocity component $\omega/k_{\|}$ and the particle velocity component $v_{\|}$ fulfill the requirement: $v_{\|} - \omega/k_{\|} \approx 0$. This is called Landau damping.

If the wave has circularly polarized component it can also couple to the gyro-motion of the particles. Resonant interaction requires $v_{\|} - \omega/k_{\|} - l\Omega/k_{\|} \approx 0$ where l is the number of the harmonic. This process is called Landau cyclotron damping. The resonance condition says that energy transfer between the wave and the resonant particles is possible not only if the Doppler-shifted wave frequency matches the gyro-frequency of the particle Ω but also if it is a multiple l of this frequency. If $l \neq 1$ it is necessary that the wave field has a gradient perpendicular to the magnetic field. Consider heating at the first harmonic, i.e. $l = 2$. Let's say that at one point particle and electric field point in the same direction and the particle is being accelerated. After the particle has rotated half a gyro-orbit, the electric field has already completed a full revolution. Thus the electric field points again in the same direction, yet the velocity direction of the particle is reversed and the particle is decelerated during the second half of its gyro-motion. On average no net energy transfer takes place. If, however, the electric field changes magnitude over the plane of the gyro-orbit of the particle, i.e. if the electric field has a gradient, net energy transfer does become possible.

Similar processes exist involving the interaction between the magnetic moment of the gyrating particle and the magnetic field of the wave. They are called transit time magnetic pumping (TTMP).

Concludingly, an RF wave that can propagate into a plasma and is not hindered by cutoffs from accessing a perpendicular wave resonance, can be absorbed there. The absorption coefficient depends on

1. the amount of the wave power that is converted into a wave that has the
2. proper polarization and phase velocity to be resonant with particles of the plasma and
3. the slope of the velocity distribution function of the resonant particles.

In addition, large field amplitudes can lead to a nonlinear enhancement of the wave absorption process.

The changes in the distribution function, in particular if a tail of fast, confined particles with decreased collision frequencies is created, can be useful for current drive if the toroidal symmetry is broken and the waves are predominantly launched into one direction.

In the cold plasma dispersion relation resonances do occur if $n_\perp^2$ goes to infinity which is the case when

$$\varepsilon_\perp \equiv 1 - \sum_s \frac{\pi_s^2}{\omega^2 - \Omega_s^2} = 0 \,,$$

where π_s is the plasma frequency and Ω_s is the signed cyclotron frequency of species s. This yields resonances at the lower hybrid frequency $\omega_{LH}^2 \equiv \pi_i^2/(1+\pi_e^2/\omega_e^2)$, the upper hybrid frequency $\omega_{UH} \equiv \Omega_e^2 + \pi_e^2$ and at the ion-ion-hybrid frequency (close to the ion cyclotron frequencies). The latter occurs only in a multi species plasma. Surprisingly no resonances occur at the ion cyclotron or the electron cyclotron frequencies Ω_i and Ω_e, respectively. At these frequencies the cyclotron motion of the ions and electrons short-circuits the circularly polarized wave component that rotates in the same direction as the considered species, thus completely quelling a possible resonance. As mentioned earlier, FLR contributions or relativistic corrections in the case of electrons need to be included to obtain the cyclotron resonances.

These resonances define the predominant frequency ranges used for RF plasma heating in today's large magnetic confinement experiments. They will be discussed in detail in the following. For completeness also Alfvén waves will be discussed briefly even though none of the large experiments employs them in a heating scheme.

5.4.1 Heating in the ion cyclotron range of frequencies

Near the plasma edge an arrangement of current carrying poloidal conductors, called current straps, excites fast waves in the plasma. They travel almost perpendicular to the magnetic field lines into the plasma center where they can be absorbed at an ion cyclotron resonance or an ion-ion-hybrid resonance. The location of these resonances depends predominantly on the magnetic field strength. In a tokamak, for example, the toroidal magnetic field decreases radially proportional to 1/R, thus the resonant zones are vertical layers where $\Omega_i(R) = \omega$.

In this frequency range $\omega \approx \Omega_i$ except at very low density the slow wave is evanescent. Then $|\varepsilon_\parallel| \gg |\varepsilon_\perp|, |\varepsilon_{xy}|$ and the fast wave dispersion relation is given by

$$n_\perp^2 = \varepsilon_\perp - n_\parallel^2 - \frac{{\varepsilon_{xy}}^2}{\varepsilon_\perp - n_\parallel^2} \,.$$

This wave is elliptically polarized with a small component of the electric field in the direction of the magnetic field. There is a cutoff at the plasma edge for densities $< 2\times10^{18}\,\mathrm{m}^{-3}$. Note

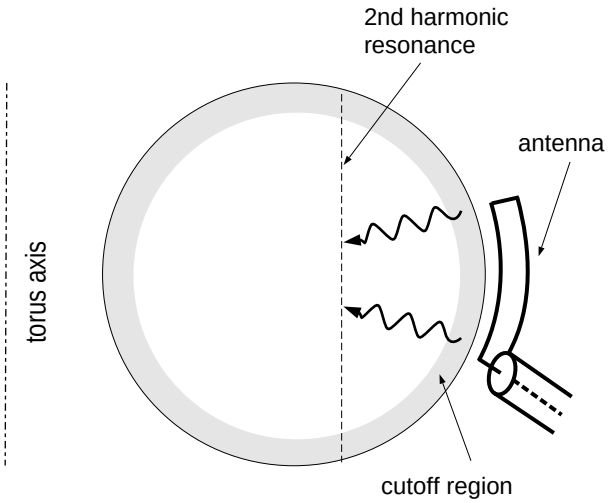

Figure 5.3: Principle of 2nd harmonic ion cyclotron heating.

that, as said before, for a single species plasma this dispersion relation does not have a resonance even though $\varepsilon_\perp$ goes to infinity at the ion cyclotron resonance. The situation changes if finite Larmor radius effects are taken into account or the plasma is allowed to have more than one ion species.

After FLR contributions have been added to the fast wave dispersion relation one finds that due to the parallel electric field component and for higher electron temperatures there is weak Landau and TTMP damping of the electrons even if no ion resonance is in the plasma. Using this process is called *fast wave heating* and is often used to drive a current in the plasma by phasing the current straps such that the radiated $k_\parallel$-spectrum is skewed. The current is not only an effect of the local changes in the velocity distribution function but also due to the decreasing collision frequency at higher velocities that alleviates sustaining the changes in the distribution function.

With the addition of the FLR contribution to the dielectric tensor elements absorption zones appear in the vicinity of the harmonics of the ion cyclotron layers and Landau cyclotron damping can occur. The resonance width is usually small compared to the minor radius of the plasma. Using this process is called *cyclotron harmonic damping*. To determine the strength of the damping also the polarization of the wave in the vicinity of the resonance has to be included. Even with FLR effects the damping at the fundamental resonance is small due to the unfavorable polarization. It has its maximum at the second harmonic and decreases to higher harmonics. Fig. 5.3 shows the evanescent zone near the plasma edge where $n_\perp^2 < 0$ and the resonance layer for 2nd harmonic heating in a tokamak-like cross-section.

At the fundamental the change in the distribution is uniform over all velocities, at the higher harmonics a tail of fast particles is created that becomes more anisotropic with velocity since the particles predominantly gain perpendicular energy.

If the plasma consists of another species of low concentration, say the omnipresent hydrogen in a deuterium plasma, absorption at the hydrogen resonance becomes very strong due to Landau cyclotron damping on the hydrogen. This is possible because in the vicinity of the hydrogen resonance a considerable fraction of the wave power is left circularly polarized because the polarization is determined by the majority deuterium. This scheme is called minority heating. Because all the power is absorbed by the minority ions, a strong tail in the distribution function

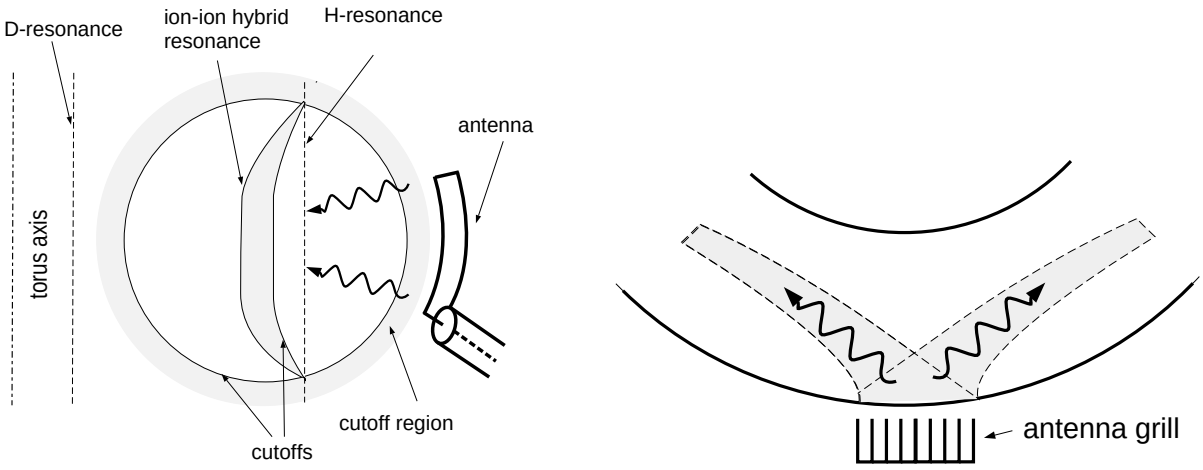

Figure 5.4: Left: Principle of mode-conversion heating.
Right: Wave propagation for lower hybrid heating.

is created. The energies are often higher than the critical energy E_c and the tail relaxes mostly due to collisions with electrons.

For a higher concentration of the second species the beneficial effect on the polarization in the vicinity of the resonance decreases and so does the damping. However, above a critical concentration of a few per cent a new resonance and an associated cutoff occur: The ion-ion-hybrid resonance. The location of cutoffs and resonances are shown schematically in Fig. 5.4 right for the case of hydrogen in deuterium. The resonance calls again for a more detailed analysis using the FLR expension. It is found that near this resonance a mode-conversion of the fast wave to an ion-Bernstein wave occurs. The ion-Bernstein wave has an electric field component in the direction of the magnetic field and is strong Landau damped on electrons. Now the location of the antenna becomes important. If it is located on the low field side the wave is only weakly damped at the cyclotron resonance. At the cutoff it is partly reflected and it partly tunnels to the resonance layer where it then couples to an IBW. There is an upper limit of about 25% of the power of the fast wave that can mode convert to an IBW on a single pass. If the antenna is located on the high field side direct coupling to the IBW is possible. Except for some stellarator-like experiments RF antennas are usually installed on the low field side for practical reasons.

The direct heating of the electrons through this mode-conversion scheme makes it again possible to use it for current drive. However, the location of the mode-conversion layer is critically dependent on the concentration of the minority species thus the repeatability of the experiments very much depends on the gas inventory of the apparatus walls.

Low loss coaxial transmission lines and generators (that were developed for radio communications etc.) are readily available. Usually in antennas the radiated power is only a small fraction of the reactive power. Therefore they are coupled with other reactive elements to form a resonant circuit. This causes large electric fields in the antenna that need to be screened from the plasma.

Good absorption efficiencies, in particular in dense and hot plasmas, have been obtained. The large electric fields in the antenna and the dependence of the plasma coupling on the plasma properties intrinsically link the RF system to the plasma such that separate testing and conditioning are of limited use only.

Present research focuses on a better understanding of the antenna plasma coupling, more detailed investigation of the absorption mechanisms and the development of higher power cw generators.

5.4.2 Lower hybrid heating

A slow wave is launched with a wave guide. In the plasma it travels at a small angle with respect to the magnetic field lines, this causes the wave to circle the torus several times until the center of the plasma is reached. Landau damping along the path often becomes more important than ion damping near the lower hybrid resonance.

In the lower hybrid frequency domain the ordering is $\Omega_i \ll \omega_{LH} \ll \Omega_e$. The dispersion relation of the slow mode is approximately given by

$$n_\perp^2 = \varepsilon_3(1 - n_\parallel^2/\varepsilon_1) \; .$$

As in the preceding RF heating schemes the wave has to tunnel through an evanescent region in front of the antenna until a minimal density given by the perpendicular Alfven resonance is reached. A typical cutoff density is $10^{18}\,\mathrm{m}^{-3}$.

Depending on the $k_\parallel$ of the launched spectrum the slow wave can couple to the fast wave and since the group velocity of the fast wave is such as to transport the power back to the plasma edge the wave energy then becomes trapped in the plasma periphery. This occurs for $n_\parallel$ smaller than a critical density n_c given by

$$n_c^2 = \frac{1}{1 - \omega^2/(|\Omega_e \Omega_i|)} \; .$$

For typical parameters this means that the parallel wavelength needs to be shorter than 0.2 m. For slow waves that well fulfill this requirement the ratio of group velocity perpendicular and parallel to the magnetic field is independent of $k_\parallel$, thus the wave energy travels into the plasma along well collimated beams mainly along the toroidal direction. With approach of the resonance the angle to the magnetic field lines decreases further. This behavior is schematically shown in Fig. 5.4 right.

Even though the wave might not yet have reached the resonance its electric field component parallel to the toroidal magnetic field causes Landau damping on the electrons. Since the $k_\parallel$-spectrum of the launched waves is often quite wide (limited by the accessibility condition and the upper end of the antenna spectrum) the resonant velocities extend from the electron thermal velocities up to a substantial fraction of the speed of light. Thus an electron tail is created extending to very high energies. Near the lower hybrid resonance strong ion damping occurs, predominantly through nonlinear stochastic damping on the ion cyclotron motion.

The antenna arrays consist of a phased array of open rectangular waveguides arranged with the RF electric field aligned with the magnetic field. The shape of the antenna face resembles the plasma shape to be able to move the antenna as close as possible to the plasma surface. However, experiments have shown that the antenna creates its own plasma, thus coupling is usually not at problem. The RF generators used are klystrons.

The creation of the long tail in the electron distribution function and the natural occurance near the plasma edge have sparked interest in lower hybrid current drive. Today's technologies of antenna grill launchers allow the necessary tailoring of the $k_{\|}$-spectrum. Experimentally the current drive efficiencies are the best achieved, particularly at low densities and high magnetic fields.

5.4.3 Electron cyclotron resonance heating

In contrast to the two preceding RF heating methods, at electron cyclotron frequencies no evanescent region between the antenna and the plasma exists. Thus the proper polarization can be chosen at the antenna and the desired plasma wave can be excited with good conversion ratio. Only since the mid 70s generators, called gyrotrons, have become available that operate in the frequency range of the electron cyclotron resonance. In this range only electrons respond to the waves since $\omega \approx \Omega_e \approx \pi_e \gg \Omega_i, \pi_i$.

Two plasma modes exist: The O-mode and the X-mode. The O-Mode is linearly polarized with $E \parallel B$ and the X-mode is elliptically polarized with $E \perp B$. For perpendicular propagation ($n_{\|} = 0$), the dispersion relations are given by

$$\text{O-mode:} \qquad n_{\perp}^2 = 1 - \pi_e^2/\omega^2 \,, \tag{5.1}$$

$$\text{X-mode:} \quad n_{\perp}^2 = \left(1 - \frac{\pi_e^2}{\omega^2} - \frac{\Omega_e}{\omega}\right)\left(1 - \frac{\pi_e^2}{\omega^2} + \frac{\Omega_e}{\omega}\right)\left(1 - \frac{\pi_e^2}{\omega^2} + \frac{\Omega_e^2}{\omega^2}\right)^{-1} . \tag{5.2}$$

The O-mode has a cutoff at the electron plasma frequency. The X-mode has a cutoff below the electron plasma frequency and above the upper hybrid frequency. Fig. 5.5 left and Fig. 5.5 right schematically show the location of resonances and cutoffs for O- and X-mode. For O-mode heating the electron cyclotron resonance is only accessible for densities below the cutoff given by $\pi_e^2 = \omega^2$. For X-mode heating, because of the additional cutoff, the electron cyclotron resonance is only accessible from the high field side. For perpendicular propagation the polarization of the X-mode nearly linear. Efficient absorption requires oblique propagation, whereby the X-mode attains an increasingly right-handed polarization. Strong absorption is obtained at the second harmonic. The absorption process is dependent on thermal (FLR) and relativistic corrections, yet the absorption region is usually very narrow and much smaller than the plasma radius, thus making ECRH also useful for localized heating in order to suppress MHD activity.

The limitation to use ECR heating at densities higher than cutoff has recently been overcome by coupling from an O-mode to an X-mode that finally mode-converted to an Electron-Bernstein-wave. This tricky scheme is possible at a particular angle of incidence. The experimental proof is a fine example of the predictive power of the warm plasma dispersion relation as well as how sophisticated ECRH experiments have become.

The RF power in the electron cyclotron range of frequencies is generated using gyrotrons. In these devices an electromagnetic wave is coupled to spiraling electrons in a steady magnetic field. The bunching of the electrons in phase space amplifies the wave. Care is taken to amplify only one waveguide mode, e.g. the TE_{02}. Output powers of up to 1 000 kW for continuos operation at frequencies of 28–170 GHz have been obtained and research is aiming at 2 MW cw gyrotrons. The RF power is coupled out of the gyrotrons using ceramic and lately diamond windows. Latter have very low absorption and high thermal conduction coefficients allowing edge cooling.

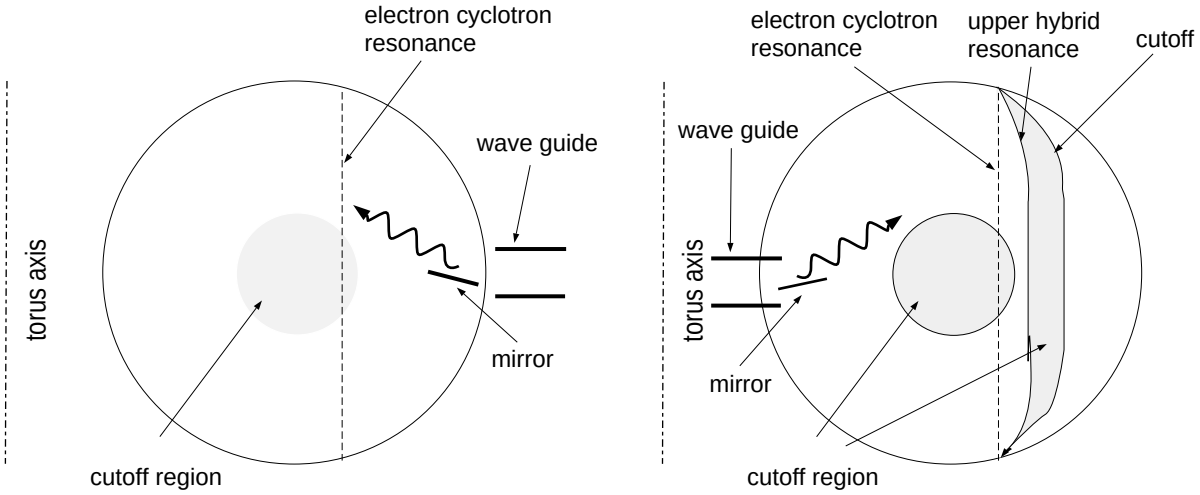

Figure 5.5: Left: Principle of fundamental O-mode heating.
Right: Principle of fundamental X-mode heating from high field side.

Transmission lines consist of waveguides with different mode converters to change the gyrotron output mode into an TE_{11}-mode for O-mode heating or an HE_{11} for X-mode heating. Transmission of Gaussian beams using quasi-optical lines have recently also become available. Finally inside of the torus the direction of the beam can be changed using movable mirrors, allowing off-axis heating without changing the frequency or magnetic field.

The pinpoint accuracy of ECRH due to its narrow deposition profile and the possibility of ray-tracing calculations in an inhomogeneous plasma have made ECRH a valuable and reliable tool. Technical development and testing can be done independently of the plasma. Thus the *power horse* of W7-X will be ECRH with the ambitious goal of 10×1 MW cw gyrotrons.

5.5 α-particle heating

The collisional energy transfer between the 3.5 MeV α-particles to the bulk plasma is the process that will sustain the plasma temperature is a fusion reactor, since the neutrons leave the plasma without interaction. However, even the α-particles might not be confined sufficiently long by the magnetic field to thermalize completely. Possible loss mechanisms involve the toroidal field ripple and interaction with coherent MHD activity (toroidal Alfvén eigenmodes). In tokamaks the α-particle confinement improves with plasma current and in stellarators the magnetic field configuration can be optimized. First experimental studies of α-particles were done during D,T shots in fusion experiments TFTR and JET basically confirming the understandings of the loss mechanisms.

5.6 Non-inductive current drive

The discussed heating schemes usually heat only a small fraction of the plasma particles. This can be taken advantage of by asymmetric wave launching or by tangential neutral particle injection to drive a current in the plasma. This is useful in order to reduce or eliminate the necessity of ohmic current in a tokamak or to compensate for the pressure-driven bootstrap current in a stellarator.

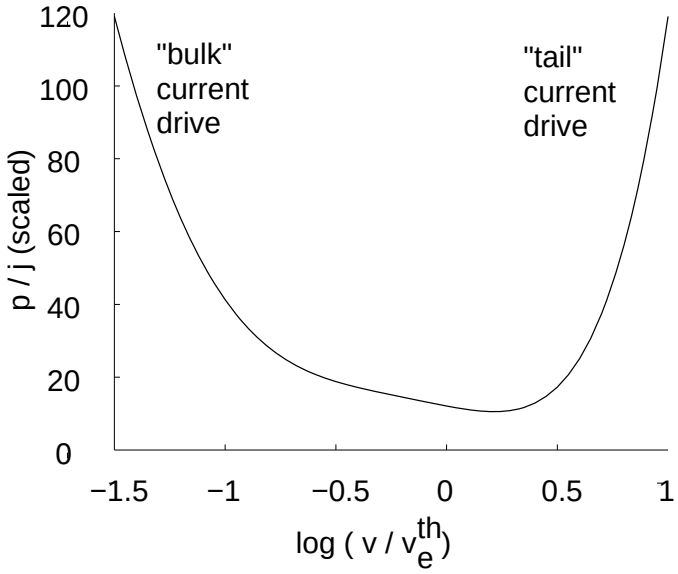

Figure 5.6: Normalized current drive efficiency for Landau damping.

A current drive efficiency γ_{th} can unambiguously be defined as the ratio of local parallel current density, j, and the local absorbed power density p: $\gamma_{th} = j/p$. Different experiments are often compared using a scaled figure of merit γ_{ex} defined as

$$\gamma_{ex} = \frac{\bar{n}_e[10^{20}m^{-3}]R[m]I[A]}{P[W]},$$

where $\bar{n}_e$ is the line-averaged density, R is the major radius of the plasma, i.e. the distance between the torus axis and the center of the plasma column, I is the plasma current and P is the total absorbed power. With $I \approx \pi a^2 j$ and $P = \pi a^2 \cdot 2\pi R \cdot p$ and $j/p \propto 1/\bar{n}_e$ it is easy to confirm that $\gamma_{th} \propto \gamma_{ex}$.

A number of physical concepts can be used to drive a current in a plasma. The following will be mentioned briefly: Pushing of electrons, asymmetric electron collisionality and difference in electron and ion drift.

Electrons are being pushed along the magnetic field lines using Landau damping of waves that are launched in the plasma. This changes the velocity distribution of the resonant electrons until the collisional relaxation balances the driving force. If the antenna current straps are phased properly the waves are launched predominantly in one direction inside the torus, thus a net electron current results. For $\omega/k_{\|} \ll v_e^{th}$ the absolute change in electron momentum for a given loss of energy of the wave is large, but a large fraction of the electrons are trapped in the toroidal field ripple and the collision frequency is large. For $\omega/k_{\|} \gg v_e^{th}$ the collision frequencies are small but there are also few electrons in the distribution function. The compilation of these two effects leads to a theoretical curve shown in Fig. 5.6 identifying the regions of *bulk* and *tail* current drive. Lower hybrid, fast wave and ion-Bernstein wave mode-conversion change the tail of the electron distribution function. Alfvén wave current drive is expected to change the bulk with good efficiency.

Electron cyclotron heating predominantly changes the perpendicular temperature of the electrons and does not impart much parallel momentum. Still current drive is possible since the electrons that fulfill the resonance condition $v_{\|} = (\omega - \Omega_e)/k_{\|}$ (relativistic effects are neglected) and are heated will attain a lower collision frequency due to their higher velocity.

Therefore their collisional relaxation will be reduced. Actually, this effect is also of great importance for current drive based on Landau damping. Yet there is a small caveat. Because of the radial dependence on the magnetic field, this resonance occurs only a small region next to the location where $\omega = \Omega(r)$. Electrons on the high field side of this resonance will also meet the requirement $v_{\|} = (\omega - \Omega_e)/k_{\|}$, albeit for reversed velocity. Therefore it is necessary that the wave is strongly damped. Otherwise one creates a shear layer in the current profile with without any change in the total current.

If a neutral beam is injected at an angle, the slowing down of the beam ions on the electrons drags the electrons along. This electron current only partially cancels the ion current for two reasons. Firstly, if the plasma consists of two species of different charge states the different ion-electron collision times cause the electron drift to match more closely the ions of the highest charge state. Secondly, electron trapping in the toroidal magnetic field ripple reduces the electron drift. Current drive efficiencies of $\gamma_{ex} \approx 0.03$ have been obtained.

References

[1] V. Erckmann and U. Gasparino, *Electron cyclotron resonance heating and current drive in toroidal fusion plasmas*, Plasma Phys. Control. Fusion 36 (1994) 1869.

[2] V. Erckmann et al., *20 years of ECRH at W7-A and W7-AS*, Nucl. Fusion 43 (2003) 1313.

[3] Speth et al., *Neutral beam heating of fusion plasmas*, Rep. Prog. Phys. 52 (1989) 57.

[4] R.A. Cairns, *Radiofrequency Heating in Plasmas*, Hilber, Bristol 1991.

[5] T.H. Stix, *Waves in Plasmas*, AIP, New York 1992.

Chapter 6

Plasma wall interaction in nuclear fusion devices

Karl Krieger

6.1 Overview

A major issue for design and construction of a nuclear fusion reactor with a magnetically confined plasma is the interaction of the hot plasma with the material components of such a device. On the one hand, the plasma facing vessel components represent a sink for energy and particles released by the plasma. On the other hand, the particle bombardment of the material surface may lead to release of wall atoms and of previously implanted fuel atoms which in turn may enter the plasma.

The contamination of the plasma by impurities released from the vessel structure is one of the main problems caused by plasma wall interaction processes. An additional problem is the alteration of the material structure by the particle bombardment and the high energy flux which may limit the lifetime of the plasma facing components significantly. These problems must be solved under the constraint that the generated power has to pass through the vessel components at some location. The wall may further act as a reservoir for the hydrogen fuel isotopes leading to an uncontrollable additional source of fuel atoms, which may cause problems in maintaining stationary discharge conditions.

In the following we will first introduce a basic model of the edge plasma region in contact with the walls, the so-called scrape-off layer (SOL). Then the basic interaction processes between plasma and material walls will be discussed. This includes in particular wall erosion processes leading to impurity production and mechanisms involved in the formation of hydrogen wall inventories and the corresponding recycling processes. Finally, the main diagnostic methods for investigation of plasma wall interaction processes will be discussed.

6.1.1 Plasma facing components

In a fusion reactor, we find several components facing the plasma directly. The largest surface consists of the first wall which surrounds the bulk region of the plasma torus. The plasma shape may be restricted by additional limiters to protect the vessel wall or equipment like

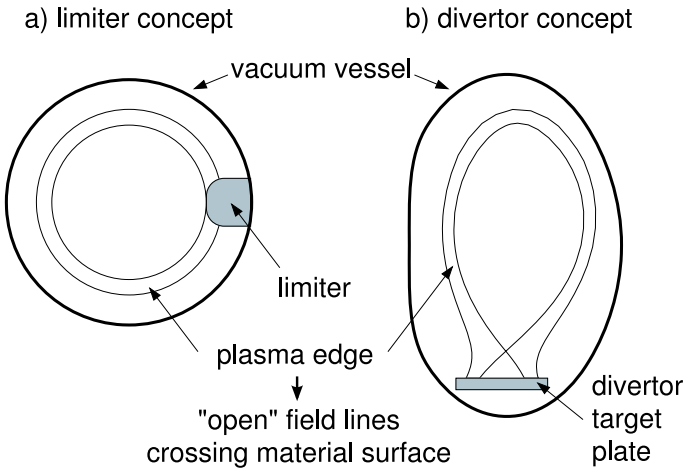

Figure 6.1: Poloidal cross-section of a limiter type (a) and a divertor type (b) plasma configuration with principal plasma facing wall components.

antennas for radio-frequency heating which cannot withstand excessive heat loads. Finally, a very important part of the plasma facing components in current and future fusion devices are the divertor target plates. In a diverted plasma configuration these plates provide the main plasma-surface interaction zone. The fraction of the fusion power carried by the produced α-particles is coupled out to a large extent through these areas.

Fig. 6.1 shows poloidal cross-sections of a limiter type (a) and a divertor type (b) plasma configuration. In a divertor configuration the distance of the plasma wetted surface areas to the confined plasma region is much larger than for limiter configurations. Due to the correspondingly lower penetration probability of eroded material, it is much easier to maintain a low impurity level in diverted plasma discharges.

6.1.2 Bombardment of the walls with plasma particles

If the plasma is in direct contact with wall components, electrons and ions will hit the surface. This particle bombardment leads to release of atoms by collisions and, for certain materials by chemical reactions. In addition the wall material will be heated by the corresponding energy transfer. Finally, electron impact may produce secondary electrons which are reemitted back into the plasma.

The incident plasma ions will be neutralized with a fraction of them being reflected, while the remaining part will be implanted and may be released with some delay. Neutralized particles entering the plasma are ionized again by electron impact or by charge exchange processes with plasma ions. Charge exchange processes in hot plasma regions will produce neutral particles at high energies, which can escape the plasma hitting also plasma facing components without direct plasma contact. high energetic particles and about one half of these will hit the walls again and might be reemitted with some probability.

In fusion plasmas facing components are also subject to intense irradiation by neutrons, which leads to modifications of the material structure and to corresponding degradation of mechanical stability and thermal conductivity.

Wall atoms eroded by the particle bombardment and, in case of excessive heat loads, by evaporation processes, will enter the plasma as impurities with detrimental effects on plasma performance. The erosion of wall surfaces will also limit the lifetime of the respective components.

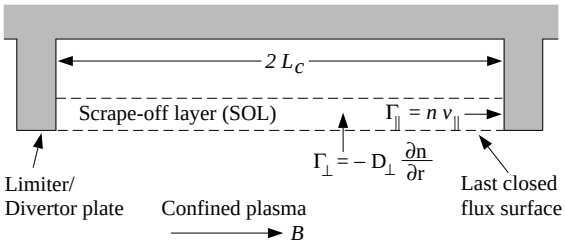

Figure 6.2: Schematic view of the scrape off layer in a magnetically confined plasma [1]. a is the minor plasma radius, B is the magnetic field, L_c is the connection length, $\Gamma_\perp$ is the diffusive flux of particles perpendicular to B and $\Gamma_\parallel$ is the flux of particles streaming along B.

The eroded material will, however, migrate through the plasma until it is finally redeposited, which may balance the erosion to a certain extent.

6.2 The scrape-off layer

As shown in Fig. 6.1 the plasma edge in a magnetically confined plasma is either defined by a material limiter or, in the case of a diverted plasma, by a magnetic separatrix (see Fig. 6.2). Inside the so defined boundary, the magnetic surfaces are closed while in the region between the boundary and the wall surface, the so called scrape-off layer, the field lines intersect material components. The particle exhaust and the α-particle fraction of the produced power (as well as the additional heating power during start-up) are coupled out to a large extent through this region and transferred to the limiters or divertor plates.

The variation of plasma density and temperature in the scrape-off layer as a function of the minor radius can be approximately described by an exponential decay. Using a simple model of particle balance with purely diffusive transport perpendicular to the magnetic field and sonic flow along the field lines, one can estimate the decay length λ_n as a function of the perpendicular diffusion coefficient, $D_\perp$, and the ion sound velocity, c_s. The rate $\dot{N}_\perp$ of particles per unit poloidal length W diffusing across the separatrix into the SOL must be equal to the rate $2\dot{N}_\parallel$ of particles per unit poloidal length streaming along the magnetic field lines towards the two limiters or target plates. $\dot{N}_\perp$ and $\dot{N}_\parallel$ are given by

$$\begin{aligned} \dot{N}_\perp &= D_\perp \partial n/(\partial r)|_{r=a} L_c W &&= D_\perp n(a)/\lambda_n L_c W &&= \Gamma_\perp L_c W \quad \text{and} \\ \dot{N}_\parallel &= \int_a^\infty n(a)\exp(-(r-a)/\lambda_n)\, dr\, c_s W &&= n(a) c_s \lambda_n W &&= \Gamma \lambda_n W\ , \end{aligned} \tag{6.1}$$

where $2L_c$ is the connection length and $c_s = ((T_e + T_i)/m_i)^{1/2}$. Solving $\dot{N}_\perp = 2\dot{N}_\parallel$ one obtains an exponential decrease of n with a characteristic decay length of $\lambda_n = (D_\perp L_c/c_s)^{1/2}$. A similar analysis holds for the temperature assuming convective energy transport. Inserting typical parameters ($D_\perp = 1\,\mathrm{m}^2/\mathrm{s}$, $L_c = 10$–$100\,\mathrm{m}$, $T_{e,i} = 10$–$100\,\mathrm{eV}$), one obtains a decay length in the range from 1–5 cm which is in good agreement with measured values. The decay length of the power flux is smaller because it is determined by the product of n and T.

Since the total energy and particle flux leaving the plasma is concentrated in a very narrow region of the target plates, the incident flux will be strongly amplified over the flux across the plasma boundary. Assuming a circular shaped plasma torus with major radius R and minor

radius a, one obtains a torus surface of $4\pi^2 aR$. The plasma wetted surface of a divertor or limiter in contact with the plasma boundary is $2\pi R\lambda$. The radial flux crossing the boundary of the confined plasma is therefore amplified by the ratio of these surfaces $\pi a/\lambda \simeq 100$ with $a = O(1\,\mathrm{m})$ and $\lambda = O(1\,\mathrm{cm})$. For a fusion machine like ITER, the α-particle heating power is $\simeq 200\,\mathrm{MW}$. With a major plasma radius of $\simeq 6\,\mathrm{m}$ one obtains a heat flux at the target plates of $\simeq 100\,\mathrm{MW/m^2}$, which exceeds by far the engineering limits of any material. It is therefore necessary, to distribute the power to a larger area of the vessel, for example by increasing edge radiation from impurities and charge exchange processes.

6.3 Electric coupling of plasma and wall

When the magnetic field intersects a solid surface, the surface will charge up negatively with respect to the plasma. Consider a small plasma cube with one side limited by a wall and with electrons and ions in thermodynamic equilibrium i.e. with a Maxwellian velocity distribution. For the particle flux to the wall one obtains $\Gamma_e = n\bar{v_e}/4$ and $\Gamma_i = n\bar{v_i}/4$. With $\bar{v} = (8kT/\pi m)^{1/2}$ one sees readily that $\Gamma_e = \Gamma_i (m_i/m_e)^{1/2} \gg \Gamma_i$. A repelling potential for the electrons will build up until the fluxes are balanced which is necessary to maintain the quasi neutrality of the plasma. Because of the screening effect of the plasma, the potential is restricted to a sheath with a width of some Debye lengths $\lambda_D = \left(kT_e/4n_e^2\right)^{1/2}$.

To determine the value of the potential, we consider the balance of ion and electron flux along the field lines. The ions enter the electrostatic sheath with ion sound velocity, thus $\Gamma_i = nc_s$. The electron flux to the wall is modified by the sheath potential

$$\Gamma_e = \frac{n_e}{4}\sqrt{\frac{8kT_e}{\pi m_e}}\,\exp\left(-e\Phi/kT_e\right). \tag{6.2}$$

The electron hitting the wall material will produce secondary electrons which reenter the plasma with a flux $\Gamma_{es} = -\gamma\Gamma_e$ with γ being the secondary electron emission coefficient. From the balance of ion and electron flux $\Gamma_i = (1-\gamma)\Gamma_e$ we obtain

$$e\Phi = -\frac{kT_e}{2}\ln\left(\frac{2\pi m_e}{m_i}\left(1+\frac{T_i}{T_e}\right)\frac{1}{(1-\gamma)^2}\right). \tag{6.3}$$

For a cold hydrogen plasma ($\gamma \ll 1$) with $T_i \simeq T_e$ one obtains $\Phi \simeq 3kT_e/e$. Obviously, if γ increases, the argument of the logarithm will increase as well and become undetermined for $\gamma = 1$. In reality, for $\gamma \geq 0.8$, an electron space charge layer will form at the surface inhibiting any further secondary emission. In that case, the equation above does not hold anymore.

Because only the fast electrons will reach the wall, the electrons are cooled in the sheath. The ions, however, gain additional energy because they are accelerated in the sheath potential. For a Maxwellian plasma the energy flux in one direction is given by $Q = 2kT\Gamma$. The convective energy fluxes to the wall surface are then given by

$$Q_e = 2kT_e\Gamma_e = 2kT + e\frac{\Gamma_i}{1-\gamma}, \qquad Q_i - \left(2kT_i + \frac{kT_e}{2} - e\Phi\right)\Gamma_i, \tag{6.4}$$

where the contribution of $kT_e/2$ for the ions has it's origin by an additional acceleration in a pre-sheath potential drop. Obviously, the major part of the energy flux is deposited by the ions

because of the acceleration by the sheath potential. With increasing edge temperatures the secondary electron emission may come closer to one, thus leading to very high energy fluxes to the wall through the electron channel.

In addition the energy deposition is increased by the neutralization energy of the ions and, for hydrogen, by the recombination energy of the hydrogen atoms.

6.4 Hydrogen fuel cycle

The hydrogen isotopes used as fuel for nuclear fusion interact with most of the relevant reactor materials. This is important in particular because of

- radiological reasons: The storage of tritium in the first wall is responsible for the major fraction of the tritium inventory in fusion reactors;
- engineering aspects: Hydrogen in solids may alter their mechanical properties in an unfortunate way;
- density control of the plasma: The hydrogen inventory in the walls during a stationary discharge will be much higher than the hydrogen content of the plasma itself, leading to possible difficulties in maintaining a stable plasma density.

At low plasma temperatures, neutral atoms and ions hitting the wall will usually be reflected after transferring a part of their kinetic energy to the material.

For high plasma temperatures, the particles can penetrate deeply into the material. In this case, the recycling of the particles will be determined by kinetic reflection, but in addition, the particles may be implanted and reemitted after diffusion back to the surface. In the following, these processes will be discussed in more detail.

6.4.1 Reflection

Ions and neutral particles hitting the wall material will not be reflected right at the solid surface. Usually they will penetrate the material and be scattered by the atoms and electrons in the crystal lattice. Collisions with nuclei will lead to energy transfer and deflection while collisions with electrons will only lead to energy loss. If the path of the penetrating particles leads them back to the surface, they will be reemitted. The particle reflection coefficient R_n and energy reflection coefficient R_E defined by

$$R_n = \frac{\text{number of reflected particles}}{\text{number of incident particles}} \quad \text{and} \quad R_E = \frac{\text{energy of reflected particles}}{\text{energy of incident particles}} \tag{6.5}$$

can be determined by computer simulations where the particle trajectory and the energy transfer in the scattering processes is calculated assuming binary collisions. Experimental results are obtained from backscattering experiments, which are, however, very difficult at energies below 10 eV due to strongly decreasing detector sensitivities.

Fig. 6.3 left shows the reflection coefficients of hydrogen for two reactor relevant materials, carbon and tungsten, as a function of the energy of the incident hydrogen atoms. The reflection

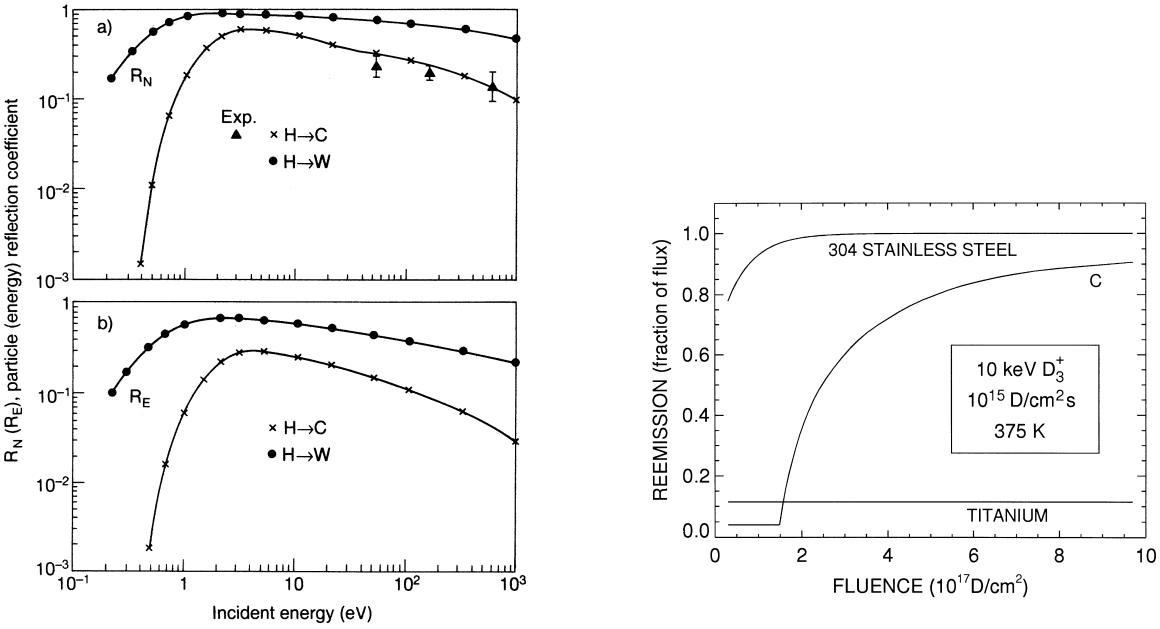

Figure 6.3: Left: Particle (a) and energy reflection coefficients (b) for hydrogen ions incident on carbon and tungsten solid surfaces as a function of the impact energy.
Right: Reemission as a function of fluence (total number of implanted atoms) for different materials. The reemission is expressed in units of the implantation flux.

is mainly determined by backscattering processes and therefore increases with the target atom mass. With increasing energy the incident particles will penetrate more deeply into the bulk material, which leads to the observed decrease of the reflection coefficients towards higher energies. The simulations assume an attractive surface potential, which leads to the strong decrease of the reflection coefficients at energies below 1 eV. The determination of the precise form of the surface potential is, however, a very difficult problem. In addition, adsorbed hydrogen at the surface will strongly modify the surface potential function.

6.4.2 Implantation, diffusion and reemission

The fraction of implanted hydrogen ions which are not reflected, i.e. which do not find their way back to the surface right after penetration, are slowed down by subsequent scattering and will eventually be trapped, either at grain boundaries or at vacancies in the bulk. In addition they may be bound in form of a metal hydride.

When the ions enter the solid surface they recombine to atoms and the fraction which is not trapped within the course of the thermalization process may then travel through the material by diffusion. If the atoms reach a surface, they will recombine to molecules and may be released by thermal desorption.

Metals

Diffusive propagation of neutral hydrogen in a metal is described approximately by a transport equation for the concentration $c(x)$ of free atoms in a depth x

$$\frac{\partial c}{\partial t} = D\frac{\partial^2 c}{\partial x^2} + Q - \frac{\partial c_T}{\partial t} \,, \tag{6.6}$$

where Q is the source function of implanted hydrogen atoms and c_T is the concentration of trapped atoms. The maximal concentration will be found in a depth approximately equal to the mean ion range R_p. From there, the atoms diffuse back to the surface as well as deeper into the bulk material. At the surface, the rate of release is determined by the recombination rate coefficient to H_2 because energetically only molecules can be released. For the H_2-flux one obtains

$$\Gamma_{H_2} = -D\frac{\partial c}{\partial x}|_{x=0} = Kc(x=0)^2 \,, \tag{6.7}$$

where K is the molecular recombination rate constant.

The final equilibrium distribution depends further on the solubility of the hydrogen in the material. For metals in which hydrogen dissolves exothermically like titanium, the surface is a potential barrier. Therefore, the reemission of hydrogen will be very low, the hydrogen is collected in Ti, forming TiH_2 (see Fig. 6.3 right).

In metals like steel, where hydrogen is dissolved endothermically, the reemission depends on the temperature. At low temperatures the diffusion coefficient is small and the reemission is determined by the diffusive transport. A steady state concentration builds up until the flux of implanted atoms is equal to the reemission flux (see Fig. 6.3 right). After stopping the implantation process, the hydrogen inventory in the material will be reemitted. This situation is typical for present fusion experiments with steel walls where the wall temperature remains low because of the short discharge times.

With higher temperatures (500°C for steel) the diffusion increases strongly. In that case, the reemission is mainly determined by the recombination to H_2 at the surface. This situation would occur in a fusion reactor and is important with respect to the tritium fuel. The tritium inventory in the wall will be small but on the other hand, a considerable fraction of the tritium atoms will diffuse through the wall and must be captured for example by a double wall structure with a pumped interspace.

Carbon

For carbon as wall material, the situation is different to the metals. For temperatures 400°C like in present fusion experiments with graphite as wall material, there is practically no diffusion. Implanted hydrogen will be collected until a saturation level of 0.4 H/C is reached. If the implantation continues, the additional hydrogen will be reemitted immediately (see Fig. 6.3 right). After stopping the implantation, the reemission will be much smaller than for metals. In present fusion experiments, the saturation level is reached after some discharges which may cause problems in controlling the plasma density. With so called conditioning discharges using helium, one can decrease the hydrogen inventory if necessary.

In a fusion reactor with wall temperatures above 500°C, diffusion and recombination to H_2 become important also for carbon with similar problems for the tritium handling as for the metals.

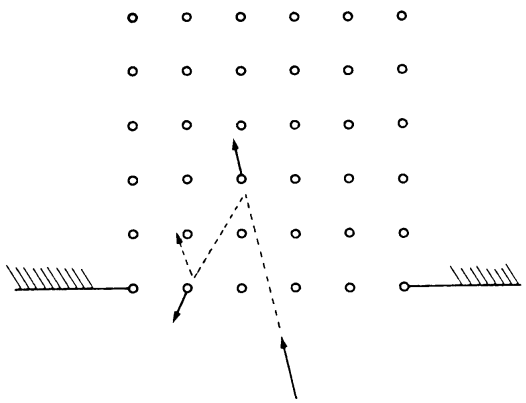

Figure 6.4: Schematic view of the physical sputtering process. The ion incident from the left is reflected in a first collision to the surface where it releases a lattice atom in the second collision.

A further process leading to trapping of hydrogen in carbon will occur in devices with divertor plates made of carbon. Carbon atoms produced by erosion of the plate surfaces may be deposited at other locations where they will collect more hydrogen. This leads to a further increase of the hydrogen inventory in the vessel.

6.5 Impurity production

As mentioned in sec. 6.1, the bombardment of the wall elements by particles escaping the plasma or streaming along field lines which intersect a solid surface will produce in turn a source of neutral atoms from the wall material. Depending on the location of the surface and the plasma properties in the vicinity of the source, a certain fraction of the wall atoms will penetrate the plasma becoming ionized there. The presence of these impurities may degrade severely the plasma properties necessary for nuclear fusion. In this section, we will discuss the most important processes responsible for the contamination of the plasma.

6.5.1 Sputtering

When an ion or neutral atom is hitting a solid surface, it follows a complicated trajectory because of collisions with the lattice atoms in the solid. During this collision cascade the incident particle will be reflected or trapped as described in the previous section. In addition, if a surface atom receives sufficient energy from a collision, it is sputtered away from the solid (see Fig. 6.4). This is only possible if the energy of the incident particle is above a certain threshold E_{th}. The sputtering yield Y is defined by

$$Y = \frac{\text{average number of sputtered particles}}{\text{incident ion}} \,. \tag{6.8}$$

For central collisions, the fraction of the kinetic energy E_0 of an incident particle with mass m_1 which is transferred to a target atom with mass m_2 is given by $\gamma = 4m_1m_2/(m_1+m_2)^2$. For

light projectiles sputtering will occur only if the incident particle is reflected in a first collision towards the surface as shown in Fig. 6.4. It's energy after the collision is $E_0(1-\gamma)$. To sputter a surface atom, the transferred energy in the following collision $E_0\gamma(1-\gamma)$ must be high enough to exceed the surface binding energy E_s. This leads to a threshold energy of

$$E_{th} = \frac{E_s}{\gamma(1-\gamma)} \,. \tag{6.9}$$

For most materials E_s is in the range 3.5–9 eV. Therefore, for the same projectile mass, the threshold energy is mainly determined by the mass of the target atoms. However, if $m_1 m_2$, e.g. if the projectile and the target atoms are the same (self sputtering), the collision cascades are much larger and the model described above does not hold any longer. In that case, the threshold energy is $E_{th} = 4E_s$.

The left part of Fig. 6.5 shows the sputtering yields Y of different targets for bombardment with D atoms. Apart from the described dependence of the threshold energy from the mass of the target atoms the position of the maximum in Y increases to higher target masses.

To determine the sputtering yield of a material exposed to a plasma, one has to integrate the sputtering yields over the energy distribution function of the incident plasma ions. In the plasma the ions usually are close to a Maxwellian distribution. Ions impinging on a solid surface are, however, accelerated by the sheath potential, which significantly increases their impact energy. The right plot of Fig. 6.5 shows results for a D-plasma. The ions from the high energy tail of the temperature distribution and the effect of the sheath acceleration lead to significant sputtering even at plasma temperatures fairly below the monoenergetic sputtering threshold energy.

For heavy projectiles, in particular in the case of self sputtering, the yield may even become greater than one which will lead to an unlimited increase of the impurity content in the plasma.

For light projectiles $Y_{\max}$ is always < 1. This is, however, only true for normal incidence. If the angle of incidence increases from the normal, the sputtering yield increases as well and may become > 1.

The sputtered wall particles are practically all neutral. Except for single crystal targets their angular distribution is given approximately by a $\cos(\theta)$ distribution. Their energy distribution has typically a maximum at $0.5E_s \simeq 2$–3 eV. Therefore, they can deeply penetrate the plasma before they become ionized which gives them a high probability to become confined in the plasma.

6.5.2 Chemical erosion

Another erosion process will be found if the incident particles produce volatile compounds with the target material. This is observed in particular for carbon surfaces with hydrogen plasmas or with oxygen as a plasma impurity. In the first case, methane and higher carbohydrates are produced while in the latter case, production of carbon monoxide (CO) can be observed. These gases are set free very easily from the surface by thermal desorption or collisions.

For the most important case $D^+ \rightarrow C$, chemical erosion by high energy particle bombardment will occur mainly at surface temperatures in the range 500–600°C. However, if the energy of the incident deuterons is smaller than 100 eV, chemical erosion processes will dominate the physical sputtering processes. Fig. 6.6 shows sputtering yields for hydrogen, deuterium and

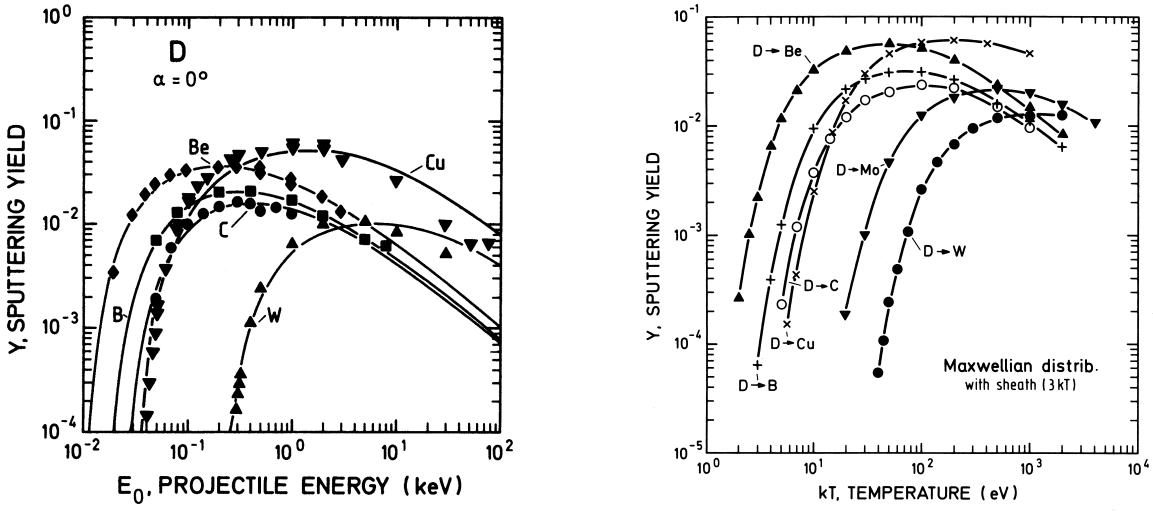

Figure 6.5: Left: Calculated sputtering yield Y of various target materials for bombardment by D ions as a function of impacy energy.
Right: sputtering yields for exposure to a D-plasma as a function of the plasma temperature including acceleration by the sheath potential.

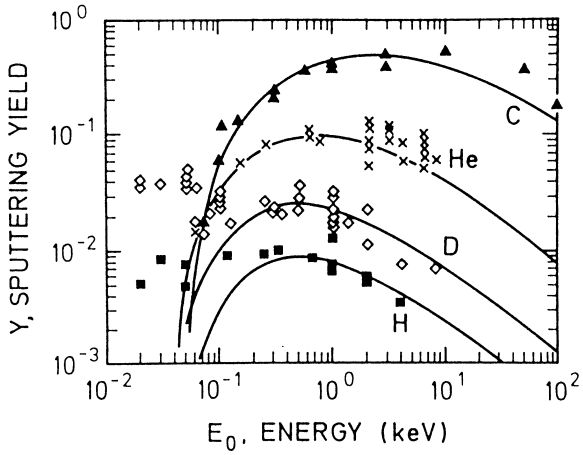

Figure 6.6: Dependence of the sputtering yield of graphite for H, D, He and C ions at normal incidence. The solid curves represent results from simulations of physical sputtering.

helium impact on a carbon surface. The solid lines represent results from calculations with a simulation code for physical sputtering. Obviously, for hydrogen and deuterium sputtering/erosion occurs even below the threshold energy for physical sputtering.

E results from ASDEX Upgrade which is equipped with graphite wall tiles and divertor plates, confirm that the carbon content of the plasma is indeed to a large extent produced by chemical erosion of the main chamber graphite tiles.

6.5.3 Sublimation, evaporation

In a closed system, sublimation from a solid surface or evaporation of fluid material is in equilibrium with the condensation from the gas phase. The equilibrium is determined by the temperature and the steam-pressure of the material. For steam pressures above 10^{-6} mbar,

sublimation or evaporation will be the dominant process. For beryllium which is considered as a possible wall material, the corresponding temperature is 800°C while sublimation of carbon will only occur for temperatures $> 2\,000$°C.

Furthermore, laboratory experiments show that in carbon exposed to high levels of particle influx, interstitial atoms are produced which can reach the surface by diffusion where they sublimate. This process starts at much lower surface temperatures ($\gtrsim 800$°C) and could lead to increased carbon production in a fusion reactor.

6.5.4 Desorption

The surfaces inside the vacuum vessel are covered with thin layers of water, cleaning agents and residue of manufacturing processes. Depending on their surface binding energy, they will be released from the wall by the particle bombardment from the plasma thus producing an additional source of plasma impurities. It is possible to remove the weakly bound layers by glow discharges, however, the remaining oxide layers and adsorbed water molecules cannot be removed and are the main source for the oxygen contamination of the plasma.

6.5.5 Arcing and melting

If metals are used as wall material, the surface can be destroyed by melting, if the heat load from the plasma becomes so high that it cannot be removed by conduction and cooling. Droplets of molten material from the upper vessel regions can fall into the plasma where the sudden rise of the radiation losses may cause a break down of the discharge.

As less spectacular erosion process can be observed under certain discharge conditions. Because of the potential difference between edge plasma and wall, electric arcs are ignited by field emission from ridges and peaks in the surface which last for times $1\,\mu$s with a size of some mm. After ignition the cathode spot on the material surface is heated up by ion bombardment from the arc and cooled by the melting and conduction. The cathode spot grows because of the increasing erosion and after reaching a critical size the arc breaks down and may ignite again in the vicinity.

6.5.6 Positive and negative aspects of impurity contamination

The impurity contamination of the plasma in a fusion reactor can only be tolerated below a critical level which depends mainly on the charge number of the impurity atoms. However, if one can restrict the zone with higher impurity concentration to the plasma edge and the divertor plasma, the presence of impurities can also have a beneficial effect as described below.

High-Z – cooling of the central reaction zone

Heavy impurities like tungsten, molybdenum and to a certain extent nickel and iron are not fully ionized in a fusion plasma. The power loss by their line radiation is a function of the plasma temperature which has for high-Z elements a maximum in the temperature range of 10^6–10^7 K relevant for nuclear fusion. Therefore, concentrations higher than 0.01% (for W, Mo) and higher than 0.1–1% (for Fe, Ni) will lead to a power losses which inhibit the ignition of the plasma.

Fuel dilution

Light impurities like beryllium, boron and carbon and also helium as a product of the fusion process will be fully ionized in the plasma core. Therefore, they do not emit line radiation in the central region in contrast to the cooler edge regions. The radiation losses in the outer plasma zone will not inhibit the ignition and the burning of the plasma. However, they still can degrade the overall energy balance of the fusion reactions. A further negative effect is the dilution of the fuel ions in the core because of the quasi neutrality of the plasma which will decrease the fusion rate. For these reasons, the concentrations of light impurities in the confined plasma must not be higher than 2–5%.

Edge cooling and power exhaust

Under certain plasma conditions, in particular at high densities, it turned out that it is possible to confine the impurities in the divertor region of a tokamak plasma. There are attempts to use the intense line radiation produced by light impurities in this cooler zone as a means to spread the power flux generated from the plasma onto a larger area of the vessel surface thus decreasing the power load of the divertor target plates. The impurities can be introduced into the divertor plasma either by sputtering from the walls or by additional puffing of impurities in gas form. This concept is known as *radiative divertor*.

Another concept to make use of radiation to decrease the power load of the divertor plates consists basically in trying to increase the divertor density to very high values and to puff in additional gas. Then, a cold plasma zone will establish above the divertor plates in which the plasma ions streaming towards the plates are cooled by charge exchange radiation. However, in these processes, as mentioned above, fast neutral atoms are produced which may increase the wall sputtering. This concept is known as *cold gas target*.

6.6 Diagnostics for plasma surface interaction

Many diagnostics are needed to provide the information for a more detailed understanding of the edge plasma and plasma-wall interaction. A detailed description would break the size limit for this manuscript, therefore only a short overview is given over diagnostics used directly in fusion experiments and diagnostic methods used in laboratory experiments for example to analyze wall materials and surfaces.

6.6.1 In situ diagnostics

- *Electron density and temperature* are measured by Thomson scattering and from spectral emission of neutral atom beams injected into the plasma edge. A further possibility is the use of electrical Langmuir probes which allow the measurement of n_e and T_e and in addition the *floating potential* of the plasma.
- *Impurity densities and fluxes* and the *densities of molecules* are measured by spectroscopy and laser resonance fluorescence. With good spectral resolution, *impurity temperatures* can be measured as well. However, there is no good method to obtain the *temperature of the plasma ions*.

- *The composition of the neutral gas* is determined by mass spectrometry. This gives valuable information for example on the molecules produced by chemical erosion.
- *Velocity spectra of escaping neutrals* are measured by time of flight spectrometers. These provide information on the ion temperature in the plasma and allows to estimate the effects of the neutral wall bombardment.
- *Surface temperatures and heat flux deposited on surfaces* are measured by infra red cameras.
- *Surface erosion and deposition* are investigated with long term marker probes where materials are vaporized as thin layers onto surface elements. To analyze single discharges, collector probes are used which allow in addition the determination of *impurity flux, mean energy and mass* and *plasma ion fluxes and mean energy*. After exposure to the plasma for a certain time, the probes are removed and analyzed by surface analytical techniques described in the next paragraph. As a further method to measure *erosion and redeposition of thin material layers* one can measure the thickness of such layers by interferometric methods.

6.6.2 Laboratory experiments

- *Analysis of collector probes and long term exposition probes*. The surface structure of the probes is examined by raster electron microscopy. The electron beam of the microscope will produce bremsstrahlung when hitting the examined surface which is characteristic for each element and allows the determination of the material composition. A quantitative determination of the distribution of an element in the material is possible by scanning the surface with high energy ion beams (in the MeV range) of protons, deuterons or α-particles. One can measure the energy distribution of the ions from R utherford backscattering processes (RBS) or, in case of a proton beam, the spectrum of the proton-induced X-ray emission (PIXE). A further possibility is the detection of products of nuclear reactions induced by the incident ion beam which are also characteristic for a certain element. To measure the erosion of the probe surface, a trace element is implanted in a surface layer with known thickness. The erosion rate is determined by measuring the thickness of the remaining layer after exposition of the probe.
- *Hydrogen recycling* is studied by implanting protons or deuterons in materials until steady state is reached and measuring the pressure of the reemitted atoms as a function of time after switching off the beam.
- *Sputtering coefficients* can be measured by bombarding a probe with an ion beam and measuring the weight loss after a certain exposition time. In addition, the sputtered material can be analyzed by laser resonance fluorescence.
- *Reflection coefficients* are determined by estimating the amount of trapped atoms or by detecting the reflected particles using ion spectroscopy.

References

[1] J. Wesson, *Tokamaks*, p. 424 (1996).

[2] W. Hofer, J. Roth (Ed.), *Physical Processes of the Interaction of Fusion Plasmas with Solids*, San Diego (1996).

[3] R. Behrisch and D.E. Post (Ed.), *Physics of Plasma Wall Interactions in Controlled Fusion*, Proceedings of a NATO Advanced Study Institute, New York (1985).

[4] P.C. Stangeby, *The Plasma Boundary of Magnetic Fusion Devices*, Bristol (2000).

[5] O. Auciello, D.L. Flamm (Ed.), *Plasma Diagnostics - Surface Analysis and Interactions*, San Diego (1989).

[6] J.C. Vickermann (Ed.), *Surface Analysis - The Principa Techniques*, West Sussex (1997).

Chapter 7

Introduction to plasma diagnostics

Hans-Jürgen Hartfuß

7.1 Introduction

Investigating hot magnetized plasmas in the frame of fusion research, a large number of different diagnostic methods must be applied. Common to all diagnostic techniques is that plasma probing is conducted without any material contact between the measuring instrument and the plasma. Material probes can only be used in the very plasma edge and only for short moments.

The physics principles underlying the various techniques originate from almost all fields of physics. They are complementing one another with respect to dynamic range or concerning certain information gained by other diagnostic systems necessary to interpret the measurements. The whole diagnostic system has redundancy which means that a given physical quantity, say the electron temperature, is measured simultaneously by a number of different measuring systems which are based on different physics principles, ensuring that systematic errors do not remain unrecognized.

Although a large number of diagnostic methods is well developed and established, growing new fields of research demand for additional information, or higher spatial and temporal resolution, stimulating the development of new methods and even more refined techniques. Recent developments are often related to turbulence characterization, measuring fluctuating plasma parameters with high time and space resolution and determining correlations between various fluctuating quantities.

Typically more than 50 different diagnostic systems are installed at modern large fusion experiments. They provide the data which form the basis for the scientific work conducted, and they provide as well the bulk of information necessary for the safe operation of the fusion experiment and the protection of its components. Diagnostic data rate of the whole system typically exceeds 100 Mbyte per second. The data must reliably be stored in such a way that data access remains possible even after many years.

To characterize the plasma in an adequate way and to understand its complex behaviour as complete as possible, a large number of different plasma parameters must be determined simultaneously. These are the density of the electrons and the ions, the composition and density of certain impurities in the plasma, the temperature of the electrons and of the ions which can differ significantly depending on the heating scenarios conducted, the total stored energy, the

plasma pressure, the radiation loss, currents and electric fields in the plasma and many others. Most of them are local quantities varying with the radial coordinate. Examples are the electron temperature and density being typically maximal at the plasma axis and approaching low values at the plasma edge varying over orders of magnitude. Most of the quantities are time dependent with characteristic times varying significantly. While fluctuating quantities are characterized by time scales of the order of 1 μs, certain currents in the plasma or the energy content vary slower by five orders of magnitude. The demanded accuracy of all the diagnostic measuring systems is typically 1–10%. The spatial resolution aimed at is 1–5 cm and the time resolution of the order of 0.1 ms. This short introduction to the subject concentrates on the physics behind the most important diagnostic methods, factoring out completely the wide field of technical realizations.

7.2 Categorization

The various diagnostic methods can be arranged according to different ordering principles. A natural distinction divides into active and passive methods whereas in each case waves or particles must be considered. Moreover Langmuir-probes form a separate class of techniques which could be assigned to both passive and active particle diagnostics. Another class is formed by magnetic diagnostics.

A more physics oriented categorization distinguishes the physics processes involved: Electron or ion processes, processes leading to the emission of electromagnetic radiation, light scattering processes, processes connected with the refractive index of the plasma and so on. Other organizing principles used in literature are based on the techniques involved, like laser-, spectroscopic-, X-ray-, microwave-, atomic beam techniques, etc. We will adapt an ordering scheme according to the first one given above. The chapters following directly reflect this choice.

7.3 Sightlines

Plasma probing with waves or by particles occurs along a sightline through the plasma determined by the experimental conditions of the measuring system.

- In a single sightline arrangement one cannot distinguish from which point of the sightline the information is coming from. Only line integrated information can be gained (examples: spectroscopy, interferometry).
- Using 10 to 15 sightlines simultaneously, however, local information can be derived from a reconstruction process called Abel-inversion (multi-channel interferometry).
- Modern computer based reconstruction methods allow for the application of tomography. Local information is obtained from a large number of typically several hundreds of line-integrated signals from pinhole camera systems (soft X-ray bremsstrahlung, bolometry).
- A special case of passive wave diagnostics, gives local information from a single sightline since the origin of radiation is connected with the frequency of the emission that mapping between frequency and location is possible (electron cyclotron emission).

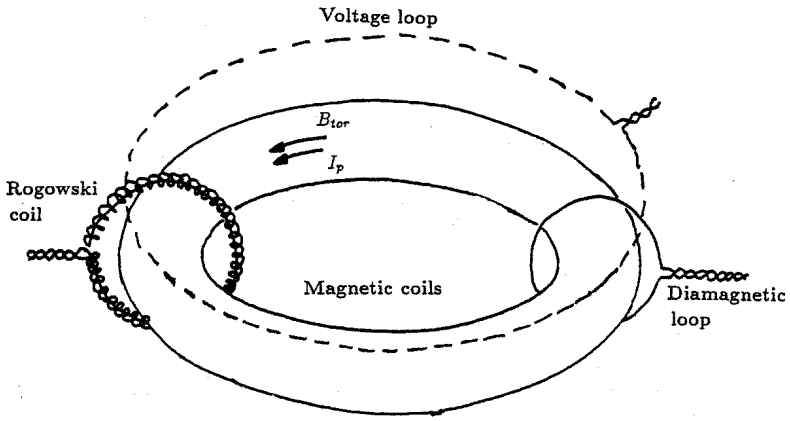

Figure 7.1: Arrangement of the most important inductive loops forming the set of magnetic diagnostics in a toroidal fusion device: The Rogowski-coil to measure the total plasma current, the voltage-loop to measure the current driving loop voltage, and the diamagnetic-loop which allows to determine the total stored energy in the plasma.

- Applying active techniques with atomic or laser beams, the origin of the information detected is defined by the crossing volumes of primary beam and detection beams, resulting in local information (Thomson scattering, neutral hydrogen diagnostic beam).

All diagnostic methods out of the categories active and passive wave or particle diagnostics belong to one of these five different observation schemes. Using Langmuir-probes the location is defined by the tip of the material metallic probe. Magnetic diagnostics have no spatial resolution since they measure the total flux changes enclosed by loops outside the plasma column.

7.4 Magnetic diagnostics

Magnetic measurements are conducted with induction loops wound around the torus in various orientations. The voltage V obtained at the clamps of a loop with N turns and area A is determined by the temporal flux change enclosed by the loop

$$V = -\int_F \frac{\partial B}{\partial t} dF = -NA\dot{B}\,. \tag{7.1}$$

The magnetic field B is obtained by integration accomplished electronically. The most important magnetic diagnostics reveal the total plasma current with the Rogowski-coil, the loop voltage with the voltage-loop, and the total stored energy in the plasma with the diamagnetic-loop. The basic arrangements are shown in Fig. 7.1.

7.4.1 Rogowski-coil

The Rogowski-coil is a solenoid enclosing the whole plasma current i.e. the torus in one poloidal plane. It is sensitive only to the poloidal field generated by the net current I_p consisting of electron and ion currents in opposite directions. No information is gained on the current distribution. The plasma current I_p is derived by integrating the measured voltage V over time which is for a coil with n windings per unit length and area A given by

$$V = \dot{\Phi} = nA\mu_0 \dot{I}_p \, . \tag{7.2}$$

7.4.2 Voltage-loop

In tokamak experiments the plasma current is driven by the voltage generated by the external transformer. This so-called loop voltage is measured by an inductive loop consisting of a single wire which encloses the total flux generated by the transformer. The voltage loop lies parallel to the torus ring. Knowledge of the loop voltage V_l and the plasma current I_p are connected through the plasma conductivity and since the conductivity is temperature dependent, also the average electron temperature can be derived

$$\frac{I_p}{V_l} \propto \sigma \propto T_e^{3/2} \, . \tag{7.3}$$

7.4.3 Diamagnetic-loop

The average plasma pressure or equivalently the average energy density can also be determined from purely inductive measurements. In a magnetized plasma electrons and ions are gyrating around the field lines in a way that the external field is weakened giving rise to the plasma diamagnetism. The flux change $\Delta\Phi$ caused by the plasma built up in the magnetic field is proportional to the average plasma pressure $\langle p \rangle$ equivalently to the average energy density

$$\Delta\Phi \propto \langle p \rangle = k_B \langle n_e T_e + n_i T_i \rangle \, . \tag{7.4}$$

It is measured with the simple flux loop wound around the torus in poloidal direction. It must be integrated in time to get the actual stored *diamagnetic* energy.

7.5 Wave diagnostics

Wave diagnostics gain information either by analyzing the spectral composition of the emitted radiation from the plasma (standard spectroscopy) or by measuring the changes in amplitude, phase, polarisation or k-vector a wave undergoes when passing the plasma.

The hot magnetized plasma is emitting radiation in a very wide spectral range. To gain the full information contained, passive probing must therefore be done at wavelengths extending from about 10 mm to 0.1 nm over about eight orders of magnitude covering the ranges from micro-waves to X-rays. Basically also absorption spectroscopy can be done in this range. It has gained, however, only minor importance.

In active probing experiments the wave particle interaction is almost completely governed by the mobile electron component of the plasma. The electron density determines a cut-off frequency below which no propagation is possible and beyond which the refractive index of the plasma varies in a characteristic way. Largest changes occur in the mm and sub-mm spectral regions which therefore have the highest diagnostic potential.

At frequencies far above this cut-off, the refractive index approaches the vacuum value, however, electrons can still be accelerated by the wave's E-field causing wave scattering which carries important information about the scattering centres.

7.5.1 Active wave measurements

Microwave diagnostics

Propagation of an electromagnetic wave through the plasma is described by the dispersion relation connecting the wave k-vector to the frequency $k = k(\omega)$, from which the refractive index N can be derived.

Neglecting ion motion and collisions between particles in a non-magnetized plasma, the dispersion relation and the refractive index are

$$\omega^2 - \omega_p^2 = k^2 c^2 \; ; \qquad N = \sqrt{1 - \left(\frac{\omega}{\omega_p}\right)^2} \; . \tag{7.5}$$

ω_p is the plasma frequency determined by the electron density

$$\omega_p^2 = n_e \frac{e^2}{\varepsilon_0 m_e} \; . \tag{7.6}$$

Propagation is only possible for $\omega > \omega_p$. Since electron densities are typically in the 10^{19}–$10^{20}\,\mathrm{m}^{-3}$ range, propagation is only possible beyond about $f = \omega/2\pi > 100\,\mathrm{GHz}$. It is the mm-wave range where the strongest changes of the refractive index occur, which is therefore used for probing (see Fig. 7.2 left).

Contrary to this a magnetized plasma is a strongly anisotropic medium. General expressions for the dispersion relation are complicated.

However, in case a linear polarized wave propagates perpendicular to the B-field through the plasma with its E-field parallel to B (ordinary mode) the dispersion relation is identical to that one of the non-magnetized plasma, as given above. The relation is the basis for two important diagnostic systems interferometry and reflectometry operated under the above described conditions.

1. Interferometry
   Since the refractive index depends on the electron density via the plasma frequency, measurements based on the refractive index give information on the electron density. The measurement is done by comparing the optical path difference between a microwave signal through the plasma and one through free space which can easily deduced from the phase difference of the two signals. If the probing frequency is large compared to the

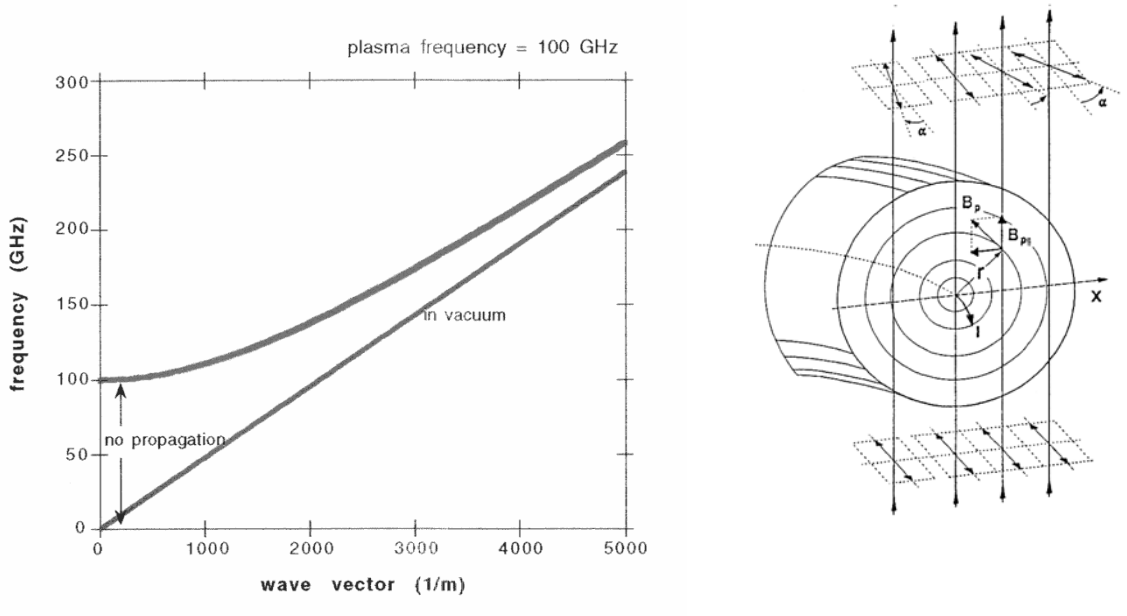

Figure 7.2: Left: Dispersion relation of a non-magnetized plasma (red). The plasma frequency is chosen 100 GHz corresponding to an electron density of 1.26×10^{20} m^{-3}. At frequencies below the plasma frequency no propagation is possible.
Right: Principle arrangement of a polarimetry system to measure the poloidal field generated by the plasma current. The Faraday-effect gives rise to a rotation of the polarization plane by the angle α. The rays through the plasma can be used as well as interferometer channels to determine simultaneously the electron density (H. Soltwisch, Transactions of Fusion Technology **25**, 304 (1994)).

plasma frequency, the phase difference is proportional to the electron density integrated along the line of sight

$$\varphi = \frac{2\pi}{\lambda}\int_{z_1}^{z_2}(N_V - N(z))\,dz \propto \int_{z_1}^{z_2} n(z)dz\,. \tag{7.7}$$

The integral quantity determined in this way is called the line-density and is one of the most important parameters in fusion diagnostics. Local information can be gained by operating simultaneously a number of interferometers with parallel sightlines covering the plasma cross section and by applying mathematical inversion techniques (Abel-inversion).

2. Reflectometry
While interferometry uses frequencies in the range 200 GHz to 30 THz far above the plasma frequency, in reflectometry the probing frequency range is chosen just to meet it. As mentioned before plasma frequencies range from about 30–100 GHz. Reflectometry then launches a wave in this frequency range and determines the position inside the plasma where $N(\omega)$ approaches zero and from where the launched wave is reflected. The position of the reflecting cut-off layer is determined applying RADAR techniques by measuring the time delay to the cut-off layer and back. This can be done electronically in various ways, either with short microwave pulses of sub-ns duration or by sweeping

the frequency of a continuous wave and measuring the resulting phase change. Other methods are basically combinations of these two. The local electron density $n_e(r)$ is determined from a scan of the probing frequency relating time delay τ and cut-off frequency $\omega(\tau)$.

3. Polarimetry
   The dielectric properties of the magnetized plasma give rise to additional effects which can favourably be used for diagnostic applications. Considering here only active wave probing with propagation parallel and perpendicular to any *B*-field of a magnetized plasma. In case of parallel propagation, the two characteristic waves are the left and the right hand circular polarized waves. Due to the gyration motion of the electrons with frequency ω_c, the magnetized plasma is circular birefringent, which means the refractive indices of the left and right hand circular waves N_L and N_R differ. A magnetized plasma therefore shows the Faraday-effect: The polarization plane of a linear polarized wave propagating along the *B*-field is rotated by a small angle α given by

$$\alpha = \frac{1}{2}\frac{2\pi}{\lambda}\int_{z_1}^{z_2}(N_L - N_R)\,dz \approx \frac{1}{2c}\int_{z_1}^{z_2}\omega_p^2\omega_c\frac{dz}{\omega^2} \propto \int_{z_1}^{z_2} n_e(z)B_{\parallel}(z)dz\,. \tag{7.8}$$

   The measurement is a line-integrated measurement in an arrangement almost identical to that of an interferometer. Therefore often the two are combined to form an interfero-polarimeter arrangement measuring simultaneously the phase to determine the electron density and the rotation of polarization to determine the parallel *B*-field component along the line of sight. If the line of sight is chosen within one poloidal plane, the parallel *B*-field is the one generated by the plasma current. In case many sightlines are used simultaneously, the plasma current density can be determined (see Fig. 7.2 right).

In case of propagation perpendicular to a *B*-field field, the two characteristic waves are linear polarized waves with the *E*-field parallel to *B*, the one used for interferometry, called ordinary wave (O-mode) and the extraordinary wave (X-mode) polarized perpendicular to *B*. Again the refractive indices for the two waves differ, which means the magnetized plasma is linear birefringent as well, it shows the Cotton-Mouton-effect. This means the ellipticity of a linear polarized wave composed of an X- and an O-mode component is changed when passing the plasma. Analysis of the polarization state gives line-integrated information on the electron density and the perpendicular *B*-field components involved.

Thomson scattering

At frequencies very large compared to the plasma frequency, the plasma refractive index approaches the vacuum value $N = 1$. However, individual plasma electrons are periodically accelerated in the *E*-field of a propagating wave launched as a laser beam for example. The oscillating charges are then origin of secondary radiation. The total intensity observed is composed of contributions of the individual electrons. The process is called incoherent Thomson scattering. Since the scattering centres are moving, the secondary waves have characteristic frequency shifts reflecting the particle's velocity, so carrying information about the velocity distribution function of the electrons. With a Maxwellian velocity distribution characterized by the temperature T_e of the electrons, a continuous spectrum around the primary laser frequency

$$I_s \propto \sqrt{\frac{m_e}{2\pi T_e}}\,n_e e^{-m_e\omega^2/(2k^2T_e)} \tag{7.9}$$

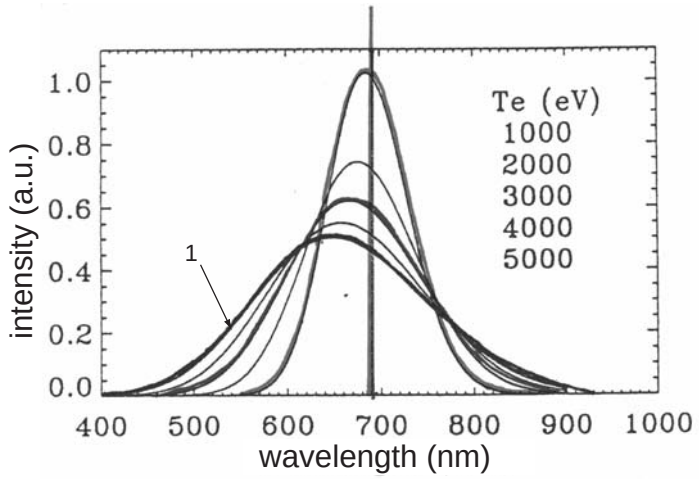

Figure 7.3: The spectra of the Thomson scattered radiation for various temperatures T_e. The primary laser line is at about 700 nm. With increasing temperature relativistic effects cause an asymmetry in the scattering spectra (line 1).

is observed from which the temperature can be derived (see Fig. 7.3). The scattering intensity I_s is proportional to the number of scattering centres, i.e. proportional to the electron density.

Observation geometry and laser beam define the scattering volume. The arrangement therefore gives local information about electron density and temperature.

7.5.2 Passive wave measurements

Electromagnetic radiation emitted by fusion plasmas is composed of parts created in many different physical generation processes. In a fully ionized pure hydrogen plasma there is continuum radiation caused by bremsstrahlung owing to the accelerated motion of electrons in the field of the ions, cyclotron radiation due to the gyration motion of the charged particles in the external magnetic field, and recombination radiation after electron capture of ions. This continuous emission is superimposed by line radiation of recombined hydrogen atoms at the cool very edge of the plasma (Balmer-lines).

In addition to these unavoidable emission processes of a magnetically confined ideal hydrogen plasma, emission caused by impurities in the plasma must be considered. The impurities are ions of higher atomic number $Z > 1$. If these ions are fully ionized, they contribute to the emission with the processes listed before.

In case they are not fully ionized, which is true in particular for high Z ions, collision processes in the plasma lead to inner shell electronic excitation followed by spontaneous emission of characteristic line radiation with quantum energies typically in the keV range. Since this emission is connected with a significant energy loss, the impurity concentration of a fusion plasma must be kept sufficiently small. With regard to a future fusion reactor, impurity concentration of light atoms like C or O might reach the 1% level, however, the concentration of high-Z materials like W or Mo must not exceed the 0.1% level.

The small unavoidable impurity content can favourably be used for diagnostic purposes. The analysis of this radiation is done with regard to the wavelength which is characteristic for the

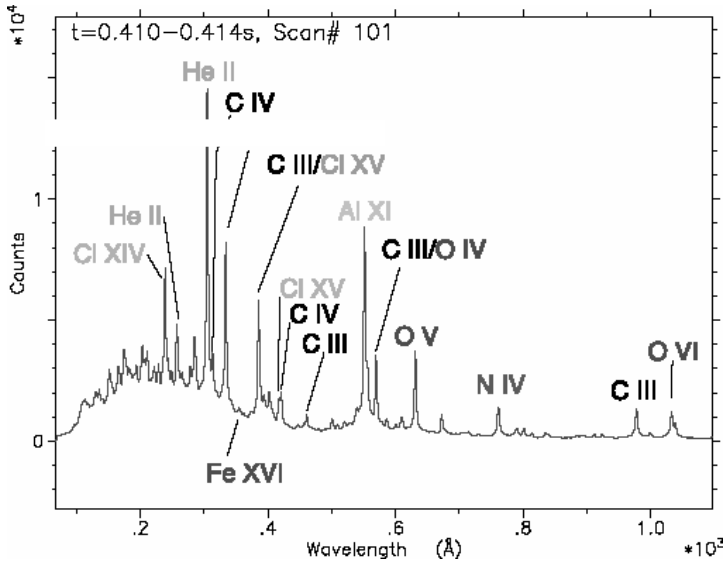

Figure 7.4: Typical VUV spectrum emitted from an impurity contaminated plasma. Characteristic lines of various charge states (roman numbers) of various elements like He, C, O, Cl, N, Al, and Fe could be identified. A continuous radiation background is also present (courtesy R. Burhenn, W7-AS).

element and its charge state. Analyzing also the line width and an eventual Doppler-shift, the ion temperature and collective drifts of the ions can be evaluated.

Line radiation

Main aim when analyzing the spectrum of line radiation is the determination of the impurity composition and the concentration of the various elements. To enable this, additional information is necessary. From the wavelength the element can uniquely be determined. The intensity of the emission depends on the concentration of this element but also on the excitation conditions, in particular on the local electron temperature and density. This makes the application of extensive code calculations necessary considering all excitation and de-excitation processes, to interpret the measured line intensities of the spectra.

The observation is typically along a sightline through the plasma centre. Since the plasma is optically thin a line integrated measurement results. Without additional knowledge no localization is possible.

A gross estimation, however, can be based on the fact that since the electron temperature profile is maximal in the plasma centre, the individual ionization states are not equally distributed in the plasma cross section but rather distributed like an onionskin in layers of a certain temperature range resulting in a localization of the individual charge states of an ion. The known electron temperature profile allows in this way an allocation of the emission of different charge states observed.

One of the most direct interpretations is based on the evaluation of the Doppler-broadening of the spectral lines. The line width reflects the ion temperature of the majority of ions of the bulk plasma since due to collisional interaction full thermalization is normally obtained (see Fig. 7.5 left). Measuring the line widths of elements in various charge states, the ion temperature profile can be reconstructed, at least estimated.

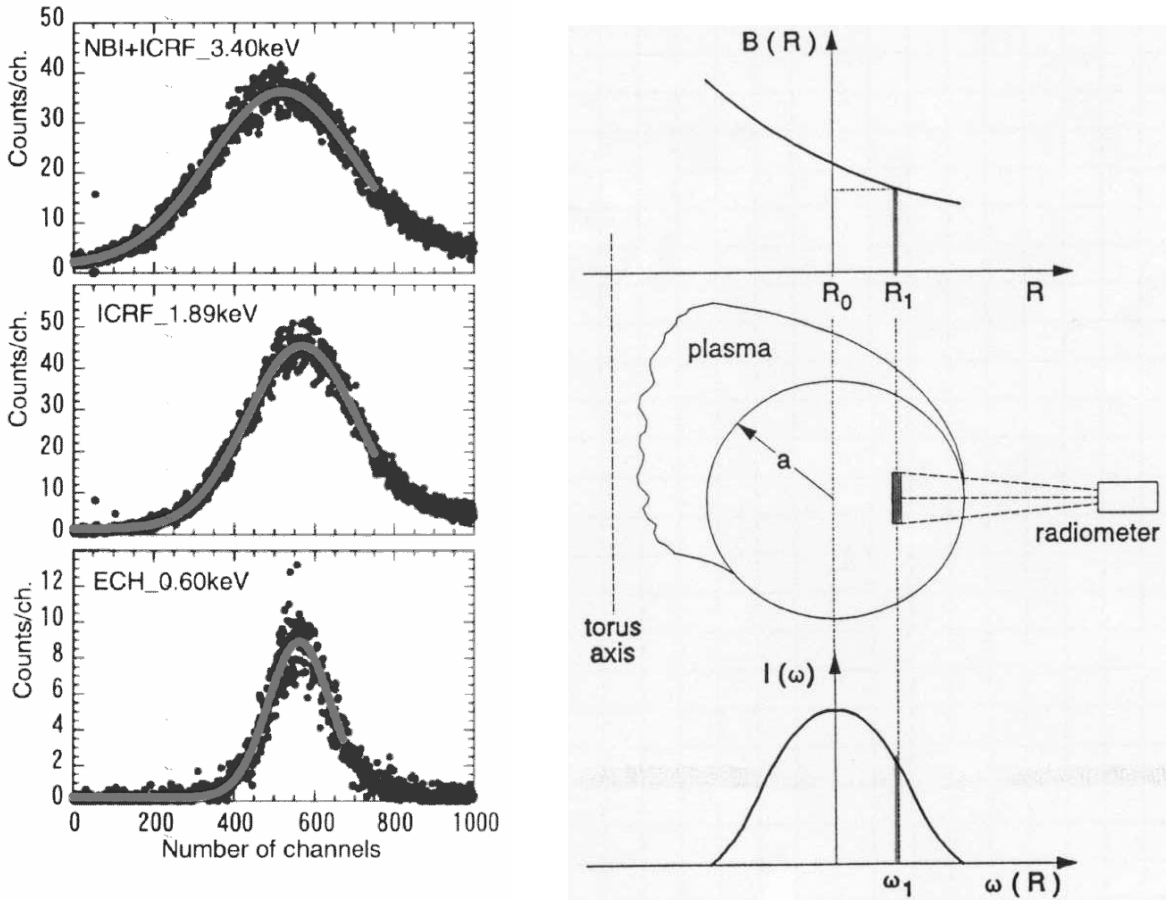

Figure 7.5: Left: The line width of a Doppler-broadened spectral line of the 20-fold ionized Ti for various heating scenarios NBI + ICRF, ICRF, and ECRH resulting in ion temperatures of 3.4, 1.89, and 0.6 keV. Measurements (dark) and simulations of the width assuming a Maxwellian energy distribution nicely agree (courtesy of S. Morita, LHD, Japan). Right: In a toroidal confinement device the *B*-field monotonically decreases with *R* across the plasma cross section. As a result the gyration frequency varies with *R* too. The frequency of the emission is therefore connected with the position of generation. The intensity of the emission is proportional to the local temperature.

Continuum radiation

Continuum radiation is generated in the plasma due to the action of electric and magnetic forces on the electrons. The acceleration of the ions is small. Their emission can usually be neglected.

1. Bremsstrahlung
   The accelerated motion of an electron in the field of an ion is the classical process to generate bremsstrahlung. Since the electron is before and after the interaction in a free state the process is called free-free transition. In case the electron is bound in its final state, recombined with an ion, the process is a free-bound transition. Both processes lead to the emission of continuous radiation, forming a continuous background in the spectral range from mm to X-ray regions. While recombination is dominant in the cool plasma edge, at the higher temperatures in the plasma bulk free-free transitions are dominant.

The total power emitted within a certain finite spectral interval is proportional to the local densities of ions and electrons, the ion charge squared and to the square root of the electron temperature

$$P \propto Z^2 n_e n_i \sqrt{T_e} \,. \tag{7.10}$$

Due to this strong dependence on quantities which are in most cases constant on flux surfaces, bremsstrahlung emission can be used to reconstruct the flux surfaces, their shift under the action of plasma pressure as well as to determine MHD-phenomena. To limit the bremsstrahlung power loss, high-Z impurities must be avoided in a future fusion reactor.

The measurements are made in the soft X-ray spectral region using multi sightline pinhole camera systems with hundreds of sightlines. The local emissivity is reconstructed from the line integrated measurements applying tomographic reconstruction techniques.

The spectrum shows a characteristic exponential decay with frequency ω

$$I_\omega \, d\omega \propto e^{-(\hbar\omega)/(kT_e)} d\omega \tag{7.11}$$

from which the electron temperature can be determined without absolute calibration of the detection system.

2. Cyclotron radiation
In a magnetically confined plasma the Lorentz-force causes the electrons to gyrate around the field lines with a frequency

$$\omega_0 = \frac{e}{m_e} B \,. \tag{7.12}$$

This accelerated motion leads to the emission of electromagnetic radiation at the cyclotron frequency ω_0 and its harmonics. At B-fields of the order of a few T emission is in the mm-wave range. Since the energy density of the emission is proportional to the acceleration squared, the intensity of the emission caused by the ion gyration motion at the same energy is completely negligible. Only the electron cyclotron emission (ECE) has therefore gained diagnostic importance. With the line of sight in a poloidal plane perpendicular to the plasma axis, the width of the emission spectrum is dominated by the B-field variation through the plasma, resulting in a continuous spectrum with a width of typically several 10 GHz. At sufficiently high electron temperature and density, the plasma is optically thick in the range of cyclotron frequencies. The intensity of the emission then reaches the black-body level which, through Plancks law, is solely determined by the electron temperature. Since the frequency is determined by the known local field $B(R)$, a local electron temperature $T_e(R)$ can be deduced from the measured intensity $I(\omega)$. The classical Rayleigh-Jeans approximation of Plancks law then gives a linear relation between electron temperature T_e and the intensity I

$$I_\omega \, d\omega = \frac{\omega^2}{8\pi^3 c^2} \frac{\hbar\omega}{\exp\left(\hbar\omega/(kT_e)\right) - 1} \, d\omega \approx \frac{\omega^2}{8\pi^3 c^2} kT_e \, d\omega \,. \tag{7.13}$$

In this simplified picture the energy of individual electrons of a thermalized population has not been considered. It causes, as a result of the relativistic mass increase with kinetic energy, a downshift of the emission frequency, or -accordingly- at given observation frequency a shift of the emitting layer away from the so-called cold resonance into regions of higher B-field.

As a result, the emission of the electrons at the various energies of a Maxwellian distribution is smeared out over a certain radial range behind the cold resonance. However, due to the multi-step emission and reabsorption processes of the radiation on the way to the observer, radiation can escape only from a layer right behind the cold resonance whose temperature is being reflected in the observed blackbody intensity. The mechanism only holds in case the *B*-field is monotonically decreasing to the observer, which is the necessary condition of the method. A radiometer calibrated against a blackbody source of known physical temperature determines basically the ECE radiation temperature T_{rad}

$$T_{rad} = T_e \left[1 - e^{-\tau}\right] \tag{7.14}$$

approaching the electron temperature T_e in case the optical depth τ is sufficiently high. The optical depth is obtained integrating the absorption along the line of sight. The leading parameters determining the absorption are the local electron density and temperature. Densities in the $10^{19}\,\mathrm{m}^{-3}$ and temperatures of about 50 eV are sufficient to fulfil the conditions.

7.6 Particle diagnostics

Atoms and ions are injected to diagnose the plasma in various ways. While impurity pellets are injected to study their excitation, ionization, their dwell time, and motion with the passive spectroscopic diagnostics described, well collimated low and high energy H, He, or Li atomic beams are used to investigate local phenomena occurring along the beam as a result of its interaction with the plasma particles. Neutral atoms are used to avoid deflection in the magnetic field. However, also ions of high energy and mass are sent into the plasma to probe its local electric potential.

Passive particle diagnostics analyze neutral atoms escaping from the plasma after charge exchange interaction with fast H-atoms injected by a so-called diagnostic injector. Also the diagnostic of neutrons produced in fusion reactions fall into this category.

7.6.1 Active particle diagnostics

Li-beam

A well collimated beam of neutral Li-atoms is being injected into the plasma, directed to the plasma axis. Beam energy and electron density in the plasma determine the penetration depth. With energies of some 10 keV it is of the order of a few 10 cm. In electronic collision the beam atoms are excited

$$\mathrm{Li}\,(E_0) + e^- \;\rightarrow\; \mathrm{Li}^\star + \mathrm{e}^- \,, \tag{7.15}$$

$$\mathrm{Li}^\star = \mathrm{Li}(2p) \;\rightarrow\; \mathrm{Li}(2s) + \hbar\omega \tag{7.16}$$

and the intensity of the resonance line from the $2p$ to $2s$ transition is being detected perpendicular to the beam. Arrays of detectors allow for the simultaneous observation along the beam. The intensity reflects almost directly the electron density, which can be determined in this way with high spatial resolution in the very important edge region of the plasma where density gradients are often very high and where its exact knowledge is of great importance.

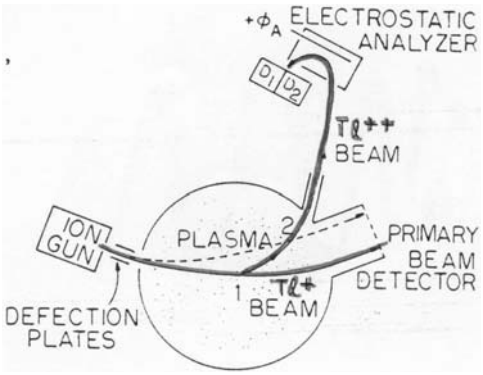

Figure 7.6: Experimental arrangement of a heavy ion beam probe diagnostic. Tl^{+} ions are generated in an ion gun and launched into the plasma (trajectory 1). If the ion is further ionized to Tl^{++}, the gyro-radius is decreased (trajectory 2). From the energy change of the Tl^{++} ions, the local plasma potential at the position of the ionization can be deduced (T. Dolan, Fusion Research, p. 246).

Heavy ion beam probe

High energy, heavy mass singly charged ions are shot into the plasma in a well collimated beam of small divergence. Typical energies range from 100 keV to several MeV. Ions used for this purpose are typically Cs^{+}, Ta^{+} or Au^{+}. Due to the Lorentz-force the ions gyrate around the field direction, with a gyro-radius larger than the plasma radius. Along the only slightly bended beam path, in electronic collisions ionization processes change the charge q of the primary beam ions from e to 2e

$$\mathrm{I}^{+}(E_0) + \mathrm{e}^{-} \rightarrow \mathrm{I}^{++}(E_0) + \mathrm{e}^{-} \; . \tag{7.17}$$

As a result the ion gyro-radius

$$r_g = \frac{vM_I}{qB} \tag{7.18}$$

is decreased by a factor of two right at the location where the ionization occurs. The new trajectory of the *secondaries* now differs clearly from the primary injected ions. If the plasma has a locally varying finite electric potential $\Phi(s)$ along the beam path s, the energy of the ion passing the plasma changes by $e\Phi(s)$ reaching the initial value E_1 again when leaving it, since the plasma is electrically neutral and energy gained when entering is lost when leaving the plasma or vice versa. If, however, at position s_0 higher-ionization by one step occurs, the two-fold ionized particle leaves the plasma with an energy $E_2 = E_1 + e\Phi(s_0)$, reflecting the local potential at position s_0. The energy difference $E_2 - E_1$ is determined via deflection in electric fields. Scanning the primary beam and the detection geometries, the potential distribution across the plasma can be determined, which is of importance to interpret transport processes in the plasma.

High energy neutral hydrogen injection

A beam of high energy neutral hydrogen atoms H^0 generated in a system called diagnostic injector with sufficient energy $E_0 > 50$ keV to penetrate the plasma as much as possible produces along its trajectory due to charge exchange processes with the hydrogen bulk ions neutral

hydrogen atoms which can leave the plasma almost unopposed

$$H^0(E_0) + H^+(E) \rightarrow H^+(E_0) + H^0(E) \ . \tag{7.19}$$

The velocity distribution of these atoms leaving the plasma reflects the velocity distribution of the plasma ions since in the interaction process to a good approximation only charge has been transferred, not energy and momentum. Energy and momentum analysis of escaping atoms in electric and magnetic fields after a new external ionization therefore gives detailed local information about the ion energy distribution i.e. the ion temperature in the plasma. The position is defined by the overlap of the primary beam and detection geometry.

The diagnostic injector can successfully be used in a further application. For this purpose a small amount of He atoms is introduced into the hydrogen plasma as a tracer element. At the typical electron temperatures He is fully ionized. In a similar process as described before, the He^{++} ions exchange charge with the neutral hydrogen atoms of the injected beam to result in electronically excited singly charged He^+ ions

$$H^0(E_0) + He^{++}(E) \rightarrow H^+(E_0) + He^{+^\star}(E) \ , \tag{7.20}$$

$$He^{+^\star}(E) \rightarrow He^+ + \frac{hc}{\lambda} \tag{7.21}$$

with $\lambda = 468.4\,\mathrm{nm}$. Again, since no energy is transferred in this process, the excited He^+ ions still reflect the He^{++} initial energy distribution. The Doppler-width of the spectral line at wavelength λ emitted in the de-excitation process then reflects the ion temperature of the plasma bulk ions since thermal equilibrium can be considered. The crossed beam-sightline geometry enables a local measurement of the ion temperature.

7.6.2 Passive particle diagnostics

Charge exchange neutrals leaving the plasma are already discussed together with the active diagnostics. Langmuir-probes extracting particle from the plasma are discussed in a separate chapter. Only fusion neutrons need to be briefly discussed here.

Neutron diagnostics

Neutron diagnostics will play a major role in future burning plasma experiments (BPX) like ITER where the analysis of the 14.2 MeV fusion neutrons becomes most important. In existing fusion experiments operating with mixtures of deuterium and hydrogen or with pure deuterium plasmas, neutrons are produced in two different reaction schemes with the kinetic energies of the reaction products given in brackets

$$D + D \rightarrow p\,(3.02\,\mathrm{MeV}) + T\,(1.01\,\mathrm{MeV}) \ , \tag{7.22}$$

$$D + D \rightarrow n\,(2.45\,\mathrm{MeV}) + {}^3\mathrm{He}\,(0.8\,\mathrm{MeV}) \ . \tag{7.23}$$

The first scheme produces charged products only which can leave the plasma in nowadays medium sized experiments due to their high energy but will stay confined in future large machines. The neutrons from the second reaction, however, will leave the plasma. Energy analysis of the Doppler-broadened line at 2.45 MeV gives information about the energy of the reacting ions in the plasma.

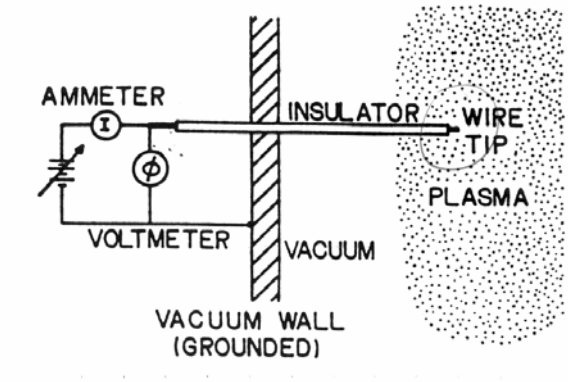

Figure 7.7: Langmuir-probes consist of a tiny electrode of about 1 mm length which is in direct contact with the plasma edge. Depending on the bias voltage, either ions or electrons are extracted from the plasma. From the measured I–V characteristic information can be gained about the electron and ion energy distribution function as well as about the plasma potential. (T. Dolan, Fusion Research, p. 239).

7.7 Langmuir-probes

Langmuir-probes are counted among the oldest plasma diagnostics with still high importance in both fields fusion high temperature and in particular low temperature plasma diagnostics. The Langmuir-probe is a tiny metallic electrode in direct contact with the plasma. Retroaction to the plasma can therefore not completely excluded. In fusion experiments probes are moved into the plasma only for some 10 ms to avoid overheating of the device. Dependent on the potential applied, the small electrode either injects or extracts charged particles from the plasma. Currents to the probe are governed by the electron density and the electron temperature as well as the plasma potential. All three quantities can be derived from the measured current-voltage characteristic of the probe, which is obtained conducting a fast voltage sweep.

7.8 Summarizing remarks

To summarize the various techniques, Tab. 7.8 connects the main methods and some important quantities they are aiming at. The diagnostic methods briefly discussed in the frame of this introduction to the field are linked matrix-like with the physical quantities the measuring systems are diagnosing.

The various diagnostic techniques given in the rows are based on measurements of magnetic flux changes and particle fluxes from the plasma, measurements of the plasma dielectric properties, the radiometry of the cyclotron emission, the spectroscopy of the continuous bremsstrahlung and the discrete impurity line emission, on laser light scattering and charge exchange processes and based as well on nuclear reactions resulting in neutrons leaving the plasma.

The most important parameters as given in the columns are: $f_{e,i}$, energy distribution function of electrons and ions, $n_{e,i}$, electron and ion densities, $T_{e,i}$, electron and ion temperatures, p plasma pressure, E and B electric and magnetic fields. This is of course only a small part of

Table 7.1: Main methods and some important quantities. Diagnostic techniques given in the rows, most important parameters in the columns.

	f_e	f_i	n_e	n_i	n_Z	T_e	T_i	p	E	B
Magnetics						×		×		×
Particle flux	×	×	×	×		×	×		×	
Refractive index			×							×
Cyclotron emission	×					×				
Bremsstrahlung			×		×	×				
Line radiation					×		×		×	×
Scattering	×		×			×		×		
Charge exchange		×			×		×			
Nuclear reaction		(×)		×			×			

the plasma parameters to be measured. However, to list them all would definitely go beyond the scope of this introductory chapter.

References

[1] W. Lochte-Holtgreven, *Plasma Diagnostics*, AIP, New York, 1995

[2] I.H. Hutchinson, *Principles of Plasma Diagnostics*, Cambridge University Press, Cambridge, MA, 1987

[3] T.J. Dolan, *Fusion Research*, Pergamon Press, New York, 1982

[4] T.J.M. Boyd, J.J. Sanderson *The Physics of Plasma*, Cambridge University Press, Cambridge, UK, 2003

[5] Transaction of Fusion Technology, *Carolus Magnus Summer School on Plasma Physics*, **25**, 2T, 289-340 (1994)

Chapter 8

Tokamaks: equilibrium, stability and transport

Hartmut Zohm

8.1 Introduction

The goal of confining a plasma in a magnetic field can be achieved in various geometries. The quality of the magnetic confinement is characterized by different criteria. For nuclear fusion, the following points are of special interest:

- The ratio of kinetic plasma pressure, averaged over the plasma volume, to magnetic pressure $\beta = \langle p \rangle / (B^2/(2\mu_0))$. This number is a measure of the economic efficiency of the confinement since the fusion power output roughly scales as p^2 and B is the magnetic field which has to be provided externally. Usually, β is limited by the occurrence of MHD (Magneto-Hydrodynamic) instabilities.
- The energy confinement time $\tau_E = W_{pl}/P_{heat}$ which is one of the quantities appearing in the Lawson criterion $n_i \tau_E T_i \geq f(T_i)$ and characterizes the quality of the heat insulation, i.e. the transport properties of the configuration.

The simplest approach is a linear configuration (mirror, pinch) which suffers from losses appearing at the ends. These points are optimized in devices with toroidal geometry. Today, the *Tokamak* configuration is the best developed; the *Stellarator* is expected to show confinement properties of similar quality.

8.2 Plasma equilibrium

8.2.1 The steady state MHD-equations

The equilibrium of a plasma in a magnetic field can be described by the MHD equations. It is described by neglecting the temporal derivatives. If, in addition, no flow is considered ($\mathrm{v} = 0$), the equations reduce to

$$\nabla p = \mathrm{j} \times \mathrm{B} \,, \tag{8.1}$$

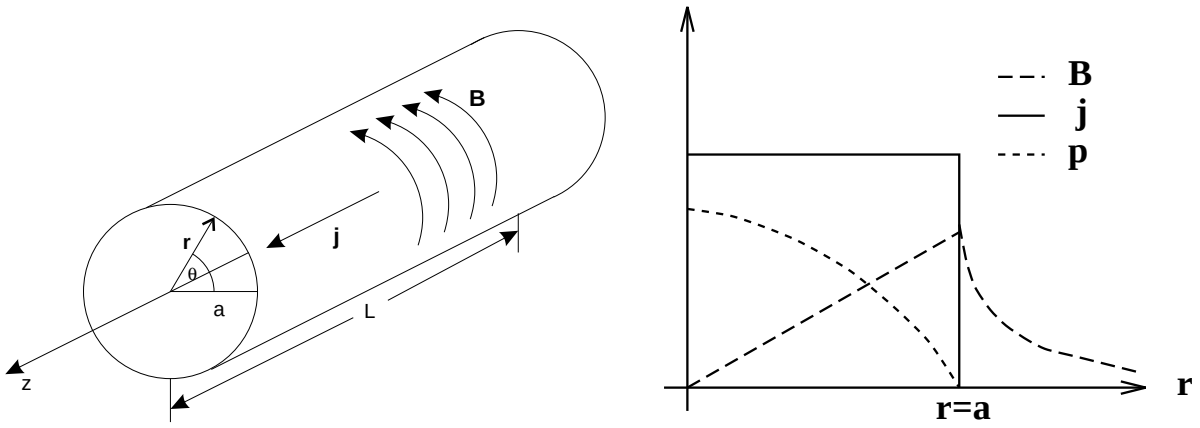

Figure 8.1: The linear *z*-pinch: geometry and radial profiles of j_z, B_θ and p for the example shown in the text.

$$\nabla \times \mathrm{B} = \mu_0 \mathrm{j} \,, \tag{8.2}$$

$$\nabla \cdot \mathrm{B} = 0 \,. \tag{8.3}$$

The first equation (8.1) is the force balance which states that a current flowing perpendicular to the magnetic field exerts a force on the fluid element. In equilibrium, this force balances the plasma kinetic pressure, i.e. everywhere in the plasma, the local pressure gradient is balanced by the Lorentz force. In particular, for $\nabla p = 0$, the fields j and B are collinear (*force free region*). Eq. (8.2) and (8.3) are Maxwell's equations for a static magnetic field.

8.2.2 Equilibrium in the linear pinch

A simple analytic solution of (8.1)–(8.3) can be given in the case of a linear cylindrical configuration, the so-called pinch. The simplest case is a *z*-pinch, i.e. a cylinder carrying a current in the *z*-direction (see Fig. 8.1).

Here, the magnetic field is purely azimuthal and the force balance reads

$$\frac{dp}{dr} = -j_z \cdot B_\theta \,. \tag{8.4}$$

To explicitly calculate the radial profile $p(r)$, we have to specify a current density profile $j_z(r)$. For simplicity, we chose $j_z = const. = j_0$ inside the plasma of radius a and $j_z = 0$ outside. Then we can solve (8.2) in cylindrical geometry to obtain

$$B_\theta = \frac{\mu_0 I_p}{2\pi a^2} r \qquad \text{for } r \le a \,, \tag{8.5}$$

$$B_\theta = \frac{\mu_0 I_p}{2\pi r} \qquad \text{for } r > a \,, \tag{8.6}$$

where $I_p = j_0 \pi a^2$ is the total current flowing in the plasma. Using this result, we can integrate (8.4) to yield

$$p(r) = \frac{\mu_0 I_p^2}{4\pi^2 a^2} \left(1 - \left(\frac{r}{a}\right)^2\right) . \tag{8.7}$$

Fig. 8.1 shows a plot of the profiles. Calculating β_p, i.e. the ratio of average kinetic pressure and magnetic pressure associated with the poloidal field

$$\beta_p = \frac{2\mu_0 \langle p \rangle}{B_\theta^2} \tag{8.8}$$

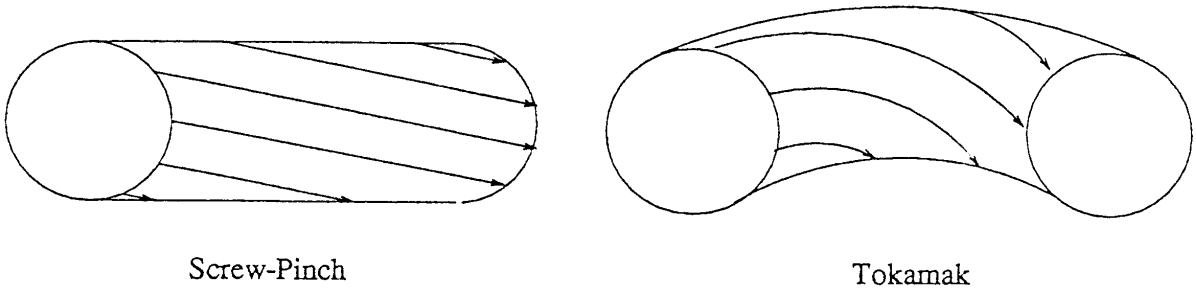

Figure 8.2: Magnetic configuration of the screw-pinch and analogous tokamak.

we find $\beta_p = 1$ for this particular example. It can be shown that this is a general result for the z-pinch, independent of the profiles specified.

This simple equilibrium calculation does not include a stability analysis, i.e. we have shown that a state with $\partial t \to 0$ exists, but we do not know whether this is a stable solution. This will be done in the next section. For the z-pinch, one can show that it is unstable unless we add a magnetic field in the z-direction. Fig. 8.2 shows this magnetic configuration (*screw pinch*).

As can be seen, the magnetic field lines helically wind around the magnetic axis. If we bend the cylindrical screw-pinch to form a torus, we obtain a tokamak geometry. For large aspect ratio (i.e. ratio of major and minor radius $A = R/a$), a tokamak can be approximated by a screw-pinch periodic in z with period $2\pi R$. The properties of the field lines are characterized by the safety factor q defined by

$$q = \frac{\mathrm{numberoftoroidalwindings}}{\mathrm{numberofpoloidalwindings}} \tag{8.9}$$

of a field line on the torus. In the limit of the screw-pinch, the relation $q = (r/R)(B_t/B_\theta)$ holds. From stability considerations it follows that $q \geq 1$ (see below), so that $B_t \approx B_\theta qR/r$. Inserting typical tokamak values (e.g. ASDEX-Upgrade $a = 0.5\,\mathrm{m}$, $R = 1.65\,\mathrm{m}$ and $q = 3$), we arrive at $B_t \approx 10 B_\theta$, i.e. for this screw pinch $\beta_t = 2\mu_0\langle p\rangle/B_t^2 \approx 1\,\%$. Thus stability requirements have a severe impact on the economic properties of the device.

In a screw pinch or tokamak, there is the possibility of poloidal currents that exert a force on the plasma. For $\mathrm{j}_p \times \mathrm{B}_t \uparrow\uparrow \mathrm{j}_t \times \mathrm{B}_p$, the plasma pressure balanced by the magnetic field is higher than in the pure z-pinch; in this case $\beta_p > 1$ and the poloidal current weakens the original B_t, therefore the plasma is said to be *diamagnetic*. In the opposite case, $\mathrm{j}_p \times \mathrm{B}_t \uparrow\downarrow \mathrm{j}_t \times \mathrm{B}_p$, we can sustain less pressure, and $\beta_p < 1$ (*paramagnetic* plasma).

8.2.3 The Grad-Shafranov equation

For an axisymmetric system like the tokamak, it is convenient to re-write the force balance (8.1). For this purpose, we need the following ideas:

- As $\nabla p = \mathrm{j} \times \mathrm{B}$, $\nabla p \cdot \mathrm{j} = \nabla p \cdot \mathrm{B} = 0$. Therefore the field lines of j and B lie in the surfaces of constant pressure.
- The flux integrals $\int \mathrm{B}\, d\mathrm{A}$, $\int \mathrm{j}\, d\mathrm{A}$ have a constant value on the $p = const$ surfaces for an arbitrary curve C on this surface, since j and B lie in this surface and thus any part of the integrals on the surface vanishes. These surfaces are therefore called *flux surfaces* and can be labelled by the (scalar) fluxes. Also, p is only a function of the fluxes.

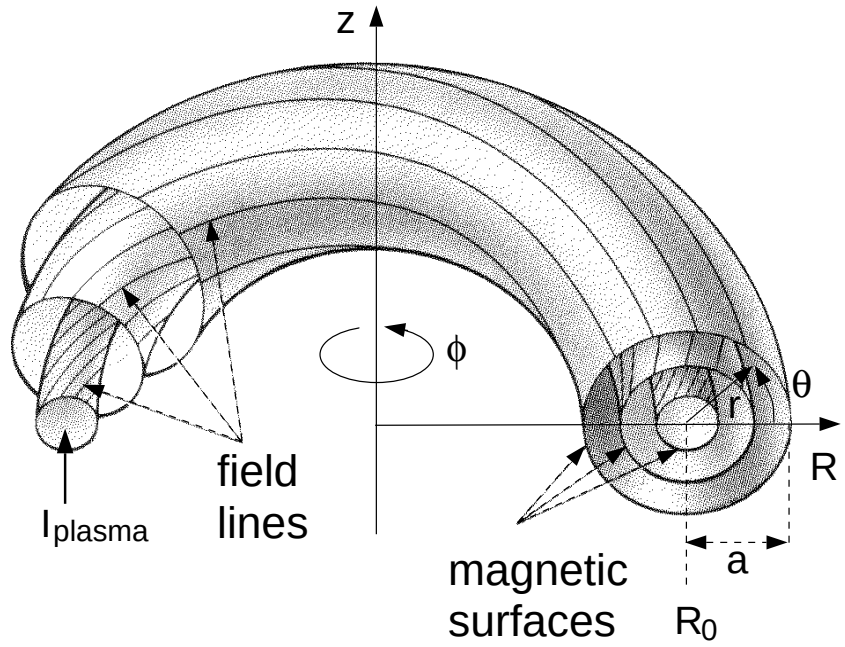

Figure 8.3: Co-ordinates used for the Grad-Shafranov equation.

- As $\nabla \cdot \mathrm{B} = \nabla \cdot \mathrm{j} = 0$, any flux integral $\int \mathrm{B}\, d\mathrm{A}$, $\int \mathrm{j}\, d\mathrm{A}$ has a constant value if the arbitrary surface A is surrounded by the same curve C and thus we are free to chose the surface A. This means that each flux surface can be assigned a unique value of the flux, independent of the geometry in which the flux was calculated.

On a torus, there are two topologically different types of curves: Those winding around the torus in the toroidal direction and those winding around the torus in the poloidal direction. If we chose a curve winding around in the toroidal direction, integration over the domain enclosed by this surface yields the poloidal magnetic flux function Ψ and the total poloidal current I_{pol}. Both functions are constant on the flux surface and the magnetic field can be calculated as

$$B_\phi = \frac{\mu_0 I_{pol}}{2\pi R}, \tag{8.10}$$

$$B_R = -\frac{1}{2\pi R}\frac{\partial \Psi}{\partial Z}, \tag{8.11}$$

$$B_Z = \frac{1}{2\pi R}\frac{\partial \Psi}{\partial R}, \tag{8.12}$$

where the co-ordinates from Fig. 8.3 have been used. Note that with this definition, Ψ denotes the poloidal flux per unit length in toroidal direction ($[\Psi]$ = Vs/m). Using these quantities, the force balance can be re-written as

$$-\Delta^* \Psi \equiv -\left[R\frac{\partial}{\partial R}\left(\frac{1}{R}\frac{\partial \Psi}{\partial R}\right) + \frac{\partial^2 \Psi}{\partial z^2}\right] = \mu_0 (2\pi R)^2 p(\Psi)' + \mu_0^2 I_{pol}(\Psi) I'_{pol}(\Psi) \tag{8.13}$$

known as the Grad-Shafranov equation. The prime denotes the derivative of a flux surface quantity with respect to Ψ. Eq. (8.13) is usually nonlinear in Ψ. To solve it, we can e.g. specify $p(\Psi)$ and $I_{pol}(\Psi)$ and then solve for $\Psi(R,Z)$. Usually, one will specify boundary conditions. If the plasma is surrounded by a perfectly conducting vacuum vessel, the vessel is a flux surface and therefore $\Psi = const$ at the vessel determines shape and position of the

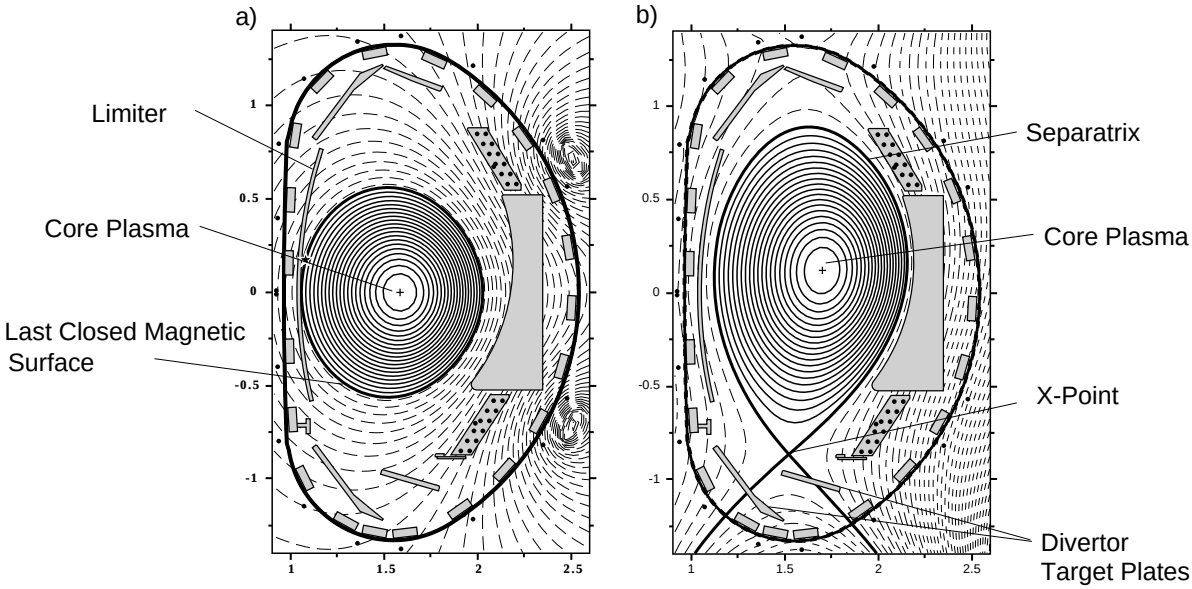

Figure 8.4: Typical poloidal cross-sections of a tokamak.

plasma boundary. To satisfy these conditions, we have to add a solution of the homogeneous equation, i.e. a function Ψ_{ext} with $\Delta^*\Psi_{ext} = 0$. Such a field is produced by external coils, i.e. the solution of the Grad-Shafranov equation with fixed boundary and profile functions tells us how to arrange external control currents to maintain the plasma in equilibrium.

8.2.4 The tokamak

The tokamak principle was already introduced in chap. 2. The plasma acts as a secondary winding of a transformer. Ramping the current in the primary coil induces a loop voltage inside the discharge vessel; after breakdown, a toroidal current flows in the plasma. This current heats the plasma via its resistance (Ohmic Heating (OH), the primary coil is also called the OH coil). The current itself creates the poloidal magnetic field, the toroidal field is produced by external coils (a stellarator produces all its field components by external coils). The poloidal field coils maintain the plasma in force equilibrium as described by (8.13). A sketch of the tokamak principle is shown in Fig. 2.9.

Fig. 8.4 shows typical examples for poloidal cross-sections calculated with (8.13). One can see that the flux surfaces are not centered to one axis, but are slightly shifted. This *Shafranov shift* is due to the forces trying to expand the torus radially outward:

- The kinetic pressure of the plasma.
- The expansion force of a current loop due to the j $\times$ B force.

The sum of these two forces is called *hoop force*. In Fig. 8.4 b), one can see that the plasma cross-section does not necessarily have to be circular; in fact, elongation and triangularity produced with additional poloidal field coils enhance plasma performance (see next section). One also sees the different ways to limit a plasma: Fig. 8.4 a) shows a so called *limiter* case, where a material limiter defines the last closed flux surface, in Fig. 8.4 b), this last closed flux surface is defined magnetically by a so-called *separatrix*; plasma crossing the separatrix flows along field lines to the material plates at the bottom of the vessel. This configuration is called a magnetic *divertor*.

8.3 Stability of an equilibrium state

As has been mentioned before, the Grad-Shafranov (8.13) describes a force equilibrium, but it does not tell us if the equilibrium is stable, i.e. if a small variation of the plasma parameters or the external control currents will lead to another equilibrium or to an unstable situation. Therefore, we have to analyze the stability properties of a configuration by a separate treatment.

MHD instabilities can deteriorate the plasma performance due to various effects: Large-scale instabilities can lead to a loss of plasma control (e.g. during a *disruption*, the plasma current collapses in an uncontrollable way) whereas small scale perturbations and MHD turbulence can significantly enhance radial transport of particles and energy. Nevertheless, in some cases instabilities may help to control parameters; e.g. ELMs (Edge Localized Modes) periodically expel impurities from the plasma edge and help keep the plasma clean.

8.3.1 Methods of stability analysis

From MHD theory, there are different ways to analyze the stability of a given equilibrium. Often, the analysis is done by introducing a perturbation of the equilibrium configuration as a displacement ξ of a fluid element. Two methods are especially useful to check the stability against such displacements:

- The energy principle: This approach calculates the energy W_{MHD} of the configuration as a functional of the displacement vector. Stability is obtained if the second order change in energy $\delta^2 W_{MHD}\{\xi\}$ is positive for an arbitrary ξ (the linear variation is zero due to the equilibrium condition). This method is useful to prove that a configuration is *not* stable, because it is sufficient to find one unstable ξ; on the other hand, stability is hard to prove.

- Eigenmode analysis: Here, the time-dependent MHD equations are solved with an eigenmode ansatz for the displacement ξ. An ansatz often used is the Fourier decomposition in time and space. For the screw pinch, the spatial Fourier ansatz means periodicity in poloidal and toroidal co-ordinate θ and ϕ. Note that in a real torus, symmetry in the θ direction is only an approximation and coupling of poloidal harmonics will occur. For linearized MHD equations, this leads to an eigenvalue problem for each single Fourier mode

$$\xi = \xi_{mn}(r) e^{i(m\theta - n\phi)} e^{\gamma t} \,. \tag{8.14}$$

  The indices m and n are called poloidal and toroidal mode-numbers, for real γ, stability means $\gamma < 0$. If γ has an imaginary part, the eigenmode is called overstable and will exhibit a temporal oscillation. If γ is real and positive, it can be interpreted as a linear growth rate. The saturated amplitude of an instability can only be found by introducing nonlinear effects such as changes in the equilibrium introduced by the perturbation.

Perturbations are easily excited if the field lines do not ergodically cover a flux surface but close upon themselves after few revolutions in the torus. These flux surfaces are the ones with rational safety factor q; they are called *resonant surfaces* and a standing wave with mode numbers $q = m/n$ can occur.

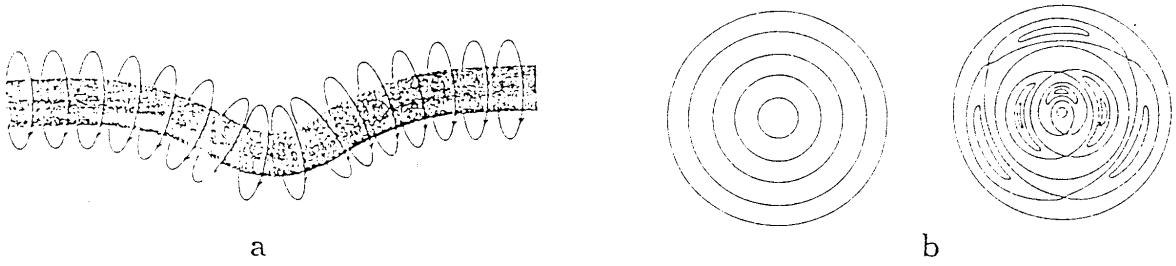

Figure 8.5: Ideal kink (a) and resistive tearing (b) instability. In (b), magnetic islands are formed.

8.3.2 Classification of instabilities

In a confined plasma, an instability is driven by the free energy contained in the equilibrium configuration. In a tokamak, there are two main sources of free energy: The kinetic energy of the plasma and the energy of the magnetic field generated by the plasma. Instabilities can therefore be driven by the radial gradient of either the pressure or the current profile. At low β, the magnetic energy is much higher than the kinetic energy and the instabilities will mainly be current-driven; at high β, we expect the pressure driven instabilities to become significant.

In cylindrical approximation, the perturbed magnetic field has a radial component. The growth of this field is governed by Faraday's law. Inserting Ohm's law for the plasma yields in the linearized case

$$\frac{\partial B_{1r}}{\partial t} = -\frac{1}{r}\frac{\partial E_{1z}}{\partial \theta} = \frac{1}{r}\frac{\partial}{\partial \theta}\left(\eta j_{1z} + (\mathrm{v}_1 \times \mathrm{B}_0)_z\right), \tag{8.15}$$

where the subscript "1" refers to the perturbed quantities and the subscript "0" to the equilibrium quantities. From this we deduce that there are two ways for a perturbation to grow:

- Ideal case (no resistivity, i.e. $\eta \to 0$): Flow of plasma perpendicular to the field lines; in this case, $\mathrm{v} \times \mathrm{B}$ balances the E-field and in the fluid frame ($\mathrm{v} = 0$), magnetic flux is conserved, i.e. B moves with the fluid. This means that there is no change in the *topology*.
- Resistive case ($\eta \neq 0$): A current flows along the equilibrium field lines and generates the B-field; in this case, the topology is changed (*tearing* and *reconnection* of field lines).

Fig. 8.5 shows two examples: The so-called *kink* as a typical ideal instability, the *tearing mode* as a resistive one. In the case of the tearing mode, so-called *magnetic islands* form. Note that the magnetic island is a nonlinear solution of the MHD equations.

8.3.3 Examples

A simple example of an unstable situation is the case of an elongated plasma. In order to vertically elongate a plasma cross-section, we have to run coil currents of the same sign and order of magnitude than the plasma current. For a perfectly centered plasma, the net force is zero. However, any shift δz of the plasma current center increases the attractive force of the coil towards which the plasma moves, so that further acceleration results. The plasma experiences a vertical displacement event (VDE). As the plasma has negligible mass, this is a very fast event (on the order of the Alfven time scale, i.e. $\approx \mu$s). In order to feedback control

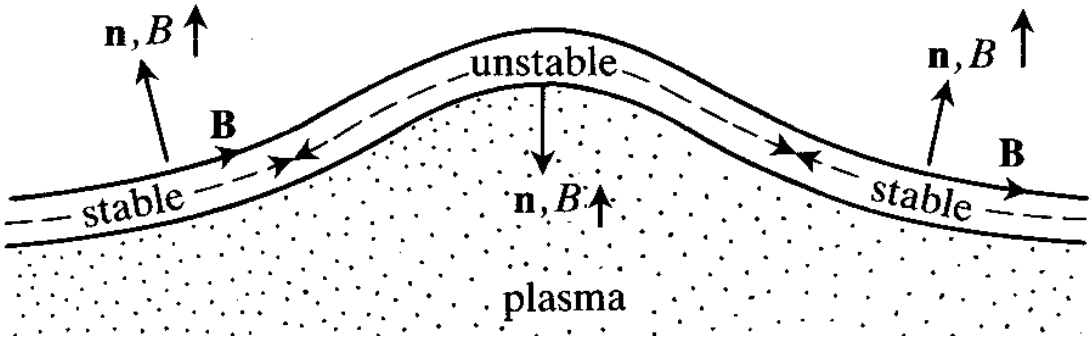

Figure 8.6: Interchange instability in a curved magnetic field.

this instability, one therefore has to provide conducting structures that, via induction, slow down the motion to a ms timescale.

Other MHD phenomena have been shown to influence the achievable β of a configuration. An example is the *external kink* driven by current gradients near the edge imposing restrictions on the possible current profiles. Restrictions on the pressure profile come from the so-called interchange instability. Here, neighbouring flux tubes can change place, analogous to the Rayleigh-Taylor instability of a normal fluid, if the field line can shorten and thus lose magnetic energy due to this process. As can be seen in Fig. 8.6, this is the case when the radius of curvature is parallel to the pressure gradient (so-called *bad curvature*). Conversely, if the radius of curvature is anti-parallel to the pressure gradient, an interchange of plasma and magnetic field will increase the magnetic energy and thus be stabilising (*good curvature*). In a screw pinch, only the poloidal field is curved and its curvature is *bad*, i.e. potentially destabilising. Stability is then achieved by sufficient shear dq/dr so that adjacent field lines have a different pitch angle and are not easily interchanged. In a torus, the toroidal field is also curved, exhibiting an area of good curvature on the inside and bad curvature on the outside of the torus. Thus, stability has to be determined by integrating along a field line and summing up the various stabilising and destabilising contributions. This leads to the Mercier criterion

$$\left(\frac{q'}{q}\right)^2 > -\frac{8\mu_0 p'}{rB_0^2}(1-q^2)\,. \tag{8.16}$$

As $p' < 0$, this means stability for all pressure profiles with $q > 1$; for $q \leq 1$, the shear has to be nonzero to provide stability. At high β, however, a new type of mode, the so-called *ballooning instability*, can develop. This mode has a small perturbation component along the magnetic filed, which allows a variation of the amplitude such that it concentrates on the outside of the torus, i.e. in the bad curvature region. Above a (shear dependent) critical pressure gradient, the energy gained by concentrating there is higher than the energy needed to bend the equilibrium field lines, and the mode becomes unstable.

A simultaneous optimization of pressure and current profiles yields a limit for the achievable β for given safety factor q_a and with $q_0 > 1$

$$\beta_{max}[\%] = c\frac{I[\mathrm{MA}]}{a[\mathrm{m}]B_t[\mathrm{T}]}\,. \tag{8.17}$$

This limit is known as the *Troyon limit*, the constant c depends only on the plasma shape and varies between $\approx$ three and five. Theory predicts an increase in c with elongation and triangularity; this is confirmed by various experiments.

Other examples for MHD instabilities are sawteeth and disruptions, each of them linked to a special rational surface ($q = 1$ and $q = 2$, respectively). This is treated in the section on experimental results of the tokamak.

8.4 Transport in a fusion plasma

8.4.1 Transport equations

For one single particle in a toroidal device, the confinement is perfect. In reality, collisions, drifts and MHD turbulence lead to a radial transport of particles and energy (i.e. perpendicular to the magnetic flux surfaces). It is this transport which determines the global energy and particle confinement times τ_E and τ_p.

To analyse the nature of transport, we define the particle flux Γ as the number of particles passing through a magnetic surface per unit area and time. For Γ we make the following ansatz

$$\Gamma = -D\nabla n + n\mathrm{v} \tag{8.18}$$

stating that there is a diffusive part driven by the density gradient (characterized by the diffusion coefficient D) due to the statistical random walk of particles and a convective part due to a directed motion v. The equation of continuity links Γ to the temporal change in density via

$$\frac{\partial n}{\partial t} = -\nabla\Gamma + S\,, \tag{8.19}$$

where $S(r,t)$ is a source term describing the change in plasma density due to ionisation or recombination (i.e. processes which cannot be described as a flux into or out of the volume element). Finally, in equilibrium, n does not change in time and we obtain

$$\nabla(D\nabla n) + \nabla\cdot(n\mathrm{v}) = S\,. \tag{8.20}$$

For a known source function and with given D and v, we can therefore determine the plasma density profile. On the other hand, measured density profiles are used to determine D and, with some additional assumptions, v. Transport of other quantities as e.g. energy can be treated analogously.

8.4.2 Transport coefficients

In a magnetized plasma, we distinguish between transport coefficients parallel and perpendicular to the magnetic field, e.g. $D_\parallel$ and $D_\perp$. In general, the condition $D_\parallel \gg D_\perp$ holds. Since the confinement properties of a magnetic configuration are governed by the perpendicular coefficients, we will therefore focus on those.

The simplest approach to calculate diffusion coefficients comes from the random-walk ansatz. Here, we assume that, due to collisions with other particles, a particle makes a step Δx perpendicular to the magnetic field after a time Δt. If the step can be done in either direction $\pm\Delta x$ with equal probability, the process is purely diffusive and the diffusion coefficient D is given by

$$D \approx \frac{\Delta x^2}{2\Delta t}\,. \tag{8.21}$$

In order to estimate D, we have to evaluate Δx and Δt. The latter is given by the inverse of the collision frequency ν_c. With appropriate averaging we obtain the following relations for a 90^o scattering (made up of many small angle scatterings) for electron-electron (ee), electron-ion (ei) and ion-ion (ii) collisions (we assume a pure hydrogen plasma, i.e. $Z = 1$)

$$\nu_{ee} \approx \nu_{ei} \propto \frac{ne^4}{\sqrt{m_e}T_e^{3/2}} , \tag{8.22}$$

$$\nu_{ie} = \left(\frac{m_e}{m_i}\right)\nu_{ee} , \tag{8.23}$$

$$\nu_{ii} = \left(\frac{m_e}{m_i}\right)^{1/2}\left(\frac{T_e}{T_i}\right)^{3/2}\nu_{ee} . \tag{8.24}$$

In the so-called classical approach to transport, we take Δx to be the Larmor radius r_L

$$\Delta x = r_L = \frac{\sqrt{2mkT}}{eB} . \tag{8.25}$$

However, the location R of the guiding centre of the gyro-orbit is given by

$$\mathrm{R} = \frac{\mathrm{p}\times\mathrm{B}}{q_C B^2} , \tag{8.26}$$

with q_C denoting the charge of the particle. In a collision, momentum balance requires $\Delta \mathrm{p}_a = -\Delta \mathrm{p}_b$, and thus, for like-particle collisions, $\Delta \mathrm{R}_a = -\Delta \mathrm{R}_b$. Therefore, at each collision, the particles just change place so that like-particle collisions do not contribute to particle transport (note that heat can be transferred that way, because a hot particle may change place with a cold one).

The situation changes for electron-ion collisions. Here, $q_a = -q_b$ and therefore $\Delta \mathrm{p}_a = -\Delta \mathrm{p}_b$ leads to $\Delta \mathrm{R}_a = \Delta \mathrm{R}_b$. Thus diffusion is ambipolar, electrons and ions make a step of equal magnitude and direction per collision. The diffusion coefficient is then given by

$$D_{e,class} = \nu_{ei} r_{L,e}^2 = \nu_{ie} r_{L,i}^2 = D_{i,class} . \tag{8.27}$$

For the thermal conductivities, similar arguments can be applied to show that the relation $\chi_i \approx (m_i/m_e)^{1/2}\chi_e \approx 40\chi_e$ should hold. However, experimentally determined diffusion coefficients are larger by a factor of $\approx 10^5$. Also, the electron heat conductivity is found to be comparable to that of the ions. Therefore, classical transport cannot be the dominating transport process in a fusion plasma.

So far, we did not consider the effects of the toroidal geometry. This is the subject of the so-called *neoclassical* transport theory. The main differences to classical transport theory arise from two facts:

- Along a magnetic field line, $|B|$ is not constant; a particle moving along a field line sees a higher field on the inside of the torus and, for sufficient $v_\perp/v_\parallel$, may be reflected in this magnetic mirror (see chap. 1). Therefore we have to distinguish between *trapped* and *passing* particles. It can be shown that the number of trapped particles is given by $n_t/n = \sqrt{2\varepsilon}$, where $\varepsilon = r/R$ is the inverse aspect ratio of the flux surface. A simple result of this effect is that the electrical conductivity is lowered in neoclassical theory as trapped particles cannot contribute to the toroidal current.

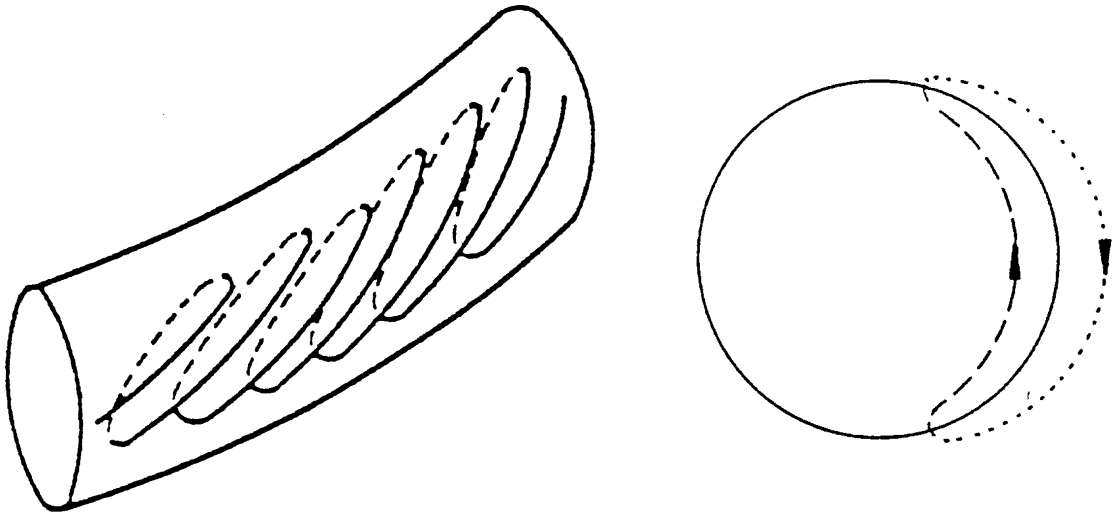

Figure 8.7: Banana Orbits in a toroidal configuration.

- Due to ∇B and curvature drifts, the path of a trapped particle deviates from the magnetic surface. Therefore, the projection of the trapped particle orbit in a poloidal plane is not a sector of a circle, but rather has a banana-like shape (see Fig. 8.7). These orbits are known as *banana orbits*. One can show that the banana width is given by

$$r_B = \frac{r_L q}{\sqrt{\varepsilon}} \,. \tag{8.28}$$

For trapped particles, an *effective* collision frequency $\nu_{eff} \approx \nu_c/(2\varepsilon)$, where ν_c can be any of the collisionalities discussed above, is defined. This takes into account, that a trapped particle becomes a passing one when its pitch angle has changed by $(2\varepsilon)^{1/2}$. Finally the ratio $\nu_* = \nu_{eff}/\nu_t$, where ν_t is the inverse of the time a particle needs to transit the banana, determines wheter the particle can complete a banana orbit between two collisions.

There are three different regimes of neoclassical transport:

- Collisional or Pfirsch-Schlüter regime: Here, $\nu_* > 1$, particles do not complete their banana orbits but are scattered before. In this case, D is evaluated to be

$$D_{PS} = q^2 r_L^2 \nu_c = q^2 D_{class} \,. \tag{8.29}$$

  As we have seen, q typically ranges between two and five, so transport is strongly increased.

- Banana regime: Here, $\nu_* < \varepsilon^{3/2}$, particles follow the banana orbit several times before they are scattered. We can apply the random walk argument for the $\sqrt{2\varepsilon}$ trapped particles with step size r_B and typical time interval $1/\nu_{eff}$

$$D_B \propto \sqrt{2\varepsilon}\, r_B^2 \nu_{eff} \approx \frac{r_L^2 q^2}{\varepsilon^{3/2}} \nu_c = \frac{q^2}{\varepsilon^{3/2}} D_{class} \,. \tag{8.30}$$

  For typical values, e.g. $\varepsilon = 1/3$ and $q = 5$, this yields $D_B = 130\, D_{class}$.

- Plateau regime: Here, $1 > \nu_* > \varepsilon^{3/2}$ and one can derive $D_{Pl} \approx v_{th} r_L^2 q/R$. This result is independent of ν_c (hence the name). Numerical values for D_{Pl} are in between the Pfirsch-Schlüter and the Banana regimes, so that, with rising collisionality, a smooth transition occurs between the regimes.

These neoclassical terms have to be added to the classical terms, however, they completely dominate the latter. We have seen that, due to neoclassical effects, transport coefficients can be increased by two orders of magnitude, nevertheless, they still cannot explain the experimental observations, especially for the electron channel. Today, theory tries to explain this so-called *anomalous* transport by nonlinear MHD turbulence models. It is found both theoretically and experimentally that the plasma exhibits turbulent eddies of a radial extension Δx of a few cm and a lifetime Δt of several 100 μs. If we calculate the diffusion coefficient according to (8.21), we arrive indeed at typical values of $1\,\mathrm{m}^2/\mathrm{s}$ which could explain the experimental observations. However, the precise identification of the responsible small-scale MHD instabilities is a subject of ongoing research in the field of fusion plasma physics. In particular, it has become clear that a simple description in terms of one dominant mode does not exist and several contribution must be taken into account, for the different species and the large variation of plasma parameters from the edge to the core.

Chapter 9

Experimental results from tokamaks

Wolfgang Suttrop

9.1 Tokamak plasmas

9.1.1 The tokamak principle

Nuclear fusion can be achieved in plasmas which are composed of a mixture of deuterium and tritium. At the high temperatures necessary for nuclear fusion, in the vicinity of 10 keV or 100 Million degrees K, the plasma is fully ionised, i.e. consists only of ions and electrons. In order to reach these temperatures, good thermal insulation is necessary, which can be provided by a magnetic field. The Lorentz force makes charged particles spiral (*gyrate*) around magnetic field lines. Electrons and ions can freely move along field lines. If magnetic field lines close themselves inside the plasma volume, the free parallel motion does not result in particle losses from the plasma. Consequently, toroidal field geometry (as sketched in Fig. 9.1 left is most effective for confinement of high temperature plasmas and in fact most magnetic fusion concepts involve this topology.

The toroidal shape of the plasmas implies a non-uniform magnetic field strength. This results in a particle drift (Grad-B and curvature drift) perpendicular to the magnetic field and its gradient. This drift originates from a different gyro-radius at the low and high field sides of the particle orbit. The drift is directed parallel to the torus (vertical) axis in different directions for electrons and ions and hence leads to a separation of charge and a vertical electrical field. The electrical field induces an additional $E \times B$ drift which leads to fast radial losses of electrons and ions (see Fig. 9.1 right). Hence, a simple toroidal magnetic field is not sufficient for plasma confinement.

The losses induced by these drifts can be eliminated by introduction of an additional poloidal magnetic field. The resulting helical field directs field lines successively below and above the equator of the device so that vertical drifts result in inward and outward motion, respectively. As a result, the trajectories of the centers of the gyromotion (*gyrocenters*) are displaced from the magnetic field lines but are also closed in themselves. The magnetic moment of the gyromotion is conserved and with increasing magnetic field strength the velocity parallel to the field reduces. Fig. 9.2 shows poloidal sections of two basic types of gyro-center trajectories: *Trapped particles*, see Fig. 9.2 left do not have a sufficiently large parallel velocity at the lwo field side to reach the location of maximum magnetic field strength. They are confined to the

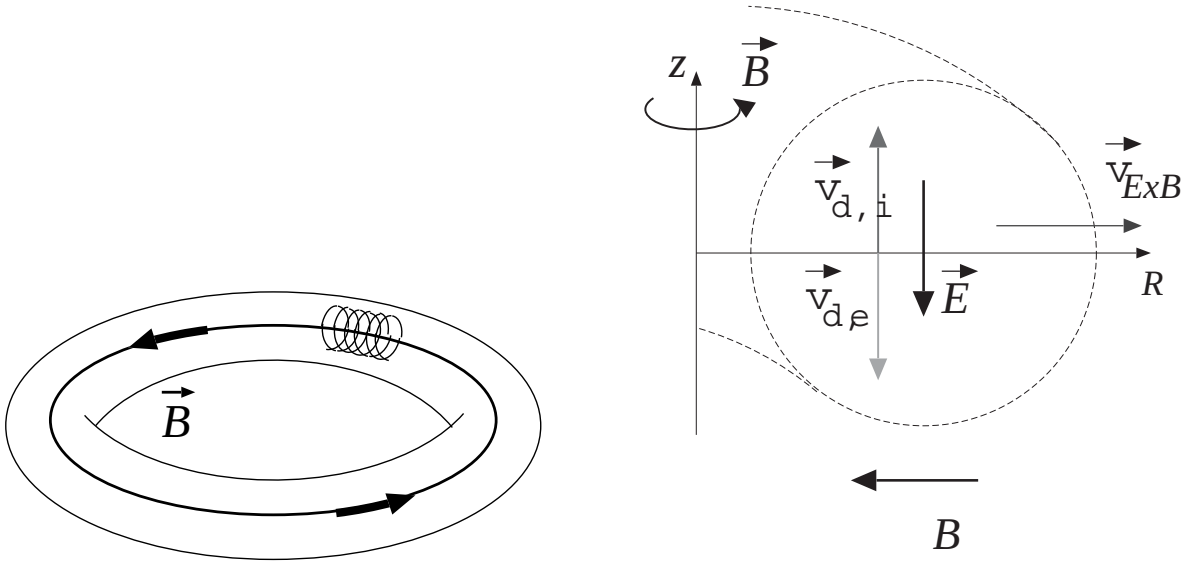

Figure 9.1: Left: Closed field lines in toroidal geometry.
Right: Outward particle drift in toroidal geometry.

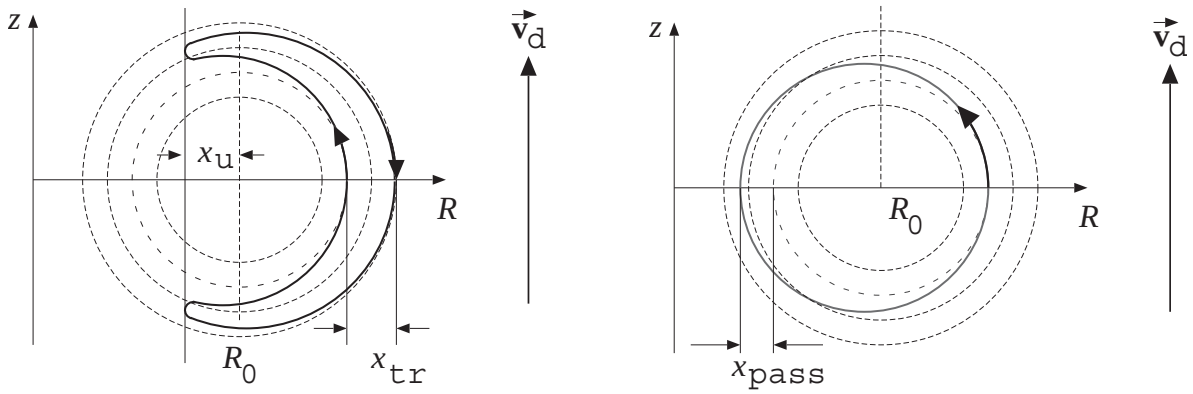

Figure 9.2: Particle trajectories in toroidal geometry:
Left: Trapped particles,
Right: Passing particles.

magnetic low field side and move in poloidally and toroidally opposite directions on the inner and outer halves of their orbit. The characteristic *banana* shape as viewn in a poloidal section gives rise to the nick-name *banana orbits* for these trajectories (see section on *magnetic mirror* above). *Passing particles* have a sufficiently large parallel velocity to continue their motion on the high field side, Fig. 9.2 right. The associated radial displacement with respect to field lines, Δx, is larger by a factor $(R/a)^{1/2} \equiv 1/(\varepsilon)^{1/2}$ for trapped particles than for passing particles, where R is the *major radius* (distance from torus axis to plasma center) and a the *minor radius* (half of the diameter of the plasma column) of the toroidal plasma.

The effects of toroidicity on particle orbits have several important consequences. Cross-field diffusion by Coulomb collisions is enhanced by the larger radial displacement of the particle orbits compared to their gyroradius (*neo-classical* diffusion). In presence of a pressure or density gradient, the average toroidal velocity of trapped particles at a given radial location is not zero. Momentum is transferred by Coulomb collisions to passing particles resulting in a plasma current (*bootstrap current*).

The additional poloidal field needed for confinement can be created in different ways. *Stel-*

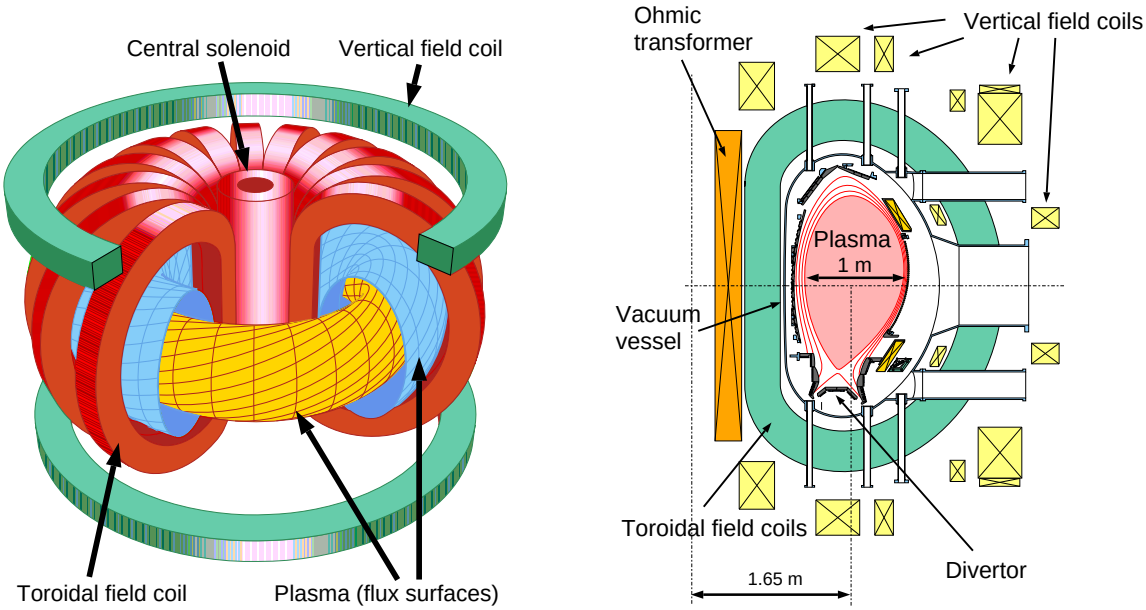

Figure 9.3: Left: Tokamak: Schematic view of main components.
Right: Cross section of ASDEX Upgrade (Axi-Symmetric Divertor EXperiment), installed at Max-Planck-Institut für Plasmaphysik, Garching, Germany.

larators generate a helical field entirely by external field coils. *Tokamaks* use a plasma current to produce the poloidal field component, while the toroidal field is generated by an axisymmetric arrangement of external coils. The word *tokamak* stems from a Russian acronym for *Toroidal chamber with magnetic coils*. In the following, we concentrate on tokamaks.

9.1.2 Components of a tokamak

The main components of a tokamak are illustrated in Fig. 9.3 left. Helical magnetic field lines span nested surfaces of constant magnetic flux (*flux surfaces*). The plasma is enclosed in a vacuum chamber (not shown) which is needed to remove air and control the hydrogen pressure outside the plasma. The axisymmetric toroidal field is produced by poloidal currents in a set of magnetic coils surrounding the plasma. A central solenoid is used to produce a time-varying poloidal magnetic flux which induces a toroidal loop voltage, and due to finite plasma resistivity, a plasma current. The plasma is subject to a poloidally and radially outward directed force which results from a finite plasma pressure gradient. This force is balanced by the $j \times B$ force acting on the plasma current due to the helical field and an additional vertical field produced by toroidal currents in external conductors (*vertical field coils*).

As an example, the poloidal cross section of ASDEX Upgrade (Axi-Symmetric Divertor EXperiment) at Max-Planck-Institut für Plasmaphysik, Garching (Germany), is shown in Fig. 9.3 right. This machine can produce plasmas with major radius $R = 1.65$ and horizontal minor radius $a = 0.5\,\mathrm{m}$. An array of vertical field coils is installed which do not only produce the vertical field for compensation of the radial outward force but also can create suitable poloidal fields to create a wide range of plasma shapes. Typically, vertically elongated plasmas are produced by toroidal currents in upper and lower shaping coils which have the same direction as the plasma current. This configuration is inherently unstable against vertical displacements. A small upward displacement from the equilibrium position will result in a larger attracting force

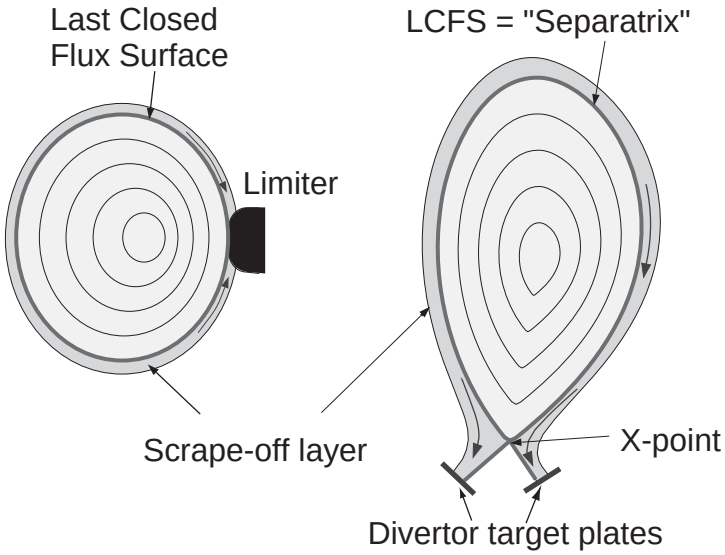

Figure 9.4: Limiter and divertor configurations.

on the plasma current of the upper coil current than of the lower coil, thereby amplifying the perturbation. This position instability is damped by induced currents in a passive saddle-loop near the plasma (*passive stabilizing loop*). On time scales longer than the L/R time constant of the saddle loop (about 1 ms), the vertical position is actively controlled with an external radial field, i.e. by a differential current in the upper and lower vertical field coils.

9.1.3 Divertor tokamaks

Quadrupole currents in the poloidal field coils are also used to form a *magnetic divertor* configuration. Fig. 9.4 illustrates two basic magnetic configurations of a tokamak plasma.

Radial diffusion of particles and heat across the magnetic field will lead to expansion of the plasma until a material wall is intersected. Without a magnetic divertor, this first material contact will be close to the main confined plasma volume, and hence be subjected to strong heat load and particle fluxes. This region, called the *limiter*, must be appropriately designed in order to prevent excessive materials erosion. With a suitable axi-symmetric quadrupole field a magnetic X-point is introduced which defines a magnetic surface (*separatrix*) that intersects the material wall only at a distance from the main plasma. Particles and energy from the main plasma flow along field lines to a separated divertor region where particles are neutralized at the material wall (*target plates*). A fraction of the neutral particles is reflected towards the separatrix, re-ionised and is streaming back again to the target plates. This recycling flux effectively increases the plasma density in the divertor region. Under normal conditions, the plasma pressure is constant along magnetic field lines, hence the plasma temperature in the divertor is smaller than that at the separatrix near the main plasma. As a result, the erosion damage at the material wall produced by ions can be strongly reduced and cleaner plasmas are obtained compared with a limiter configuration. This favourable property of divertors is exploited in most modern magnetic fusion devices, both tokamaks and stellarators. Fig. 9.5 shows cross sections of four tokamaks: ASDEX (Max-Planck-Institut für Plasmaphysik, Garching, Germany), PBX-M (Princeton Plasma Physics Laboratory, Princeton, New Jersey, USA), TCV (Centre de Recherche en Physique des Plasmas, Lausanne, Switzerland) and JET (Joint Euro-

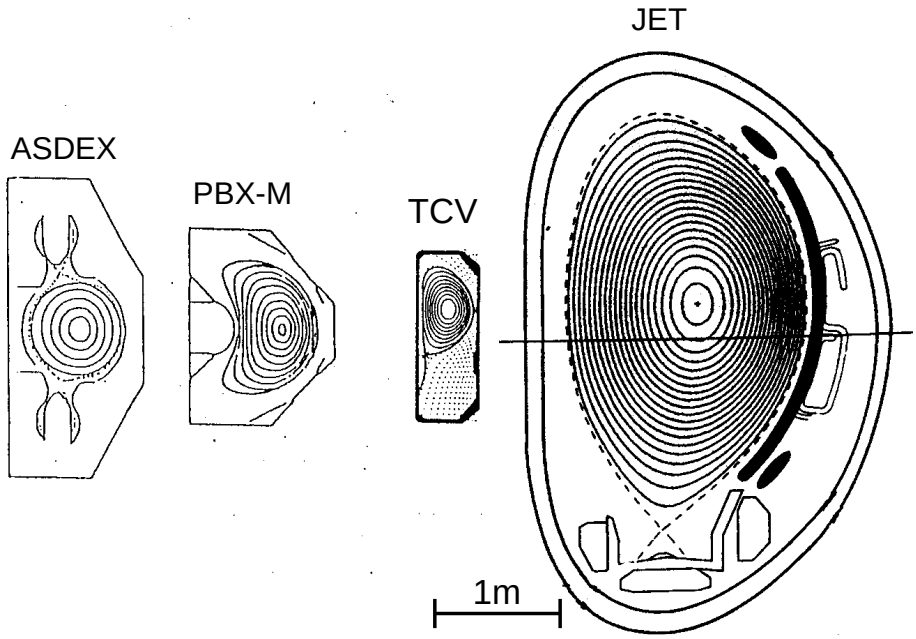

Figure 9.5: Variations of magnetic configurations (poloidal cross sections) in different experiments in shape (ASDEX, PBX-M) and plasma size (TCV, JET).

pean Torus, Culham, United Kingdom). These examples illustrate a variety of plasma sizes, cross sections and divertor geometries used in tokamaks.

9.1.4 Magnetic configuration

At the densities and temperatures reached in fusion plasmas, significant kinetic pressure is obtained in the plasma core and large pressure gradients produce strong forces on the plasma column. The ∇p forces are balanced by $j \times B$ forces arising from the magnetic field interacting with internal (toroidal and poloidal) plasma currents. This force balance is often called the *magnetic equilibrium* of a plasma configuration. (It has to be stressed that this terminology does not imply the existence of a thermodynamic equilibrium state. In the contrary, because of the presence of strong heat flows into and out of the plasma, fusion plasmas are always open thermodynamic systems, far from thermodynamic equilibrium).

The poloidal magnetic field components B_R, B_z can be expressed by the derivatives of the poloidal magnetic flux ψ through a circle co-axial with the torus axis $B_R = -(1/2\pi R)\partial\psi/\partial z$, $B_z = (1/2\pi R)\partial\psi/\partial R$. From Ampere's law (toroidal derivatives vanish due to axi-symmetry) the toroidal current density can be expressed as

$$j_{tor} = -\frac{1}{2\pi\mu_0}\left[\frac{1}{R}\frac{\partial^2\psi}{\partial z^2} + \frac{\partial}{\partial R}\left(\frac{1}{R}\frac{\partial\psi}{\partial R}\right)\right] \equiv -\frac{1}{2\pi\mu_0}\frac{1}{R}\Delta^*\psi\,. \tag{9.1}$$

The magnetic field lines span nested toroidal surfaces of constant plasma pressure which can be labelled with the flux ψ (*flux surfaces*). Expressing the toroidal field B_t by the *poloidal* current I_{pol} within a flux surface, $(\partial(RB_t)/\partial R) = (\mu_0/2\pi)\,(\partial(I_{pol})/\partial R)$, and using Ampere's law again, one obtains the famous Grad-Shafranov-Schlüter equation

$$\Delta^*\psi = -4\pi^2\mu_0 R^2 p' - \mu_0^2 I_{pol} I'_{pol}\,, \tag{9.2}$$

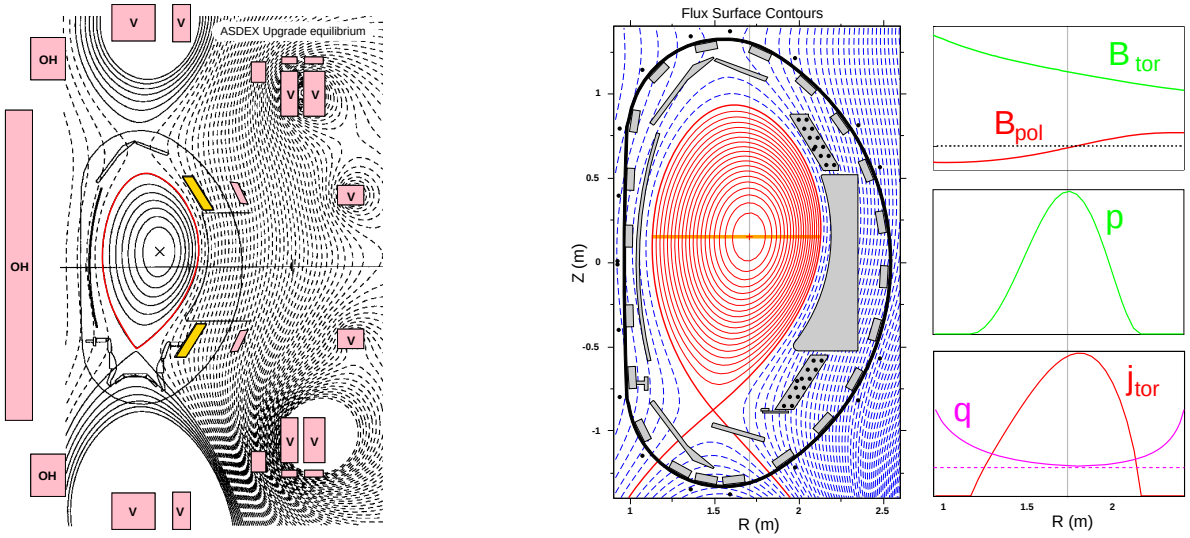

Figure 9.6: Left: Poloidal magnetic flux in and around a shaped tokamak plasma (poloidal section), which is created by toroidal currents – plasma current and a set of external poloidal field coils.
Right: Tokamak equilibrium: Flux surfaces, radial midplane profiles of B_{tor}, B_{pol}, pressure p, toroidal plasma current j_{tor} and safety factor q.

where the prime ($'$) denotes the derivative with respect to ψ. Solutions of (9.2) describe the magnetic flux and toroidal current density for an axisymmetric magnetic equilibrium configuration characterized by toroidal current density $j_{tor}(R,z)$ (which contains plasma currents and external shaping coil currents), plasma pressure gradient p' and poloidal current profile I_{pol}.

Fig. 9.6 left shows (in a poloidal cross-section) contours of constant magnetic flux for an experimental magnetic equilibrium of a plasma in ASDEX Upgrade. The toroidal plasma current generates poloidal magnetic flux which, in superposition with the flux generated by the poloidal field coils, defines a region of magnetic surfaces which are closed in themselves and have no intersection with a material wall. The boundary of this region (*last closed flux surface*, or *separatrix*) is highlighted in Fig. 9.6 left. Measurements of the magnetic flux are taken at many positions inside the vacuum vessel to reconstruct the experimental magnetic surfaces using (9.2). The shape of these surfaces can be controlled (feed-forward or feed-back) by the currents in the shaping coils.

Fig. 9.6 rightshows a close-up of the vacuum vessel, the region of closed magnetic surfaces and profiles of the toroidal magnetic field B_{tor}, poloidal magnetic field $B_{pol} = (B_R^2 + B_z^2)^{1/2}$, plasma pressure p and toroidal current density j_{tor} along a horizontal section across the plasma center (indicated in the figure). Magnetic field lines follow a helical path on flux surfaces around the torus. A field line returns to a given poloidal position at a certain increment of the toroidal angle $\Delta\Phi$, which depends on B_t and B_{pol} along the field line. The *safety factor* $q = \Delta\Phi/2\pi$ counts how often a field line passes toroidally around the torus before it returns to the same poloidal position. For cylindrical cross-section and $R/a \gg 1$, $q(r)$ can be approximated as $q = (r/R)(B_t/B_{pol})$. The profile of q is also shown in Fig. 9.6 right. For a sufficiently peaked j_{tor} profile, q rises monotonically from the plasma center to the edge. This is typically the case if the plasma current is driven entirely by the induced loop voltage so that j_{tor} is determined by the radial resistivity profile. For irrational q, field lines span the entire flux surface. For rational q, field lines join up into themselves after a finite number of passes around the torus, so that helical perturbations can easily occur. Magnetic flux surfaces with integer or low rational q

values are important for the stability of tokamak plasmas. In particular, q at the plasma edge has to be above a value of two to avoid a large scale disruptive instability (see sec. 9.2.3). This defines a minimum toroidal field for any given plasma current. The safety factor in the plasma center is usually clamped to values near or above unity by sawtooth oscillations (see sec. 9.2.3) or other types of magnetohydrodynamic activity.

9.1.5 Plasma heating

In order to balance heat losses from the plasma, a continuous heat source must exist to maintain the temperatures needed for fusion reactions to occur.

A heat source inherent for tokamaks is the Joule heat ηj^2 which originates from the plasma current and the low but finite resistivity η of a high temperature plasma (*Ohmic heating*). The plasma resistivity is proportional to $T_e^{-3/2}$ so that the Ohmic heating power reduces with increasing plasma temperatures, while the heat loss increases with increasing temperatures and their gradients. In practice Ohmic heating is limited to temperatures up to about 1 500 eV, significantly below the temperatures needed to initiate fusion reactions. Neutral particle injection (NBI) or absorption of radio-frequency waves can be used to heat the plasma to temperatures significantly higher than those achieved with Ohmic heating.

For NBI heating, a beam of ionized deuterium is produced and accelerated in an electric field. Typical particle energies are 60–140 keV and beam currents range up to 100 A per NBI source. The deuterium beam is guided through a neutralizer chamber filled with neutral deuterium gas. Charge exchange reactions occur for 60–90% of the ions (depending on beam energy). Particles not neutralized are deflected by a magnetic field towards the wall of the chamber where they recombine and are pumped out. The fast neutral particles can pass through the tokamak periphery without being affected by the magnetic field. In the plasma, the neutral beam particles undergo charge exchange reactions which produce a population of fast ions. The plasma is heated by collisions of the fast ions with the thermal particles.

Radio frequency heating makes use of resonances in the dispersion relation for waves in plasmas, in particular resonances with the cyclotron motion of ions and electrons (*cyclotron resonance*). Electromagnetic waves are absorbed at the cyclotron resonance (and their harmonics) and the wave energy is converted into increased kinetic energy perpendicular to the magnetic field of the resonant particles. Collisions lead to thermalization of the energy distribution at increased temperature. Due to the different mass of ions and electrons different frequencies must be used. While for ion cyclotron heating (ICRH) frequencies in the range of several ten MHz are used, electron cyclotron resonance heating (ECRH) requires frequencies of the order of 100 GHz. ICRH heating systems typically use vacuum tube amplifiers, coaxial conductors and loop antennas mounted inside the vacuum vessel close to the plasma surface. ECRH power is generated by strong electron beams in a magnetic field with properly tuned magnetic fields (in devices called *gyrotrons*). The microwave power is transmitted in oversized waveguides or by quasi-optical imaging. Antennas are steerable mirrors which launch Gaussian beams that can be directed for variable power deposition positions.

9.1.6 Anatomy of a tokamak plasma

Figure 9.7 left shows for a typical tokamak discharge (example taken from the ASDEX Upgrade tokamak) several measurements as a function of time. After start-up of the discharge, the

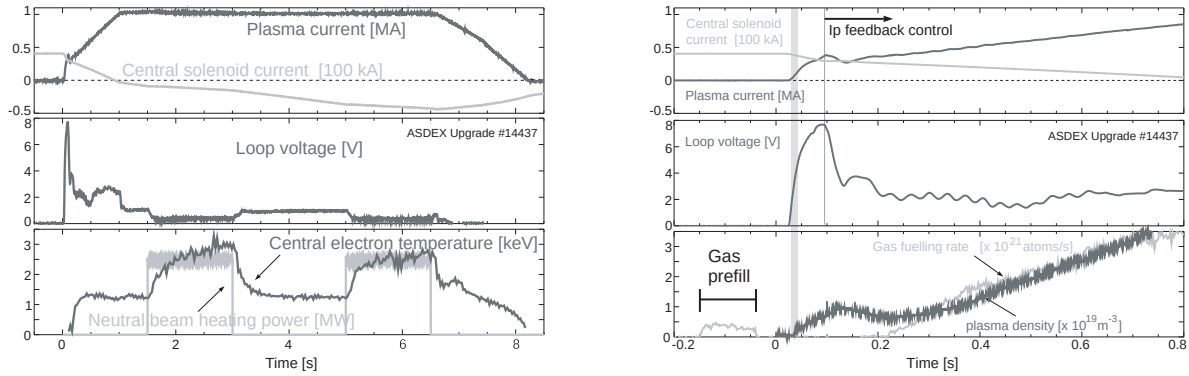

Figure 9.7: Left: Measured time traces for a tokamak plasma during start and plasma current ramp-up phase, flat-top phase, and ramp-down phase. Right: Start-up phase of a tokamak plasma: A high loop voltage, generated by a fast central solenoid current ramp, ionises an initial neutral gas prefill.

plasma current I_p is ramped up within one second to its flat-top value of 1 MA. The discharge is terminated after 6.5 s by a ramp down of I_p. The same panel shows I_{OH}, the current in the central solenoid needed to achieve the requested plasma current: Before the start of the pulse, I_{OH} is set to 40 kA. Initially, a large loop voltage (second panel) is needed for break-down. This is achieved with a fast step in I_{OH}. During current ramp up, large flux is consumed due to the inductance of the plasma. During current flat top, flux consumption depends on plasma resistivity. In our example, neutral beams are injected during two time intervals (1.5–3 s and 5–6.5 s) resulting in an increase of plasma temperature and consequently a decrease of resistivity. This results in the measured reduction of the loop voltage and reduced ramp rate of I_{OH} during the time intervals with auxiliary heating.

Details of the start-up phase of this discharge are shown in Fig. 9.7 right. A carefully dosed amount of deuterium gas (*gas prefill*) is introduced into the vacuum chamber and then a fast step of I_{OH} is applied to generate a large loop voltage. This results in ionisation of the neutral gas. The resulting free electrons are accelerated and help to further ionize the neutral gas. The plasma density (bottom panel) rises along with the plasma current. After about $t = 100$ ms, the plasma current is feedback-controlled and slowly ramped up. After $t = 200$ ms the plasma density is also feed-back controlled with the gas fuelling rate.

9.2 Experimental results

9.2.1 Confinement and transport

Confinement time

One of the main requirements for a nuclear fusion plasma is a sufficiently large *energy confinement time*, defined as $\tau_E = W_{th}/P_{heat}$, where W_{th} is the thermal stored energy and P_{heat} the heating power required to obtain this energy. The confinement time is a major figure of merit for tokamak performance and is relatively easy to measure. The heating power is the sum of ohmic heating ($V_{loop} \times I_p$) and auxiliary heating power, plus alpha particle power (small in today's tokamaks). The thermal stored energy can be obtained from density and temperature

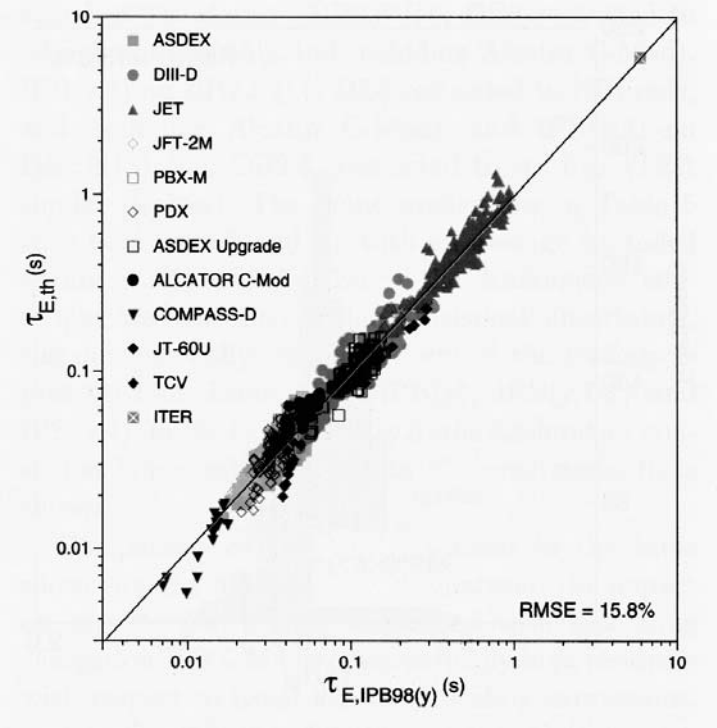

Figure 9.8: Energy confinement time scaling of the International confinement database for a large set of tokamaks.

profiles, or approximated by the total stored energy (e.g. from diamagnetic measurements), corrected for the measured or estimated energy of fast (non-thermal) particles, which mainly depends on heating method, heating power and plasma density.

Fig. 9.8 shows a scaling of the confinement time (experimental vs. predicted τ_E) for a relatively large number of tokamak experiments with different plasma size. This scaling, termed IPB98(y), is used to predict the performance of the planned International Thermonuclear Experimental Reactor (ITER) from present-day machines and has the form

$$\tau_{E,IPB98(y)} = 0.0365\, I_p^{0.97}\, B_t^{0.08}\, P_{heat}^{-0.63}\, n_e^{0.41}\, M^{0.2}\, R^{1.93}\, \varepsilon^{0.23}\, \kappa^{0.67}\,, \tag{9.3}$$

$\tau_{E,IPB98(y)}$ is the predicted confinement time in seconds, I_p plasma current in MA, B_t toroidal magnetic field in T, P_{heat} auxiliary heating power in MW, n_e line averaged electron density ($10^{19}\,\mathrm{m}^{-3}$), M ion mass number, R major radius (m), $\varepsilon = a/R$, κ is the elongation (ratio of vertical and horizontal minor plasma radius). Energy confinement depends most strongly on plasma current I_p, plasma size (radius R) and elongation κ.

The experimental data base spans more than two orders of magnitude of τ_E in similar plasma types (High confinement mode, see sec. 9.2.2 below). ITER is designed for $\tau_E \approx 6\,\mathrm{s}$, which is less than a factor of ten above the largest confinement times obtained in tokamaks to date. Naturally there are uncertainties with such extrapolations, originating from variance in the data base, and possible physics regime changes from current experimental parameters to a reactor-size plasma. It is therefore interesting to study the physics of heat transport in more detail.

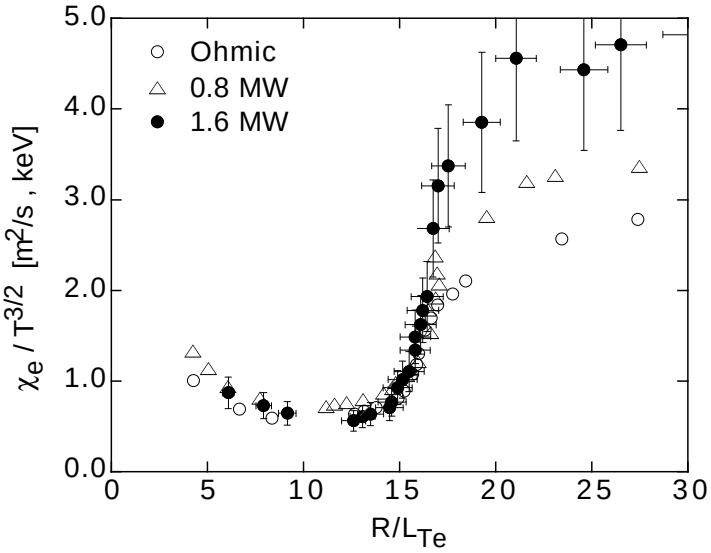

Figure 9.9: Normalized electron heat diffusivity $\chi_e/T^{3/2}$, measured as a function of normalized electron temperature gradient $(\nabla T_e)R/T_e = R/L_{T_e}$.

Heat diffusion

Heat transport can be expressed in terms of a local power balance for the electron and ion heat conduction channels

$$q_{\perp e,i} \;=\; -n_{e,i}\,\chi_{e,i}\,\mathrm{grad}\,T_{e,i} \;\pm\; Q_{e,i}\;, \tag{9.4}$$

where $\chi_{e,i}$ is the *heat diffusivity*, $n_{e,i}$ the density, grad$T_{e,i}$ the temperature gradient and $q_{\perp e,i}$ the heat flux of the considered species (electrons or ions). $Q_{e,i}$ is the collisional heat transfer between electrons and ions.

For *random walk* radial diffusion dominated by Coulomb collisions, one expects a diffusivity of the order of $\chi_{e,i} \approx \Delta x^2/\tau_{e,i}$ where Δx is the radial step size (gyroradius for classical diffusion, banana orbit width for neo-classical diffusion in a toroidal plasma) and $\tau_{e,i}$ is the electron-ion collision time. However, is it found that the actual diffusivity in tokamak plasmas is normally significantly larger than the neo-classical value. In addition, heat diffusivity increases with increased heat flux. Historically, this behaviour has been termed *anomalous* transport and it is now known to originate from small-scale turbulence which creates fluctuating poloidal electrical fields. As a result, fluctuating radial $E \times B$ drifts occur which exchange plasma between hot and cold regions.

Various instability mechanisms exist that can drive transport-relevant turbulence. A common feature is that destabilization occurs if the temperature gradient length $L_T = T/\nabla T$ drops below a critical threshold $L_{T,crit}$. The heat diffusivity strongly depends on $L_T/L_{T,crit}$ and scales with $T^{3/2}$ (*gyro-Bohm* dependence). This behaviour is indeed found in experiments, as shown for electron by measurements of χ in ASDEX Upgrade (evaluated using (9.4)). Fig. 9.9 is a plot of electron heat diffusivity χ_e (normalised by $T_e^{3/2}$) as a function of inverse gradient length $R/L_{T_e} = R\nabla T_e/T_e$ (R is the major radius at midplane on the low-field side). Three different levels of electron heating power are employed: Ohmic heating and ECRH with 0.8 MW and 1.6 MW RF power. The data points correspond to measurements at different radial locations, central points have low heat flux and low inverse gradient length R/L_T (lower left), plasma edge data appears at high diffusivity (upper right corner of the diagram). The experiment

shows the predicted increase of χ_e at $R/L_T \approx 15$. Furthermore, data with different heating power (and different temperature) is described by the same normalisation of χ_e by $T_e^{3/2}$.

The existence of a critical threshold for χ_e above which heat transport increases strongly leads to the formation of *canonical* temperature profiles, where L_T is near $L_{T,crit}$, almost independently of the heating power. This is the origin of the strong deterioration of confinement time τ_E with heating power (9.3). For fixed gradient length, the central temperature depends strongly on the edge temperature, which is limited by edge instabilities (see sec. 9.2.2 and sec. 9.2.3 below). Consequently, high edge pressure and high edge temperature help to achieve high stored energy in the core of a tokamak plasma.

9.2.2 Confinement improvement

High-confinement mode

The level of radial particle and energy transport found in tokamaks is mainly caused by small-scale turbulence. Nevertheless, suppression of this turbulence can be observed in specific cases, leading to a reduction of the particle and heat diffusivity in a restricted plasma volume. This behaviour is often called the formation of a *transport barrier*. With the introduction of a divertor, spontaneous formation of a transport barrier at the plasma edge has been found in the ASDEX tokamak (Garching, 1984). This regime has been termed the *high-confinement* mode (*H-mode*). The effect of the edge transport barrier is demonstrated in Fig. 9.10 left for a discharge of the ASDEX Upgrade tokamak before and after transition to H-mode. Since the discovery of H-mode, the plasma state before the transition to H-mode is usually termed *L-mode* (*low confinement* mode). In H-mode, the pressure gradient steepens up at the plasma edge (r between 0.43–0.45 m for the profile shown), giving rise to a pressure *pedestal*, i.e. additional stored energy in the plasma from the pressure offset at the edge. The temperature just inside the transport barrier is significantly higher than in L-mode, allowing (for the same gradient length $L_T = T/\nabla T$) a higher plasma core temperature gradient than in L-mode, resulting in an additional confinement benefit.

The condition to enter High-confinement mode is a minimum heating power across the plasma boundary. Empirically, the threshold power depends on the product of plasma edge density and magnetic field, $P_{heat} \propto n_{e,edge} \times B_t$. Fig. 9.10 right illustrates this dependence for the case of two divertor geometries in ASDEX Upgrade. Little influence of the divertor geometry (and other parameters such as heating method) is found.

A typical time history around the transition to H-mode is shown in Fig. 9.11 left. The heating power is being stepped up to just above the H-mode threshold at $t = 1.65$ s. Large heat flux in L-mode leads to turbulence that can be seen as broad-band density fluctuations in the $\tilde{n}$ spectrogram contour plot. Transport occurs in bursts that appear in the divertor heat flux (C-III spectral line intensity) and main plasma magnetic probes ($\dot{B}$). After the transition to H-mode (at $t = 1.705$ s in the example), the level of density fluctuations is much reduced and the C-III signal in the divertor drops.

While in L-mode additional heating power creates steeper gradients and thus generates more free energy to drive turbulence and enhanced losses, it can also trigger a transition to H-mode, a self-organising process that results in a bifurcation to a state of reduced transport. This transition to H-mode is accompanied with the creation of a radial electrical field gradient, corresponding to sheared rotation of the centers of the particle gyro-motion. It is believed that

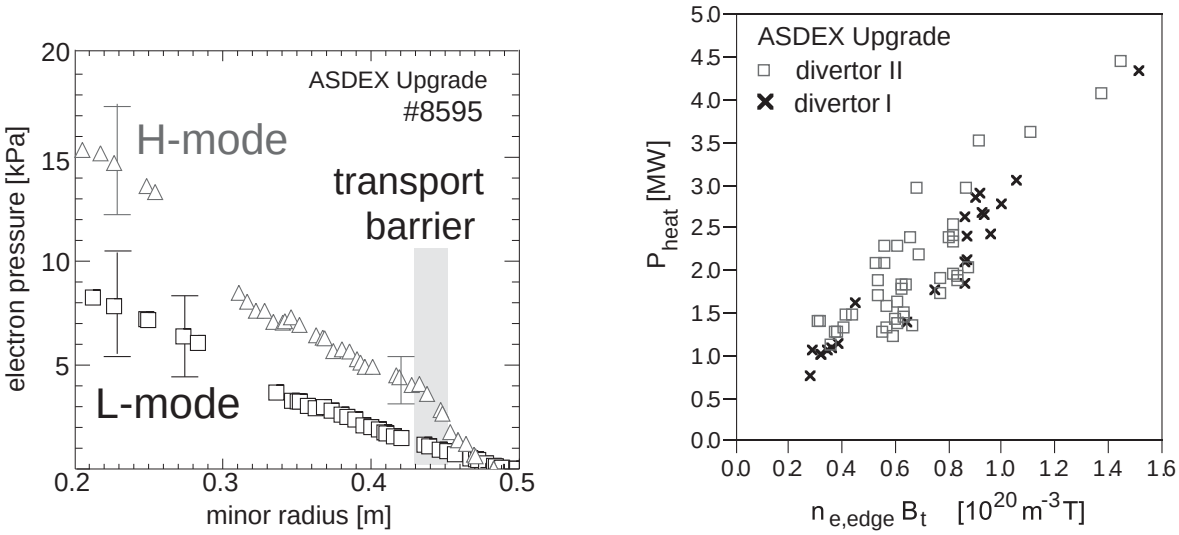

Figure 9.10: Left: Comparison of electron pressure profiles in L-mode and H-mode.
Right: Experimental power threshold for barrier formation.

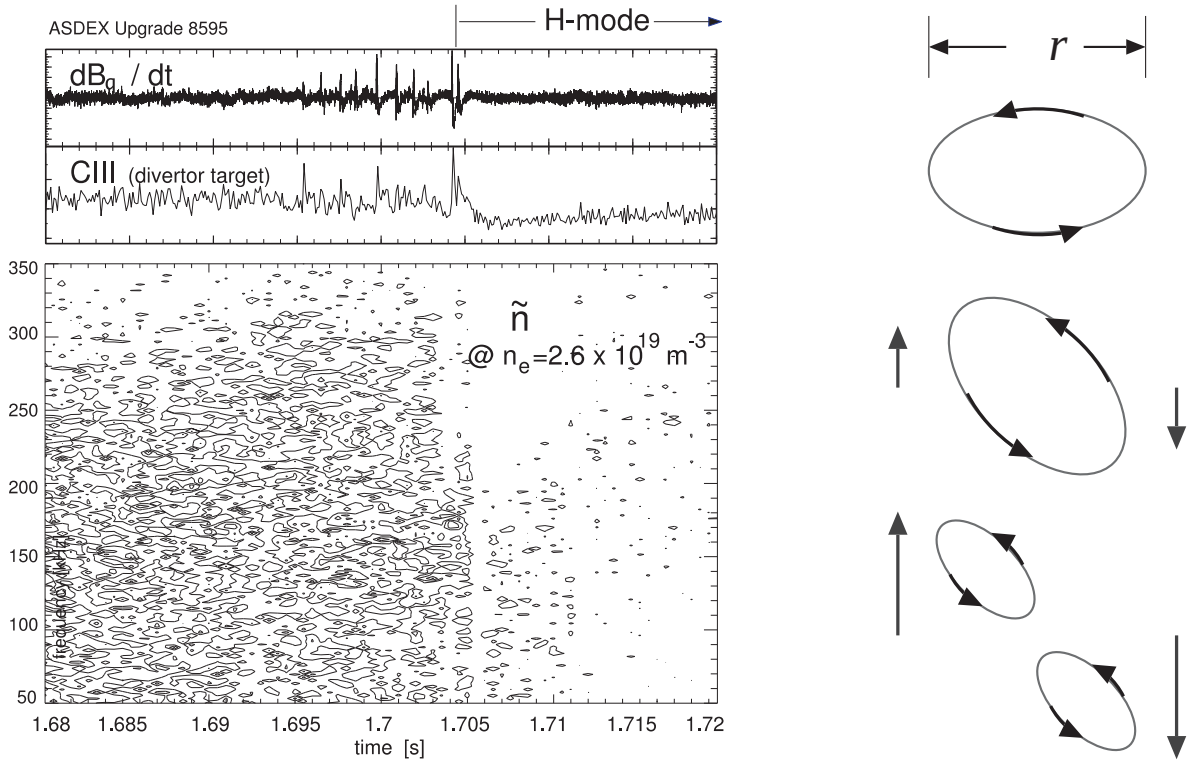

Figure 9.11: Left: Fluctuations are reduced at the transition from L-mode to H-mode.
Right: H-mode model: $E \times B$ shear flow reduces radial size of turbulent eddies.

de-correlation of turbulent $E \times B$ convection cells by sufficiently fast sheared rotation is the origin of the transport reduction (cf. cartoon Fig. 9.11 right). However, although a number of possible mechanisms has been proposed the physics that drives the radial electrical field is still unknown and subject to ongoing research effort.

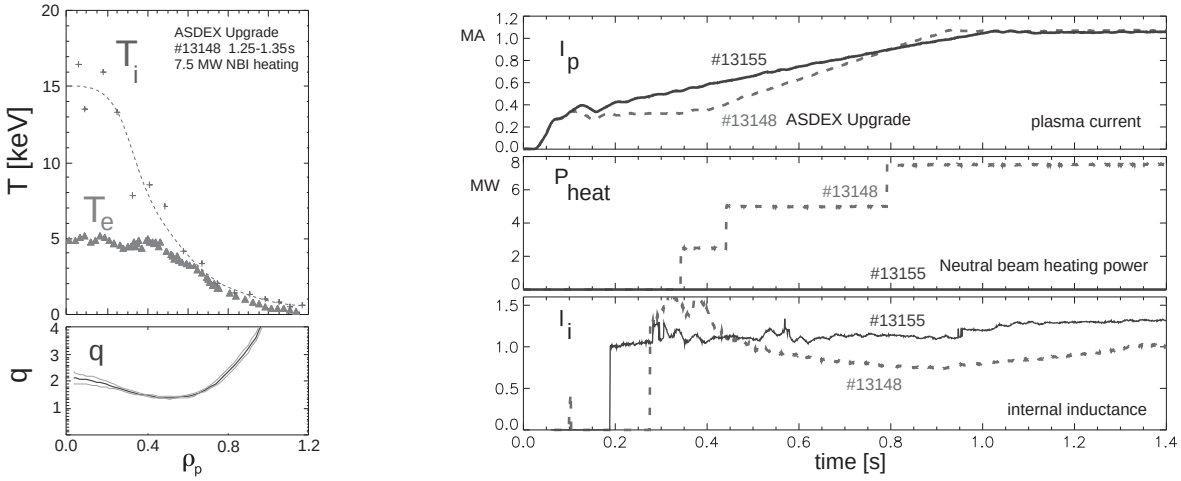

Figure 9.12: Internal transport barrier example:
Left: Profiles of T_i, T_e and safety factor q.
Right: Comparison of discharges with (13148) and without (13155): Early heating during the current ramp leads to broader current profile as seen by a reduced value of ℓ_i.

Internal transport barriers

Transport barriers can exist not only at the plasma edge, but also in the plasma core, causing steep temperature and/or density profiles, thereby increasing the central pressure. *Internal transport barriers* (ITB) arise from an influence of the magnetic shear $s = (r/q)\,\mathrm{d}q/\mathrm{d}r$ on the growth of micro-instabilities and thereby the heat diffusivity. In conventional tokamak plasmas without ITB, q increases monotonically from the center towards the edge, i.e. the magnetic shear is positive across the entire plasma radius. It is observed that heat transport can be reduced at low or negative magnetic shear.

Fig. 9.12 left shows profiles of the electron and ion temperature and the safety factor q in a discharge with ITB in the ASDEX Upgrade tokamak. The q profile is flat or slightly reversed inside a normalized radius of $\rho = 0.6$. A strong ion temperature gradient is maintained around $\rho = 0.4$, leading to a central ion temperature of 15 keV. This temperature, obtained in a tokamak much smaller than an envisaged fusion reactor, is near the optimum temperature for D-T fusion reactions. Fig. 9.12 right shows how this result is achieved. A conventional plasma (shot #13155) is compared with an ITB discharge (#13148). In the ITB pulse, heating power is applied early in the plasma current ramp, resulting in higher T_e. Due to the increased resistive skin time the initial flat or slightly hollow plasma current profile remains *frozen* for the duration of the experiment. This is seen by the slow evolution of the *internal inductance* ℓ_i which indicates by its lower value after $t = 0.45$ s a broader (less peaked) current profile.

The *advanced* tokamak

For truly stationary tokamak operation the plasma current has to be driven entirely non-inductively, for example by the bootstrap effect due to the pressure gradient in the plasma. This leads to the interesting concept of the *Advanced Tokamak*, where the bootstrap current profile maintains the low or reversed shear profile required for the transport reduction which causes the ITB. Fig. 9.13 compares profiles of the pressure, toroidal current density and safety factor

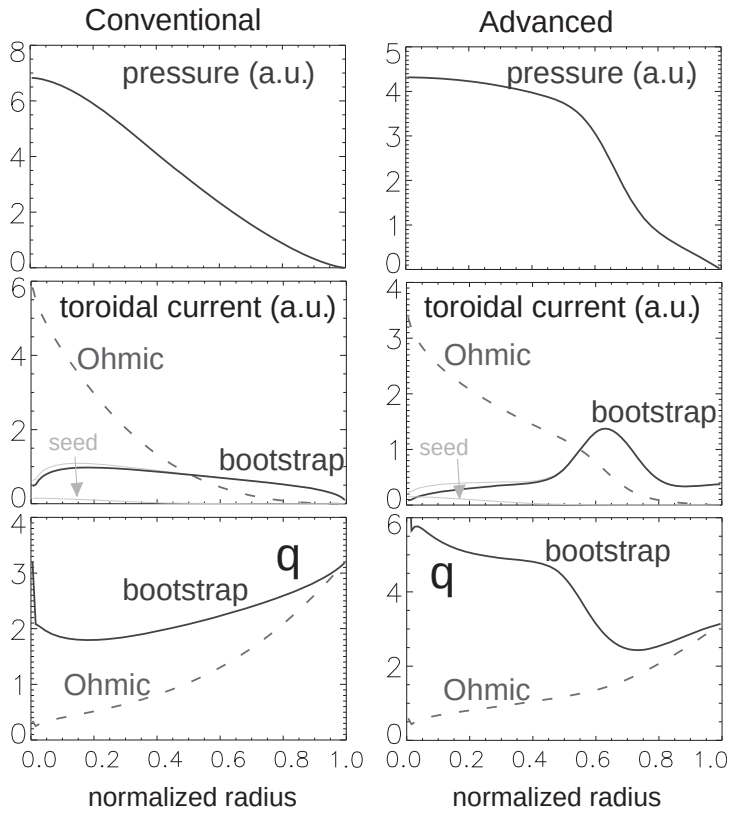

Figure 9.13: Profiles of plasma pressure p, current density j and safety factor q comparing conventional and advanced scenarios. A conventional plasma has a monotonously rising q profile. Flat or reversed reversed q profile can lead to a transport barrier. In an ideal advanced scenario, the resulting steep pressure gradient creates a bootstrap current that maintains the q-profile non-inductively in steady state. Ohmic and bootstrap contributions to j and q are shown separately.

q (assuming pure ohmic or pure bootstrap current) for both a *conventional* (non-ITB) and an ITB plasma.

In the conventional scenario the ohmic (inductively driven) current dominates. The ohmic current density profile is fixed by the conductivity (electron temperature) profile. A sufficiently strong transport barrier can, in principle, sustain a reversed shear profile. The strong pressure gradient produced by the transport reduction creates a strong off-axis bootstrap current. The resulting non-monotonic current profile maintains the weak or negative magnetic shear profile that allows to sustain the transport barrier. A tokamak reactor with an ITB and this type of *self-generated* plasma current could be built smaller than a conventional tokamak and would allow true steady-state operation. A crucial condition is the alignment of the reversed shear region with the region of actual strong pressure gradient, which if not matched, leads to rapid changes of the radial position of the transport barrier. A (small) current profile correction can be applied non-inductively by external current drive techniques, e.g. by electron cyclotron or lower hybrid wave heating with toroidal component of the wave vector. Advanced tokamak scenarios with a variety of current drive methods are an important topic in most current tokamak research programs.

9.2.3 Stability and operational limits

Instability occurs if a plasma perturbation amplifies itself and grows until the plasma configuration is severely modified. Free energy sources for instability growth arise for instance from large gradients of pressure and currents present in a fusion plasma. Many instabilities involve displacements of magnetic surfaces (*MHD instabilities*), but also other types of instabilities exist, for example radiation instability originating from increased radiated power with decreasing temperatures. MHD instabilities are distinguished by their scale: Micro-instabilities occur on the gyro-radius scale and are relevant for radial particle and heat transport. Macroscopic instabilities affect the plasma on the scale of the plasma dimensions and can have large effects on confinement or even terminate a plasma discharge. In toroidal geometry one can characterize unstable modes by their integer toroidal (n) and poloidal (m) mode numbers. Most macroscopic MHD modes can become unstable only at *resonant* surfaces, i.e. magnetic surfaces where $q = m/n$, and n and m are small numbers. At finite aspect ratio, modes with different poloidal mode number m couple, giving rise to complex mode number spectra.

Instabilities are important as they define the accessible plasma parameter range for stable tokamak operation. Subsequently, we discuss the basic tokamak operation range and examine several important types of instabilities and their effects.

Tokamak operational limits

For stable tokamak operation, there are upper bounds for the plasma current and the plasma density. Fig. 9.14 shows a schematic diagram of the accessible parameter range in a plot of $1/q_a$, the reciprocal edge safety factor vs. $\overline{n_e}R/B_t$ (known as *Hugill diagram*). We note that $1/q_a \propto I_p/B_t$, so the vertical axis is proportional to the plasma current. For $1/q_a \to 0.5$ the $q = 2$ surface approaches the plasma edge and a $m = 2$, $n = 1$ *kink* instability occurs. This is a fast-growing large scale ideal MHD mode which leads to a quick termination of the plasma discharge.

Empirically, a density limit is found which is proportional to the plasma current density. In the Hugill diagram (see Fig. 9.14) this is expressed by a an upper bound of the line averaged density $\overline{n}_e R/B_t \propto I_p/aB_t$ or $\overline{n}_e \propto I_p/aR \propto I_p/a^2$ (for constant aspect ratio R/a). The physics of the density limit is quite complex, and some of its aspects are outlined in the next section.

The accessible operation range of tokamaks is bounded by these limits. High plasma density is desirable for good performance and to facilitate power exhaust with a divertor. For a tokamak reactor it is therefore desirable to operate at highest possible plasma current density. The maximum value of B_t is defined by technical limitations for toroidal field coil system. Hence, the $q = 2$ limit sets an upper bound to I_p. From these considerations, the optimum operation point is in the upper right corner of the Hugill plot.

Density limit disruptions

The density limit in tokamaks can assume quite complex phenomenology. A typical history of a density limit in a discharge with only ohmic heating is shown in Fig. 9.15 left. In this experiment, the line averaged density is slowly raised by gas puffing. The edge electron temperature (bottom trace) reduces with increasing density. When the edge has sufficiently cooled

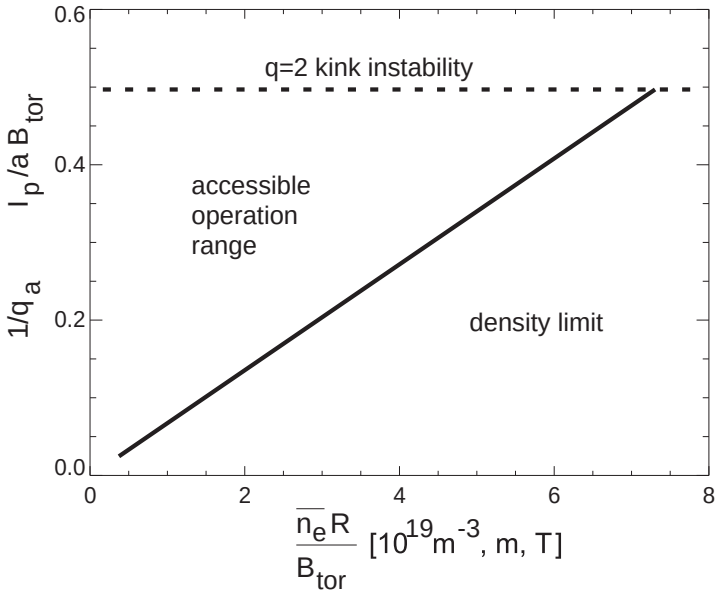

Figure 9.14: Hugill-Diagram showing the basic tokamak operational range. An upper limit to the plasma current is given by the onset of $n = 1, m = 2$ kink instability for $q = 2$ at the plasma edge. A density limit exists at $\overline{n}_e \propto B_t/(Rq) \propto I_p/a^2$.

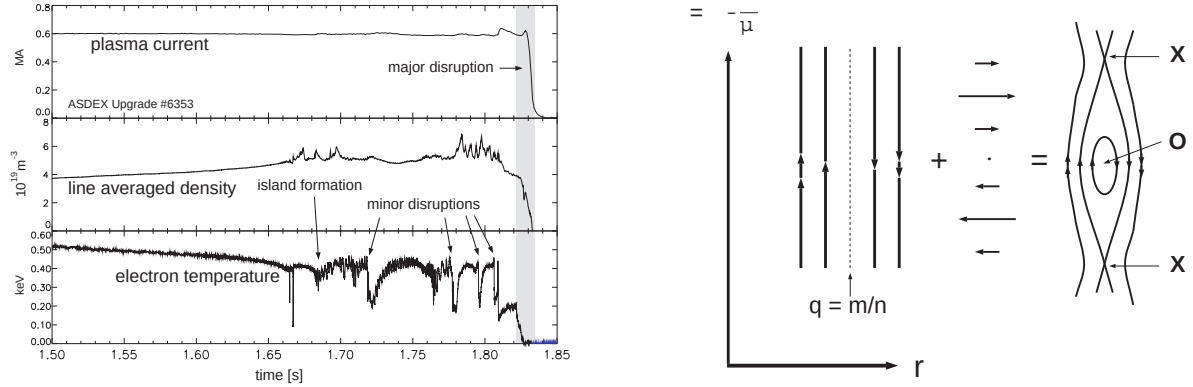

Figure 9.15: Left: History of a density limit disruption. With increasing density the plasma edge is cooled and magnetic islands grow. Finally a *major* disruption occurs with thermal and plasma current quench.
Right: Formation of magnetic islands by superposition of an unperturbed sheared magnetic field and a helical B_r field.

down, *tearing mode* instability occurs which results in the formation of magnetic islands by reconnection.

Fig. 9.15 right shows the structure of magnetic islands (in helical and radial coordinates). Magnetic islands result from helically periodical perturbation currents which give rise to a radial magnetic field with helical symmetry. They can grow only at resonant rational surfaces, i.e. where $q = m/n$. At the density limit, several islands with $m/n = 4/1$, $3/1$ and $2/1$ appear. Since heat transport is faster along magnetic field lines than perpendicular to the field, radial heat flux effectively bypasses the island interior (*O-point*) and concentrates near the X-point. Consequently the temperature is flat inside the island, while near the X-point a gradient is maintained. Plasma rotation makes this modulation visible as an oscillation of the temperature (bottom panel in Fig. 9.15 left).

After islands have grown to a certain radial extent, fast confinement loss events (*minor disruptions*) occur, which lead to a flattening of the temperature profile around a resonant surface. The volume inside this surface cools down and islands on inner resonant surfaces begin to grow. After several minor disruptions, several island chains can exist simultaneously and the rotation velocity reduces to zero (*mode locking*). A *major disruption* occurs, with a fast loss of plasma energy (*energy quench*) and subsequent quench of the plasma current. Because of the inductivity of the plasma, the plasma current quench results in *halo currents* in the vacuum vessel wall, which lead to very large forces on the material structure of a tokamak. The vacuum vessel and the support structure of all magnetic coils must be designed to withstand these forces.

Nevertheless, the disruptive termination of a plasma can be avoided or at least mitigated. If the density is kept below the density limit, the phenomenology described above does not occur. If the density limit is encountered, one can delay tearing mode growth by localized electron cyclotron current drive which replaces the missing helical current in the O-point. Several techniques have been successfully applied to delay or avoid mode locking. Finally, during a disruption the kinetic and magnetic energy in the plasma can be disposed by radiation from injected impurities leading to a more even distribution of energy deposition on the walls, and a reduction of halo currents.

The physics mechanism at the onset of the density limit are still under investigation. Several observations can be made depending on the confinement regime: Increase of radial transport at the edge leading to edge cooling and breakdown of the H-mode barrier; *detachment* of the divertor, i.e. loss of the parallel pressure balance between main chamber edge and divertor due to radial momentum transfer, and formation of a poloidally asymmetric condensation instability (*MARFE*) which leads to edge cooling. Several mechanisms can drive magnetic island growth: Deformations of the current profile, and helical current perturbations due to radiation losses from the island interior or loss of the bootstrap current because of pressure profile flattening around the O-point. The interplay of these mechanisms is being studied in experiments and by complex computer simulations.

Sawtooth oscillations

In many tokamak discharge scenarios, the central temperature undergoes a characteristic oscillation: After a slow linear rise (of few to several 100 ms duration) the temperature crashes very quickly (within about 100 μs) and the cycle repeats. This behaviour has been first observed in the central soft X-ray emissivity and has been named *sawtooth* oscillations for its peculiar time history (see Fig. 9.16 left, top panel). X-ray tomography can be used to reconstruct a two-dimensional image of the central emissivity which reveals the structure of the underlying perturbation. The lower part of Fig. 9.16 left shows the reconstructed X-ray emissivity for four phases before, during and after the sawtooth crash. In between sawtooth crashes the plasma center is heated and the central temperature increases. If $q(0) < 1$, an $n = 1, m = 1$ kink mode is destabilised. Because of good radial confinement the interior of this region is hot ($t = +0.54$ ms). Because of the toroidal plasma rotation, the difference of temperatures inside and outside the kink structure appears as fast oscillations (black areas) in the X-ray signals (see Fig. 9.16 left top). With increasing central current density the structure becomes unstable and reconnection sets in ($t = +0.96$ ms and $t = +1.1$ ms). Hot plasma streams into a larger volume and the peak temperature and emissivity are reduced, but the $1/1$ mode re-appears and the cycle starts over ($t = +1.45$ ms).

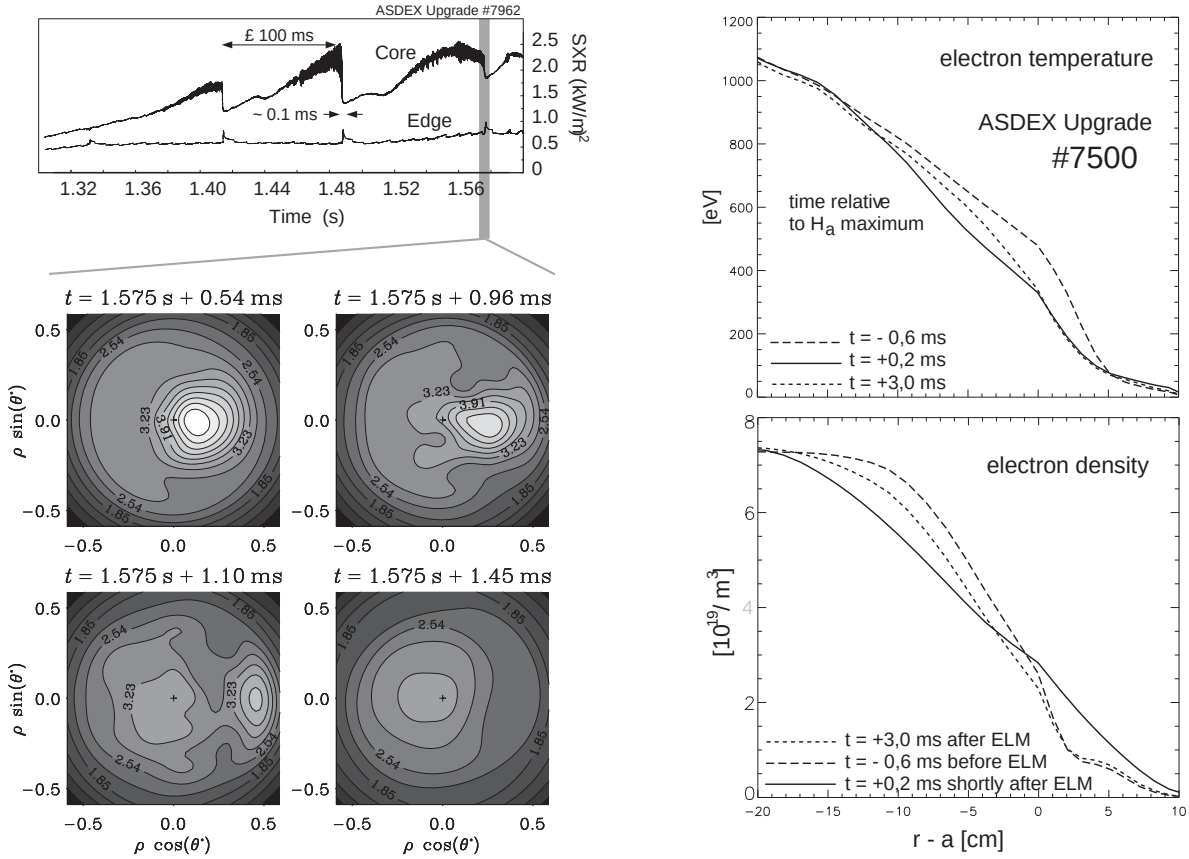

Figure 9.16: Left: Sawtooth oscillations as seen by soft X-ray measurements. Bottom right: Tomographic reconstruction of soft X-ray emissivity before, during and after the sawtooth crash.
Right: Edge electron temperature and density profiles (A) before an ELM, (B) shortly after an ELM, (C) in the recovery phase in between ELMs.

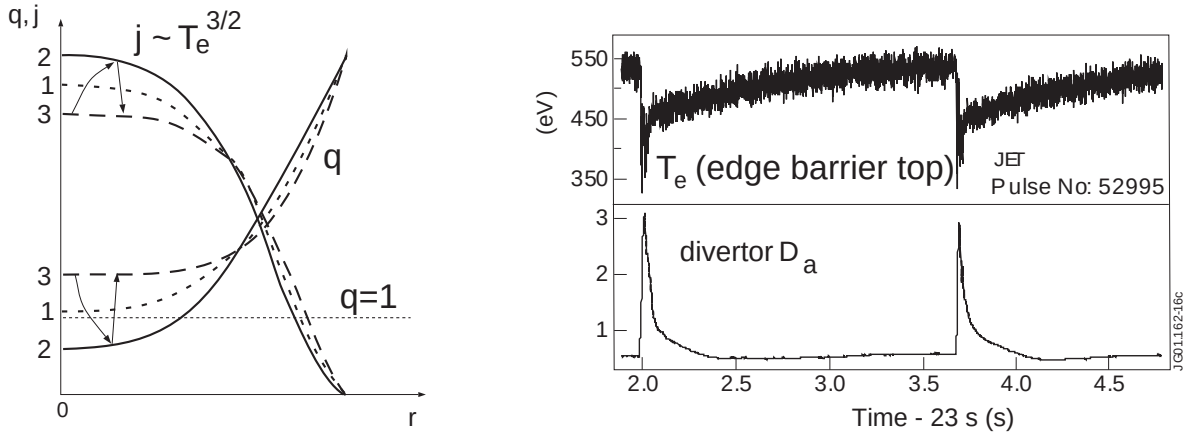

Figure 9.17: Left: Profiles of j during a sawtooth cycle.
Right: Time traces of edge electron temperature and divertor D_α showing repetitive losses at the edge and increased recycling during ELMs.

Fig. 9.17 left schematically shows the temporal evolution of the profiles of the central current density and associated safety factor q. In between sawtooth crashes, $j(0)$ (and $T_e(0)$) both rise, resulting in a drop of central q (1). Eventually $q(0)$ falls significantly below unity (2). A quick

reconnection event flattens the central j (and T_e) profile and q rises again above one; the cycle starts over.

Edge localized modes

Edge Localized Modes (ELMs) are instabilities that occur in H-mode where a transport barrier leads to a steep pressure gradient at the plasma edge. The edge temperature (shown in Fig. 9.17 right, top time trace) and edge density (not shown) increase until sudden heat and particle losses occur. These losses can be detected as a characteristic spike in the D_α line radiation intensity in the divertor due to increasing recycling particle flux and increasing ionisation because of the heat loss (Fig. 9.17 right, bottom trace).

The particle and heat losses are also seen as a sudden partial erosion of the edge temperature and density profiles (see Fig. 9.16 right). Steep profiles (A) in the edge barrier region before ELMs flatten within few 100 μs (B) and recover slowly (C) by radial heat and particle transport from within the plasma core until the maximum pressure is reached again and a new ELM occurs. This results in a characteristic oscillation cycle which repeats itself many times, often hundreds of times in one plasma discharge. Along with hydrogen, also impurities are lost which otherwise tend to accumulate in the main plasma due to the very slow out-diffusion across the H-mode transport barrier. While this feature of ELMs allows for stationary H-mode plasmas, the fast energy loss during the collapse phase can present a large peak power load to the divertor structure which can cause significant erosion of the divertor structure. For this reason, ELMs with small losses occurring at a high frequency are preferred over slow and large ELMs.

The precise physical origin of ELMs and the nature of the instability are still under investigation. The phase of enhanced transport during ELMs is characterized by a broad spectrum of MHD modes with a duration of about 100 μs. ELMs set in near values of the total edge pressure gradient where one expects *ballooning* instability, i.e. short wavelength modes driven by the pressure gradient at the magnetic low field side where the curvature of the magnetic field is not stabilizing. Fig. 9.18 left shows a stability diagram for ballooning modes. The attainable normalized pressure gradient (first stability limit) $\alpha = 2\mu_0 R\,(\nabla p)\, q_a^2/B_t^2$ increases with magnetic shear $s = (r/q)\,\mathrm{d}q/\mathrm{d}r$. Interestingly, at low shear a second stable regime can exist. Low local shear at the magnetic low field side can be produced by suitable plasma shaping or by high edge current density.

Ballooning modes are typically small scale modes, most unstable for high mode numbers and thus do not explain the large perturbations associated with ELMs. Furthermore, it is often observed experimentally that the pressure gradient saturates well before an ELM occurs indicating a more complex physics process involved. Recent models for ELMs consider a variety of instabilities, including modes driven by the large toroidal current gradient at the plasma edge. A large edge current density originates from the bootstrap current driven by the large edge pressure gradient in the H-mode transport barrier. In this picture the ELM cycle can be described as follows (see Fig. 9.18 right).

In between ELMs (1) the (normalized) pressure gradient α rises on the transport time scale (few ms for heat and particle diffusion over a few cm) until the ballooning pressure gradient limit is reached. Small scale instability leads to enhanced losses, effectively clamping the pressure gradient while the edge current density $j_\parallel$ builds up within the resistive skin time (10–100 ms for the edge of current tokamaks). Ultimately the stability limit for coupled peeling (i.e.

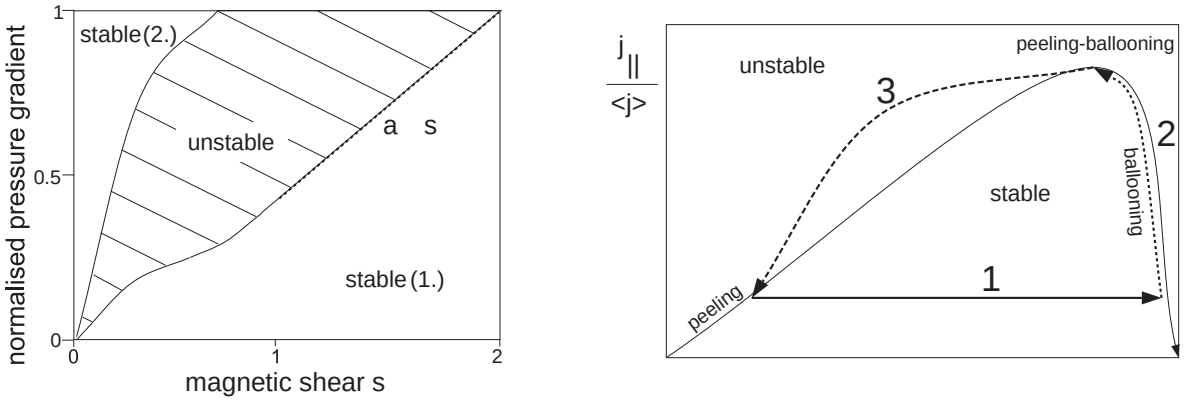

Figure 9.18: Left: Stability diagram for ballooning modes. Stability occurs for high magnetic shear (*first* stable regime) or very low magnetic shear (*second* stable regime). Access to the second stable regime is often blocked by an unstable region as shown.
Right: Schematic model for the ELM cycle: Different time scales for evolution of edge pressure gradient α and edge current density $j_\parallel$ result in several stability limitations during the cycle (see text).

medium-n kink) and ballooning modes is reached, leading to macroscopic instability, the ELM crash (3). Pressure and current are expelled and the cycle repeats itself. At present, the ELM cycle and stability limits are qualitatively and quantitatively described. Current theoretical and experimental work focuses to understand and predict the magnitude of the ELM losses and to tailor the plasma edge in order to reliably obtain ELM types with smaller energy losses.

9.3 Summary and outlook

Tokamaks can confine a nuclear fusion plasma with a combination of external toroidal field and poloidal magnetic field created by an internal plasma current. The plasma current can be driven inductively by a magnetic flux ramp created with a central solenoid which limits the duration of tokamak discharges. Non-inductive current drive by externally driven current or bootstrap (pressure gradient current) current can extend the pulse duration and possibly allow stationary tokamak operation. Heat and particle transport in tokamaks is usually dominated by fluctuating $E \times B$ convection from micro-instabilities which are driven by the strong temperature gradients. However, transport barriers at the plasma edge and in the plasma interior can be produced which reduce the heat diffusivity to near a level expected for collisional transport. The strong pressure and current density gradients present in a well-confined tokamak plasma can also drive a range of macroscopical instabilities, which often take the form of limit-cycle oscillations. Examples are sawtooth oscillations, associated with central $m = 1, n = 1$ kink modes that undergo fast reconnection events and a flattening of the central temperature, and Edge Localized Modes, driven by the steep pressure gradient of an edge transport barrier resulting in repetitive energy and particle losses. While these instabilities do not prevent stationary plasma operation and in some cases even help avoiding accumulation of impurities, other instabilities lead to severe confinement deterioration or even a termination of the plasma. The accessible tokamak parameter range is bounded by the conditions to avoid these instabilities.

The historical progress of nuclear fusion research can be measured by the fusion triple product $n\,T_i\,\tau_E$ which is plotted in Fig. 9.19 as a function of T_i for tokamaks and other magnetic con-

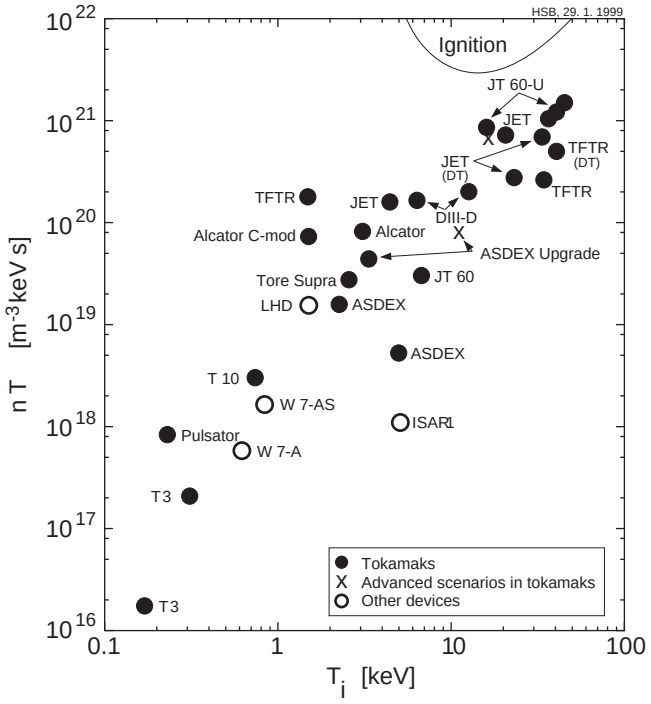

Figure 9.19: Historical performance of tokamaks and other devices, fusion triple product $n\,T_i\,\tau_E$ as a function of T_i.

finement devices (mostly stellarators). The values of $n\,T_i\,\tau_E$ have increased over several orders of magnitude in the last few decades and plasma temperatures and densities needed for a fusion reactor are obtained in contemporary tokamaks. In order to reach ignition (self-sustained plasma heating by alpha particles resulting from fusion reactions) an increase of the energy confinement time to values of several seconds is needed. This can be achieved by a larger plasma size, such as that of the planned International Thermonuclear Experimental Reactor (ITER), a tokamak with major radius $R = 6.2$, about twice as large as that of the presently largest tokamak, JET ($R = 3\,\mathrm{m}$). The step to a reactor-scale experiment with large fusion power and significant neutron production will allow to study dominant plasma heating by fast alpha particles, confinement and plasma-wall interaction, and test first-wall and low-activation structural materials needed for an integrated power plant concept. Alternative confinement concepts such as stellarators will further develop and demonstrate their attractive potential in new experiments, for example for steady state operation. Nevertheless, one can expect that tokamaks will remain at least for some foreseeable future the reliable *workhorse* and universal test-bed for magnetic fusion research they have been in the last three decades.

Further reading

General

- M. Kaufmann, Plasmaphysik und Fusionsforschung (in German), Teubner Verlag, Stuttgart, Leipzig, Wiesbaden 2002, ISBN 3-519-00349-X.

- F.F. Chen, Introduction to Plasma Physics, Vol. 1, second edition, Plenum Press, New York 1984, ISBN 0-306-41332-9.

- R.J. Goldston, P.H. Rutherford, Introduction to Plasma Physics, IOP Publishing, Bristol 2000, ISBN 0-750-30183-X.
- K. Miyamoto, Plasma Physics for Nuclear Fusion, MIT Press, Cambridge 1989, ISBN 0-262-13237-0.
- J.A. Wesson, Tokamaks, Oxford University Press 1987, ISBN 0-19-856328-0.

Specific topics

- F. Ryter et al., Empirical studies of electron transport, Plasma Phys. Control. Fusion **43** (2001) A323.
- R.J. Groebner, An emerging understanding of H-mode discharges in tokamaks, Phys. Fluids **B 5** (1993) 2343.
- J.W. Connor and H.R. Wilson, A review of theories of the L-H transition, Plasma Phys. Control. Fusion **42** (2000) R1.
- H. Zohm, Edge Localized Modes, Plasma Phys. Control. Fusion **38** (1996) 105.
- J.W. Connor, A review of models for ELMs, Plasma Phys. Control. Fusion **40** (1998) 191.
- H.R. Wilson et al., Ideal magnetohydrodynamic stability of the tokamak high-confinement edge region, Physics of Plasmas **6** (1999) 1925.
- J.P. Freidberg, Ideal Magnetohydrodynamics, Plenum Press, New York 1987, ISBN 0-306-42512-2.
- D. Biskamp, Nonlinear Magnetohydrodynamics, Cambridge University Press, Cambridge 1993, ISBN 0-521-59918-0.
- ITER-Team, ITER Physics Base, Nuclear Fusion **39** (1999) 2137-2638,
- R. Aymar et al., The ITER design, Plasma Phys. Control. Fusion **44** (2002) 519 and `http://www.iter.org`.
- ASDEX Upgrade: `http://www.aug.ipp.mpg.de`.

Chapter 10

Computational plasma physics

Frank Jenko

10.1 Introductory remarks

10.1.1 A bit of a philosophical foreword

As a physics student, one is regularly confronted with homework problems which share one important property: They are exactly solvable by analytical methods. It is therefore tempting to believe that this is also true for every-day physics research. However, the number of important open questions which fall into that category is in fact rather limited. Moreover, towards the end of the 20th century, there has been kind of a paradigm shift in the physics community. Whereas before, a central goal was to discover the basic constituents of our material world and their interaction rules, today a growing number of physicists is concerned about the large variety of complex phenomena arising from the interplay of these very constituents. Some areas of research which exemplify this trend are

- biophysics,
- condensed matter physics,
- material science,
- plasma physics.

Even if one idealizes and simplifies the physical description of many respective systems, one is often left with some of the following irreducible ingredients

- high dimensionality of the problem,
- coupling of disparate spatio-temporal scales,
- symmetry breaking (translational, rotational etc.),
- nonlinearity.

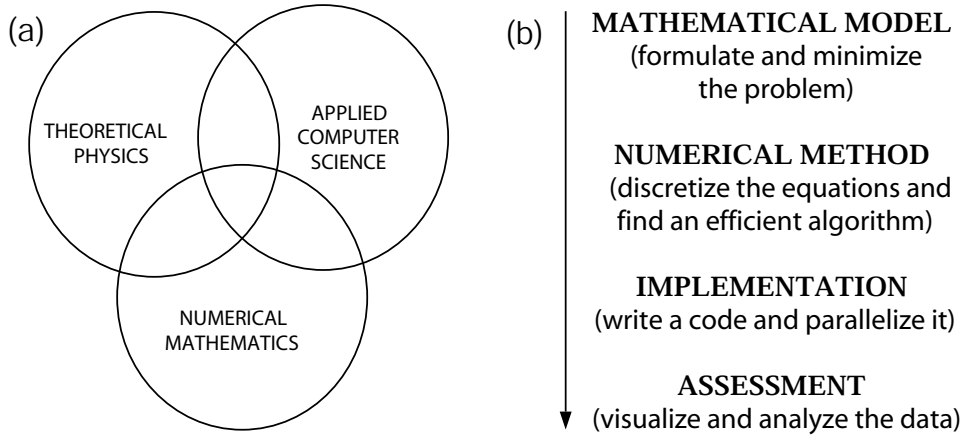

Figure 10.1: On the nature of computational physics: (a) It combines various aspects from physics, mathematics, and computer science and (b) it usually works as a four-stage process.

The latter effect is of special importance, since it implies that the superposition principle and most standard techniques (like Fourier transforms) cannot be applied. Not surprisingly, there are only very few nonlinear equations which can be solved exactly (among these exceptions is the so-called Burgers equation, a one-dimensional relative of the well-known Navier-Stokes equation). Usually, progress in such cases can often only be achieved by resorting to computational solution methods. Given the impressive and steady increase of computer power as well as the progress in trying to find new and more effective numerical methods over the last several decades, the number of problems which may be addressed this way has been increasing continuously. Therefore, it is certainly fair to say that computers play a crucial role in present-day physics research, and will do so even more in the years to come.

10.1.2 The nature of computational physics

As has often been said, modern physics (and neighbouring sciences) should be viewed as being tri-partite: Studied by experimental, theoretical and computational physicists. Each of these subgroups has its own specific set of tools, techniques, and approaches, associated with certain advantages and limitations. The goal of computational physics is to explore computationally the properties of mathematical models of physical systems, thus providing deeper understanding and predictive or interpretative capability. Thus one is enabled to address questions which lie beyond analytical or experimental possibilities. Model equations which are inaccessible to mathematical physics can be solved. In addition, models can be modified and diagnosed in more or less arbitrary ways. The main disadvantages, on the other hand, are that one can only study specific situations - not derive general formulas, and that the degree of realism which can be achieved is often limited by the available computer resources. In practice, computational physics is used to inspire or test theories, and to predict or interpret experiments. It can be a very powerful way to identify the physical mechanisms underlying certain phenomena. In the central process of performing and analyzing numerical experiments, intuition and insight are both required and trained.

Another characteristic feature of computational physics is that it is a cross-disciplinary effort. This makes it a challenging but also fascinating field of study. It basically draws from three different sources

1. theoretical physics,
2. numerical mathematics, and
3. applied computer science

(see Fig. 10.1(a)). In order to solve a particular problem one is interested in, one typically has to go through a series of four stages (see Fig. 10.1(b)). First, one has to find an appropriate mathematical model which describes the system under consideration as simply as possible but also as detailed as necessary. In this context, one is often able to greatly reduce the problem size, e.g., by removing unnecessary spatio-temporal scales. Second, one has to discretize the basic equations and find an efficient algorithm to solve the resulting equations. Third, the numerical method has to be implemented as a simulation code. In many cases, the latter also has to be parallelized so that it can be run on massively parallel computers. Fourth, the output data has to be visualized and analyzed. At this stage, a lot of experience and physical insight is needed. In all four stages, the main goal is to minimize the effort and to maximize the accuracy. But in the end it boils down to asking the right questions and drawing the right conclusions.

After these introductory remarks, I would now like to turn to a very practical question, namely: How are differential equations solved on a computer? This issue turns out to be at the heart of many physical problems. At the same time, one can thus get a taste of the beauty and power of computational physics.

10.2 Solving differential equations on a computer

10.2.1 Ordinary differential equations

A classic application of computational physics is the solution of ordinary differential equations which occur in numerous contexts, e.g., in Newtonian mechanics. Here, the task usually is to compute the solution $\boldsymbol{x}(t)$ of the initial value problem

$$\dot{\boldsymbol{x}} = \boldsymbol{f}(\boldsymbol{x},t)\,, \quad \boldsymbol{x}(t=0) = \boldsymbol{x}_0 \tag{10.1}$$

where the dot denotes a time derivative. For simplicity, let us consider the scalar version of this equation

$$\dot{x} = f(x,t)\,, \quad x(t=0) = x_0\,. \tag{10.2}$$

It will be straightforward to generalize our results to the multidimensional case later. Now, it is clear that on a computer, we are only able to work with a finite number of points in time. In other words, we have to discretize the continuous time domain. Let us assume that the distance between two consecutive time points is constant, $h = t_{n+1} - t_n = \text{const}$, and let us denote the approximative value of $x(t)$ at time $t = t_n$ by x_n. In the following, we will discuss several numerical schemes which represent discretized versions of (10.2).

Euler's algorithm

A very well-known and simple discretization method may be obtained via the Taylor expansion

$$x_{n+1} = x_n + h\dot{x}(t_n) + \mathcal{O}(h^2) = x_n + h\,f(x_n,t_n) + \mathcal{O}(h^2) \tag{10.3}$$

which leads to

$$\frac{x_{n+1}-x_n}{h} \approx f(x_n,t_n)\ . \tag{10.4}$$

Obviously, the discretization error is of order h, and (10.4) turns into (10.2) for $h \to 0$. (10.4) can also be rewritten as

$$x_{n+1} \approx x_n + h\, f(x_n,t_n)\ . \tag{10.5}$$

In this form, it is apparent that Euler's algorithm is an *explicit* scheme, i.e., x_{n+1} is given explicitly (as opposed to implicitly) in terms of known quantities. Together with the fact that it can be easily implemented, this makes it an attractive scheme for *quick-and-dirty* investigations of simple systems. As we will see, however, it is usually better to use slightly more complicated methods which yield far better results. The generalization of Euler's algorithm to second order will be discussed next.

Heun's method

We begin by extending (10.3) to

$$x_{n+1} = x_n + h\dot{x}(t_n) + \frac{h^2}{2}\ddot{x}(t_n) + \mathscr{O}(h^3)\ , \tag{10.6}$$

where

$$\dot{x}(t_n) = f(x_n,t_n) \tag{10.7}$$

and

$$\begin{aligned} \ddot{x}(t_n) &= \frac{df(x_n,t_n)}{dt} = \dot{x}(t_n)\frac{\partial f(x_n,t_n)}{\partial x} + \frac{\partial f(x_n,t_n)}{\partial t} = \\ &= f(x_n,t_n)\frac{\partial f(x_n,t_n)}{\partial x} + \frac{\partial f(x_n,t_n)}{\partial t}\ . \end{aligned} \tag{10.8}$$

This expression can be rewritten by means of the Taylor expansion

$$\begin{aligned} &f[x_n + h\, f(x_n,t_n), t_n + h] = \\ &= f(x_n,t_n) + h\, f(x_n,t_n)\frac{\partial f(x_n,t_n)}{\partial x} + h\frac{\partial f(x_n,t_n)}{\partial t} + \mathscr{O}(h^2)\ . \end{aligned} \tag{10.9}$$

From this equation, it follows that

$$\ddot{x}(t_n) = \frac{f[x_n + h\, f(x_n,t_n), t_n + h] - f(x_n,t_n)}{h} + \mathscr{O}(h)\ . \tag{10.10}$$

From (10.6), (10.7), and (10.10), we thus obtain

$$x_{n+1} \approx x_n + \frac{h\, f(x_n,t_n) + h\, f[x_n + h\, f(x_n,t_n), t_n + h]}{2}\ , \tag{10.11}$$

where the discretization error is of order h^2. In contrast to Euler's algorithm, we now have to evaluate the prescribed function f not once but twice per time step. Thus, the computational cost is about twice as big. However, this overhead is usually overcompensated by the gain in accuracy for a given time step h. Therefore, it is actually advantageous to increase the order of the scheme – at least up to a certain degree.

General structure of Runge-Kutta schemes

The two schemes just described are examples of a wider class of numerical methods called Runge-Kutta schemes. They can be cast in the form

$$x_{n+1} \approx x_n + h \sum_{i=1}^{s} \alpha_i k_i \,, \tag{10.12}$$

where

$$k_i = f\left(x_n + h \sum_{j=1}^{s} \nu_{ij} k_j, t_n + \beta_i h \right) \tag{10.13}$$

for $1 \leq i \leq s$, and s denotes the order of the discretization method. A particular scheme is thus defined by the real coefficients α_i, β_i, and ν_{ij}. However, virtually all existing Runge-Kutta methods adopt the convention

$$\beta_i = \sum_{j=1}^{s} \nu_{ij} \tag{10.14}$$

such that the β_i's are given in terms of the ν_{ij}'s. If $\nu_{ij} = 0$ for $j \leq i$, then k_i can be computed in an explicit way from $k_1, \ldots, k_{i-1}$, yielding so-called explicit Runge-Kutta (ERK) schemes. Examples of ERK methods are given by (10.5) and (10.11) which are recovered, respectively, for $s = 1$, $\alpha_1 = 1$ and for $s = 2$, $\alpha_1 = \alpha_2 = 1/2$, $\nu_{21} = 1$. Another very widely used ERK method is the 4th order scheme defined by

$$\begin{aligned} &s = 4 \,, \quad \alpha_1 = \alpha_4 = 1/6 \,, \quad \alpha_2 = \alpha_3 = 1/3 \,, \\ &\nu_{21} = \nu_{32} = 1/2 \,, \quad \nu_{31} = \nu_{41} = \nu_{42} = 0 \,, \quad \nu_{43} = 1 \,. \end{aligned} \tag{10.15}$$

Like every ERK scheme, it can be derived by means of Taylor expansions. However, it should be noted in this context that the choice of the coefficients α_i and ν_{ij} is usually not unique for a given order s. Thus, there is a lot of flexibility in deriving ERK schemes, and they can be optimized with respect to various considerations. In the literature, one finds certain standard choices, like (10.15), which are known to work accurately and robustly under most circumstances. As mentioned before, the generalization of (10.12) and (10.13) to the multi-dimensional case is not hard. One simply has to replace the scalar quantities x, f, and k by vectors. Of course, there are also many other time discretization schemes, but it is beyond the scope of an introduction to computational (plasma) physics like the present one to provide a broad overview.

In the following, we will consider a particular application which is very common in the field of plasma physics, namely the motion of charged particles in prescribed electric and/or magnetic fields. This turns out to be a good example of how to solve ordinary differential equations on a computer.

10.2.2 Example: complex particle trajectories

In this section, we will consider the motion of a particle of (positive) charge q and mass m in a static and homogeneous magnetic field $\boldsymbol{B} = B\boldsymbol{z}$ (here, $\boldsymbol{z}$ is the unit vector in the z direction). For simplicity, we will neglect the motion parallel to $\boldsymbol{B}$ and concentrate on the dynamics in the

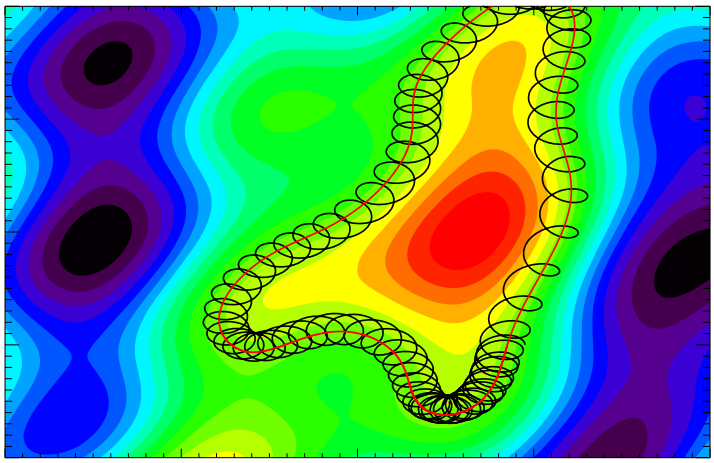

Figure 10.2: Charged particle in a homogeneous magnetic field (perpendicular to the plane) and a random electrostatic potential obtained via (10.22). The particle orbit and the trajectory of the gyrocenter are shown, respectively, as black and red lines.

perpendicular (x,y) plane. In the presence of a prescribed, space-time dependent electrostatic potential $\phi(x,y,t)$, the particle's equation of motion then reads

$$\begin{aligned} \dot{\boldsymbol{x}}(t) &= \boldsymbol{v}(t) \\ \dot{\boldsymbol{v}}(t) &= (q/m)\,[\boldsymbol{v}(t)\times\boldsymbol{B} - \nabla\phi(\boldsymbol{x}(t),t)] \end{aligned} \tag{10.16}$$

with $\boldsymbol{x} = (x,y)$ and $\boldsymbol{v} = (v_x, v_y)$. This seemingly simple equation can lead to very interesting phenomena which are inaccessible to an analytic approach.

Normalization of the basic equations

In the context of computational physics, it is common to work with the basic equations in a dimensionless form. We will do the same here. If the electrostatic potential vanishes, the particle will merely gyrate about a central field line with the gyrofrequency $\Omega = qB/m$. It is therefore natural to normalize time according to

$$\Omega t \to t\ . \tag{10.17}$$

Moreover, as long as the potential is not too large, the velocity of the particle will always stay close to its initial value v_0. We thus choose

$$\boldsymbol{v}/v_0 \to \boldsymbol{v}\ . \tag{10.18}$$

Now, from Ω and v_0, one can construct a length scale (gyroradius) via $\rho = v_0/\Omega$. This scale can be used to normalize the spatial scales according to

$$\boldsymbol{x}/\rho \to \boldsymbol{x}\ . \tag{10.19}$$

It might be useful to point out that this normalization also affects the spatial derivatives, $\rho\nabla \to \nabla$. Finally, we have

$$\frac{q\phi}{mv_0^2} \to \phi\ , \tag{10.20}$$

i.e., the particle's potential energy is measured with respect to its kinetic energy. These normalizations lead to the dimensionless equations

$$\begin{aligned} \dot{\boldsymbol{x}}(t) &= \boldsymbol{v}(t) \\ \dot{\boldsymbol{v}}(t) &= \boldsymbol{v}(t) \times \boldsymbol{z} - \nabla\phi(\boldsymbol{x}(t),t) \end{aligned} \tag{10.21}$$

which constitute a useful basis for numerical studies.

Particles in a random potential

The prescribed electrostatic potential can be created by a superposition of a large number N of plane waves

$$\phi(\boldsymbol{x},t) = A\sum_{i=1}^{N} \sin(\boldsymbol{k}_i \cdot \boldsymbol{x} + \omega_i t + \varphi_i) \; . \tag{10.22}$$

Since the wave vectors $\boldsymbol{k}_i$, frequencies ω_i, and phases φ_i are all chosen randomly (for details about how this is done in a simulation code, the reader is referred to the literature), the potential also has a random character. Such a space-time dependent potential is reminiscent of the fluctuations created by plasma microturbulence, a phenomenon which will be discussed in more detail later. A typical snapshot is shown in Fig. 10.2.

The initial value problem associated with (10.21) can certainly be written in the form of (10.1). Therefore, the ERK schemes introduced above can be used to obtain numerical solutions of this system of four (coupled) ordinary differential equations. From Fig. 10.3, one can infer that the fourth order ERK scheme defined by (10.15) is far superior to Euler's algorithm. For the same number of time steps per gyration, the accuracy of the former exceeds that of the latter by many orders of magnitude. This easily outweighs the mild increase of computational cost by roughly a factor of four. This is a classic example of how the choice of an algorithm can improve a simulation. It is thus worth remembering that computational physics is *not* primarily about using the fastest and biggest computers in kind of a *brute force* approach, but rather about using one's resources as effectively as possible.

A typical trajectory for a static potential in shown in Fig. 10.2. Here, we have again employed the fourth order ERK scheme. Obviously, the particle's gyrocenter simply follows equipotential lines in this case while the motion in time dependent potentials tends to be much more random. The observation that the particle's trajectory seems to consist of a mere superposition of a simple gyromotion and a gyrocenter drift suggests that the former may be removed from the basic equations analytically. This is indeed possible as will be shown next, leading to very significant savings in computational cost.

The drift approximation

The idea to decompose the motion of charged particles in prescribed magnetic and/or electric fields into a gyromotion and a gyrocenter drift was first put forward by the Nobel laureate Hannes Alfvén in the 1940's. Here, we shall restrict to the simple quasi-two-dimensional situation outlined above. Differentiating (10.21) with respect to time and then re-inserting it on the right-hand side yields the second-order ordinary differential equation

$$\boldsymbol{v}(t) + \ddot{\boldsymbol{v}}(t) = \boldsymbol{E}(\boldsymbol{x}(t),t) \times \boldsymbol{z} + \dot{\boldsymbol{E}}(\boldsymbol{x}(t),t) \equiv \boldsymbol{v}_E(t) + \boldsymbol{v}_P(t) \; , \tag{10.23}$$

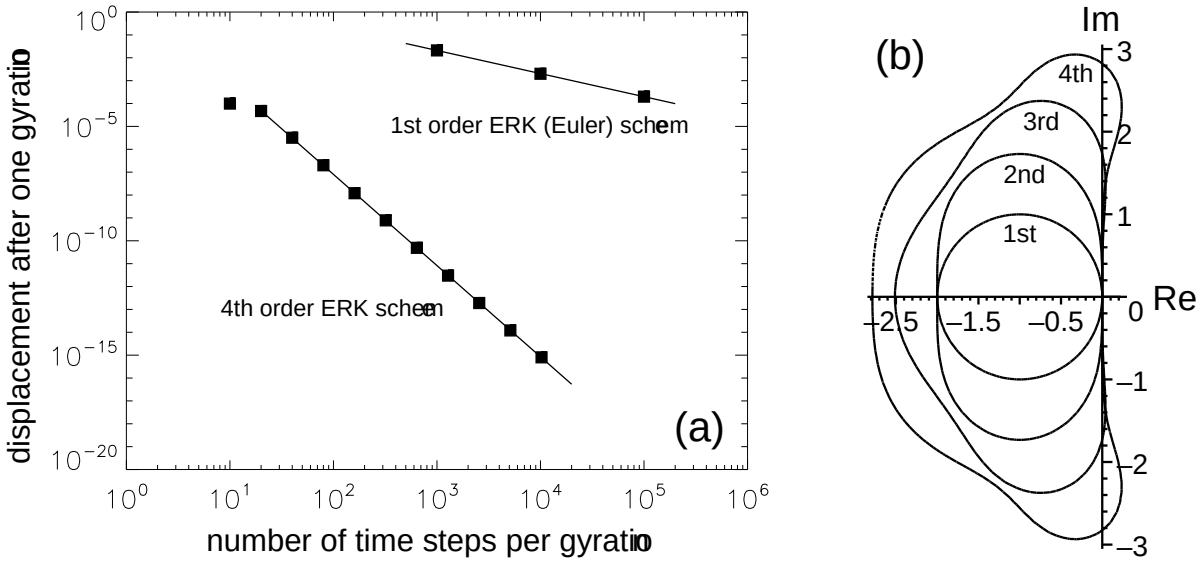

Figure 10.3: Properties of low-order explicit Runge-Kutta (ERK) schemes: (a) Numerical error for a given test problem (charged test particle in a homogeneous magnetic field) and (b) linear stability regions in the complex plane.

where $\boldsymbol{v}_E$ and $\boldsymbol{v}_P$ are called, respectively, the $\boldsymbol{E}\times\boldsymbol{B}$ drift and the polarization drift, and $\boldsymbol{E}=-\nabla\phi$ is the electric field. Note that the time derivative $\dot{\boldsymbol{E}}$ is to be interpreted as a convective derivative here: $\dot{\boldsymbol{E}}=(\partial_t+\boldsymbol{v}\cdot\nabla)\boldsymbol{E}$. This means, it is to be computed in a Lagrangian (co-moving) frame of reference. The general solution of (10.23) is given by the sum (superposition) of the solution of the homogeneous part, $\boldsymbol{v}(t)+\ddot{\boldsymbol{v}}(t)=0$, which describes the gyromotion, and a specific solution of the entire equation. For $\omega\ll 1$ (in normalized units), the latter is simply determined by the $\boldsymbol{E}\times\boldsymbol{B}$ drift velocity $\boldsymbol{v}_E$. Since in practice, the frequencies of turbulent fluctuations are clearly below the gyrofrequency, this approximation is well justified. In all of these considerations, one implicitly assumes that the gyroradius is small compared to the typical wavelengths of the fluctuations, and that the amplitude of the electrostatic potential is not too large. Under many circumstances, these conditions are fulfilled.

The bottom line of the above calculation is that one can analytically remove the fast gyromotion from the problem, leaving only the slow gyrocenter drift motion to be computed. This has, of course, great computational advantages, because the number of time steps per time unit can be reduced dramatically. Nevertheless, such a gyrocenter simulation captures the particle dynamics very well as is shown in Fig. 10.2. The present system is a nice example of a general idea: One should always try to minimize the problem as much as possible before one starts to consider specific numerical issues. This will become even clearer in the next section when we will discuss large-scale applications in plasma physics.

10.2.3 Partial differential equations

Since most theories in physics are actually based on *partial* differential equations, we should also spend some time considering their numerical solution. Fortunately, many insights gained in the context of ordinary differential equations carry over to that case. For concreteness, let

us assume we want to solve the initial value problem

$$\frac{\partial g(y,t)}{\partial t} + v\frac{\partial g(y,t)}{\partial y} = 0\,, \quad g(y,0) = G(y) \tag{10.24}$$

whose exact solution is known to be

$$g(y,t) = G(y - vt)\,. \tag{10.25}$$

Physically, this means that the initial function $G(y)$ is advected in the positive y direction with the constant speed v.

Method of lines

Although there also exist numerical methods which treat time and space dimensions together, probably the most common case is that a given partial differential equation is *first* discretized in space and thus converted to a set of coupled ordinary differential equations, and *then* solved according to time discretization methods like those mentioned before. This two-step approach is often called the *method of lines*. It allows for great flexibility and usually yields satisfactory results. Here, the first step of spatial discretization can be done in a variety of ways. In this short introduction, we will focus on only two of them: Finite difference methods and (pseudo-) spectral methods.

Finite difference methods

As an example of numerical differentiation we will first consider the first derivative of a scalar function $g(y)$, assuming that the constant grid spacing is given by the parameter λ. A Taylor expansion about y_m then yields

$$g_{m\pm1} = g_m \pm \lambda\, g'(y_m) + \frac{\lambda^2}{2} g''(y_m) \pm \frac{\lambda^3}{6} g'''(y_m) + \frac{\lambda^4}{24} g''''(y_m) + \mathcal{O}(\lambda^5)\,, \tag{10.26}$$

where g_m denotes the approximative value of $g(y)$ at $y = y_m$. From this equation, it immediately follows that

$$g'(y_m) = \frac{g_{m+1} - g_{m-1}}{2\lambda} + \mathcal{O}(\lambda^2)\,. \tag{10.27}$$

Hence we have found a second order discretization of g'. This means that the difference between the exact value and the numerical approximation will descrease as λ^2 for $\lambda \to 0$. Higher order methods can be constructed in the following way. Using the Taylor expansion

$$g_{m\pm2} = g_m \pm 2\lambda\, g'(y_m) + 2\lambda^2 g''(y_m) \pm \frac{4\lambda^3}{3} g'''(y_m) + \frac{2\lambda^4}{3} g''''(y_m) + \mathcal{O}(\lambda^5) \tag{10.28}$$

it is not hard to show that there exists a (unique) linear combination of $g_{m\pm2}$, $g_{m\pm1}$, and g_m which approximates g' such that the error is of 4th order. The result of this procedure is

$$g'(y_m) = \frac{g_{m-2} - 8g_{m-1} + 8g_{m+1} - g_{m+2}}{12\lambda} + \mathcal{O}(\lambda^4)\,. \tag{10.29}$$

By increasing the *stencil* to also include $g_{m\pm3}$, one can derive a sixth order scheme, and so on.

If one wants to assess the accuracy of a given discretization method, it is useful to do the following simple analysis. Let us consider a plane wave perturbation of the form $g(y) \propto \exp(iky)$. Its exact first derivative is given by $g'(y) = ikg(y)$. On a discrete grid, however, we have $g_m \propto \exp(iky_m)$ where $y_m = m\lambda$. Consequently, we obtain

$$\frac{g'(y_m)}{ikg(y_m)} = \frac{\exp(ik\lambda) - \exp(-ik\lambda)}{2ik\lambda} = \frac{\sin(k\lambda)}{k\lambda} = 1 - \frac{x^2}{6} + \mathscr{O}(x^4) \,. \tag{10.30}$$

From this equation, it is clear that the discretized derivative is only accurate for $k\lambda \ll 1$. In the limit $k\lambda \to 0$, one recovers the exact result, but as $k\lambda$ increases, the finite difference approximation gets worse and worse. This of course means that only wavelengths which clearly exceed the grid spacing are well represented, whereas short wavelengths are not. This problem can be somewhat diminished by employing higher order methods. E.g., the fourth order method defined by (10.29) yields

$$\frac{g'(y_m)}{ikg(y_m)} = \frac{8\sin(k\lambda) - \sin(2k\lambda)}{6k\lambda} = 1 - \frac{x^4}{30} + \mathscr{O}(x^6) \,. \tag{10.31}$$

Obviously, this scheme does somewhat better than the second order scheme. The basic problem can not be eliminated this way, however. One way out is to work in spectral (usually: Fourier) space. This approach shall be described next.

(Pseudo-) spectral methods

The solution of the linear partial differential (10.24) in a finite spatial domain (of size L) with periodic boundary conditions can also be represented as a Fourier series

$$g(y,t) = \sum_k \mathscr{G}_k(t) \exp(iky) \,, \tag{10.32}$$

where

$$\mathscr{G}_k(t) \equiv L^{-1} \int_0^L g(y,t) \exp(-iky)\, dy \tag{10.33}$$

and the wavevectors k are quantized in units of $2\pi/L$. The time evolution of each Fourier component $\mathscr{G}_k(t)$ is then determined by

$$\dot{\mathscr{G}}_k(t) + ikv\mathscr{G}_k(t) = 0 \,. \tag{10.34}$$

Although in this simple case, the solution of (10.34) can also be given explicitly [$\mathscr{G}_k(t) \propto \exp(-ikvt)$], alternatively one could use an ERK scheme to solve it numerically. In contrast to a finite difference discretization, every wavelength that is kept in the computation is represented exactly here (up to round-off errors, of course). In general, spectral representations are often advantageous as long as the PDE's coefficients do not depend on a particular coordinate. In this case, one would get convolutions in spectral space which tend to make the numerical scheme very inefficient.

Another situation which leads to similar problems is when the function $\boldsymbol{f}$ in (10.1) contains a nonlinearity. Again, such a term would lead to expensive convolutions in spectral space.

This can be seen as follows. According to (10.32), the product of two space-time dependent functions is given by

$$p(y,t) \equiv g(y,t)\,h(y,t) = \sum_{k'} \mathscr{G}_{k'}(t)\,\exp(ik'y) \sum_{k''} \mathscr{H}_{k''}(t)\,\exp(ik''y)\;, \tag{10.35}$$

and one has

$$\mathscr{P}_k = \sum_{k',k''} \mathscr{G}_{k'}(t)\,\mathscr{H}_{k''}(t) \int \exp(ik'y + ik''y - iky)\,dy/L = \sum_{k'} \mathscr{G}_{k'}(t)\,\mathscr{H}_{k-k'}(t)\;. \tag{10.36}$$

Such convolutions can be avoided, however, by means of the following procedure. All the linear terms are computed in spectral space. Then, one uses spectral (e.g., fast Fourier) transforms to return to real space. Here, the nonlinear terms reduce to mere multiplications. After this is done, one returns to spectral space and resumes the computation. Such an approach is called pseudo-spectral for obvious reasons. Although this method is used very frequently in practice, it also has a drawback. In the course of treating the nonlinear term in real space, one typically creates subgrid-scale perturbations which are then reinterpretated in spectral space as long-wavelength perturbations. (Recall the use of Bravais lattices in solid state physics in order to avoid similar problems.) In order to avoid such unphysical *aliasing* effects, one has to employ dealiasing methods many of which consist of zeroing out dangerous high k modes. Thus the efficiency of the simulation is reduced. Still, (pseudo-)spectral methods are very popular, and some of the most demanding present-day applications are based (at least in part) on them.

Linear stability analysis

If the function $\boldsymbol{f}$ is only linear in $\boldsymbol{x}$ and independent of t, (10.1) can be written as

$$\dot{\boldsymbol{x}} = \mathscr{M}\,\boldsymbol{x} \tag{10.37}$$

where $\mathscr{M}$ is a constant matrix. (10.34) is one such example. Here, $\boldsymbol{x}(t) \to \mathscr{G}_k(t)$ and $\mathscr{M} \to ikv$. Another example can be obtained if one uses (10.27) to the discretize (10.24) in space. Then $\boldsymbol{x}(t) \to \{g_m(t)\}$ and $\mathscr{M}$ is a square matrix with non-zero entries only in the secondary diagonals (up to boundary condition effects). The discretized version of (10.37) has the exact solution

$$\boldsymbol{x}_{n+1} = \exp(\mathscr{M}h)\,\boldsymbol{x}_n\,. \tag{10.38}$$

On the other hand, the ERK schemes described by (10.5) and (10.11) lead, respectively, to the expressions

$$\boldsymbol{x}_{n+1} = [\boldsymbol{1} + \mathscr{M}h]\,\boldsymbol{x}_n \tag{10.39}$$

and

$$\boldsymbol{x}_{n+1} = [\boldsymbol{1} + \mathscr{M}h + (\mathscr{M}h)^2/2]\,\boldsymbol{x}_n\;, \tag{10.40}$$

where $\boldsymbol{1}$ denotes the unit matrix. Obviously, these are low order approximations to (10.38).

Now, as long as all eigenvalues z of the matrix $\mathscr{M}h$ satisfy the constraint $|1+z| \le 1$ or $|1 + z + z^2/2| \le 1$, the series of $\boldsymbol{x}_n$'s is bounded. Otherwise, it may diverge. In case the system's dynamics is such that there is no *physical* diverence, a violation of these constraints amounts to a *numerical* instability. As it turns out, every ERK scheme can become linearly unstable if the time step h is chosen too large. The scheme is stable if and only if the cloud of eigenvalues of

$\mathscr{M}h$ lies completely within a certain stability region in the complex plane. Examples for such stability regions for low order ERK schemes are shown in Fig. 10.3. A peculiar situation arises when one is trying to solve (10.34). Since the eigenvalue lies on the imaginary axis, but the stability regions of the first and second order ERK schemes do not contain purely imaginary values, one would obtain a numerical instability for *any* choice of the time step h. In other words, one would have to use a third or even fourth order ERK scheme to solve (10.34). But even then, the time step is limited by the so-called Courant condition $kvh < \mathscr{C}$ where $\mathscr{C} \sim 1$. Physically, this means that the advection process described by (10.24) may not lead to a fluid displacement per time step of more than about one wavelength. Thus if high wavenumbers are kept or if large velocities are considered, the time step has to be reduced. Such stability constraints are of great practical significance.

With these comments, I would like to conclude this part of the presentation and move on to two sprecific applications in plasma physics which show how the above methods and principles play out in real life situations. Due to space constraints, I will restrict to some key points.

10.3 Applications in plasma physics

10.3.1 Nonlinear gyrokinetics: microturbulence

Since fusion plasmas are very hot (about 10^6 times room temperature) and at the same time very dilute (about 10^{-6} times atmospheric density), Coulomb scattering events are pretty rare in such systems. Consequently there exists a large number of kinetic effects which cannot be captured accurately by fluid theory, and the plasma has to be described in terms of single-particle distribution functions $F_\sigma(\boldsymbol{x},\boldsymbol{v},t)$ (where σ is the particle species label) whose time evolution is determined by the collisionless Boltzmann (or Vlasov) equation

$$\frac{\partial F_\sigma}{\partial t} + \boldsymbol{v}\cdot\nabla_x F_\sigma + \frac{q_\sigma}{m_\sigma}(\boldsymbol{E}+\boldsymbol{v}\times\boldsymbol{B})\cdot\nabla_v F_\sigma = 0\,. \tag{10.41}$$

The plasma-induced electric and magnetic fields occuring in these equations need to be calculated self-consistently by means of the pre-Maxwell equations

$$\nabla\cdot\boldsymbol{E} = \rho/\varepsilon_0\,, \quad \nabla\times\boldsymbol{B} = \mu_0\boldsymbol{j}\,, \quad \nabla\times\boldsymbol{E} = -\partial_t\boldsymbol{B}\,, \quad \nabla\cdot\boldsymbol{B} = 0\,. \tag{10.42}$$

Here, the displacement current has been neglected, such that the equations are Galileian invariant and electromagnetic waves are absent. The charge and current densities are calculated from the distribution functions via

$$\rho = \sum_\sigma q_\sigma \int F_\sigma\, d^3v\,, \quad \boldsymbol{j} = \sum_\sigma q_\sigma \int \boldsymbol{v} F_\sigma\, d^3v\,. \tag{10.43}$$

In addition, external magnetic and/or electric fields may be applied. Eq. (10.41) to (10.43) form a closed set of integro-differential equations in six-dimensional phase space plus time. Since the fields scale linearly with the distribution functions, the last term on the left-hand side of (10.41) is nonlinear.

In principle, (10.41) to (10.43) capture a large number of interesting phenomena in fusion plasmas, including microturbulence. (The latter is generally held responsible for the substantial heat and particle transport across flux surfaces which is observed in experiments.) Solving

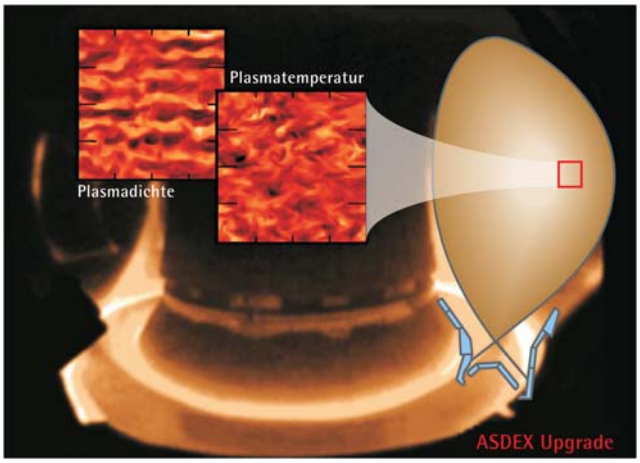

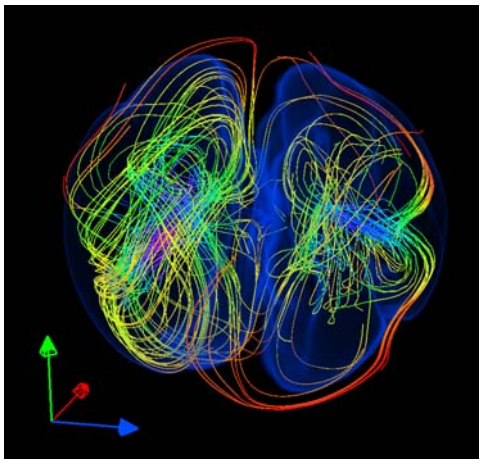

Figure 10.4: Left: Micro-scale plasma turbulence in fusion experiments leads to large cross-field fluxes of particles and heat. Shown are simulation data for the ASDEX Upgrade tokamak at IPP Garching obtained from a code called GENE.
Right: Snapshot of the velocity field in a turbulent dynamo in spherical geometry. This simulation is supposed to mimick real flows in the Madison Dynamo Experiment and has been obtained from a nonlinear MHD code named DYNAMO.

this set of nonlinear equations directly is computationally prohibitive, however. Fortunately, it is possible to simplify the problem in various ways if one is interested in microturbulence computations:

- Since the gyrofrequency clearly exceeds the turbulent frequencies, the *drift approximation* may be applied. Thus the perpendicular particle velocities are given in terms of the $\boldsymbol{E} \times \boldsymbol{B}$ drift, the curvature drift, and the ∇B drift. At the same time, Langmuir waves are removed from the system, and with them small spatio-temporal scales which are irrelevant to the turbulence.

- Given the fact that the turbulent fluctuations tend to be extremely elongated along magnetic field lines, it is very useful to use *field-aligned coordinate systems*. Thus, it suffices to employ some 20 grid points over distances of 10 m or more in the parallel direction, reducing the computational cost by a factor of 10^2–10^3.

- Since the typical perpendicular correlation lengths are of the order of 10-20 ion gyroradii (a few cm), it is usually not necessary to treat the entire torus in a single simulation. Instead, the simulation domain can be reduced to a *flux tube*. This allows to use fixed gradients which (on average) are not altered by the turbulence, obtaining statistically stationary states.

These gyroaveraged kinetic equations in field-aligned flux tubes can then be solved numerically according to the schemes outlined above. As an example, I would like to mention the gyrokinetic turbulence code GENE which has been developed at IPP over the last couple of years. It is based on the method of lines, employing a third order ERK scheme and a mixed pseudo-spectral (perpendicular directions) and finite difference (parallel direction and velocity space) discretization in phase space. GENE runs efficiently on several massively parallel machines and has been benchmarked successfully both in the linear and in the nonlinear regime.

Moreover, it has turned out to be a very useful tool for plasma microturbulence studies, leading to new discoveries and furthering the development of grid-based Vlasov solvers.

The long-term goal of this line of research is to develop a *virtual fusion plasma*, at least as far as microturbulence is concerned. This ambitious goal might become a reality in the second half of the next decade, assuming that there continues to be a significant increase in computer power every year.

10.3.2 Nonlinear MHD: turbulent dynamos

As a second area of modern computational plasma physics is dynamo theory. Here, one is concerned with the question: How do planets, stars, and galaxies create magnetic fields? In this context, it is usually assumed that the answer can be given in the framework of nonlinear magnetohydrodynamics (MHD). Over the last few decades, some of the underlying mechanisms have been identified, but there is still a long list of unsolved puzzles.

Presently, there are a number of laboratory experiments which try – for the first time – to generate a self-sustained magnetic fields in an unconstrained, turbulent flow. One such experiment is run at the University of Wisconsin at Madison. Its operation is accompanied by computer simulations with a code called `DYNAMO`, attempting to understand it better and find ways to predict and optimize its performance. This code is based on similar numerical methods as `GENE`. Additionally, state-of-the-art visualization techniques are employed to interpret the simulation results (see Fig. 10.3.1 right).

Further reading

There are many useful and well written textbooks on computational physics. Two of them which I particularly recommend are

- R.H. Landau and M.J. Páez, Computational Physics (Wiley, 1997)
- A.L. Garcia, Numerical Methods for Physics (Prentice Hall, 2000)

They provide a good introduction and overview from a more pragmatic point of view. Another standard textbook called *Numerical recipes* is available on the web at: `http://nr.com`

The reader who is interested in the more mathematical aspects of computational physics is referred to standard textbooks on numerical mathematics and scientific computing like

- J. Stoer, Numerische Mathematik 1 (Springer, 2005)
- P. Deuflhard and A. Hohmann, Numerische Mathematik I (de Gruyter, 2002)
- A. Quarteroni, R. Sacco, and F. Saleri: Numerische Mathematik (Springer, 2002)

Finally, the reader who is interested in the two applications mentioned above is invited to check out the following websites

- `http://aida.physics.wisc.edu` (Madison Dynamo Experiment)
- `http://www.ipp.mpg.de/~fsj` (Plasma Microturbulence Simulations)

Chapter 11

Plasma heating: neutral beam injection

Christian Hopf, Ursel Fantz, Peter Franzen

11.1 Introduction

A temperature of about 20 keV is required to ignite a magnetically confined fusion plasma. Once ignited, the plasma maintains its temperature by heating through the alpha particles that are produced in the D–T fusion reaction and carry 3.5 MeV or $1/5$ of the fusion energy. Initially, however, auxiliary heating is necessary to reach ignition. Furthermore, contemporary fusion experiments are too small to reach ignition at all and, with few exeptions, do not use a D/T mix as fuel. In these experiments all heating has to be achieved with external power. Various heating methods have been developed and are successfully applied in fusion experiments.

Ohmic heating (OH) is a beneficial side effect of the presence of an inductively driven plasma current I_p in a tokamak. The primary purpose of this current is to create the poloidal component of the confining magnetic field. Due to the finite conductivity of the plasma the current leads to heating by dissipation of the power $P = \mathscr{R} I_\mathrm{p}^2$, where $\mathscr{R}$ is the Ohmic resistance of the plasma. However, with increasing temperature the resistence of the plasma decreases, leading to a decrease of the deposited heating power. The maximum achievable temperatures depend on the machine parameters and the confinement regime but are generally too low for plasma ignition. In addition, ohmic heating is not the method of choice for stellarators since the current would heavily modify the magnetic field created by the external coils. Only before alternative auxiliary heating methods became readily available was ohmic heating applied in stellarators too.

Radio frequency heating (RF) uses high power electromagnetic waves to transfer energy to the plasma. Depending on the choice of frequency, plasma density and composition, different constituents of the plasma can be heated. RF heating is predominantly applied in the range of low frequency Alfvén waves (1–10 MHz), ion cyclotron frequencies (30–100 MHz), lower hybrid frequencies (1–10 GHz) and electron cyclotron frequencies (50–150 GHz).

Neutral beam injection heating (NBI), the topic of this article, is the major work horse among the auxiliary heating methods on most of the world's fusion experiments. The concept is straightforward and was suggested back in the early 1950s: neutral atoms can penetrate the confining magnetic field and are ionized in the plasma via collisions with electrons and ions. The fast ions thus generated are now confined by the magnetic field as well. If their kinetic

energy is large compared to that of the ions and electrons in the plasma they will on average transfer energy to the plasma particles by collisions, thereby heating the plasma.

Neutral beam heating has played an important role in many "milestone experiments" of fusion research. To mention a few, in 1980 NBI heating enabled the first demonstration of a current-free stellerator operation at relevant temperatures and densities and several hundred kW heating power on Wendelstein 7-A [1]. In 1982 the spontaneous transition of the plasma above a heating power threshold into a regime of significantly improved confinement, called high confinement mode or H mode, was discovered on ASDEX in NBI-heated discharges [2]. The so far highest D–T fusion power of 16 MW was achieved on JET in discharges heated with both D and T neutral beams. In the peak of the fusion reaction rate still approximately half of the rate was due to beam–plasma interaction [3, 4].

Like RF heating, NBI is not only useful for plasma heating, but also for *current drive*. If a neutral beam is injected with a toroidal velocity component the current profile is also changed. This *non-inductive current drive* is desirable in order to attain steady-state operation in a tokamak and to access advanced regimes of superior confinement that often depend on achieving a tailored current profile.

Even in a fusion reactor's burning plasma control of the current profile might still require additional ohmic heating or non-inductive current drive.

11.2 Neutral beam heating physics and current drive

The basic idea behind neutral beam heating is simple: A beam of fast particles is injected into the plasma. If the energy of the beam particles is very much greater than the thermal energy of the target plasma the plasma will be heated by collisional energy transfer from the fast particles. Acceleration of particles requires electrically charged particles, i.e. in practice ions or electrons. On the other hand, a beam of charged particles will be deflected by the confining magnetic field even before reaching the plasma. Therefore, the beam of fast charged particles must be neutralized after acceleration. This requirement rules out electrons as beam particles and leaves ions as the only choice. Usually, one of the principal atom species in the plasma is selected as the neutral beam species, i.e. H or D in a fusion experiment running in hydrogen or deuterium, and D or T in a D–T fusion reactor. This choice avoids a change in plasma composition due to NBI.

When the neutral atoms enter the plasma they become ionized by collisions with the plasma ions and electrons and hence also confined by the magnetic field. Due to collisions they thermalize and thereby heat the plasma.

The two main design parameters of an NBI system are the beam energy and the injection geometry. These two parameters determine the collision cross sections and the direction of the fast particles which in turn determine the heating profile and the current-drive properties of the injection system. An outline of the underlying physics is given in this section.

11.2.1 Beam ionization

When the neutral beam atoms—unaffected by the magnetic field and hence travelling in straight lines—enter the plasma they become ionized due to mainly three collisional processes. These are:

- *Collisional ionization by electrons:*

$$\mathrm{H_f^0 + e^-} \quad \longrightarrow \quad \mathrm{H_f^+ + 2e^-} \quad \text{cross section } \sigma_{\mathrm{ie}}$$

- *Collisional ionization by plasma ions:*

$$\mathrm{H_f^0 + H^+} \quad \longrightarrow \quad \mathrm{H_f^+ + H^+ + e^-} \quad \text{cross section } \sigma_{\mathrm{ii}}$$

- *Charge exchange with plasma ions:*

$$\mathrm{H_f^0 + H^+} \quad \longrightarrow \quad \mathrm{H_f^+ + H^0} \quad \text{cross section } \sigma_{\mathrm{cx}}$$

In these reactions H stands for any hydrogen isotope and can be replaced also by D or T. The index "f" indicates the fast beam particle.

For each of these processes the cross section σ_k ($k \in \{\mathrm{ii}, \mathrm{ie}, \mathrm{cx}\}$) depends on the relative velocity of the colliding particles, $v_{\mathrm{rel}} = |\boldsymbol{v}_{\mathrm{b}} - \boldsymbol{v}_{(\mathrm{i\ or\ e})}|$, where $\boldsymbol{v}_{\mathrm{b}}$ is the beam velocity, index "i" stands for the plasma ions and "e" stands for the plasma electrons. While the beam velocity is well defined, the plasma ions and electrons have a broad velocity distribution. Considering that neutral beam heating requires $v_{\mathrm{i}} \ll v_{\mathrm{b}}$ and, due to the electrons' much lighter mass, $v_{\mathrm{b}} \ll v_{\mathrm{e}}$ we can neglect the contribution of the ion velocity to the relative velocity in beam–ion collisions and write the total ionization cross section as

$$\sigma_\Sigma = \sigma_{\mathrm{cx}}(v_{\mathrm{b}}) + \sigma_{\mathrm{ii}}(v_{\mathrm{b}}) + \frac{\langle \sigma_{\mathrm{ie}} v \rangle}{v_{\mathrm{b}}} \,.$$

The expression in the numerator of the last term is the rate coefficient defined by

$$\langle \sigma_{\mathrm{ie}} v \rangle = \frac{\int \sigma_{\mathrm{ie}}(v_{\mathrm{rel}}) v_{\mathrm{rel}} f(v_{\mathrm{rel}}) \mathrm{d}v_{\mathrm{rel}}}{\int f(v_{\mathrm{rel}}) \mathrm{d}v_{\mathrm{rel}}}$$

where $f(v_{\mathrm{rel}})$ is the distribution function of the relative velocity.

In the ideal case of a uniform, pure hydrogen plasma of density n ionization leads to an exponential attenuation of the neutral beam of intensity I_0 along its direction x,

$$I = I_0 \exp\left(-\frac{x}{\lambda}\right) ,$$

where λ is the mean free path for ionizing collisions, given by

$$\lambda = \frac{1}{n\,\sigma_\Sigma} \,.$$

The ionized fast beam particles are no longer unaffected, but confined, by the magnetic field.[1]

The cross sections as a function of beam energy per nucleon are shown in Fig. 11.1. At injection energies below $50\,\mathrm{keV/amu}$, commonly found in many present-day NBI systems, charge exchange dominates beam ionization. At higher energies ionization by ions takes over the leading role, while ionization by electron impact is always only a minor contribution.

[1] The ionization of the neutral beam is sometimes also referred to as *beam trapping* or as *beam absorption*. Both these terms tend to be misleading. "Beam trapping" does not necessarily create "trapped" ions, i.e. ions on a banana orbit. "Beam absorption" only means that the absorbed particles are not transmitted through the plasma. However, the energy of the beam particles is only absorbed much later after slowing down of the fast ions.

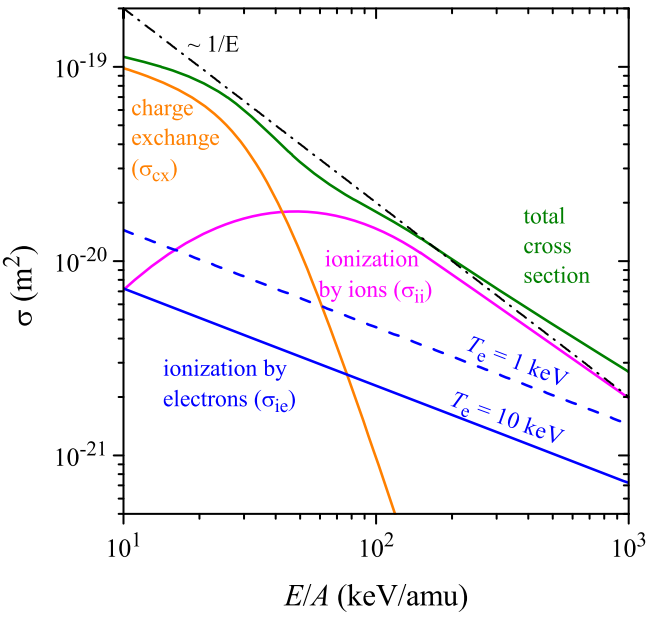

Figure 11.1: Ionization cross sections taken from referenc

The total ionization cross section falls roughly as $1/E$. This pronounced energy dependence makes it possible to choose the mean free path by variation of the beam energy. In order to achieve central heating of the plasma the mean free path should approximately match the minor radius a. We can test this match for typical ASDEX Upgrade parameters using the total cross section in Fig. 11.1. For the 93 keV deuterium beams and a plasma density of $5 \times 10^{19}\,\mathrm{m}^{-3}$ we obtain $\lambda = 0.66\,\mathrm{m}$. ASDEX Upgrade's minor radius is $a = 0.65\,\mathrm{m}$. To obtain $\lambda = a = 2\,\mathrm{m}$ for ITER at $n = 10^{20}\,\mathrm{m}^{-3}$ a very much higher energy of $500\,\mathrm{keV/amu}$ is required. In fact, the ITER NBI system is designed to deliver 1 MeV deuterium beams. More detailed calculations show that the power deposition profile is already peaked in the plasma center for $\lambda > (1/4) \cdot a$. Hence, the reason for the choice of the high acceleration voltage for ITER is not only central heating but also achieving the necessary heating power.

If the mean free path is long—a condition that can occur for example when the plasma density is low during plasma startup—not the whole beam may be ionized in the plasma. The non-ionized fraction of the beam that hits the far wall is called *shine through*. As the power load to the wall caused by shine through can be substantial—for 100% shine through it is of the order of several tens of $\mathrm{MW/m^2}$—appropriate safety interlocks are required to protect the wall from excessive shine-though heat load.

11.2.2 Fast ion orbits and orbit losses

The now confined fast ions follow drift orbits and exchange energy with the plasma particles in collisions. As the ion mean free path in the plasma is very much larger than the circumference of the torus, $\lambda_i \gg 2\pi R$ (R = major radius), the ions will on average complete several full orbits before being substantially scattered or slowed down. Therefore we discuss the fast ion orbits first. Fig. 11.2 illustrates various types of orbits.

Two general types of orbits can be distinguished: Passing orbits (blue in Fig. 11.2) and trapped "banana" orbits (green in Fig. 11.2). While travelling around the torus the ions see a periodically varying magnetic field strength as they follow the helically twisted field lines. When moving in the direction of increasing magnetic field the ion's kinetic energy parallel to the

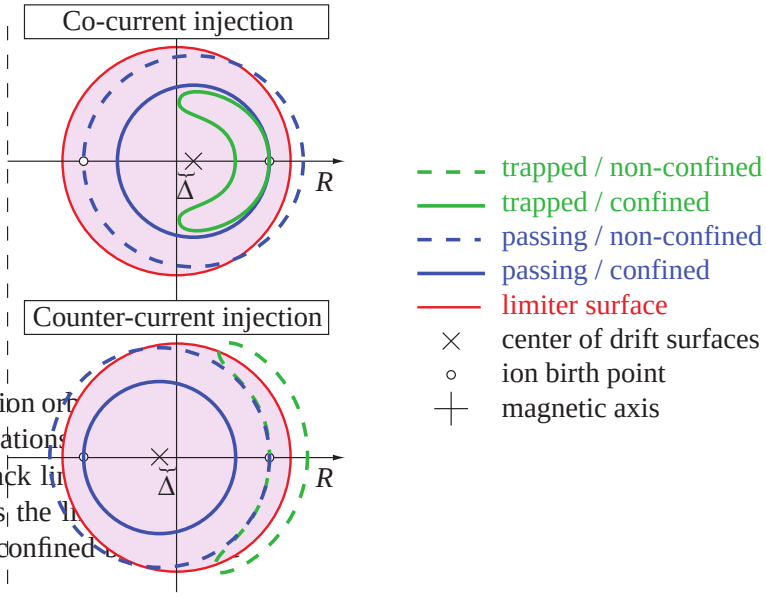

ure 11.2: Schematic of passing (blue) and trapped (green) ion orb
are projected into a poloidal plane. The birth locations
indicated by small open circles. The dashed black li
center of the torus. The red solid line indicates the li
Orbits intersecting the limiter (dashed) are not confined
ion collides with the limiter.

magnetic field decreases and is converted into perpendicular kinetic energy. If the ion's initial ratio of momentum parallel to the magnetic field to the momentum perpendicular to the magnetic field is too low, the ion's parallel velocity becomes zero at a certain magnetic field and it is reflected. The ion is trapped and travels back and forth between two such reflection points.

Due to the grad-B and curvature drifts the ions in a toroidal device do not exactly follow the magnetic field lines but their guiding center orbits are slightly shifted by a distance Δ with respect to the flux tube that the ion was born on, i.e. where ionization occurred. As a result the poloidal projection of a passing orbit looks approximately like the shifted cross section of a flux tube, while a trapped orbit looks like a banana. If the resulting orbit intersects the wall the ion will be lost. Such losses are called first orbit losses.

Whether the shift of a passing particle's drift surface is inward or outward and whether banana orbits lie inside or outside the ion's birth location depends on the direction of the toroidal velocity component of the beam. If this velocity component is in the direction of the plasma current the situation is called *co-current injection*. As can be seen from Fig. 11.2 only the orbits of ions born on the high field side close to the inner wall may intersect the wall. In the opposite case, counter-current injection, the banana orbits lie outside the birth location and may intersect the outer wall. Additionally, passing orbits of ions born close to the edge on the outer mid plane may intersect the inner wall. This is the reason why first orbit losses are especially high for counter-current, near-radial NBI.

11.2.3 Slowing down

Ions on confined orbits, i.e. orbits that do not intersect the walls, travel many times around the torus and transfer their energy to ions and electrons in successive collisions. The energy dependence of the instantaneous energy loss per unit path length is fairly well described by

$$\frac{\mathrm{d}E}{\mathrm{d}x} = \underbrace{-\frac{\alpha}{E}}_{\text{to ions}} \underbrace{-\beta\sqrt{E}}_{\text{to electrons}}, \tag{11.1}$$

where α and β are coefficients that depend on the beam and plasma species as well as plasma density and electron temperature. While the energy transfer to the ions decreases with increas-

ing beam energy, the transfer to the electrons increases. The energy at which the cross over occurs is called *critical energy* and given by,

$$E_\mathrm{c} = \left(\frac{\alpha}{\beta}\right)^{2/3} = 14.8\,T_\mathrm{e}\left(\frac{A^{3/2}}{n_\mathrm{e}}\sum\frac{n_j Z_j^2}{A_j}\right)^{2/3} ,$$

where A_j, Z_j, and n_j are the atomic mass, charge, and density of plasma ion species j, n_e is the electron density, and A is the atomic mass of the beam species. For a pure hydrogen plasma this gives

$$\mathrm{H}^0 \to \mathrm{H}^+ (\mathrm{D}^0 \to \mathrm{D}^+): \quad E_\mathrm{c}[\mathrm{keV}] = 14.8\,(18.6)\,T_\mathrm{e}[\mathrm{keV}] .$$

The fractions of energy transferred to ions and electrons during the entire slowing down process can be calculated by integration of the terms in (11.1). The result is that the threshold for dominant electron heating is at $2.5\,E_\mathrm{c}$

$$E \begin{cases} < 2.5\,E_\mathrm{c} & \text{dominant ion heating,} \\ > 2.5\,E_\mathrm{c} & \text{dominant electron heating.} \end{cases}$$

In contemporary experiments ion heating usually clearly dominates. In ITER, however, both NBI and α-particle heating will predominantly heat the electrons.

The time it takes for ions to slow down to thermal energies can also be obtained by integration using (11.1). For present-day machines the *slowing down time* is typically 20–100 ms. In ASDEX Upgrade the ion circles the torus about 10^4 times during this time, as we will see later.

11.2.4 Particle losses

Besides the first orbit losses already mentioned also fast ions born on confined orbits can be lost in the course of slowing down. Two mechanisms are mainly responsible for these losses.

First, *pitch angle scattering*, i.e. a change in the ratio of parallel to perpendicular velocity due to collisions, can scatter ions into non-confined orbits such as banana orbits that intersect the wall. These losses are typically of the order of 5–10% of the heating power.

Second, in the presence of neutral hydrogen in the plasma charge exchange collisions can convert the fast ions into fast neutrals that escape the confining magnetic field. This mechanism accounts for typically a loss of 5% of the beam power.[2]

11.2.5 Neutral beam current drive (NBCD)

If the neutral beam is injected tangentially into the plasma, the ionized fast particles will travel around the torus in a well defined direction. As they are charged particles an electric current is associated with this motion of fast particles. This current is called the *circulating current*.

We can estimate the circulating current, taking ASDEX Upgrade as an example. ASDEX Upgrade has two tangential current drive beams operating at 93 kV in deuterium with a power

[2]The numbers are taken from typical results of Monte Carlo simulations of NBI heating of ASDEX Upgrade discharges.

of 2.5 MW per beam. Hence, the injected current is $I_0 = P_{\mathrm{NBI}}/U_{\mathrm{acc}} = 54\,\mathrm{A}$. For the mean velocity during slowing down we make the crude, yet for our purposes sufficient, assumption that it is half the beam velocity, $\langle v\rangle = v_0/2 = 1.5\times 10^6\,\mathrm{m/s}$. The slowing down path length is then given by $\langle v\rangle\tau_{\mathrm{s}}$, where τ_{s} is the slowing down time. In ASDEX Upgrade $\tau_{\mathrm{s}} \approx 70\,\mathrm{ms}$ and $\langle v\rangle\tau_{\mathrm{s}} \approx 10^5\,\mathrm{m}$. With a circumference of $2\pi R \approx 10\,\mathrm{m}$ this means the ions travel on average 10^4 times around the torus. Hence, the circulating current can be estimated as

$$I_{\mathrm{circ}} = 10^4 I_0 = 550\,\mathrm{A}$$

or about half the plasma current.

Unfortunately, this simple picture leaves out an important process; if fast ions travel through a plasma they drag along plasma electrons. These electrons cancel a part or all of the ion current. Cancellation of the ion current is complete when beam and plasma have the same effective charge, $Z_{\mathrm{beam}} = Z_{\mathrm{eff}} = \sum Z_j^2 n_j/(Z_j n_j)$, where Z_j and n_j are the charge and density of plasma species j. To make this last point plausible, let us consider two groups of ions at two different velocities v_{a} (e. g. background plasma) and v_{b} (e. g. beam). We can find a frame of reference in which the associated ion currents cancel, i.e. $v'_{\mathrm{a}} n_{\mathrm{a}} = -v'_{\mathrm{b}} n_{\mathrm{b}}$. If these two groups of ions produce equal drag on the electrons, the resulting electron current in this frame of reference—and hence the resulting Lorentz-invariant total current—also vanishes. Only if the two groups of ions produce *different* drag, e.g. by having different charge (collision cross section $\propto Z^2$, current $\propto Z$), the resulting electron currents do not cancel.

In other words, one way to rescue current drive is to increase Z_{eff}—an approach that opposes the usual quest for a clean plasma. There is, however, another aspect that was missed in the simple picture so far.

In a toroidal geometry a certain fraction of the electrons are on trapped orbits due to a low ratio of parallel to perpendicular velocity. These electrons cannot contribute to a toroidal current as they are toroidally confined. Hence, the cancellation of the circulating current by the electrons is reduced by the trapped electron fraction

$$I_{\mathrm{cd}} = I_{\mathrm{circ}}\left[1 - \frac{Z_{\mathrm{beam}}}{Z_{\mathrm{eff}}}\Big(1 - G(Z_{\mathrm{eff}},\varepsilon)\Big)\right] .$$

In this equation I_{cd} is the driven current, I_{circ} is the circulating current, and $G(Z_{\mathrm{eff}},\varepsilon)$ is the trapped electron fraction that depends of Z_{eff} and the torus' inverse aspect ratio $\varepsilon = r/R$. Due to the effect of trapped electrons the driven current in a tokamak is typically more than half of the circulating current. A detailed prediction of driven current (density profiles) is done with numerical codes.

Neutral beam current drive is considered as one of the possible means of achieving steady state operation in a tokamak reactor. For this application the energetic efficiency of the current drive is an important factor. The efficiency (gain/investment) of a current drive system is defined as the current driven per power coupled to the plasma,

$$\varepsilon_{\mathrm{cd}} = \frac{I_{\mathrm{cd}}}{P} \quad \left[\frac{\mathrm{A}}{\mathrm{W}}\right] .$$

As for all current drive systems

$$I_{\mathrm{cd}} \propto P \cdot \frac{1}{n_{\mathrm{e}}} \cdot \frac{1}{R}$$

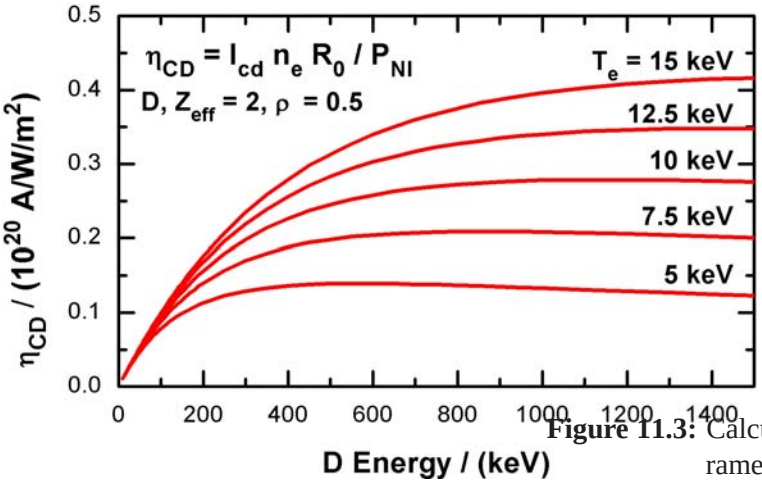

Figure 11.3: Calculated current drive efficiency as a function of beam ene
rameters are given in the figure.

a more convenient figure of merit to compare systems is

$$\eta_{\mathrm{cd}} = R n_{\mathrm{e}} \frac{I_{\mathrm{cd}}}{P}, \qquad \text{usually given in } \left[\frac{10^{20}\mathrm{A}}{\mathrm{Wm}^2}\right] .$$

The current drive efficiency as a function of beam energy calculated for a deuterium beam deposition at half minor radius and for $Z_{\mathrm{eff}} = 2$ is shown in Fig. 11.3. For a given electron temperature the curves go through a broad maximum. The beneficial consequence of this observation is that at given electron temperature the beam energy can be substantially reduced without sacrificing much of the current drive efficiency. At about half the energy of the maximum the efficiency is still 90% of the maximum efficiency. As the value of the acceleration voltage has a huge impact on the installation cost of an NBI system one wants to keep the beam energy as low as possible. We can also see from the graph that at high beam energies only an increase of the electron temperature can increase the efficiency further whereas at low beam energies an increase of the beam voltage has more effect. In ITER, up to 2 MA current can be driven by the neutral beams operating at 1 MV, 33 MW heating power, $R = 6.2\,\mathrm{m}$, $n_{\mathrm{e}} = 10^{20}\,\mathrm{m}^{-3}$ and $T_{\mathrm{e}} = 15\,\mathrm{keV}$.

Experimentally, fully non-inductive current drive using NBCD has been demonstrated in JT-60U in low-density, low-current, high-T_{e} discharges [6]. The bootstrap current, a self generated plasma current due to radial gradients in the plasma, also delivered an important contribution to the total driven current.

11.3 Neutral beam injection systems

The generation of a neutral beam can be divided into three successive steps, schematically shown in Fig. 11.4:

- the generation of a powerful ion beam in the ion source,
- the neutralization of the ion beam in the neutralizer, and
- the transport of the neutral beam to the plasma vessel.

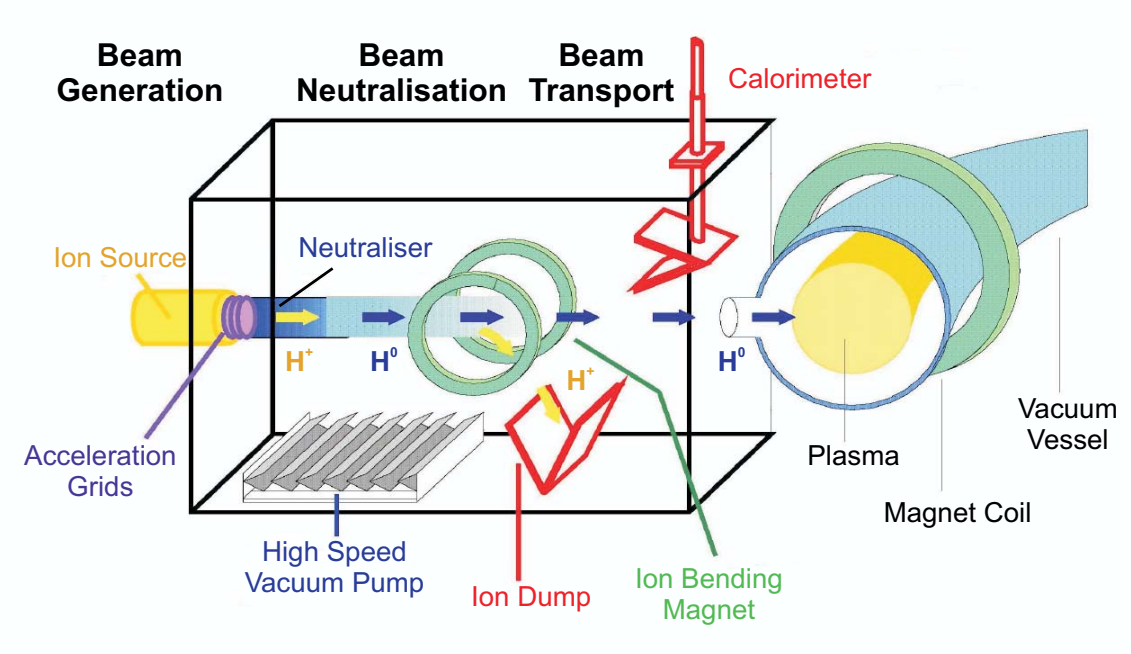

Figure 11.4: Schematic view of a neutral beam heating system.

Generation of the ion beam is accomplished by extraction of the ions from a hydrogen plasma.

The neutralization of the extracted ions occurs in the neutralizer via charge exchange collisions of the fast ions with the cold hydrogen molecules. The neutralizer is usually a drift tube directly attached to the ion source with a permanent inflow of hydrogen gas.

After leaving the neutralizer a significant fraction of the beam is still ionized. During the transport of the neutral beam these ions are removed from the beam by a bending magnet and they hit an efficiently water cooled residual ion dump.

A further indispensable component of a neutral beam system is a calorimeter that can be moved into the beam. It usually consists of efficiently cooled target plates of a design similar or identical to the beam dumps. It allows to fire beams for test or conditioning purposes when no plasma is available as absorbing target. Furthermore, the deposited heating power can be derived from the known flow of cooling water through the calorimeter plates and the temperature difference between inlet and outlet.

A cutaway view of the NBI system on JET is shown in Fig. 11.5. The beamline has eight sources. Parameters are given in Tab. 11.1.

In the following sections ion beam generation, neutralization, and beam transport are discussed in more detail.

Table 11.1: Performance of the NBI systems on various fusion experiments. The maximum current density for positive ion systems is limited by the power supplies, not by the source.

Fusion Device	**AUG**		**W7-X***	**JET**	**LHD**	**JT-60U**	
Beam Species	H^+/D^+	H^+/D^+	H^+/D^+	H^+/D^+	H^-	H^+/D^+	H^-/D^-
Type of Source	Arc	RF	RF	Arc	Arc	Arc	Arc
Extraction Area (cm^2)	390		390	300	1150	128	1660
Max. Energy (keV)	55/60	72/93	55/60 (72/100)	80/130	180	75/95	360/380
Injected Power per Source (MW)	1.6/2.5	1.4/2.5	1.4/2.5	1.5/1.4	3.75	0.9/1.4	3.3/2.7
Sources per Beamline	4		1 (4)	8	2	2	2
Number of Beamlines	1 + 1		2	3	3	14	1
Total Power (MW)	12/20		2.8/5 (11.2/20)	36/32	15	27/40	13.2/10.8
Pulse duration (s)	4/8	4/8	10	10	10	5	10
Max. Current Density (mA/cm^2)	250/200	160/160	250/200	160/160	35	270/210	13/9

*Two stage construction planned, otherwise copy of the AUG RF system.

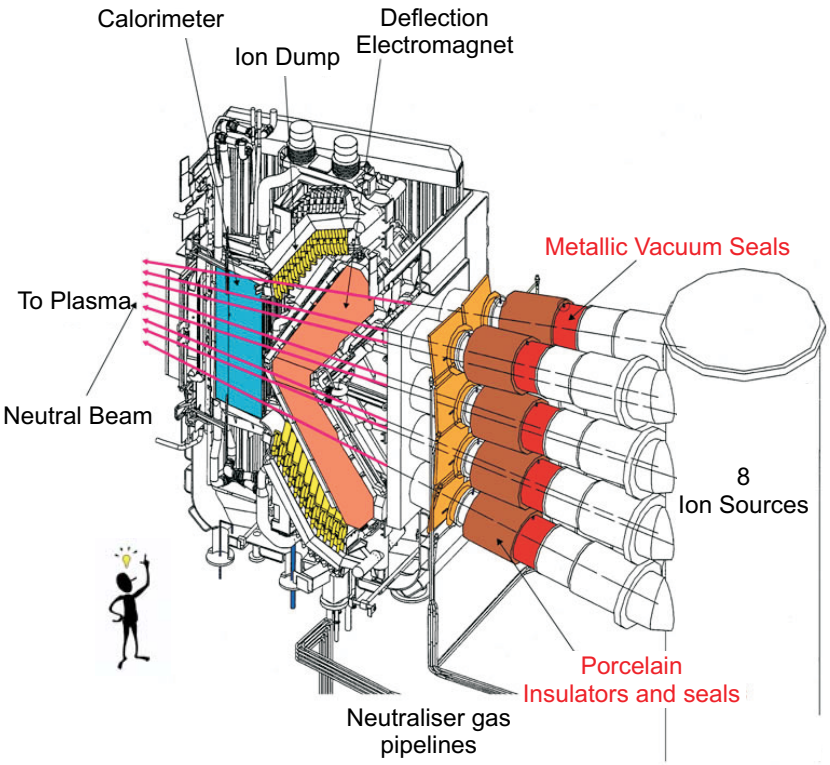

Figure 11.5: NBI System at JET with eight ion sources.

11.3.1 Generation of the ion beam

Sources for positive ions

The general principle of ion beam generation by extraction of ions from a plasma is well established and applied for many purposes. The unique requirement that NBI ion sources have to fulfill is the high beam power of several MW at reasonably low beam divergence in order to satisfy the heating power demands and accomplish good beam transmission through often narrow ports. The acceleration voltage is determined by the required mean free path of the neutrals in the plasma and, hence, ultimately by the geometric dimensions of the fusion experiment. It is between several tens of keV on existing devices and 1 MeV for ITER. Consequently, the beam current has to be of the order of several tens of amperes which in turn demands a large cross section of the beam of several hundreds of cm^2. The necessary high ion flux densities of typically a few hundred mA/cm^2 over the large area demands a sufficiently high plasma density and a reasonable uniformity in space and time ($< 10\%$).

Two different types of ion sources have become popular for NBI systems, arc sources and RF sources.

In an *arc sources* electrons are thermally emitted by a number of hot tungsten-filament cathodes and accelerated into the ion source volume by a DC voltage of about 100 V. There they ionize the gas molecules and create the plasma. The arc current is of the order of 1 kA.

In an *RF source* the power is coupled to the plasma via a coil wound around the electriclly non-conducting walls of the plasma source. The coil is powered by radio frequency (RF) in

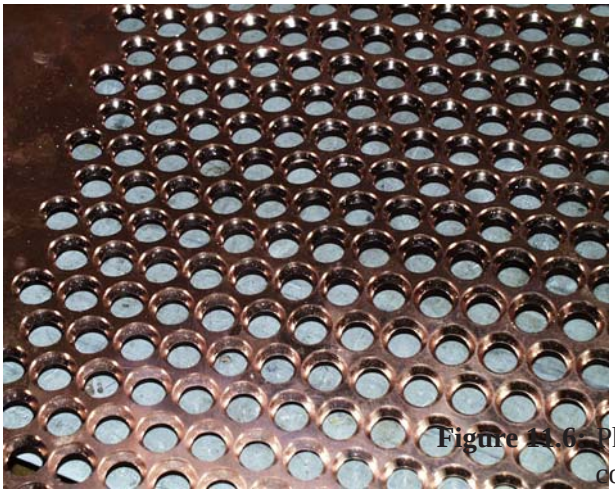

Figure 11.6: Photograph of a grid of the ASDEX Upgrade NBI system. The grid consist of 774 apertures with 8 mm in diameter.

the 1 MHz range. The coil's time-dependent magnetic field induces oszillating, closed electric field lines that periodically accelerate the electrons and lead to ionization. A plasma generated by this concept is called inductively coupled plasma (ICP). The typical RF power is around 100 kW.

RF sources have a number of advantages compared to arc sources. The RF power delivered by the generator can be quickly adjusted, allowing for a rapidly responding feedback control of the ion current axtracted from the source. In arc sources such a quick feedback is not possible due to the thermal inertia of the filaments. Furthermore, while in an arc source every of the several tens of filaments has to be individually connected with a cable, an RF source needs only one high voltage connection and the connection for the coil. As the whole ion source is at acceleration voltage with respect to the grounded torus this greatly simplifies the wiring. The RF can even be supplied to the coil via an electrically insulating transformer such that the RF generator can be kept at ground potential.

For long pulse operation and operation in environments that require remote handling an additional advantage is that the RF sources require almost no maitenance due to the absence of filaments with limited lifetime.

Independent of their type, positive ion sources do not only produce H^+ ions, but also molecular H_2^+ and H_3^+ ions that are also accelerated. After acceleration these molecular ions have the same kinetic energy as the atomic ions. Hence, the energy per H in the ion is only a half and a third of the full energy, respectively. The neutral atoms produced from these molecular ions in the neutralizer also have half and third energy. Generally, the molecular ion fraction decreases with the coupled power density and increases with pressure. As an example, the RF sources on ASDEX Upgrade have a ratio of H^+:H_2^+:H_3^+ of approximately 7:2:1 when running at full parameters.

Extraction and acceleration of positive ions beams

It is intuitively clear that in order to create not too inhomogeneous acceleration field the diameter of the extraction aperture should not be very much larger than the acceleration gap. Hence, the large extraction area means that the beam has to be extracted through multiple apertures, e.g. 774 in the case of the ASDEX Upgrade grids. This is achieved by assembling a set of carefully aligned grids. A photograph of a grid is shown in Fig. 11.6. The holes of the aligned grids form multiple channels through each of which one beamlet is extracted, accelerated, and

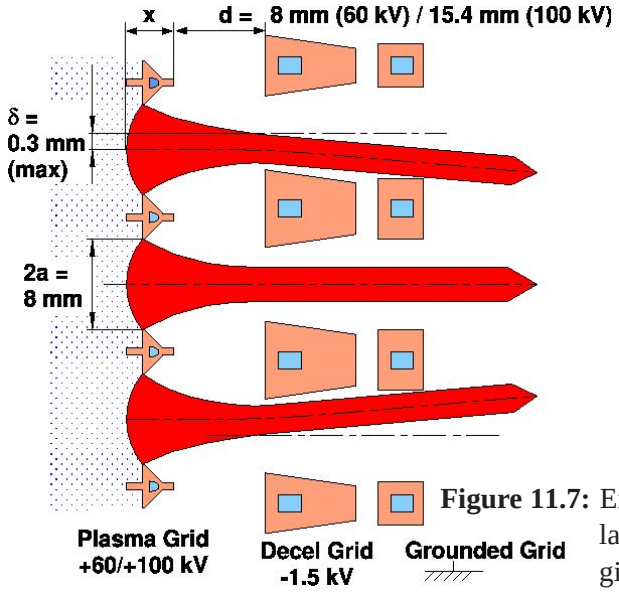

Figure 11.7: Extraction geometry for a three-electrode system for three ci lar beamlets with offset focussing (beam steering). Dimensions given for the ASDEX Upgrade NBI system.

focussed. The geometry of the accelerating channels, shaping and gap distances, are carefully designed to control beam optics by proper use of electrostatic lenses. In contrast to single beam extraction systems, such as accelerators in high energy physics, where additional beam optics can be placed anywhere along the beamline, the NBI beam receives its final properties already at this point.

The extraction system consists of three or more metallic grids. Fig. 11.7 shows a three-grid system. The first grid, called plasma grid, separates the source plasma from the accelerator. The acceleration field is generated by the potential difference between plasma grid and grounded grid. The decel grid, a third grid in between plasma grid and grounded grid, is negatively biased by a few kV with respect to the grounded grid. Its role is twofold. First, it serves to prevent electrons created in ionizing collisions in the neutralizer from being accelerated in opposite beam direction into the source and damaging the back of the source by excessive heat flux. A potential barrier of a few hundred volts is sufficient for the purpose. Second, the decel grid exerts an electrostatic divergent lens effect upon the ion beam.

In the following paragraphs we will briefly discuss three concepts important in beam extraction. These are perveance, divergence, and steering.

Perveance: The current that can be extracted from a single aperture is basically determined by the space-charge-limited flow described by the Langmuir-Child law for non-relativistic charged particles

$$I = \Pi \cdot V^{3/2} \,,$$

where I is the extracted current and V is the applied extraction voltage. The factor Π is called *perveance* and inversely proportional to the square of acceleration gap d,

$$\Pi \propto \frac{1}{d^2} \,.$$

The perveance of an extraction system, and hence the extracted current, is ultimately limited by the minimum gap d required between the grids to hold the acceleration voltage without electrical breakdowns. Furthermore, for a given extraction system there is an optimum perveance at which the beam divergence is minimal.

Divergence: In contrast to electron emitters there is no fixed boundary from where the ions are emitted. Instead, the boundary between the undisturbed, field-free source plasma and the acceleration region is a curved surface (see Fig. 11.7) that is the self-consistent solution of the space-charge-limited flow of ions. For a given extraction geometry there is an optimum match between the ion flux density delivered by the plasma and the electrostatical acceleration potential V, i.e. an optimum perveance, such that the resulting plasma curvature yields a minimum beam divergence. In practice, the minimum achievable divergence is limited by aberrations, space-charge forces and transverse beam energy due to a finite ion temperature in the source plasma. Typical values are of the order of 0.8° for the ASDEX Upgrade injectors. Because the matching condition for optimum beam divergence has to be met in every single aperture, the ion source has to produce an ion flux density which is reasonably uniform in space and time. Typically, non-uniformities larger than 10% lead to a degradation of beam divergence.

Steering: The beam dimensions at some distance from the ion source, e.g. at the porthole of the plasma device, are determined on the one hand by the divergence of the single beamlets and on the other hand by the finite dimensions of the plasma grid. The latter effect can be made negligibly small by aiming or steering the individual beamlets or groups of beamlets onto a common focal point or line. Apart from the obvious techniques of curving the electrodes or subdividing them and tilting the subsections with respect to each other there is a more subtle way of utilizing the defocusing effect of the electrostatic divergent lens formed by the electrostatic field distribution behind the decel electrode. Displacing an aperture in the negative grid with respect to the corresponding aperture in the plasma grid results in a deflection of the beamlet. The direction of deflection is opposite to the direction of displacement, i.e. it requires an outward (with respect to the axis of the whole beam) displacement of the decel aperture to create the desired inwards deflection of the beamlet. Beam steering is schematically shown in Fig. 11.7.

11.3.2 Neutralization

Neutralization happens via charge exchange collisions of the fast ions with the cold hydrogen molecules with the cross section shown in Fig. 11.1. The neutralizer is usually a drift tube directly attached to the ion source with a relatively high pressure $p_\mathrm{n} > 10^{-3}\,\mathrm{mbar}$ that is maintained by a constant inflow of neutral hydrogen gas.

Once neutralized, the fast atoms may also be ionized again in subsequent collisions. After a sufficient length ℓ of the neutraizer, or more precisely a sufficient $p_\mathrm{n}\ell$, a steady state is reached in which the reaction rates of both neutralization and re-ionization are equal and the ratio of neutral to charged fast beam particles does no longer change. The ratio depends on the cross sections of both reactions that in turn depend on velocity. The optimal length of a neutralizer is such that the mentioned steady state is just reached. If the neuralizer is shorter, less ions are neutralized, if it is longer the losses of beam particles due to scattering in collisions increase.

The resulting neutral fraction of the beam at the end of the neutralizer is called neutralization efficiency. It is shown in Fig. 11.8. At low ion energies of $< 20\,\mathrm{keV/amu}$ the efficiency can be as high as 90%. Above $\sim 20\,\mathrm{keV/amu}$ the efficiency decreases for positive ions and becomes smaller than 50% above $\sim 100\,\mathrm{keV/amu}$. The decrease is mainly due to the decrease of the neutralization cross section shown in Fig. 11.1. Neutralization efficiencies smaller than 50% are unattractive because more than half of the energy invested for beam acceleration is wasted on the non-neutralized fraction of the beam.

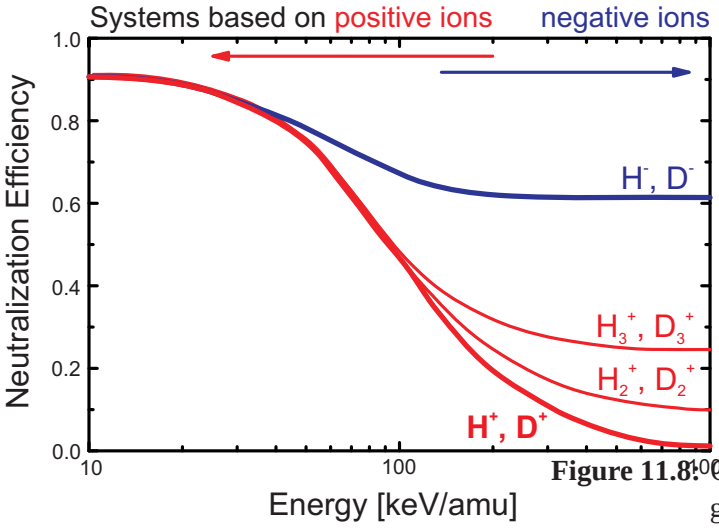

Figure 11.8: Optimum neutralization efficiency for positive and ne
gen ions versus beam energy per nucleon.

Fig. 11.8 also shows that for negative ions the neutralization efficiency stays high throughout the depicted energy range. For negative ions neutralization happens via the stripping of the weakly bound additional electron. It is hence obvious that injection energies in excess of $\sim 100\,\mathrm{keV/amu}$ require negative-ion-based systems. Negative-ion-based NBI is used on the LHD stellerator in Japan, was used on the JT-60U tokamak and will be operated on its upgrade, JT-60SA, also situated in Japan (see Tab. 11.1). The NBI system for ITER, designed for 1 MV acceleration voltage, will necessarily have to start from negative ions.

11.3.3 Beam transport

Ion removal

When the beam leaves the neutralizer it is only partially neutralized. The previous argument that neutralization efficiencies lower than 50% are unattractive implies, on the other hand, that up to 50% of the beam can still be ionized and the ions carry up to the same power as the neutral beam. If no provisions were made these ions would be deflected by the fringe field of the fusion experiment and strike the walls of the beam line somewhere. On unprotected walls severe melting damage would occur. Therefore, the ions are removed from the beam in a controlled fashion and directed on specially designed residual ion dumps.

Removal of the ion beam is accomplished by the magnetic field of a bending magnet. The angle by which the beam is bent may be up to 180°, as in the case of th ASDEX Upgrade injectors.

The beam dumps are copper panels with a dense arrangement of cooling channels close to the surface. High pressure cooling water ensures a fast flow of water through theses channels. A typical figure of merit for these advanced thermal sinks is a power density limit of $25\,\mathrm{MW/m^2}$ perpendicular to the surface. To reduce the power density of the ion beam to below these acceptable limits the panels are inclined with respect to the direction of incidence.

Vacuum requirements

Downstream of the neutralizer the pressure should be significantly lower than in the neutralizer for mainly two reasons.

First, ionization and scattering of beam neutrals outside the neutralizer leads to a loss of particles and hence power from the beam. Furtheremore, the ionized fast atoms are deflected by the fusion experiment's fringe field and hit the wall of the beam line. High fluxes of such ions can cause thermal damage to the walls. Moreover, ions hitting the walls can lead to desorption of gas from the surface that it turn leads to more ionization. This positive feedback can eventually lead to a catastrophic event known as beam blocking, in which most of the beam is becoming ionized in the beam line and hits the walls. The condition can be detected by the strong light emission associated with it and an interlock can stop the beams.

Second, NBI beam lines have to be connected to the torus via a duct with rather large diameter. A high pressure in the beam line would consequently also lead to a high flux of cold neutral gas to the torus. Such a huge flow of gas would render density control difficult to impossible, especially in low density discharges.

Both, estimates and experience tell that the pressure must be below 10^{-4} mbar to avoid both problems. The necessary pumping speed is determined by this allowed upper limit of the pressure and the gas flow into the beam line. This flow of gas comes from gas inlets into the ion source and the neutralizer and amounts to approximately 20 mbar ℓ/s of H_2 on each of the eight ion sources per beam line on JET.

The resulting total gas flow of the order of 100 mbar ℓ/s requires a pumping speed of several $10^6\,\ell$/s to reach a pressure below 10^4 mbar. This cannot be achieved by conventional turbo or diffusion pumps as the open diameter of their flanges limits their pumping speed. Instead, large area cryo-condensation pumps cooled to 4 K with liquid He or titanium getter pumps (operated at room temperature) are used. In these systems a specific pumping speed of 10–20 $\ell/(\mathrm{s}\cdot\mathrm{cm}^2)$ for H_2 can be achieved perpendicular to the pump's front surface. Hence, a total pumping surface of several 10 m^2 is required. This is one of the reasons why conventional neutral beam systems are so big.

11.4 NBI systems based on negative ions

As discussed in sec. 11.2.1 ITER's NBI system is specified to have an acceleration voltage of 1 MeV for reasons of achieving the required heating power and central heating. Future devices such as DEMO or a fusion power plant—if they will have NBI—may require even higher beam energies. At these energies the neutralization efficiency for positive hydrogen ions is unacceptably low (see Fig. 11.8). For negative hydrogen ions, on the other hand, it never drops below 60%. Hence, the designs of NBI systems for ITER and for other large devices are based on negative hydrogen ions despite the fact that negative ion beams are much more difficult to produce than beams of positive ions.

The use of negative ions comes at a price. The additional electron has a low binding energy of 0.75 eV and can be easily detached in collisions with electrons or ions. While this is an advantage in terms of beam neutralization, it also means that the negative ions have a very limited lifetime in the source plasma. Therefore, the extracted current densities from negative ion sources are typically a factor of ten lower than those from positive ion sources. The low current densities have to be compensated by the size of the extraction area.

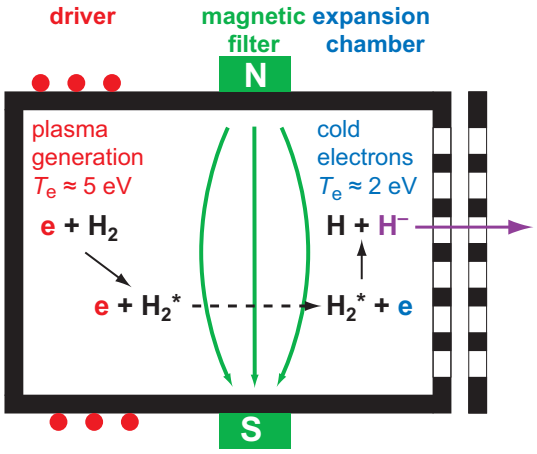

Figure 11.9: Volume production of H^- in a tandem source.

11.4.1 Generation of negative hydrogen ions

There are basically two mechanisms that create negative hydrogen ions in a plasma source, *volume production* and *surface production*.

Volume production

Volume production is a two-step process. It is schematically shown in Fig. 11.9. In the first step a hydrogen molecule is excited in a collision with a sufficiently energetic electron to a high vibrational level ($v \geq 4$). In the second step, an additional electron is captured by the excited molecule forming an itermediate molecular negative ion. The melecular ion then dissociates into a neutral hydrogen atom and a negative hydrogen ion. The whole reaction reads

$$\mathrm{H_2 + e_{fast}} \longrightarrow \mathrm{H_2^* + e'_{fast}}\,,$$

$$\mathrm{H_2^* + e} \longrightarrow \mathrm{H_2^-} \longrightarrow \mathrm{H + H^-}\,,$$

where the prime on the electron in the first reaction indicates that its energy has changed.

The vibrational excitation of the hydrogen molecules requires a high electron temperature, typically $T_e \sim 5$–$10\,\mathrm{eV}$. On the other hand, a low T_e around 1–2 eV maximizes the dissociative attachment reaction rates and simultaneously minimizes the destruction of H^- by electronic and ionic collisions. For this reason, the most common type of volume-production source, the tandem source shown in Fig. 11.9, has two distinct regions separated by a magnetic filter field, the driver and the extraction chamber. In the driver either an arc or an RF discharge is generated in hydrogen gas as described earlier for positive ion sources. External magnets create the magnetic filter near the plasma grid perpendicular to the extraction direction. The filter field reduces electron transport from the driver leading to reduced n_e and T_e in the extraction region.

Efficient volume production requires a high density of all species involved in the two-step reaction. On the other hand, a high density also shortens the mean free path of negative ions before destruction. Furthermore, a high density in the source also increases the gas density and hence the stripping losses in the acceleration system. For this reason volume production is not a viable concept for the large ion sources used for NBI.

Surface production

The generation mechanism better suited for large ion sources is surface production. In surface production, a neutral hydrogen atom or a or a positive hydrogen ion captures one or two electrons upon backscattering from a surface with a low work function,

$$\mathrm{H\ or\ H}_n^+ + \mathrm{surface} \quad \longrightarrow \quad \mathrm{H}^- + \ldots, \qquad n = 1, 2, 3 \quad .$$

The probability of this electron capture reaction depends on the work function Φ of the surface, the affinity A of the electron—being 0.75 eV for negative hydrogen ions—and also on the perpendicular velocity $v_\perp$ of the escaping ion. The negative ion yield per H impact on a wall can be predicted by

$$Y(\mathrm{H}^-/\mathrm{H}^+) = \exp\left(-\frac{\Phi - A}{C v_\perp}\right),$$

where C is a constant, and $(\Phi - A)$ represents the difference of energy between the Fermi level of the surface and the affinity level; it should be as small as possible to enhance the electron capture probability.

The most widely used method to lower the surface work function is to cover a metal with cesium. The optimal coverage with cesium is about 0.6 monolayers ($3.3 \times 10^{14}\,\mathrm{Cs/cm^2}$) with an energy-dependent production yield of up to 0.67 H^- per incident H atom. For tungsten, for example, the work function of W(110) is reduced to 1.45 eV compared to 5.25 eV for pure tungsten. For the surface conditions found on most cesiated sources, the expected yield $Y(\mathrm{H}^-/\mathrm{H})$ or $Y(\mathrm{H}^-/\mathrm{H}^+)$ is in the range 10^{-2}–10^{-1}, in agreement with experiments.

The cesium coating is usually achieved by evaporating Cs into the chamber and redistribution through the plasma. The transport in these cesium-seeded discharges is governed by complex physics and plasma chemistry. Achieving long pulse stability therefore requires a basic understanding of the dynamical behaviour of the cesium distribution in the source.

Due to the short survival path length of H^- only negative ions produced on surfaces in direct proximity to the extraction holes have a sufficient chance of being extracted. However, negative ions created at the plasma grid surface are accelerated by the plasma sheath backwards into the source. Thus, they initially start in the wrong direction and have to effectively turn towards the extraction grid. Two processes are mainly responsible for this required change of direction. Firstly, the magnetic fields of the electron-deflection magnets in the extraction grid and the filter field bend the trajectories of the negative ions such that they may eventually become extracted. Secondly, charge exchange collisions of the type $\mathrm{H}^- + \mathrm{H} \rightarrow \mathrm{H} + \mathrm{H}^-$ can transfer the additional charge to a hydrogen atom that travels in a different direction. The use of chamfered apertures instead of a flat design improves the extraction probability by increasing the effective area for production of negative ions and by providing a more favorable starting angle of H^- from the surface. Simulated trajectories of H^- are shown in Fig. 11.10. The sharp bends correspond to charge exchange while the smooth bends are a result of the magnetic fields.

Destruction of H^-

The destruction of negative ions in the plasma is dominated by three processes. These are electron stripping

$$\mathrm{H}^- + \mathrm{e}^- \quad \longrightarrow \quad \mathrm{H} + 2\mathrm{e}^-$$

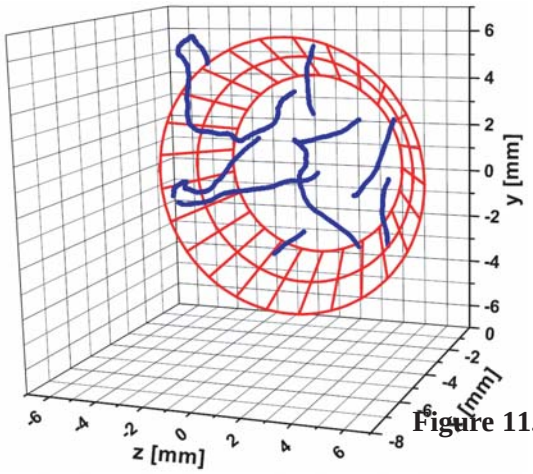

Figure 11.10: Simulated extraction trajectories from a chamfered plasma gr aperture.

which is very effective for electron temperatures in the range of a few electronvolts, mutual neutralization

$$H^- + H^+ \quad \longrightarrow \quad 2H$$

that depends slightly on the ion temperature, and, finally, associative detachment

$$H^- + H \quad \longrightarrow \quad H_2 + e \quad \text{or} \quad 2H + e$$

that has a weak dependence on the temperature of the atoms.

Electron stripping can be minimized by reducing T_e to approximately 2 eV, but then mutual neutralization will take over. In either case this results in survival lengths for the negative ions that are short compared to the source dimensions. Nevertheless, a reduction of the electron temperature below 2 eV helps to increase the survival length and is achieved by the magnetic filter field. Furthermore, the formation of H^- has to be maximized on surfaces close to the extraction holes, i.e. on the plasma grid surface.

11.4.2 Co-extraction of electrons

Extracting negative ions will unavoidably also lead to the extraction of electrons, as the charges of both have the same sign. Accelerating these electrons to full beam energy is a waste of energy (and money) and bears the risk of causing heat flux damage at the locations struck by these electrons. Therefore, the extraction systems for negative ions have a first stage with rather low acceleration voltage of ~ 10 kV between the plasma and the *extraction grid*. The extraction grid is equipped with permanent magnets to bend the electron trajectories onto this heavily cooled grid. Besides, biasing the plasma grid positively with respect to the source body reduces the co-extracted electron current and can increase the extracted negative ion current significantly.

11.4.3 Wall plug efficiency and neutralization efficiency

The current drive efficiency defined in sec. 11.2.5 relates the driven current to the heating power coupled to the plasma and is determined by the physics of current drive. From an engineering and economic standpoint it is more important to ask how much of the electric power produced by the fusion power plant P_{el} is the gross power P_{NBI} needed to run the NBI

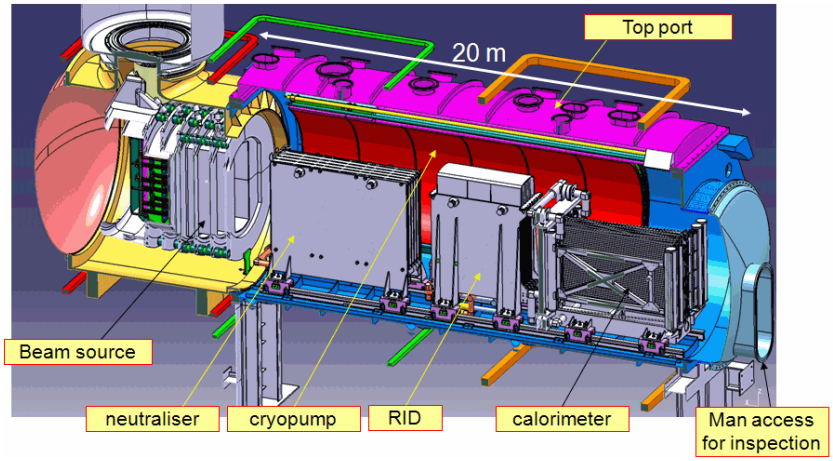

Figure 11.11: Sketch of the ITER neutral be

system to achieve the required non-inductive current drive. P_{NBI} is larger than the coupled power P_{c} by all the power losses in the system and the power needed for auxiliary systems. The ratio $P_{\mathrm{NBI}}/P_{\mathrm{el}}$ is called circulating power fraction. The wall plug efficiency is defined by

$$\eta_{\mathrm{wp}} = \frac{I_{\mathrm{cd}}}{P_{\mathrm{NBI}}} = \frac{I_{\mathrm{cd}}}{P_{\mathrm{c}}}\frac{P_{\mathrm{c}}}{P_{\mathrm{NBI}}} = \varepsilon_{\mathrm{cd}}\eta_{\mathrm{syst}}.$$

For DEMO, $\eta_{\mathrm{syst}} > 0.6$ is required.

The main losses of present-day NBI systems are the power carried by the non-neutralized beam fraction, i.e. the power to the residual ion dump, and, in the case of negative ions, the power carried by the co-extracted and co-accelerated electrons. Minimizing these losses is of paramount importance if NBI is used in DEMO or a power plant.

Like positive ions, negative ion beams are conventionally neutralized during the transit through a neutral hydrogen-gas-filled tube, however by stripping of the additional electron instead of charge exchange. The achievable neutralization efficiency is $\approx 60\%$ at high extraction voltages. The remaining $\approx 40\%$ of the beam are more or less equally partitioned between H^- and H^+.

A totally different concept might provide still higher neutralization efficiencies and therefore less energy loss. Photo detachment, the detachment of the additional electron by the photons of a laser in an optical cavity, could be of interest for future NBI systems.

11.4.4 Development of a negative-ion-based system for ITER

ITER will have two NBI beamlines with one source each. According to ITER's specifications each source will have to deliver 16.7 MW of 1 MeV neutral deuterium. The extracted current will be 40 A. Given the comparatively low extracted current densities achievable with negative ion sources this requires a huge extraction area of $2000\,\mathrm{m}^2$. The total cross section of the source will be $1.9 \times 0.9\,\mathrm{m}^2$. The parameters of the ITER NBI are given in Tab. 11.2.

Fig. 11.11 shows a sketch of the neutral beam test facility MITICA (Megavolt ITER Injector & Concept Advancement) that will be constructed by Consorzio RFX in the next few years in Padua, Italy. It will be a complete prototype of the ITER injectors comprising ion source, accelerator, neutralizer, residual ion dump (RID), and calorimeter. It is designed in close collaboration with other European associations. IPP Garching contributes strongly to the design of the RF source and the RF circuits as well as to diagnostics and modelling of the RF driven plasmas.

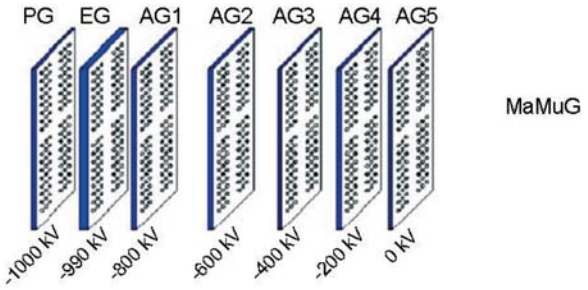

Figure 11.12: Sketch of the ITER-NBI acceleration system.

Acceleration system

In addition to plasma and extraction grid the ITER accelerator has five additional grids, forming five acceleration stages of 200 keV each (see Fig. 11.12). The gaps between the grids are 90 mm each. Due to the large number of grids beam alignment is a difficult task. The advantage of this multiple gap design is that—in contrast to a single gap design—stripped off, co-accelerated electrons can be removed from the beam onto the grids before they are accelerated to full energy. Additionally, it was found that the design with multiple gaps has better voltage holding properties.

Stripping losses, i.e. losses of the additional electron of negative ions, in the accelerator system due to collisions with the background gas depend on the source pressure. These stripping losses lead to non-fully accelerated ions and to additional heat loads on the grid system. As a compromise between these stripping losses and stable source operation ITER requires a source pressure of 0.3 Pa. For comparison, positive ion sources run at a few Pa. Even at this low pressure, the stripping losses in the ITER NBI acceleration system are estimated to about 30%.

RF-driven ion source

The development of large negative ion sources was started in the early 90s in Japan with filamented arc sources for the fusion experiments LHD and JT-60U. This development was the basis for the design of the ITER neutral beam injection system. Due to the advantages of the

Table 11.2: Parameter of the ITER NBI system.

Current Density	20 mA/cm^2 D^-
Electron Content (j_e/j_{ion})	<1
Accelerated Current	40 A
Beam Energy	1 MeV
Pulse Length	3600 s
Extraction Area	2000 cm^2
Source dimensions	$1.9 \times 0.9\,\mathrm{m}^2$
Homogeneity	10%

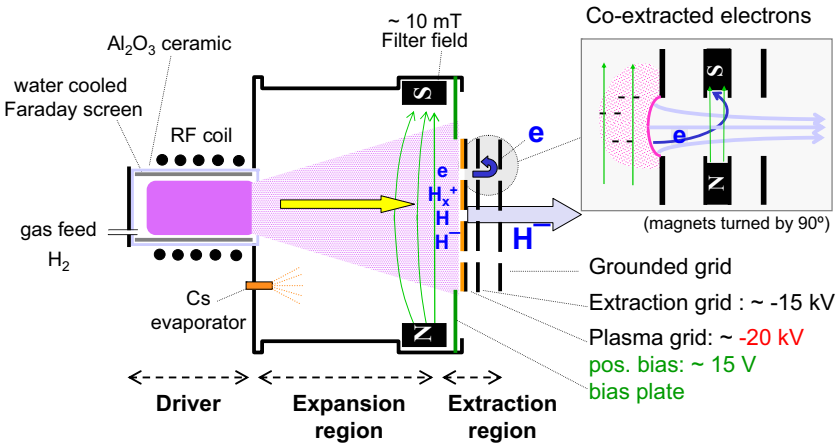

Figure 11.13: Basic layout of the IPP RF dri

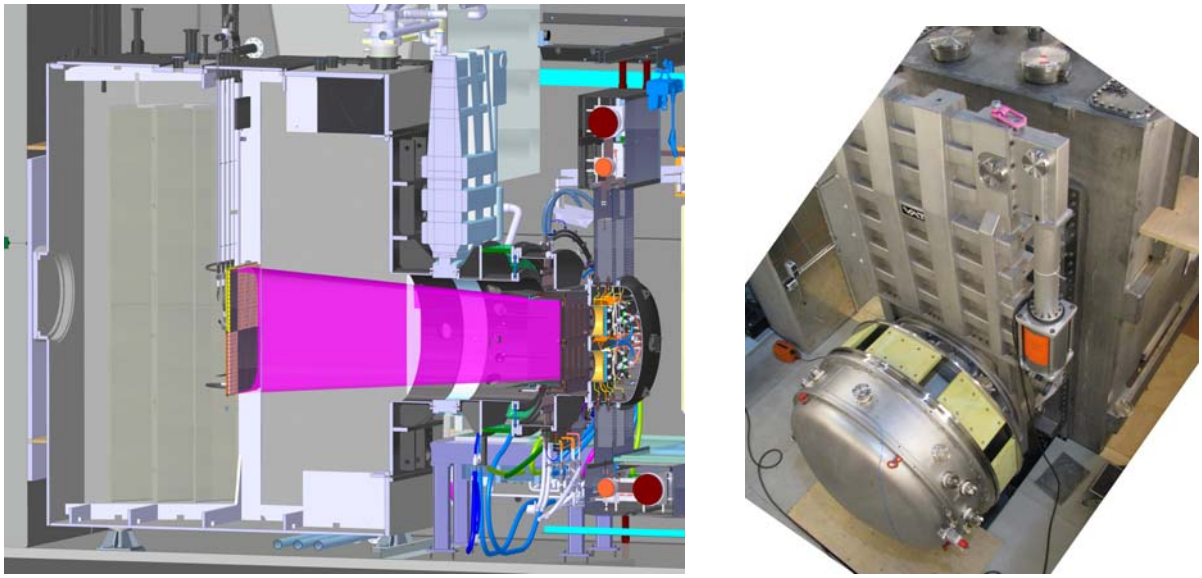

Figure 11.14: CAD drawing of the half-ITER-size source on the testbed ELISE (left side) and a photograph taken during construction in late 2011 (right side). To give an impression of the size: the big vacuum vessel is over 4 m high.

RF source mentioned above and due to the good experience with the positive ion based RF sources on the NBI system for ASDEX Upgrade, IPP Garching started the development of an RF driven negative ion source in the end of the 90 s. In July 2007 the RF source was chosen by the ITER board as the reference design. Details of the source and the current status can be found in [16].

Fig. 11.13 shows the principle design of the IPP RF-driven negative ion source. This RF source consists of three parts: the driver, where the RF is coupled to the plasma, the expansion region, where the plasma expands into the actual source body, and the extraction region. The latter two are separated by a magnetic field of the order of 10 mT parallel to the plasma grid, called filter field. This field is necessary in order to keep the hot electrons generated by the RF with energies of around 10 eV away from the extraction region. There electron temperatures below 2 eV are necessary in order to minimize the destruction rate of the negative hydrogen ions by electron collisions. The driver is mounted on the back of the source body and consists of an alumina cylinder (245 mm in diameter) with a water-cooled RF coil connected to a 1 MHz

oscillator. An internal, water-cooled copper Faraday screen protects the alumina cylinder from the plasma and reduces capacitive coupling.

Current densities of $33\,\mathrm{mA/cm^2}$ with H^- and $23\,\mathrm{mA/cm^2}$ with D^- have been achieved with the IPP RF source on the small test facility BATMAN (Bavarian Test Machine for Negative Ions) at the required source pressure of 0.3 Pa and electron/ion ratio < 1, but with a small extraction area of only $74\,\mathrm{cm^2}$ and limited pulse length $< 4\,\mathrm{s}$. BATMAN is equipped with the standard size IPP RF source, a rectangular body with the dimensions of $32 \times 59\,\mathrm{cm^2}$ and 23 cm depth.

Long pulses were investigated on the long pulse test facility MANITU (Multi Ampere Negative Ion Test Unit). Its extraction area could be extended up to $300\,\mathrm{cm^2}$ and the pulse length up to 3600 s, using the same driver and source body as on BATMAN.

The extension of the source dimensions to those required for ITER follows a modular concept; instead of upscaling the whole driver eight drivers of the size used on the previous test beds will be mounted on the back of the source. The feasibility of the modular concept and the achievable plasma uniformity were investigated on the test bed RADI, featuring four drivers on a half-ITER-size source without beam extraction.

At present the all parameters defined in the ITER NBI specifications have been achieved one at a time, but not yet simultaneously. This is partly due to the lack of adequate large-scale and long-pulse test facilities so far. As a consequence, the European ITER domestic agency F4E has defined an R&D roadmap for the construction of ITER's NBI system. An important step herein is IPP's new test bed ELISE (see Fig. 11.14), a half-ITER-size RF-driven ion source with the aim of demonstrating the extraction of a 60 kV, 20 A beam, that will commence operation in 2012. ELISE will give significant input for the design of neutral beam test facility PRIMA, currently under construction by Consorzio RFX in Padua, Italy. PRIMA will comprise two individual test facilities, SPIDER, a full-size ion source with 100 kV extraction, and the full power NBI prototype MITICA, entering operation in 2017.

Further reading

A general overview of heating methods can be found in Wesson's book [7]. The physics of NBI heating are treated in detail by Cordey [8] and in Speth's review article [9]. Fish [10] gives an extensive overview of current drive methods in general while Mikkelsen and Singer [11] focus on NBI current drive. Good overviews of neutral beam systems are in Duesing's [12] and Speth's [9] articles. The physics of negative ion generation was compiled by Pamela [13] and details on the development of negative ion based systems can be found in references [14, 15, 16]. The current status of the development of RF-driven negative ion sources for ITER is reported in references [17, 18].

References

[1] W7-A Team, Proceedings of the IAEA Fusion Energy Conference (1980) 185.

[2] F. Wagner et al., Phys. Rev. Lett. 49 (1982) 1408

[3] R. J. Hawryluk et al., Rev. Mod. Phys. 70 (1998) 553

[4] M. Keilhacker et al., Nucl. Fusion 39 (1999) 209

[5] A. C. Riviere, Nucl. Fusion 11 (1971) 363.

[6] T. Oikawa et. al., Proceedings of the IAEA Fusion Energy Conference (2000)

[7] J. Wesson, *Tokamaks*, Oxford University Press, 4th ed. (2011)

[8] J. G. Cordey in *Applied atomic collision physics; Volume 2*, edited by H. S. W. Massey, E. W. McDaniel and B. Bederson, Academic Press, Orlando (1984) 327

[9] E. Speth, *Neutral beam heating of fusion plasmas*, Rep. Prog. Phys. 52 (1989) 57.

[10] N. Fish, Rev. Mod. Phys. 59 (1987) 175

[11] D. R. Mikkelson and C. E. Singer, Nucl. Technol./Fusion 4 (1983) 238

[12] G. Duesing et al., *Neutral beam injection system*, Fus. Techn. 11 (1987) 163.

[13] J. Pamela, *The physics of production, acceleration and neutralization of large negative ion beams*, Plasma Phys. Contr. Fusion 37 (1995) A325.

[14] Y. Ohara, *Development of high power ion sources for fusion*, Rev. Sci. Instr. 69 (1998) 908

[15] R.S. Hemsworth, *Long pulse neutral beam injection*, Nucl. Fusion 43 (2003) 851.

[16] Speth et al., *Overview of the RF source development programme at IPP Garching*, Nucl. Fusion 46 (2006) S220.

[17] U. Fantz et al., Nucl. Fusion 49 (2009) 125007

[18] P. Franzen et al., Nucl. Fusion 51 (2011) 073035

Chapter 12

Introduction to stellarator theory

Ralf Kleiber

12.1 Introduction

12.1.1 Some history

The stellarator concept was introduced in 1951 by the astrophysicist Lyman Spitzer. In order to introduce rotational transform (see sec. 12.1.2) in a toroidal configuration he proposed to twist a torus into a shape resembling the shape of the number eight (figure-eight stellarator).

Some years later the first stellarator confinement experiment was built in Princeton (Princeton C stellarator) but was not successful: The plasma was lost very quickly. As was understood later this was mainly due to an incomplete knowledge about the behaviour of resonances in magnetic surfaces. While the Princeton stellarator experiment was still plagued by a low confinement time (a few Bohm times[1] at $T_\mathrm{e} \approx 100\,\mathrm{eV}$) Russian scientists at the 1968 IAEA Novosibirsk conference showed that, with a confinement concept called tokamak, it was possible to achieve an electron temperature of about 1 keV for 30 Bohm times.

This historical situation resulted in the fact that tokamaks became the main line of fusion research in the world while the stellarator concept was pursued only in some places, mainly at the IPP Garching and at the University in Kyoto. Today there is a renewed interest in the stellarator concept as an alternative to the tokamak: A large stellarator of the torsatron[2] type (Large Helical Device (LHD)) started its operation 1998 in Japan at the NIFS; also the German-EU Wendelstein 7-X experiment is being constructed in Greifswald and scheduled to start operation in 2014. Also a new experiment (National Compact Stellarator Experiment (NCSX)) is planned in the USA. Other (smaller) stellarators are in use in the USA (HSX), Spain (TJ-II) and Australia (H-1).

[1] The Bohm time $\tau_B = a^2/D_\mathrm{B}$ (a: minor radius) is defined via the Bohm diffusion coefficient $D_\mathrm{B} = 1/16 k_\mathrm{B} T_\mathrm{e}/(eB)$.

[2] The stellarator concept appears under different names, e.g. heliotron, torsatron, heliac, which mainly distinguish the way the coil systems were historically constructed. In this text we will not elaborate on this, instead we will use just the collective notion *stellarator*.

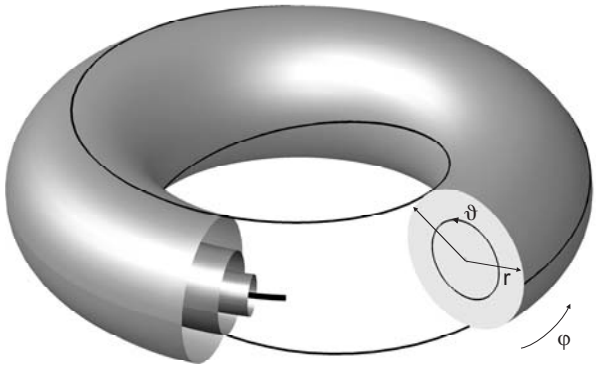

Figure 12.1: Toroidal geometry with nested flux surfaces, magnetic axis and a field line (red) with $\iota = 0.38$.

12.1.2 Some basic notions

Fig. 12.1 shows the basic torus geometry of a fusion device with the poloidal and toroidal angles ϑ and φ. The ratio $A = R/a$ of major to minor radius is called the aspect ratio.

If for a given magnetic field $\mathrm{B}(\mathrm{r})$ a function $\Psi(\mathrm{r})$ exists in a region of space such that $\mathrm{B}\cdot\nabla\Psi = 0$ then the surfaces $\Psi(\mathrm{r}) = const$ are called flux surfaces (i.e. the magnetic field is tangent to these surfaces). The existence of nested[3] flux surfaces (Fig. 12.1 shows three such surfaces), at least in the main volume of the device, is an essential prerequisite for plasma confinement by a magnetic field. The innermost flux surface that is degenerated into a line is called the magnetic axis. If the equilibrium consists only of nested flux surfaces they are distinguished by a flux surface label $s \in \mathbb{R}$.

A field line on a given flux surface can be specified by a (non-periodic) function $\vartheta = f(\varphi)$. If φ increases by $2\pi n$ ($n \in \mathbb{N}$) the angle ϑ changes by an amount ϑ_n. The quantity ι defined by $\iota := \lim_{n\to\infty} \vartheta_\mathrm{n}/(2\pi n)$ is called the rotational transform[4] and has the same value for each field line on a given flux surface; in general ι is a function of the flux surface label. The s-derivative of the rotational transform is called shear ι'. A flux surface s_0 where the rotational transform is rational $\iota(s_0) = n/m$ ($m, n \in \mathbb{Z}$) is called a rational surface[5]. On a rational surface all field lines are closed lines while on a non-rational surface one field line fills the surface ergodically.

Even if magnetic surfaces do not exist one can obtain a good impression of the field structure by following a field line for many turns and marking with a point the positions where it intersects an arbitrarily chosen poloidal plane. The collection of these points is called a Poincaré plot (examples can be seen in Fig. 12.2.4, top). In such a plot a flux surface shows up by points forming a closed curve.

[3] Be M_S the set of points enclosed by a flux surface S. Then nested means that for all pairs (S_1, S_2) $M_{S_1} \subseteq M_{S_2}$ or $M_{S_2} \subseteq M_{S_1}$.

[4] In the simplest approximation ι can be regarded as the pitch of the field line on the flux surface.

[5] Since the set of rational numbers $\mathbb{Q}$ is dense in $\mathbb{R}$ the same is true for the set of rational surfaces with respect to all flux surfaces.

12.1.3 Tokamak, stellarator

The way in which the rotational transform ι is generated can be used to distinguish two classes of fusion devices: Tokamaks and stellarators. In a tokamak the plasma current, which is e.g. driven by the externally induced electric field, causes the poloidal field that in combination with the toroidal field from the (toroidal) field coils leads to a twisting of the magnetic field lines and thus to a rotational transform. Since usually the current density is highest at the center of the torus ι decreases with increasing radius.

In a stellarator the rotational transform is caused solely by a coil system externally to the plasma without any total plasma current J, i.e.

$$J := \int_{A_\mathrm{p}} \mathrm{j} \cdot d\mathrm{A} = 0 \,, \tag{12.1}$$

where j is the current density and A_p is a poloidal plasma cross section. Since the influence of the coils is strongest at larger radii the rotational transform increases with increasing radius.

So one main difference between tokamak and stellarator is the existence or absence of a total toroidal plasma current.

The beneficial role of a total plasma current for confinement in a tokamak has two main accompanying disadvantages: Firstly it can lead to violent instabilities called disruptions which destroy the plasma confinement and secondly – in a standard[6] tokamak – the operation time is limited by the necessity of inducing an electric field. An advantage of the tokamak concept is that a tokamak possesses rotational symmetry and thus is a two-dimensional configuration.

The main advantages of a stellarator are that because of $J = 0$ it is inherently disruption free and can be used to achieve steady state operation. It is easy to show that the condition $J = 0$ cannot be satisfied for an axisymmetric configuration and thus a stellarator must have three-dimensional geometry. This makes stellarators geometrically and computationally more complex than tokamaks but, as we will see in the following sections, offers much more flexibility in their design which can be used for their optimisation.

Although in principle the three-dimensional geometry of a stellarator need not have any symmetries one usually imposes two symmetry requirements (see Fig. 12.2):

- Periodicity: Invariance against a rotation by $2\pi/P$ in the toroidal direction, where P is the number of – so called – field periods.
- Stellarator symmetry: Invariance against flapping around certain lines.

In a tokamak the rotational transform is of first order in the poloidal field component B_p: $\iota \sim B_\mathrm{p}/B_0$, ($B_0$ is the total field). For a stellarator the first order effect of the helical field component B_h causes the field line to wiggle while the rotational transform, i.e. the poloidal shift that remains after averaging, is only of second order: $\iota \sim (B_\mathrm{h}/B_0)^2$. This behavior of the field line can be understood if one rewrites (12.1) (using $\mu_0 \mathrm{j} = \nabla \times \mathrm{B}$) as a line integral around a poloidally closed curve ∂A_p giving $J = \int_{\partial A_\mathrm{p}} B_\mathrm{p}\, dl = 0$. For this integral to be zero the poloidal field component B_p has to change sign which implies an oscillating behavior of the field line.

Both effects are illustrated for a straight ℓ=2 stellarator in Fig. 12.3; the wiggling is conspicuous while the rotation of the field line reflects the rotational transform.

[6] This is not the case for the so called advanced tokamak where bootstrap current (driven by density and temperature gradients) and current drive are responsible for ι.

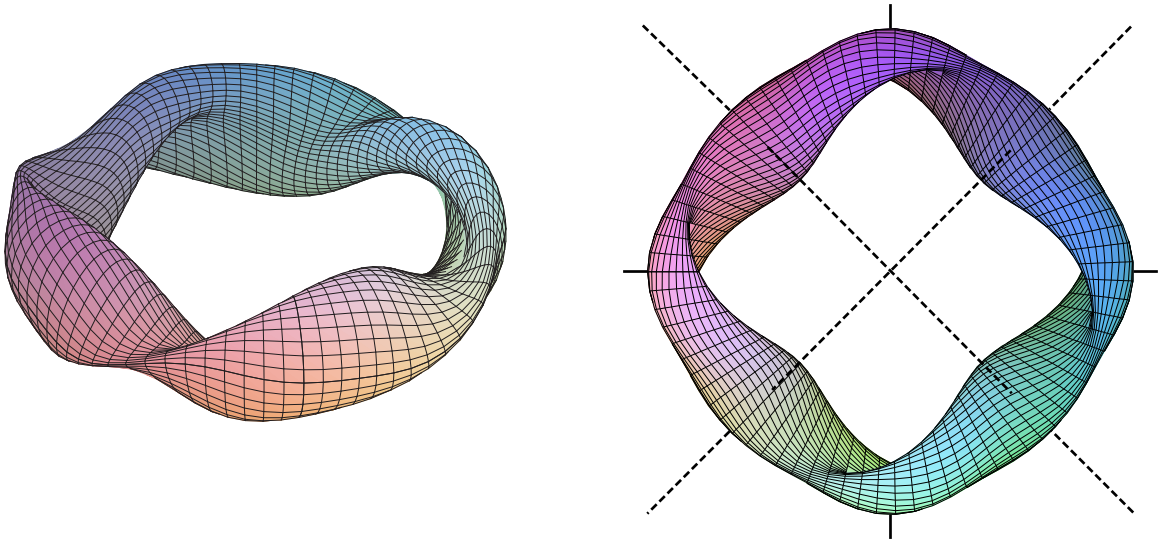

Figure 12.2: Side (left) and top (right) view of a stellarator with $P = 4$. The field periods and the lines for the stellarator symmetry are denoted by short and dashed lines, respectively (here both types of lines do have the respective complementary feature).

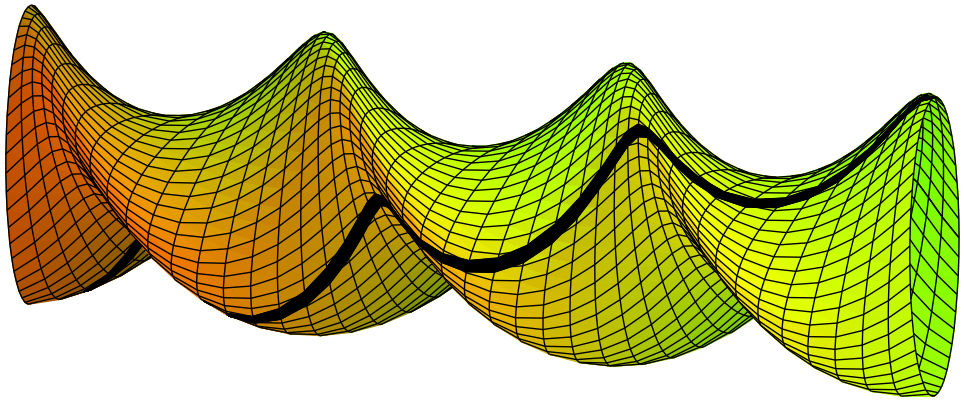

Figure 12.3: Three-dimensional view of one flux surface of a straight ℓ=2 stellarator (three field periods). The thick black line shows one field line.

12.1.4 Coil system

An important part in the engineering design of a stellarator is the question how a coil system must look like in order to produce the desired magnetic field. The classical coil system for

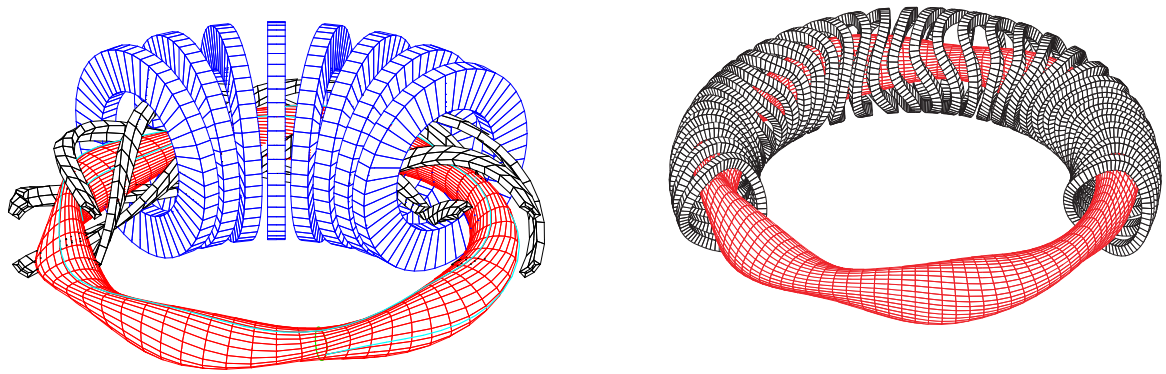

Figure 12.4: Classical (left) and modular (right) coil system for an ℓ=2 stellarator.

e.g. an ℓ=2 stellarator consists of groups of interlinked coils (Fig. 12.4 left): A set of planar coils generating the toroidal field component and four helical coils carrying currents running in alternating directions in neighboring coils[7] responsible for the helical field components. The drawback of this kind of coil system is that strong forces can arise between the interlinked coils thus making it difficult to build. Also it can only be used for relatively simple configurations due to its low flexibility with regard to design.

Another possibility for finding a suitable coil system comes from the following observation: If in a toroidal volume V a magnetic field is given that on the boundary surface ∂V is tangential it is possible to calculate a surface current distribution on a second surface outside of ∂V that generates this field; discretizing this current distribution then leads to a coil system[8]. This way of obtaining a coil system is crucial for the design of modern optimised stellarators since it allows to start from a given plasma shape, which e.g. is obtained by stellarator optimisation (see sec. 12.6), and then calculate the corresponding – so called – modular coil system, which consists of a set of non-planar coils.

12.2 Equilibrium

12.2.1 Equilibrium equations

The system of equations to be solved for a macroscopic fluid equilibrium follows from the general magnetohydrodynamic (MHD) equations by assuming $\partial/\partial t = 0$ and $\mathrm{v} = 0$

$$\mathrm{j} \times \mathrm{B} = \nabla p \,, \tag{12.2}$$

$$\nabla \times \mathrm{B} = \mu_0 \mathrm{j} \,, \tag{12.3}$$

$$\nabla \cdot \mathrm{B} = 0 \,. \tag{12.4}$$

Eq. (12.2) gives the balance between Lorentz force and pressure force while (12.3) to (12.4) are Maxwells equations. One immediate conclusion is $\mathrm{B} \cdot \nabla p = 0$, i.e. the pressure is constant along a field line and consequently – assuming the existence of flux surfaces – it must be constant on each flux surface. From $\mathrm{j} \cdot \nabla p = 0$ it follows that the current can only flow in a flux surface.

12.2.2 Straight stellarator

It was mentioned in the last section that a stellarator cannot be axisymmetric, so the simplest possible stellarator is a helical symmetric configuration, i.e. all the physical quantities (using cylindrical coordinates) depend only on r and $\varphi - kz$, where k is the parameter determining the length of a period.
For a vacuum field one has to solve the equation $\Delta\Phi = 0$ to obtain the magnetic potential (b_ℓ are free coefficients)

$$\Phi = B_0 z + \frac{1}{k} \sum_{\ell=1}^{\infty} b_\ell I_\ell(\ell k r) \sin \ell(\varphi - kz) \,.$$

[7] A configuration with currents flowing always in the same direction is called a torsatron; it does not have toroidal field coils, but instead needs two coils generating a vertical field component.

[8] Since the corresponding mathematical problem is not well posed there are many different coil systems giving nearly the same magnetic field. This allows to take into account engineering constraints in an optimisation procedure which combines aspects of field accuracy and coil flexibility.

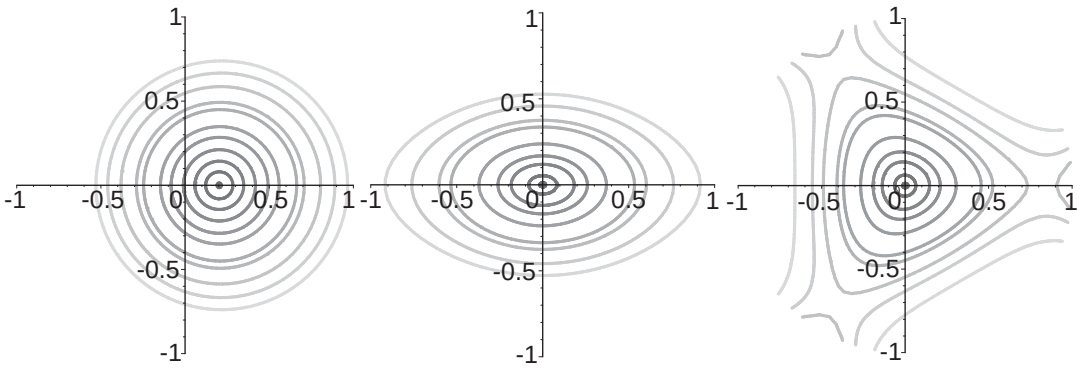

Figure 12.5: Intersection of $\Psi = const$ surfaces with the $z = 0$ plane for an $\ell = 1,2,3$ stellarator (from left).

From this follows an expression for the magnetic surfaces for a general straight stellarator

$$\Psi = B_0 \frac{kr^2}{2} - r \sum_{\ell=1}^{\infty} b_\ell I'_\ell(\ell kr) \cos \ell(\varphi - kz) = const \ . \tag{12.5}$$

Fig. 12.5 shows the cross section of stellarators each having only one ℓ component; due to the helical symmetry the curves rotate around the origin for increasing z. Note that the ℓ=1 stellarator is the only one with a non-straight magnetic axis.

Since straight configurations are only of theoretical interest we will in the following always assume toroidal topology.

12.2.3 Magnetic coordinates

Typical for a fusion plasma is the extremely high degree of anisotropy introduced by the magnetic field. As an order of magnitude estimate for the perpendicular and parallel length scale one can take the ion gyroradius which is of the order of some 10^{-2} m and the parallel mean free path of a particle which is around some 10^3 m, respectively. Thus it is highly advantageous to have at one's disposal a coordinate system in which the field line can be described by a simple functional form and a separation of the perpendicular and parallel direction is easy.

The so called magnetic coordinates (s, ϑ, φ) are a special curvilinear coordinate system fulfilling these requirements. Here $s \in [0:1]$ is the flux surface label – using magnetic coordinates requires the assumption that nested flux surfaces exist everywhere – and $\vartheta, \varphi \in [0:1]$ are angle-like coordinates. The geometric complexity of the configuration thus becomes hidden in the metric tensor g_{ij}. For calculations in this coordinate system one can use the formalism of tensor calculus.

In magnetic coordinates the magnetic field has the simple form

$$\mathrm{B} = \frac{1}{\sqrt{g}} \left(F'_\mathrm{T} \mathrm{r}_{,\varphi} + F'_\mathrm{P} \mathrm{r}_{,\vartheta} \right) ,$$

where $F'_\mathrm{T}, F'_\mathrm{P}$ is the s derivative of the toroidal $(F_\mathrm{T}(s))$ and poloidal $(F_\mathrm{P}(s))$ magnetic flux, $g^{1/2}$ is the determinant of the metric tensor and $\mathrm{r}_{,\varphi}, \mathrm{r}_{,\vartheta}$ are the covariant basic vectors. This expression shows that in magnetic coordinates the field lines are just straight lines $\vartheta = \iota \varphi$ with the rotational transform given by $\iota = F'_\mathrm{P}/F'_\mathrm{T}$.

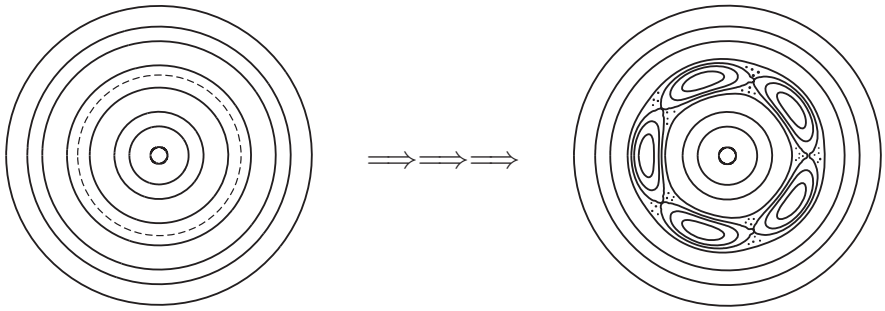

Figure 12.6: Left: Equilibrium with nested flux surfaces (the resonant surface is shown dashed).
Right: Equilibrium with perturbation, ergodic regions are indicated with dots.

12.2.4 Magnetic islands

One vital question for a fusion device is if it possesses nested flux surfaces or not.

Because of axisymmetry this question is simple to answer for a tokamak. Its symmetry allows to reduce the MHD equilibrium equations to one elliptic equation for the flux function $\Psi(r,z)$: the Grad-Shafranov-Equation

$$\left(r\frac{\partial}{\partial r}\frac{1}{r}\frac{\partial}{\partial r}+\frac{\partial^2}{\partial z^2}\right)\Psi+\mu_0 r^2\frac{\partial p(\Psi)}{\partial\Psi}+\frac{\mu_0}{8\pi^2}\frac{\partial I^2(\Psi)}{\partial\Psi}=0\,, \tag{12.6}$$

where $p(\Psi)$ and the current distribution $I(\Psi)$ are arbitrary functions. The fact that p only depends on Ψ ensures a constant pressure on each flux surface. Specifying profiles for p and I and imposing boundary conditions on Ψ (e.g. $\Psi=0$ at the given plasma boundary) this (in general) nonlinear equation can be solved and directly gives the flux surfaces. Thus there is no problem for axisymmetric equilibria.

For three-dimensional configurations it is generally not possible to show that a flux function exists making it very complicated to obtain information about the existence of flux surfaces.

The complications arising in connection with three-dimensionality can be seen by the following gedankenexperiment: Imagine bending a straight stellarator, which always possesses flux surfaces (see (12.5)), into a torus. This process can be regarded as adding perturbations with Fourier amplitude $\mathscr{P}_{mn}$ to the original straight equilibrium in order to produce the new toroidal one. It can be shown that the surface which is in resonance with the perturbation $\mathscr{P}_{mn}$ will break up into a chain of islands separated by X-points[9]. The latter are surrounded by ergodic regions where the field lines move chaotically filling out a volume instead of a surface[10]. This is illustrated in Fig. 12.6 where the effect of an $m=5$ perturbation on an equilibrium with flux surfaces is sketched.

How this looks like for a real equilibrium is shown in Fig. 12.2.4. Here a chain with large islands (light grey) is located around the flux surface where the ι profile crosses $5/5$ (note that

[9]These islands are called *natural* in order to distinguish them from island caused by effects external to the equilibrium, e.g. small errors in the coils. For natural islands the Fourier number n must be a multiple of the number of field periods.

[10]All this is analogous to nonlinear dynamics where it is shown that perturbations added to an integrable system lead to a destruction of the resonant tori in phase space (see the Poincaré-Birkhoff and Kolmogorov-Arnold-Moser (KAM) theorem). This analogy can be put on rigorous footing by noticing that the field lines in a torus can be described by a Hamiltonian function.

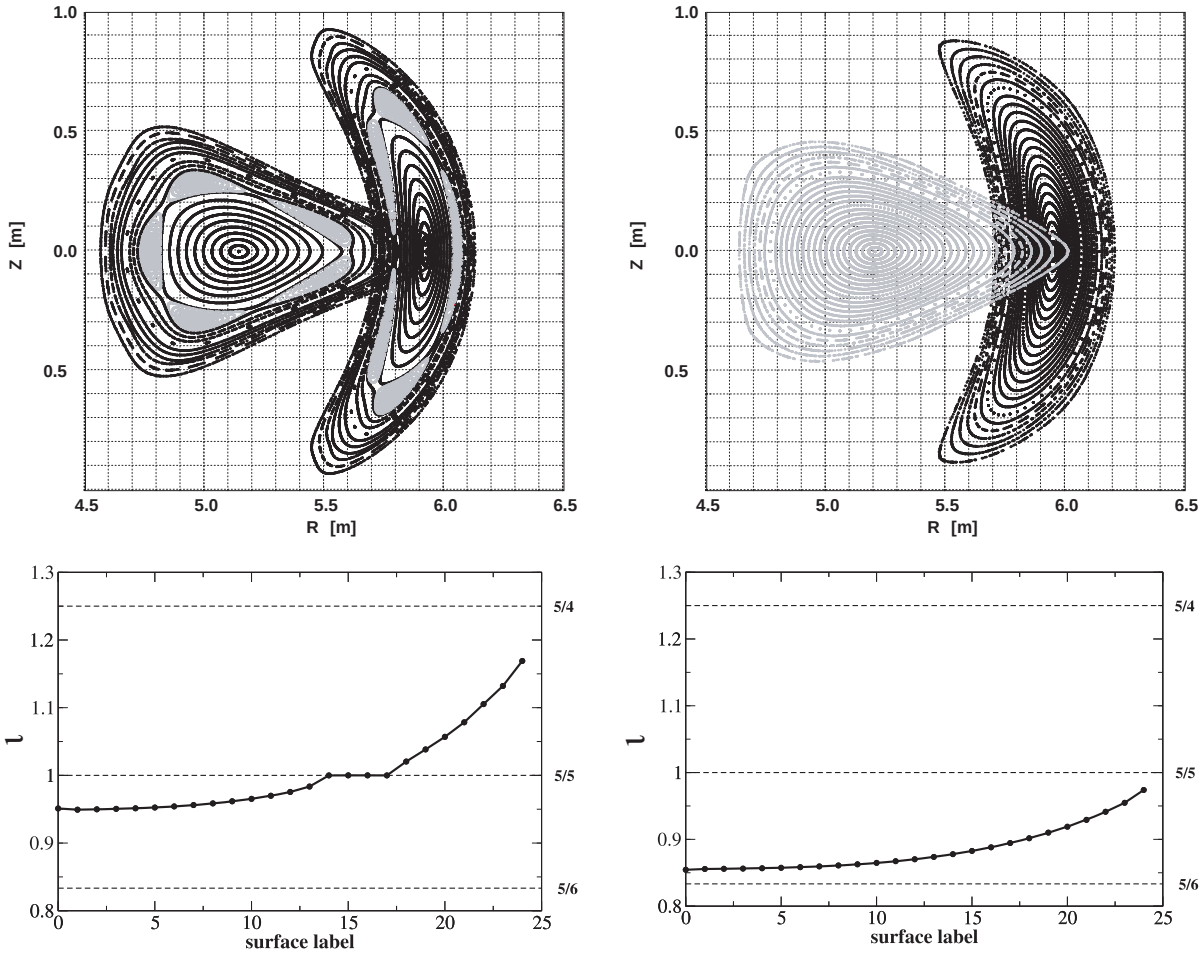

Figure 12.7: Poincaré plots of two Wendelstein 7-X variants with different ι profiles.
Left: ι profile including the $5/5$ resonance.
Right: The same calculation but with a downward shifted profile avoiding this resonance.

the ι profile is constant inside the region occupied by the islands). For a shifted ι profile that does not contain $5/5$ these islands disappear.

The width w of an island can be estimated by

$$w = 4\sqrt{\frac{R}{m\,\iota'}\,\mathscr{P}_{mn}}\,. \tag{12.7}$$

Using e.g. values typical of Wendelstein 7-X and assuming a perturbation amplitude $\mathscr{P}_{mn} \approx 10^{-4}$ one finds that this perturbation can lead to islands of width $w/a \approx 0.2$ showing that even a small perturbation can create relatively large islands. The danger of islands lies in the fact that they normally lead to a strong deterioration of plasma confinement by allowing particles to quickly cross the region occupied by the island chain. The existence of islands in an equilibrium is an inherent feature of three-dimensional systems, so it is of major interest for stellarator theory to design configurations in such a way that islands are so small that they have nearly no effect on confinement.

Eq. (12.7) shows that rational numbers n/m with low m – so called low order rationals – produce larger islands than rationals with high m and that high shear leads to smaller islands than

low shear. Hence there are two strategies to arrive at three-dimensional equilibria with small islands:

- High shear minimises the influence of low order rationals but makes it necessary for the ι profile to cross many rationals. This strategy is followed in e.g. LHD.
- Low shear allows to place the flat ι profile in a region where there are no low order rationals. This line is followed by Wendelstein 7-X.

12.2.5 3D equilibrium codes

In order to describe an equilibrium (without bootstrap current) one has to specify the radial profile of the pressure and the shape of the outer flux surface $\mathscr{S}$ (along with the boundary condition that B must be tangent to $\mathscr{S}$). For a stellarator the condition $J = 0$ is imposed – the ι-profile then follows – while for a tokamak either the current or the ι-profile must be given. Solution of (12.2) to (12.4) then gives the magnetic field inside $\mathscr{S}$.
The shape of $\mathscr{S}$ is usually described using the parametric representation

$$\begin{aligned} R &= \sum_{m,n} R_{m,n} \cos(mU - nV) , \\ Z &= \sum_{m,n} Z_{m,n} \sin(mU - nV) , \\ \phi &= V , \end{aligned}$$

where $U,V \in [0:2\pi]$ are parameters and (R,Z,ϕ) are cylindrical coordinates, together with the set of Fourier coefficients $R_{m,n}, Z_{m,n}$.

Since in three dimensions the existence of flux surfaces is not guaranteed the structure of a solution can only be found a posteriori making it non-trivial to obtain pressure profiles which are constant on each flux surface.

The numerical calculation of stellarator equilibria is e.g. carried out with the help of two tools: The Variational Magnetic Equilibrium Code (VMEC) and the Princeton Iterative Equilibrium Solver (PIES).

VMEC

In this approach one *assumes* that the equilibrium has nested flux surfaces, i.e. one ignores the possibility of islands. As we have seen this assumption is generally not true for three-dimensional equilibria. Thus the solution given by the code serves only as an approximation to the exact equilibrium and can be rather bad if this has large islands[11]. Whether the approximation is a good one can only be tested afterwards.

Under this assumption making the energy functional

$$W = \int \left(\frac{B^2}{2\mu_0} + \frac{p}{\gamma - 1} \right) dV$$

[11] Instead of islands the approximative solution shows divergences in the parallel current density $j_\parallel$ at the resonant surfaces. In the exact solution $j_\parallel$ stays finite everywhere.

(γ: adiabatic coefficient) stationary, together with the additional constraint that the mass inside each flux surface does not change by the variation, is equivalent to solving the equilibrium (12.2) to (12.4).
The attractiveness of this approach lies in the fact that it is computationally much faster than computing an equilibrium allowing for islands. Thus VMEC has become the standard tool for calculating stellarator equilibria.

PIES

The PIES code permits islands in the equilibrium solution[12]. It solves the MHD equilibrium equations employing a Picard iteration, i.e. starting with an initial guess B^0 – obtained with e.g. VMEC – it solves the equations

$$\nabla \times \mathrm{B}^{n+1} = \mu_0 \mathrm{j}\,(\mathrm{B}^n)\ , \qquad \nabla \cdot \mathrm{B}^{n+1} = 0\ ,$$

where $\mathrm{j}\,(\mathrm{B}^n)$ is found from solving

$$\mathrm{j} \times \mathrm{B}^n = \nabla p\ , \qquad \nabla \cdot \mathrm{j} = 0\ .$$

The drawback of this approach is its extremely slow convergence making the calculation of an equilibrium very time consuming[13].

12.3 Pfirsch-Schlüter current

One goal of fusion power plant design is to achieve $\beta := 2\mu_0\, p/B^2$ values of about 5% (averaged in the confinement region). Connected with an increase in the plasma pressure is a shift of the plasma center with respect to the outer plasma surface (Shafranov shift). If this shift is too large the plasma center comes close to the outer plasma surface which may cause problems. So, cautiously one limits β to β_{eq} such that the plasma center keeps a safe distance from its boundary.

For an axisymmetric equilibrium and classical stellarators the Shafranov shift Δ is given approximately by $\Delta/R = \beta/\iota^2$. Usually one defines that β_{eq} is reached if $\Delta = a/2$ resulting in $\beta_{\mathrm{eq}} \approx \iota^2/A$. Typical values are $A \approx 3,\ \iota \lesssim 1$ for a tokamak and $A \approx 10,\ \iota < 1$ for a stellarator. While for a tokamak a useful β-limit results a stellarator with too small ι and large A has a β_{eq} that is too low for fusion applications.

The way out of this difficulty is to use the freedom given by the three-dimensional structure of a stellarator to design $|\mathrm{B}|$ in such a way as to reduce the Shafranov shift.

First we have to understand what causes the Shafranov shift: From the MHD equilibrium relation $\mathrm{j} \times \mathrm{B} = \nabla p$ one obtains the diamagnetic current $\mathrm{j}_\perp = \mathrm{B} \times \nabla p/B^2$. Splitting the quasineutrality relation $\nabla \cdot \mathrm{j} = 0$ into a parallel and perpendicular component gives $\nabla \cdot \mathrm{j}_\parallel = -\nabla \cdot \mathrm{j}_\perp$. The diamagnetic current thus gives rise to a parallel current called the Pfirsch-Schlüter (PS) current. As a result one gets

$$\nabla \cdot \mathrm{j}_\parallel = -\frac{2}{B^3}\,(\nabla p \times \mathrm{B}) \cdot \nabla |\mathrm{B}| = -\frac{2|\nabla p|}{B}\,\kappa_{\mathrm{g}}$$

[12] A second code allowing for islands is the HINT code which uses the time dependent MHD equations.

[13] An equilibrium calculation for the W7-X configuration using VMEC needs a few minutes computing time on an SX-5 vector computer; the analogous calculation using PIES takes approximately one week.

with κ_g the geodesic curvature[14]. Note that ∇p is normal to the flux surface and, as a consequence, only the derivative of $|\mathrm{B}|$ in the flux surface enters this expression. The geodesic curvature will also play an important role in the next section and thus will show up as a quantity of main importance for stellarators.

For a simple axisymmetric configuration this equation can easily be solved and gives the PS current as

$$j_\parallel = \frac{\partial p}{\partial r}\frac{2}{\iota B_0}\cos\vartheta \ .$$

This parallel current density – flowing in different directions at the inside respectively outside of the torus – leads to a vertical magnetic field that in combination with the toroidal and poloidal field results in an outward shift of the plasma: The Shafranov shift.

For a helically symmetric configuration with $\mathrm{B} = \mathrm{B}(r, \vartheta - kz)$ one finds $j_\parallel \sim 1/(\iota - 1)$. It follows for $\iota \ll 1$ that the magnitude of $j_\parallel$ (and consequently the Shafranov shift) in a helically symmetric configuration is much smaller than in an axisymmetric one. Using the VMEC code it is possible to construct quasi-helically symmetric stellarator equilibria[15] for which even a β of 40% leads to nearly no Shafranov shift.

This observation shows the strategy how to reduce the Shafranov shift and increase β_{eq} for a stellarator: Using the freedom given by the three-dimensional structure one can design $|\mathrm{B}|$ and with it the geodesic curvature in such a way as to minimize the Shafranov shift (more details on this will be given later in sec. 12.6). Taking the volume averaged ratio of the parallel to the diamagnetic current $\left\langle j_\parallel^2 / j_\perp^2 \right\rangle$ as a measure for the importance of the PS current one can see the progress of stellarator design with time: While for the classical (non-optimised) stellarator W7-A this ratio is around 12 it can be reduced to three for the partly optimised W7-AS and then to 0.5 for the fully optimised W7-X (corresponding to $\beta_{\mathrm{eq}} \approx 5\%$). This is illustrated in Fig. 12.8, where W7-AS for $\beta \approx 2\%$ shows a noticeable Shafranov shift while it is hardly visible in W7-X for $\beta \approx 5\%$.

12.4 Neoclassical transport

12.4.1 Neoclassical transport

The main aim of neoclassical (transport) theory is to calculate the collisional transport of particles and heat – e.g. radial diffusion coefficients for particle and heat fluxes – as functions of the collision rates and the electric field taking into account the toroidal geometry of a fusion device[16]. The theoretical base for neoclassical calculations is collisional kinetic theory especially its drift kinetic simplification.

Fig. 12.9 gives an overview on the neoclassical transport for tokamaks and stellarators. Depending on ν_{ei} (ion-electron collision frequency) one finds different regimes: The Pfirsch-Schlüter, plateau and banana regime for high, intermediate and low collisionality, respectively.

[14] Using a triad $(\mathrm{b}, \mathrm{n}, \mathrm{n}\times\mathrm{b})$ such that b is the unit B-field vector and n is the unit normal vector of the flux surface the curvature $\kappa := (\mathrm{b}\cdot\nabla)\mathrm{b}$ can be written as $\kappa = \kappa_n \mathrm{n} + \kappa_g \mathrm{n}\times\mathrm{b}$ with the geodesic and normal curvature κ_g, κ_n. In contrast to the normal curvature the geodesic curvature is an intrinsic property of the surface geometry.

[15] In toroidal topology helically symmetric equilibria do not exist; one has to resort to so called quasi-helically symmetric equilibria (see sec. 12.4.2).

[16] In cylinder geometry one speaks of classical transport theory.

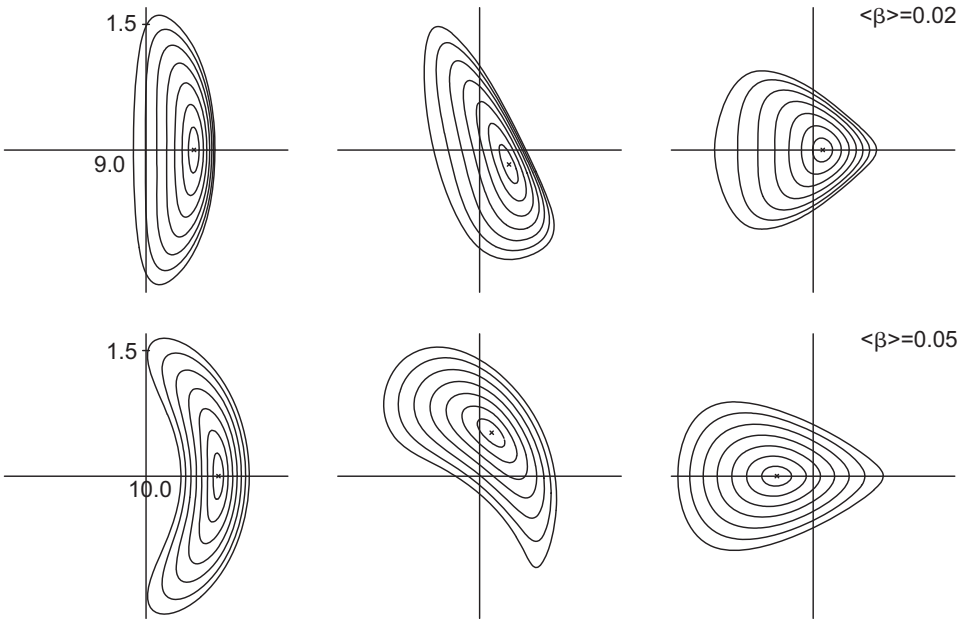

Figure 12.8: Toroidal cuts (at $\varphi = 0, 2\pi/20, 2\pi/10$) for W7-AS (top) and W7-X (bottom).

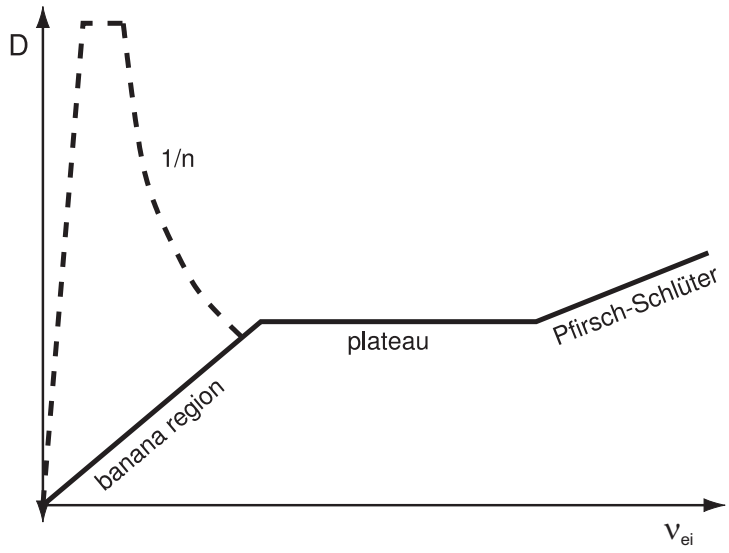

Figure 12.9: Neoclassical diffusion coefficient as a function of collision rate. Black: tokamak. Dashed: additional regimes for a stellarator.

The three-dimensional geometry of a stellarator can lead to regimes not present in a tokamak. In the long mean free path regime the helical variation of $|B|$ (helical ripple) for a classical stellarator leads to the so called $1/\nu$ regime[17] which is of paramount importance since it can lead to extremely large neoclassical losses potentially dangerous for a stellarator fusion device.

For the PS regime a fluid treatment of radial diffusion is possible: For a cylinder the equilibrium equation and Ohm's law ($\eta = m_e/(ne^2)\nu_{ei}$)

$$\mathrm{j} \times \mathrm{B} = \nabla p\,, \qquad \mathrm{E} + \mathrm{v} \times \mathrm{B} = \eta \mathrm{j}$$

[17] If an electric field is included a $\nu^{1/2}$ regime can also be present.

give the perpendicular velocity of the fluid as

$$\mathrm{v}_\perp = \frac{\mathrm{E}\times\mathrm{B}}{B^2} - \frac{1}{B^2}\eta\nabla p$$

consisting of the E×B-drift and a radial drift induced by collisions. Using the last term to calculate the radial particle flux $\Gamma = nv_\perp$ and comparing this with Fick's law $\Gamma = -D\nabla n$ leads to the classical diffusion coefficient (ρ_e: electron gyroradius)

$$D_\mathrm{c} = \left(1+\frac{T_\mathrm{i}}{T_\mathrm{e}}\right)\rho_\mathrm{e}^2\nu_\mathrm{ei}\ . \tag{12.8}$$

A more complicated calculation in toroidal geometry[18] including the PS current gives an additional factor (PS factor) and leads to the larger neoclassical diffusion coefficient $D_\mathrm{nc} = (1+\iota^{-2})D_\mathrm{c}$.

To understand the origin of the banana and $1/\nu$ regime one has to look at the motion of particles. For this task it is sufficient to use the guiding center equations of motion[19]

$$\dot{\mathrm{R}} = v_\parallel \mathrm{b} + \mathrm{v}_\mathrm{d}\ , \tag{12.9}$$

$$\dot{v}_\parallel = -\mu\,\mathrm{b}\cdot\nabla|\mathrm{B}|\ , \tag{12.10}$$

$$\dot{\mu} = 0 \tag{12.11}$$

with the perpendicular drift velocity ($\mathrm{b} := \mathrm{B}/|\mathrm{B}|$ and $\mu := v_\perp^2/(2B)$ the magnetic moment per unit mass)

$$\mathrm{v}_\mathrm{d} = \frac{\mu B + v_\parallel^2}{B\Omega}\,\mathrm{b}\times\nabla|\mathrm{B}|\ . \tag{12.12}$$

From these equations[20] follows the very important fact that particles with low enough energy can be trapped around a minimum of |B| while for higher energies they can stream (nearly) freely. A particle trapped in a minimum of B shows a fast bouncing motion superposed onto a slow drift. This slow drift motion can be separated by averaging over the fast bouncing motion (bounce average) and gives the motion of the bounce center[21] $\langle\mathrm{v}\rangle = 1/\tau_\mathrm{b}\oint \mathrm{v}\,dt$ (τ_b: bounce time).

In a tokamak trapped particles move on so called banana orbits with radial width Δ_b. The center of a banana orbit slowly drifts toroidally but not radially, i.e. $\langle\mathrm{v}\rangle$ has only a toroidal component. Collisions cause particles to jump from one banana orbit to another thus leading to a random walk with step size Δ_b resulting in a diffusion coefficient (given by $D = l^2/\tau$, where l is the diffusion step length and τ the collision time[22]) in the banana regime as $D_\mathrm{b} = \Delta_\mathrm{b}^2\nu_\mathrm{ei}$.

As a very simple model for |B| in a stellarator one often uses

$$B = B_0\left(1-\varepsilon_\mathrm{t}\cos\vartheta - \varepsilon_\mathrm{h}\cos\left(\ell\vartheta - P\varphi\right)\right)\ ,$$

[18] This can most easily be seen by using the general relation $\Gamma = n\int \eta\, j^2 dS/(|\nabla p|)$ (with $\eta_\perp \approx 2\eta_\parallel$) connecting the particle flux Γ with the resistive dissipation integrated over one flux surface. Thus the additional dissipation caused including parallel (PS) currents leads to an increase in the particle flux by the PS factor.

[19] See the lecture "Introduction to fusion plasmas".

[20] Note that (12.10) follows from (12.9), (12.11) and energy conservation.

[21] To obtain the drift kinetic theory the fast gyrating particle had been replaced via averaging by its slowly drifting guiding center. Now drift kinetic is further reduced to a theory with the bounce center as the slowly moving basic entity obtained by averaging over the comparatively faster bounce motion of the guiding center.

[22] One can show that only collisions between unlike particle species lead to particle diffusion, while for heat diffusion collisions between like particle species are important.

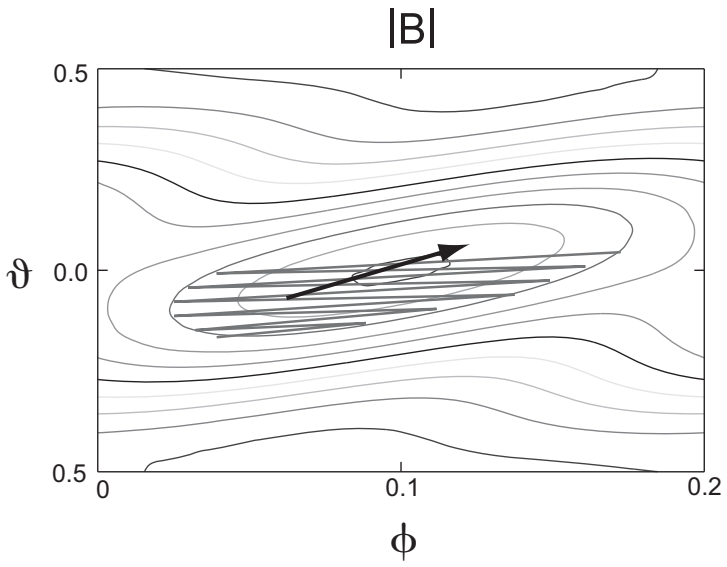

Figure 12.10: Motion of a trapped particle near a minimum of B (contour lines). The red line shows the actual motion of the guiding center while the black arrow shows the motion of the bounce center.

where $\varepsilon_{t,h}$ measures the strength of the toroidal or helical component, respectively.
For $\varepsilon_t = 0$ the bounce center drifts along the helical minimum (helically trapped particle) and $\langle \mathrm{v} \rangle$ has no component in the radial direction.
Adding a toroidal component ($\varepsilon_t \neq 0$) leads to a net radial component of $\langle \mathrm{v} \rangle$ which can be computed by performing the bounce average of

$$v^r = \mathrm{v_d} \frac{\nabla r}{|\nabla r|} = \frac{\mu B + v_\parallel^2}{\Omega} \kappa_g \, .$$

This result can be used to estimate a diffusion coefficient by noting that the diffusion step length is $l = \langle v_r \rangle / (\nu_{ei})$.

$$D_{1/\nu} = f_t \frac{\langle v^r \rangle^2}{\nu_{ei}} \sim f_t \frac{T^{\frac{7}{2}}}{nB^2} \kappa_g^2 \tag{12.13}$$

(f_t: fraction of trapped particles).

This equation also shows the crucial role played by the geodesic curvature; its importance for the PS-current we have already seen in sec. 12.3. Thus decreasing the size of the geodesic curvature in the region where particles are trapped is beneficial for minimizing the neoclassical transport.

Summarizing the above picture one can say that caused by the toroidal curvature a helically trapped particle in a stellarator in general acquires a radial drift eventually leading to its loss; these particles are responsible for the $1/\nu$ regime.

One can argue more generally: Due to its axial symmetry the toroidal momentum is a conserved quantity for particle motion in a tokamak and it follows as a consequence that the maximal deviation of a (trapped or untrapped) particle from the flux surface is limited; this results in a relatively low neoclassical transport. The situation is different for a stellarator: Caused by its three-dimensional structure a conserved quantity and the related constraint on the orbit width does in general not exist[23] possibly leading to rapid particle losses showing up as the $1/\nu$ regime.

[23] Quasi-symmetric configurations (see next section) do have conserved quantities.

The strong dependence of $D_{1/\nu}$ on T is the cause why the $1/\nu$ regime is dangerous for a (classical) stellarator: The high temperature necessary for fusion leads to losses which are too high for a fusion power plant to work. So in order to construct a viable stellarator power plant it is of utmost importance to reduce this kind of neoclassical losses. From (12.13) one can see the possible ways how to do this: Designing a stellarator in such a way that the particles get trapped in a region with small geodesic curvature leads to a small neoclassical radial transport. This path is followed in the design of W7-X and as a result neoclassical losses in W7-X are small enough to be compatible with fusion power plant requirements.

12.4.2 Quasi symmetry

Using magnetic coordinates (s,ϑ,φ) (see sec. 12.2.3) the guiding center equation of motion for $\dot{\mathrm{R}}$ (12.9) can be written as

$$\dot{s} = \frac{1}{\sqrt{g}D}\frac{e\rho_\parallel}{m}\left(\rho_{\parallel,\vartheta}I-\rho_{\parallel,\varphi}J\right), \tag{12.14}$$

$$\dot{\vartheta} = \frac{1}{\sqrt{g}D}\frac{e\rho_\parallel}{m}\left[-F_P'-\left(I\rho_\parallel\right)_{,s}+\left(\tilde{\beta}\rho_\parallel\right)_{,\varphi}\right], \tag{12.15}$$

$$\dot{\varphi} = \frac{1}{\sqrt{g}D}\frac{e\rho_\parallel}{m}\left[-F_T'+\left(J\rho_\parallel\right)_{,s}-\left(\tilde{\beta}\rho_\parallel\right)_{,\vartheta}\right] \tag{12.16}$$

with $\rho_\parallel := mv_\parallel/(eB)$, $D := 1+\rho_\parallel \mathrm{B}\cdot\mathrm{j}/B^2$, $\sqrt{g} := -(JF_P'+IF_T')/B^2$ and $\tilde{\beta}$ a function that can be calculated from B.

This formulation shows that the motion of the guiding center formulated in the special coordinate system of magnetic coordinates depends *only* on the function $B(s,\vartheta,\varphi)$ (magnetic topography) but not on the spatial structure of the flux surfaces which would show up as the metric tensor. Formulated sloppily one can say that in magnetic coordinates the particles do not *see* the real geometry of the configuration but only the magnetic topography. This observation leads to the notion of quasi-symmetry[24] as a symmetry of the magnetic topography formulated in magnetic coordinates; the configuration needs not possess a symmetry in real space.

Configurations with $B = B(s,\vartheta)$ or $B = B(s,k\vartheta - P\varphi)$ (k,P: integer parameters) are called quasi-axisymmetric or quasi-helical symmetric, respectively. They can be realized in a torus and examples are known (e.g. see Fig. 12.11). On the other hand the quasi-symmetries $B = B(s,\varphi)$ and $B = B(s)$, which would guarantee that a particle stays exactly at a flux surface[25], can not be achieved for toroidal systems.

For a configuration possessing a quasi-symmetry it follows from the guiding center equations of motion that there exists a conserved quantity[26]. This conserved quantity limits the maximal excursion of a particle from the flux surface (as noted in the last section) and thus eliminates the cause for the existence of the $1/\nu$ regime. Detailed calculations indeed show that e.g.

[24] The qualifier *quasi* is meant to indicate that this symmetry only exists for B in a specially chosen coordinate system. Additionally it hints that quasi-symmetry is attainable in a three-dimensional configuration only to some approximation but not exactly.

[25] A configuration fulfilling $B = B(s)$ exactly would be called isodynamic.

[26] For e.g. quasi-helical symmetry the quantity $F_T - F_P - \rho_\parallel(I+J)$ is conserved.

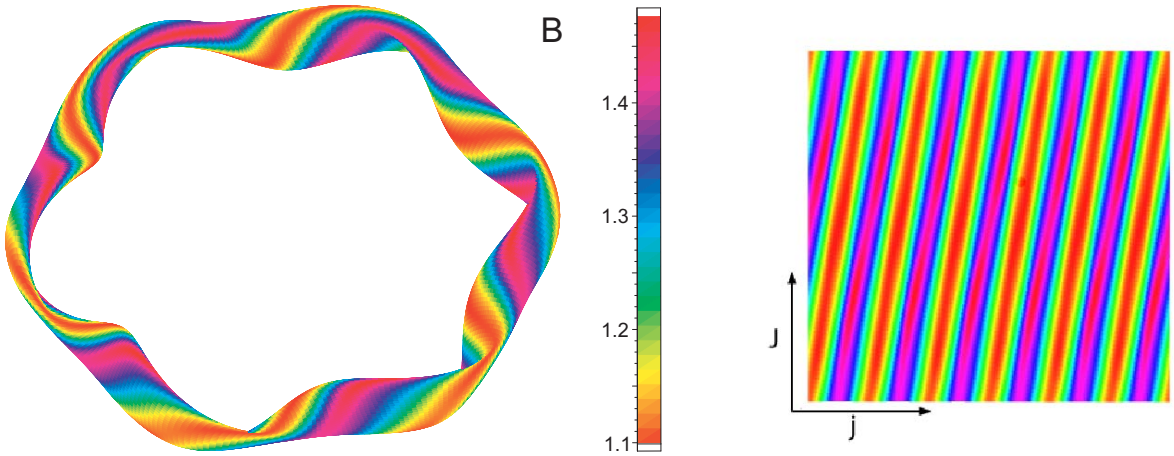

Figure 12.11: Quasi-helical symmetric stellarator in real space (left) and magnetic coordinates (right) (one flux surface is shown, color indicates the magnitude of B).

a quasi-helical symmetric stellarator shows similar neoclassical transport as a corresponding tokamak.

As an illustration Fig. 12.11 shows one flux surface of a quasi-helical symmetric configuration with six field periods. In real space it has a complicated three-dimensional structure and shows no apparent symmetries other than the ones described in sec. 12.1.3. After transformation to magnetic coordinates the helical symmetry of B becomes manifest.

Quasi-helical symmetric configurations have a bootstrap current which endangers their usefulness. Thus one considers another class of configurations, called quasi-isodynamic, where the second adiabatic invariant $J := \int v_{\|} dl$ (l: length along a field line) is nearly constant on the flux surfaces. In these configurations (without symmetry of B) the bounce center drifts poloidally. W7-X belongs to the class of quasi-isodynamic stellarators.

12.5 MHD stability

Since the vast field of stability quickly becomes very technical we will only give a short overview of the basic concepts of MHD stability.

Having found a plasma equilibrium configuration that meets the requirements described in the former sections it remains to show if a small perturbation applied to the system grows or decays with time. In the first case the equilibrium configuration is unstable and plasma confinement may be destroyed quickly.

Formally one uses time dependent equations, symbolically written as $\partial/\partial t g = \mathscr{M} g$ with g denoting the dynamical variables and $\mathscr{M}$ a nonlinear operator. The solution is split into a time independent part representing the equilibrium under investigation and a time dependent part describing the perturbation: $g(\mathrm{r},t) = g_0(\mathrm{r}) + g_1(\mathrm{r},t)$. Assuming small perturbations $g_1 \ll g_0$ the nonlinear operator $\mathscr{M}$ is linearized resulting in the linear operator $\mathscr{L}$. Usually one is interested only in solutions behaving exponentially in time[27] justifying the ansatz $g_1 =$

[27] Perturbations growing algebraically in time may exist but because of their slow growth normally are of no interest.

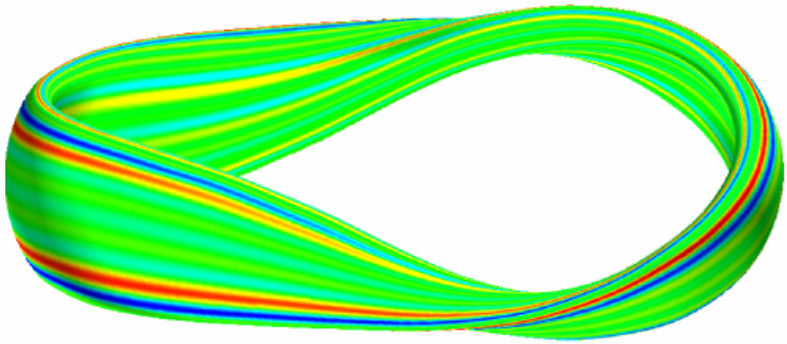

Figure 12.12: Eigenfunction for a ballooning mode. Shown is the pressure perturbation on a flux surface (high/low pressure is colored with red/green).

$\widetilde{g}(\mathrm{r})e^{-i\omega t}$ (with the complex eigenvalue ω). Specification of boundary conditions on $\widetilde{g}$ then leads to the eigenvalue problem $\mathscr{L}\widetilde{g} = \omega\widetilde{g}$. The equilibrium is unstable if $\mathrm{Im}(\omega) > 0$ showing that the initially infinitesimal perturbation is growing exponentially with time.

Since for MHD the operator $\mathscr{L}$ is self-adjoint its eigenvalue problem only has solutions with $\omega^2 \in \mathbb{R}$ and can be formulated as a variational problem: The system is unstable if a perturbation $\xi(\mathrm{r})$ exists such that $\delta^2 W[\xi] < 0$ where the functional[28] $\delta^2 W$ is given by

$$\delta^2 W[\xi] = -\frac{1}{2}\iiint \left[S^1 + S^2 + S^3 + S^4 + S^5\right] d^3r \,.$$

The expressions for $S^1(\xi)\ldots S^5(\xi)$ are complicated and instead of giving the details here it suffices to note their general properties: S^1, S^2 and S^5 describe the influence of field line bending, field compression and fluid compression, respectively; they act stabilizing on $\delta^2 W$. In contrast to this S^3 and S^4 are indefinite and depend on the pressure gradient p' and the parallel current density $j_\parallel$; these two terms can cause $\delta^2 W$ to become negative. The instabilities caused by these terms are called pressure or current driven.

From the large zoo of MHD instabilities we briefly look at the kink and the ballooning instability: The kink instability is driven by a parallel current and consequently does not exist in a stellarator. Pressure is the energy source for the ballooning instability which bear this name since e.g. in a tokamak it has its maximal amplitude in the region of unfavorable curvature (i.e. at the outside of the torus). This instability disappears for fixed pressure gradient if the pressure is low enough and thus provides a stability β-limit. W7-X is designed in such a way that it is stable against the ballooning instability for $\beta \lesssim 5\%$. For a tokamak large scale kink and ballooning instabilities limit the operation regime while for a stellarator only kink modes have been found experimentally, hitherto. As an illustration Fig. 12.12 shows a ballooning instability in a quasi-axially symmetric stellarator above the stability β-limit. This picture also demonstrates a very general structural property of modes in a magnetized plasma: The wavelength in the direction perpendicular to the field lines is much smaller than the wavelength along the field line. This high degree of anisotropy of the instability reflects the anisotropy introduced by the magnetic field.

[28] $\delta^2 W$ is the second variation of the functional W from sec. 12.2.5.

12.6 Stellarator optimisation

In sec. 12.2 to sec. 12.5 we have discussed four points which are of vital importance for a stellarator as a fusion device. Stellarator optimisation is the comprehensive framework where these points (and other) are put together in order to arrive at a viable design for a fusion device. Crucial for optimisation is the high degree of freedom provided by the three-dimensional structure of a stellarator.

Since the main goal of stellarator optimisation is to find equilibria that have good confinement properties one first has to quantify what one understands by *good confinement properties*. This is done by assigning to each equilibrium configuration from the configuration space Con[29] a real number as a quality measure by providing a function $\mathcal{Q} : \mathrm{Con} \mapsto \mathbb{R}$. The construction of this function requires the consideration of the physics one regards as relevant for confinement and the design targets.

In the design of W7-X one required:

- Nested magnetic surfaces with small islands;
- Small Shafranov shift for $\beta \approx 5\%$;
- Small neoclassical transport;
- MHD stability, especially stability against ballooning modes for $\beta \approx 5\%$;
- Good α-particle confinement:
  α-particles are needed for the heating of the plasma and thus they must not leave the fusion device in a time shorter than their slowing down time;
- Small bootstrap current:
  This is another current driven by the pressure gradient. In contrast to the PS-current it gives rise to a total toroidal current causing a shift in ι with increasing β. Since ι control is crucial for the confinement properties (see e.g. sec. 12.2.4) such a shift was considered to be undesirable[30];
- Feasible modular coils:
  For actually building a device constraints emerge motivated by engineering considerations regarding the design of the modular coils (e.g. a minimal distance between neighboring coils must be kept, the coil curvature cannot be too large). Some of them can be taken into account in the plasma optimisation.

In the optimisation procedure, which is carried out computationally, first an outer flux surface is specified from which (using VMEC) the corresponding equilibrium configuration is computed; based on this equilibrium the function $\mathcal{Q}$ is calculated. This procedure is repeated – employing an optimisation algorithm – with changed outer flux surface until $\mathcal{Q}$ has reached a maximum. When the optimised equilibrium has been found the actual coil system is calculated subsequently.

[29] Since we have seen in sec. 12.2.5 that an equilibrium (except for its profiles) can be uniquely defined by specifying its outer flux surface the space Con can be identified with the set of Fourier coefficients used in the representation of this surface.

[30] Quasi-axisymmetric configurations are an exception to this consideration.

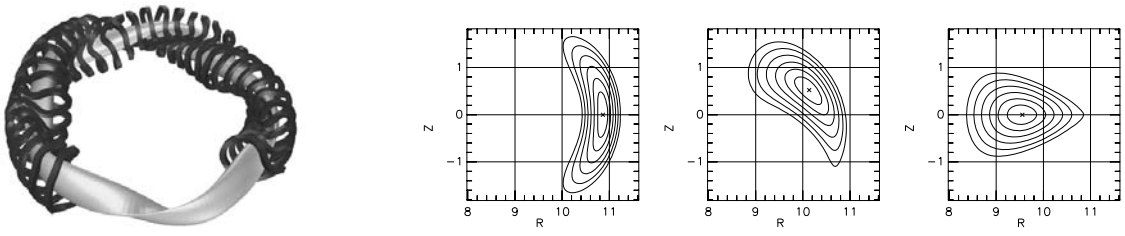

Figure 12.13: Left: Wendelstein 7-X plasma configuration with modular coils. Right: Toroidal cuts through the equilibrium configuration at $\phi = 0, 2\pi/20, 2\pi/10$.

Depending on the criteria and the design goals many different configurations can be found via optimisation. One possible result from this procedure, the optimised stellarator Wendelstein 7-X, is shown in Fig. 12.13.

References

There exists no good textbook about stellarator physics (as e.g. the book by Wesson for tokamaks). So everything is scattered in articles which generally are difficult to understand for the beginner. For this reason I here give references to some of the few more basic articles.

- A.H. Boozer, "What is a stellarator", Physics of Plasmas, vol. 1, p. 1647 (1998).
  A more advanced introductory article with an explanation of magnetic coordinates.
- G. Grieger et al., "Physics optimization of stellarators", Physics of Fluids, vol. B4, p. 2081 (1992).
  Overview on the physics design for Wendelstein 7-X; very condensed.
- G. Grieger et al., "Das Fusionsexperiment Wendelstein 7-X", Physikalische Blätter, vol. 49, p. 1001 (1993).
  Very basic article.
- W. Lotz et al., "Optimization, MHD mode and α-particle confinement behaviour of Helias equilibria", Proceedings IAEA (1992).
  Describes the optimisation leading to Wendelstein 7-X; advanced reading.
- K. Miyamoto, "Plasma Physics for Nuclear Fusion", The MIT Press (1989).
  Some chapters include stellarator specific issues.
- J. Nührenberg, "Quasi-symmetries in toroidal confinement", Europhysics News, p. 216 (Dez. 1998).
  A short introduction into the concept of quasi-symmetries.
- F. Wagner, "Stellarators and optimised stellarators", Transactions of Fusion Technology, vol. 29, p. 407 (1996).
  Very good introduction; recommended.
- F. Wagner, "Topics in toroidal confinement", Plasma Physics and Controlled Fusion, vol. 39, p. A23 (1997).
  Experimental oriented introduction.

- M. Wakatani, “Stellarator and Heliotron Devices”, Oxford University Press (1998). *One of the few books about stellarators but written very technically.*

Chapter 13

Experimental results from stellarators

Rudolf Brakel

13.1 Introduction

Stellarator, in a general sense, is the generic name for devices which confine a fusion plasma by a magnetic field that is completely generated by external coils, although it is modified to a certain extent by pressure driven currents flowing in the plasma itself. Therefore, stellarators do not need a large toroidal net plasma current for confinement, and with the advent of powerful auxiliary heating sources in the 1970's stellarators did no longer require the plasma current for ohmic heating. One of the milestones in stellarator research was the demonstration of net current free plasma sustainment by neutral beam injection in Wendelstein 7-A in 1981. Present-day stellarators are exclusively heated by electron cyclotron resonance heating (ECRH), ion cyclotron resonance heating (ICRH), neutral beam injection (NBI) and by combinations of these methods.

The absence of a large plasma current in a stellarator constitutes its inherent capability of steady state operation and there are no risks of current driven instabilities, in particular current disruptions. Beyond these obvious advantages stellarators have to prove their reactor potential by demonstrating that they can meet in particular the requirements of high β operation (required for economy), high confinement (required to reach ignition) and particle and power exhaust (required for density control, ash and heat removal). This chapter highlights, after introducing the various stellarator concepts, the experimental achievements with respect to these key issues.

13.2 The stellarator family

The use of external fields offers a large freedom of how to realize the key to magnetic confinement: The formation of toroidally closed nested magnetic surfaces by a helical twist of the magnetic field lines, the so called rotational transform ι ($\iota = 1/q$ is the inverse of the tokamak safety factor q. It denotes the angle in terms of 2π at which a magnetic field line is poloidally displaced after one toroidal turn). Accordingly, experimental work on stellarators is rather diversified. Small to medium size experiments are designed to test the feasability of various

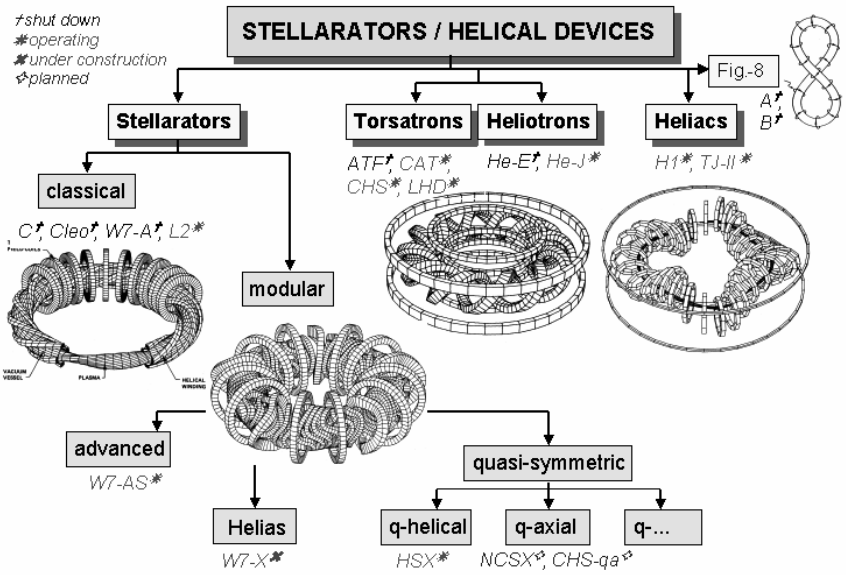

Figure 13.1: The different stellarator concepts. The coil systems shown are those of W7-A (classical l=2 stellarator), W7-AS (modular advanced stellarator), ATF (l=2 torsatron) and TJ-II (heliac).

construction and optimization principles. Superconducting large scale devices are going to close the gap to the large tokamaks with the additional option of steady state operation.

A genealogy of the different types of stellarators or helical devices is sketched in Fig. 13.1, which is intended to feature the basic principles but is far from being complete. In the first stellarators, Model A and B at Princeton University, the rotational transform was generated by bending a toroidal arrangement of coils into a *Figure-8* shape. *Classical stellarators,* in a narrow sense, such as Wendelstein 7-A use 2l toroidally closed helical conductors, the current in adjacent conductors running in opposite directions. Additional toroidal field coils are required to produce a net toroidal field. The use of the two coil sets gives experimental flexibility with respect to the magnetic field structure. However, the interlink of the coil sets and large magnetic forces make the *classical stellarator* unattractive for a reactor design. These drawbacks are somewhat alleviated by *torsatrons*, e.g. the Large Helical Device (LHD), and *heliotrons*, e.g. Heliotron-E, but at the expense of experimental flexibility. *Heliotrons/torsatrons* have l helical conductors with parallel currents. They provide a net toroidal field and the vertical field generated by the net toroidal current is balanced by additional poloidal field coils not interlinked with the helical ones. Similar to a *Figure-8* device a *heliac* produces the rotational transform by a three dimensional (3D) helical magnetic axis: The centre of the toroidal field coils follow a helical line around a central conductor. The *heliac* principle is realized for example in TJ-II.

Apart from technical problems which have to be expected for reactor-scale helical windings the magnetic field properties of the traditional stellarator types can be optimized only within the constraints imposed by the particular concept. These restrictions relaxed considerably with the invention of so called *modular stellarator coils* by Rekher and Wobig in 1972 which are 3D in shape and poloidally closed. Modular coils allow to approximate arbitrary current distributions on a toroidal surface which then completely define the magnetic field in the volume enclosed by the surface. Along with a tremendous increase in computing power the modular coil concept gave way to advanced physics optimization of stellarators. In fact, traditional stellarators

Table 13.1: Some stellarators and helical devices (M: number of field periods, R: major radius, a: minor radius, B: maximum magnetic field).

Device	Location	Type	M	R/m	a/m	B/T	shear	well	Status
ATF	Oak Ridge	torsatron	12	2.1	0.27	2	medium	central	1988–1994
CHS	Nagoya/Toki	torsatron	8	1.0	0.2	2	medium	central	1988–running
LHD	Toki	torsatron, sc[1]	10	3.9	0.6	3	medium	central	1998–running
Heliotron E	Kyoto	heliotron	19	2.2	0.2	1.9	high	hill	1980–1997
Heliotron J	Kyoto	heliotron	4	1.2	0.2	1.5	low	global	1999–running
TJ-II	Madrid	heliac	4	1.5	0.2	1	low	global	1998–running
W7-AS	Garching	advanced stell.	5	2.0	0.18	3	low	global	1988–2002
W7-X	Greifswald	helias, sc[1]	5	5.5	0.53	3	low	global	under construction
HSX	Madison	quasi helical	4	1.2	0.15	1.4	low	global	2001–running
NCSX	Princeton	quasi axial	3	1.4	0.33	1.7	medium	well	under approval
CHS-qa	Toki	quasi axial	2	1.5	0.47	1.5	low	well	under design
QPS	Oak Ridge	quasi poloidal	2	0.9	0.33	1	medium	well	under design

need to be optimized. They suffer from a rather low β-limit (β is the ratio of plasma pressure p to magnetic pressure $B^2/2\mu_0$) and from very large *neoclassical* plasma losses in the collisionless regime which is required for a reactor. The pressure is limited by a pressure induced outward shift of the magnetic surfaces, the so called Shafranov-shift (equilibrium β-limit; a further limit, the stability β-limit, is due to the onset of pressure driven MHD-instabilities that degrade the confinement). Owing to its 3D-structure, the stellarator magnetic field is strongly modulated along the field lines, causing plasma particles with a small momentum parallel to the field lines to be trapped in the local magnetic mirrors. Such locally trapped particles are rapidly lost by the $B \times \nabla B$-drift which is perpendicular to the field lines.

Wendelstein 7-AS, the proof-of-principle experiment for *advanced stellarator* optimization, is optimized with respect to a reduced Shafranov shift. Its successor, Wendelstein 7-X, is a large modular helical axis stellarator (*helias*) presently being under construction. Its design is much further optimized leading for example to a further reduction of the Shafranov shift and of the neoclassical losses. In *quasi-symmetric stellarators*, which are still 3D in Cartesian coordinates but nearly 2D in magnetic coordinates, the effective field ripple and thus the drift losses are significantly reduced. Such configurations are similar to a tokamak, which is axially symmetric. Various kinds of quasi-symmetry are currently under consideration. A quasi-symmetry has first been realized in the *helically symmetric experiment* (HSX). Further devices are being planned, e.g. the National Compact Stellarator Experiment NCSX and the Compact Helical System CHS-qa, both having *quasi axial symmetry*, and QPS with *quasi poloidal symmetry*. The modular design and a low number $M \leq 3$ of field periods allows for a compact design with comparatively small aspect ratio, $A = R/a$. Tab. 13.1 gives an overview of present stellarator experiments and of those being under construction or being planned.

13.3 Properties of the vacuum field

High quality magnetic flux surfaces are prerequisite for plasma confinement. In contrast to tokamaks flux surfaces in stellarators already exist for the vacuum field and can directly be

[1] sc = superconducting

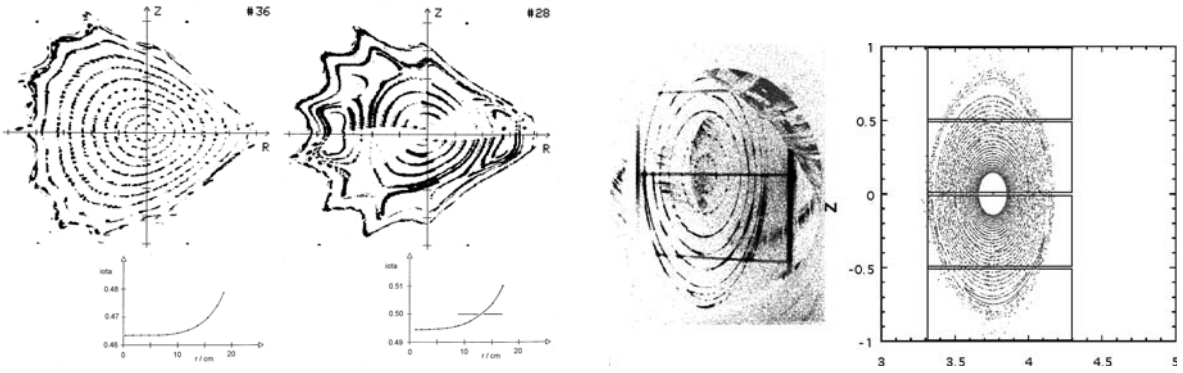

Figure 13.2: Left: Poloidal cuts through vacuum field flux surfaces in W7-AS and radial profiles of the rotational transform measured by the fluorescing rod technique. In case that the ι-profile contains rational values n/m that *resonate* with field perturbations B_{nm} the unpertubated nested surfaces (left) break up and large magnetic islands appear (right) (Jaenicke et al. 1993).
Right: Vacuum field flux surfaces in LHD measured by fluorescing mesh technique at $B = 0.0875\,\mathrm{T}$ (left) and calculated surfaces obtained from a fieldline teacing code including the earth's magnetic field (right, $B_E \approx 5\times10^{-5}\,\mathrm{T}$). The large 1/1 magnetic island at the top is inherent to the particular LHD-configuration and the small island at the bottom is attributed to the earth's magnetic field. The frame supporting the mesh can also be seen (Komori et al. 1998).

measured. For this purpose an electron beam is injected parallel to the magnetic field. The beam follows the field line and finally covers the respective flux surface (if it exists). A poloidal cut through the surface is visualized by a fluorescing rod which is swept across a poloidal cross section and imaged, e.g., by a CCD-camera. Alternatively a stationary fluorescent mesh is used. Fig. 13.2 left shows two examples of vacuum flux surfaces in W7-AS which have been measured at slightly different values of the rotational transform. In the case where ι does not assume low order rational values, such as ι = 1/3, 1/2, 2/3, etc., unperturbed nested surfaces exist. When ι = 1/2 occurs in the confinement volume so called magnetic islands appear. They arise from radial perturbation fields, i.e. being normal to the flux surfaces, with Fourier components $B_{nm} \neq 0$ and $n/m = 1/2$. Such perturbations may be due to external field errors with $n = 1$ and $m = 2$ or they are inherent to the field structure. For example, W7-AS has five toroidal field periods leading to inherent $5/m$-components. By closer inspection of the island pattern in Fig. 13.2 left, right, one realizes that ten small islands (from the $5/10$ perturbation) are embedded into two large islands (from the $1/2$ perturbation). Furthermore, the corrugated boundary indicates that the outer flux surfaces are already perturbed by the next $5/9$ island chain. Generally, magnetic islands appear when the rotational transform assumes a rational value $\iota = n/m$ and is in resonance with a field perturbation $B_{nm} \neq 0$.

External field errors can arise for example from a misalignment of the coil set or from an imperfect compensation of the current lines feeding the coils (the in- and outgoing lines must be aligned parallel, such that there is no net current producing a stray magnetic field). The susceptibility of flux surfaces to weak external perturbations has instructively been demonstrated at LHD (see Fig. 13.2 right). Measurements at $B = 0.0875\,\mathrm{T}$ show a $1/1$-island structure which can be reproduced in a flux surface calculation when the earth's magnetic field of about $B_E \approx 5\times10^{-5}\,\mathrm{T}$ is taken into account, i.e. perturbations of the order 5×10^{-4} already produce

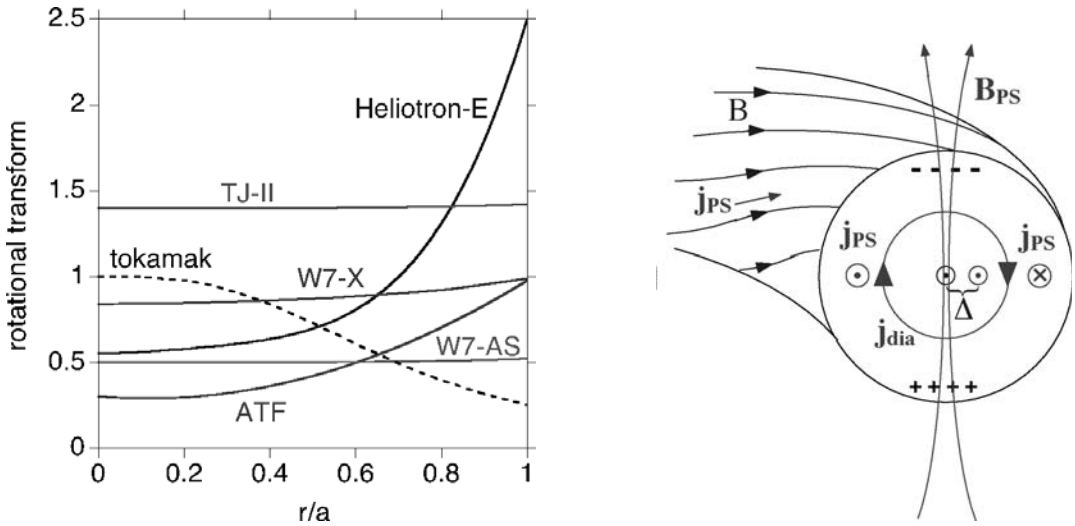

Figure 13.3: Left: Radial profiles of the rotational transform for different stellarator concepts and a tokamak.
Right: Sketch of the perpendicular (diamagnetic) and parallel (Pfirsch-Schlüter) equilibrium currents. The parallel currents lead to the Shafranov shift Δ.

significant islands. (Actually, this perturbation does not affect the usual LHD-operation at $B > 2\,\mathrm{T}$ where $B/B_E < 3\times10^{-5}\,\mathrm{T}$).

Magnetic islands short-circuit radial plasma transport. They are therefore detrimental for confinement and have to be avoided or must be made small. Precise machining and alignment of the field coils is therefore prerequisite for high quality flux surfaces in a stellarator. Residual islands can be excluded if the magnetic shear (= radial variation of ι) is very small and the value of the rotational transform is properly adjusted to avoid the major rational numbers (see Fig. 13.2 left, left). This concept is followed by the Wendelstein line. Large magnetic shear reduces the island size. This concept is followed by torsatrons and heliotrons. However, increasing shear allows more islands to enter the confinement volume which for extreme situations may even lead to ergodization of the field lines. Fig. 13.3 left shows ι-profiles typical for the various stellarator concepts.

The poloidal cross section of a flux surface is far from being circular and may even change with the toroidal position. A convenient label of a flux surface is its *effective radius r*, which is defined as the minor radius of a circular torus having the same major radius *R* and enclosing the same volume as the flux surface. The parameters of both the field and the plasma are usually expressed by their flux surface average. Such a function of *r* is referred to as a *radial profile*. Plasma parameters are almost constant on a flux surface since transport parallel to the field lines is usually very fast compared to the perpendicular (radial) transport.

Another key parameter of the magnetic field is related to the average of the magnetic field value on a flux surface. If the average of *B* increases with *r* the configuration is said to have a magnetic well, if it decreases a magnetic hill. Both, magnetic shear and magnetic well are favourable for plasma stability. Wendelstein stellarators and Heliacs have small shear and a global magnetic well; they rely on magnetic well stabilization. In contrast, Torsatrons/Heliotrons have moderate/large shear and a magnetic hill (torsatrons may have a small hill in the centre); they rely on magnetic shear stabilization. The well/hill structure can be changed by shifting the inner flux surfaces radially along *R* with respect to the outer ones.

This can be achieved with a vertical magnetic field which can be externally applied or which arises from the equilibrium currents in a confined plasma (Shafranov shift). The outward shift produces a magnetic well.

13.4 Plasma equilibrium and high-β operation

In the presence of a plasma the vacuum magnetic field is modified by currents flowing in the plasma. The pressure equilibrium requires that the pressure gradient is balanced by the magnetic force, $\nabla p = \mathrm{j} \times \mathrm{B}$ with $\nabla \cdot \mathrm{j} = 0$. It can easily be shown that the current component perpendicular to the magnetic field is $\mathrm{j}_\perp = \mathrm{j}_{dia} = \mathrm{B} \times \nabla p / B^2$. This is the diamagnetic current which decreases the magnetic field inside the plasma. The parallel component can be approximated by $\mathrm{j}_\parallel = \mathrm{j}_{PS} \approx 2 j_\perp / \iota \cos\theta \mathrm{e}_\parallel$ where θ is the poloidal angle. This is the so called Pfirsch-Schlter (PS) current. In the particle picture the PS-current cancels the separation of electrons and ions arising from the vertical $\mathrm{B} \times \nabla B \mathrm{B}$ drift in the toroidally curved field. Otherwise the resulting electric field would expel the plasma by the outward directed $\mathrm{E} \times \mathrm{B}$ drift. The currents are sketched in Fig. 13.3 right. The PS-current produces a vertical dipole field which shifts the plasma outward (Shafranov shift Δ). Approximately, the Shafranov shift is given by $\Delta/a = R/a \left(C_{01}/(r/R)\right)^2 \langle\beta\rangle / \iota^2$, where C_{01} is the toroidal curvature term in the Fourier representation of the field and $\langle\beta\rangle$ is the volume average of the normalized pressure $\beta = p/\left(B/^2/2\mu_0\right)$. Evidently, the Shafranov shift can be made small by reducing the aspect ratio, R/a, and increasing the rotational transform (the torsatron and heliotron approach) and by decreasing the toroidal curvature (the Wendelstein approach). In the line of W7 stellarators the quantity $C_{01}/(r/R)$ decreases from 1.0 (W7-A) via 0.7 (W7-AS) to 0.4 (W7-X). The equilibrium β-limit is formally defined as the pressure where the shift of the magnetic axis reaches half the minor plasma radius, $\Delta = a/2$. As a positive effect the Shafranov shift can *dig* a magnetic well, which improves the plasma stability.

Since $\langle\beta\rangle \sim \langle p\rangle / B^2 \sim (W/V_p)/B^2 \sim (\tau_E P)/\left(V_p B^2\right)$, where W is the plasma energy, V_p the plasma volume, P the heating power and τ_E the energy confinement time, high-β plasmas are achieved with strong neutral beam heating at reduced magnetic field. Actually, the dependence of β on the experimental control parameters P and B is weaker than indicated by this relations, since the confinement time increases with B and decreases with P (see sec. 13.5.2). A high-β discharge in W7-AS with $P_{NBI} = 4\,\mathrm{MW}$ at $B = 0.9\,\mathrm{T}$ is shown in Fig. 13.4. The equilibrium magnetic surfaces can be visualized by the contours of constant plasma emissivity which is a function of electron temperature, electron density and the density of plasma impurities, which are constant on flux surfaces. The soft X-ray spectral range is best suited for this purpose. The contours of constant soft-X emissivity are in good agreement with the flux surfaces calculated by the NEMEC equilibrium code. In order to prevent the plasma boundary to be shifted onto the vessel wall an external vertical field has to be superposed to the vacuum field which counteracts the dipole field of the equilibrium currents during the high-β phase. Nevertheless, a relative shift of the magnetic axis with respect to the plasma boundary cannot be avoided.

Fig. 13.5 left shows the increasing displacement with $\langle\beta\rangle$ of the magnetic axis with respect to its vacuum field position as deduced from soft X-ray measurements in various W7-AS discharges. The observed shift is roughly a factor of two smaller than that predicted for an equivalent classical $l = 2$ stellarator. This result was an important confirmation of the W7-AS optimization which has predicted a reduction of the PS-current and the associated Shafranov shift by a factor of two. Additionally, it confirms the expected decrease of the Shafranov shift with increasing rotational transform.

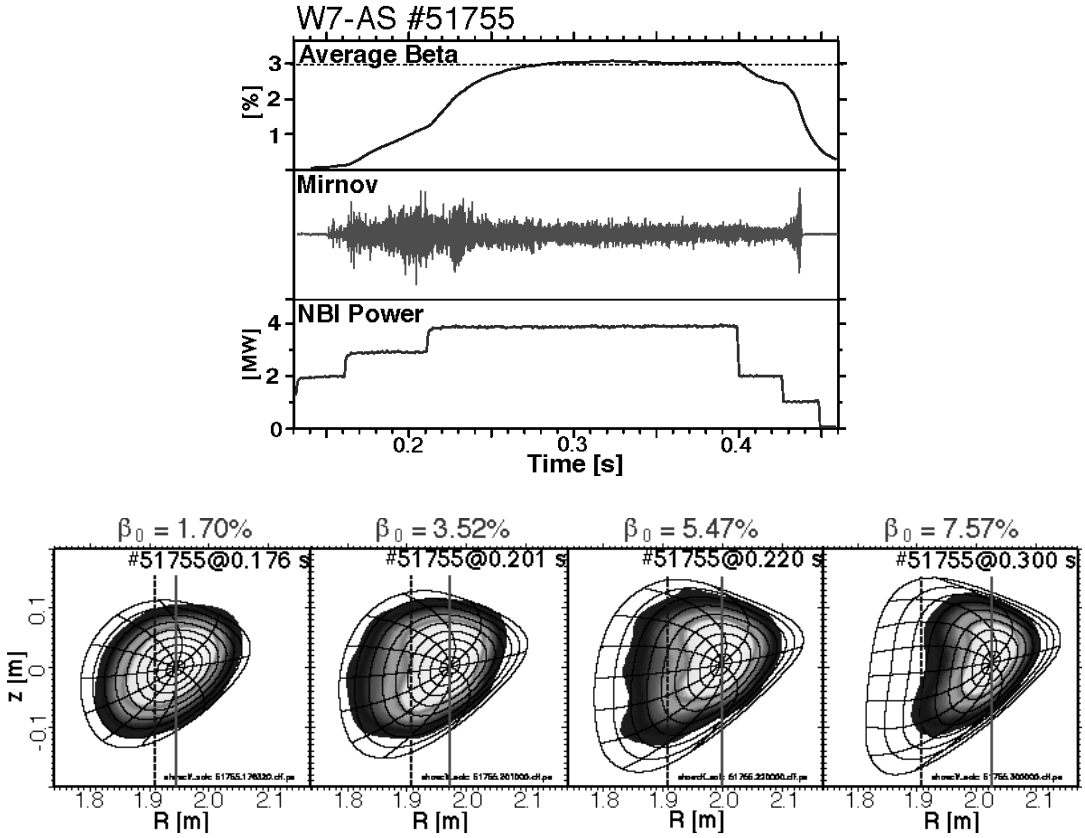

Figure 13.4: Normalized pressure, magnetic field fluctuations close to the plasma and NBI heating power for a high-β discharge in W7-AS (top). Contours of constant soft X-ray emissivity and flux surfaces calculated by the NEMEC code at selected times of the same discharge. The position of the magnetic axis is $R = 1.91$ m for the vacuum field and moves radially outward with increasing β (bottom) (Weller et al. 2002).

The maximum $\langle\beta\rangle$-values achieved so far in W7-AS (3.4%) and LHD ($\approx 4\%$) clearly exceed the predicted stability limits ($\langle\beta\rangle = 2\%$ for W7-AS) where Mercier and resistive interchange modes grow unstable. In particular, no hard stability limit with strong MHD events has been observed experimentally up to now. On the contrary, the high β phase appears to be rather quiescent with respect to magnetic activity, which is indicative for fluctuations and instabilities (see Fig. 13.4, on the top). In both devices high-β discharges are started with an inward shifted vacuum field configuration, providing a magnetic hill, which is unfavourable for stability. The high β values that can still be achieved may be related to the formation of a stabilizing magnetic well with increasing β. This is in line with observations at CHS and LHD where after an initial increase magnetic fluctuations decrease or saturate at high β (see Fig. 13.5 right). Up to now the maximum pressure in stellarators seems to be limited by the available heating power rather than by instabilities.

13.5 Transport and confinement

The outward directed radial transport of particles and energy limits the density and temperature which can be achieved at a given strength of particle and energy sources. Understanding of

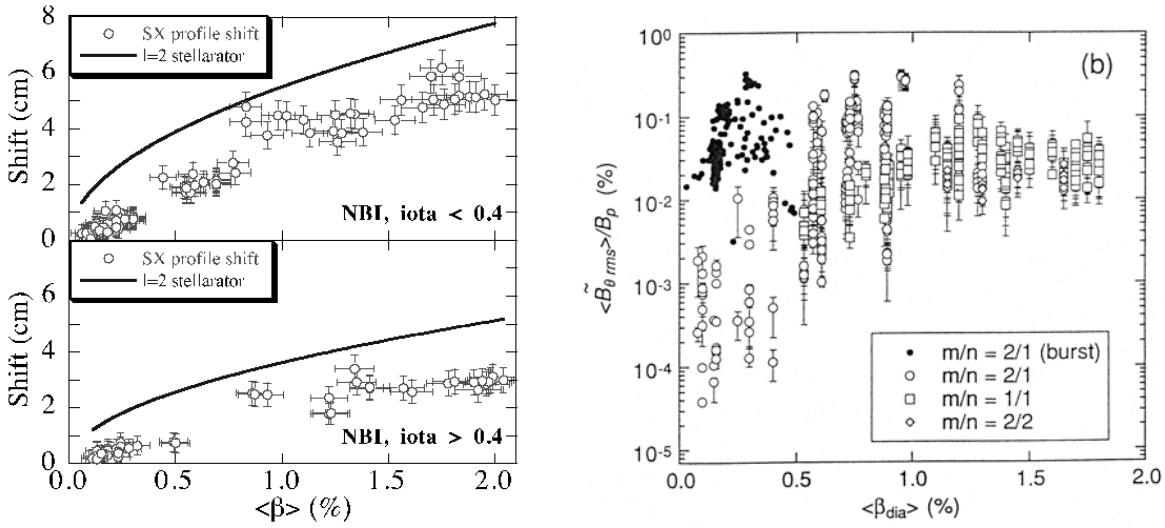

Figure 13.5: Left: Shift of the magnetic axis as a function of the average plasma pressure in W7-AS. The full lines indicate the shift expected for a classical $l = 2$ stellarator (Hofmann et al. 1996).
Right: Magnetic fluctuations in CHS measured with pick-up coils at the plasma periphery as a function of the normalized plasma pressure β. The root-mean-square fluctuation level normalized by the equilibrium poloidal field is shown for stationary coherent components with mode numbers $m \leq 2$ (open symbols) (Okamura et al. 1995).

the transport mechanisms is essential for the extrapolation towards a reactor. As in tokamaks, transport in stellarators cannot be understood only in terms of *neoclassical* diffusion processes. Additional *anomalous* transport even dominates in certain plasma regimes.

13.5.1 Neoclassical transport

Neoclassical transport is a diffusive process which can be described by a random walk model, $D = d^2\nu$, with diffusivity D, collision frequency ν and step size d. In a homogeneous magnetic field d is determined by the Larmor radius (*classical* diffusion). However, a toroidal field is inherently inhomogeneous and the particles undergo drifts in the magnetic field gradient ($\mathrm{B} \times \nabla B$ drift and curvature drift) and additional electric fields ($\mathrm{E} \times \mathrm{B}$ drift, E arises from space charges). Then d is determined by the distance which a particle can drift away from a flux surface between collisions. If collisions are rare, d becomes much larger than the Larmor radius (*neoclassical* diffusion).

In both tokamaks and stellarators B is higher at the inside (smaller R) than at the outside (larger R) of the torus. This results in a vertically directed $\mathrm{B} \times \nabla B$ drift and a modulation of B along the helical field lines. A particle following a field line thus moves in a magnetic mirror termed toroidal mirror or ripple. The particle can follow a helical trajectory if its parallel momentum is large enough (passing particle). If not, it is trapped in the ripple and bounces between reflection points located at the high field side above and below the equatorial plane. The orbits of toroidally trapped particles are called *banana orbits* since their poloidal projection resembles a banana. Without collisions both passing and toroidally trapped particles are ideally confined since on the average they spend the same time below and above the surface and there

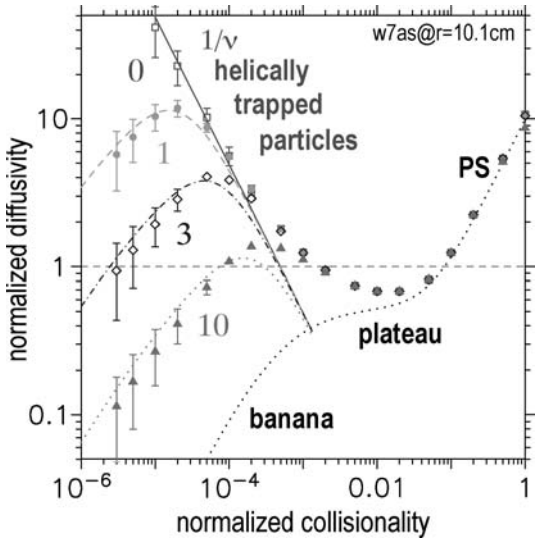

Figure 13.6: Predicted neoclassical diffusivity of a mono-energetic test particle in W7-AS (normalized to the plateau value of a circular tokamak) as a function of the normalized collisionality ν/v in cm^{-1}. v is the particle velocity. The high diffusivity in the $1/\nu$ regime is strongly reduced with increasing radial electric field, given in terms of E/v in Vs/m^2. The diffusivity in an equivalent elongated tokamak is shown for comparison (dotted line).

is no net displacement by the drift. With collisions the trapped particles can be displaced by the *banana width* which then determines d (banana- or ν-regime).

In stellarators additional ripple, the helical ripple, arises from the 3D coil structure. These ripples are localized with an extension of the order of the coil spacings (in tokamaks the finite number of coils is only a weak perturbation of axial symmetry). For particles trapped in such a local ripple the vertical drift is not averaged as it is for passing or banana particles and they are rapidly lost unless they are detrapped by collisions. Therefore the diffusivity strongly increases with decreasing collisionality ($1/\nu$-regime). Since a reactor has to operate at high temperature, i.e. low collisionality, the stellarator specific $1/\nu$-regime is detrimental unless transport can be reduced by other means.

For example, the vertical $\mathrm{B}\times\nabla B$ drift can be averaged out by a superimposed poloidal $\mathrm{E}\times\mathrm{B}$ drift in a radial electric field (see Fig. 13.6). The electric field adjusts itself selfconsistently by the ambipolarity of radial ion and electron fluxes, $\Gamma_e = \Gamma_i$, where

$$\Gamma_\alpha = -n_\alpha \left[D_{11}^\alpha \left(\nabla \frac{n_\alpha}{n_\alpha} - q_\alpha \frac{E_r}{T_\alpha} \right) + D_{12}^\alpha \nabla \frac{T_\alpha}{T_\alpha} \right] + \Gamma_{\alpha,ext} \ , \tag{13.1}$$

n_α is the density of species α, D_{11}^α is the particle diffusivity, and D_{12}^α the transport coefficient for a particle flux driven by the temperature gradient. $\Gamma_{\alpha,ext}$ denotes fluxes which are externally driven, e.g. by the heating method. Since the transport coefficients D have a nonlinear dependence on E_r, multiple solutions of the ambipolarity condition are possible and thus bifurcations may occur. In CHS limit cycle oscillations between bifurcated states of the plasma potential have indeed been observed (see Fig. 13.7 left).

The impact of a radial electric field on transport is evidenced in ECRH heated high electron temperature discharges in W7-AS (see Fig. 13.7 right, $P_{ECRH} = 1.2\,\mathrm{MW}$). In the outer plasma

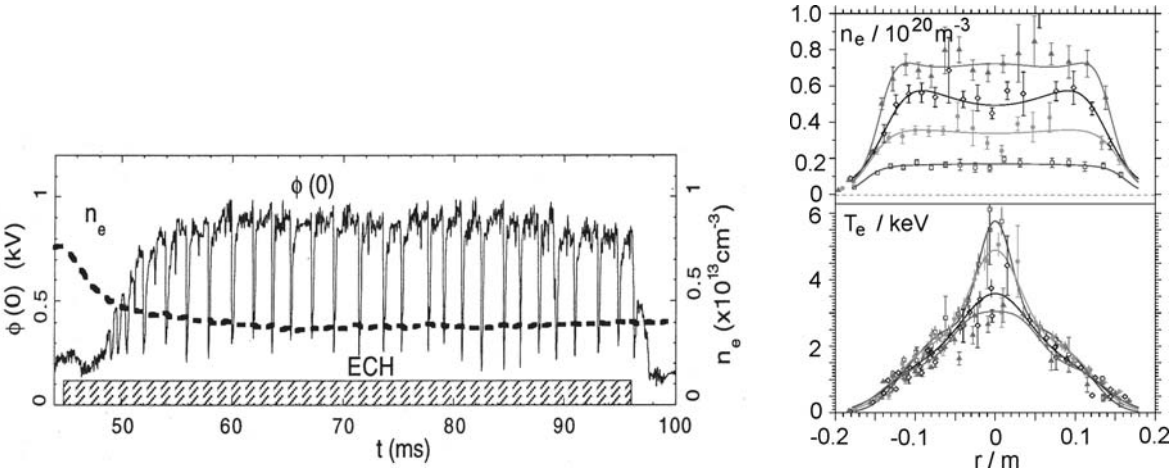

Figure 13.7: Left: Limit cycle oscilations between bifurcated states of the electric potential in the centre of a low collisionality plasma in CHS (Fujisawa et al. 1998).
Right: Electron density and temperature profiles in ECRH heated discharges at W7-AS ($P_{ECRH} = 1.2$ MW). With decreasing density a strong peaking of the central temperature is observed which is attributed to transport reduction by the formation of a radial electric field. Towards the plasma boundary the temperature profile is dependent of the density, indicating a $1/\nu$ scaling of transport (Kick et al. 1999).

region the electron temperature T_e is independent of the density which is typical for the $1/\nu$-regime ($\mathrm{d}T/dr \sim -P/(n\chi)$ does not depend on n since $\chi \sim \nu^{-1}$, χ is the heat diffusivity and P the heating power). This is different in the centre. Here, with decreasing density a strong peaking of T_e is observed and central values of 6 keV are reached. (With a power of 2 MW the highest temperature in W7-AS, $T_e = 7$ keV, has been achieved). This indicates a reduction of neoclassical transport below the $1/\nu$-level. The high central T_e is accompanied with a strong positive radial electric field (a positive field, the so called electron root, arises if the plasma charges up positive by the loss of electrons). A detailed analysis is given in Fig. 13.8 left for a similar discharge at $P_{ECRH} = 0.77$ MW. Close to the centre a radial electric field of up to $E_r = 600$ V/cm is measured by charge exchange recombination spectroscopy. E_r becomes small and even negative (ion root, the plasma charges up negative) towards the boundary. The ion root solution yields good agreement with the experiment at larger radii whereas in the centre the observed electric field is somewhat larger than the electron root solution. Calculating the neoclassical electron heat conductivity χ_e with $E_r = 0$ clearly overestimates the experimental value in the centre by an order of magnitude whereas the electron root solution agrees within a factor of two. For the central region a full consistence of experimental results and neoclassical predictions could not be achieved with thermal fluxes as the generating mechanism for the electric field. It is therefore assumed that the strong positive electric field is essentially due to an additional electron flux generated by the ECRH, which produces suprathermal electrons trapped in a local magnetic mirror. These electrons are then lost by the $\mathrm{B} \times \nabla B$ drift. (This is similar to a regime with high ion confinement observed earlier in W7-A, where neoclassical ion plateau transport was reduced by a strong negative E_r arising from the orbit losses of perpendicular injected NBI.) At the boundary electron heat transport is clearly anomalous, i.e. it exceeds by far the neoclassical predictions.

At higher density and with NBI-heating in addition to ECRH a higher ion temperature ap-

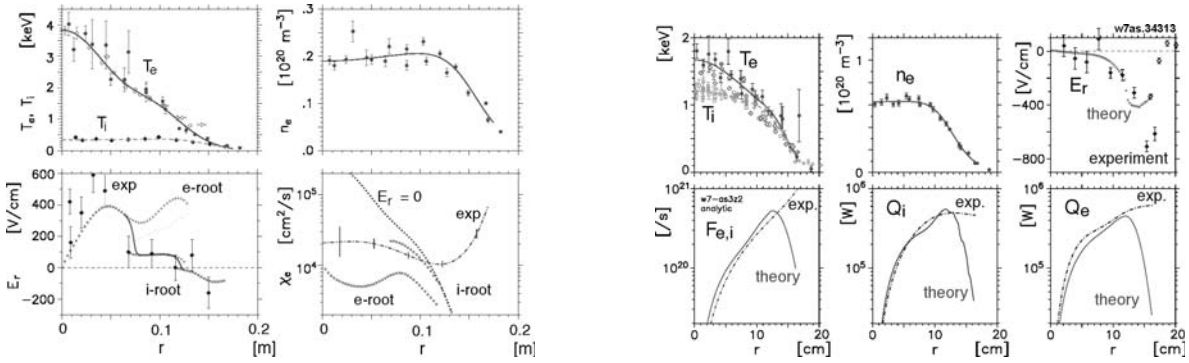

Figure 13.8: Left: Profiles of T_e, T_i, n_e, E_r and χ_e for a low density ECRH discharge at W7-AS ($P_{ECRH} = 0.77$ MW). For E_r and χ_e the neoclassical predictions from the various roots of the ambipolarity condition are also given. Because of strong electron heating and small collisional energy transfer to the ions T_i is much smaller than T_e (Brakel et al. 1997).
Right: Profiles of temperatures, density and radial electric field and of the particle fluxes $F_e = F_i$ and ion and electron heat flux Q_i and Q_e for a high ion temperature discharge at W7-AS heated by ECRH and NBI ($P_{ECRH} = 0.4$ MW, $P_{NBI} = 0.9$ MW). The experimental fluxes are compared to the neoclassical predictions (Jaenicke et al. 1995).

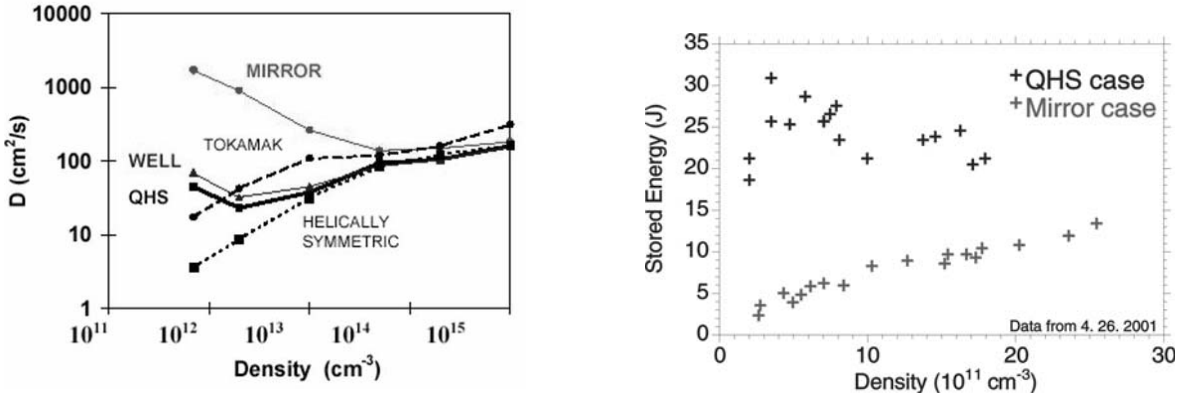

Figure 13.9: Left: Predicted diffusivity D as a function of density for various magnetic configurations in HSX. For comparison D is also given for an equivalent tokamak and for full helical symmetry.
Right: Measured plasma energy as a function of density for the QHS- and the mirror-configurations in HSX (Anderson et al. 1999).

proaching the electron temperature can be achieved. The analysis of a high ion temperature discharge in W7-AS shows, that in the central plasma region ions and electrons behave neoclassically (see Fig. 13.8 right). For the conditions with $T_e \approx T_i$ a negative electric field (ion root) is neoclassically expected and experimentally found throughout the plasma. The electric field is sufficient to overcome the unfavourable $1/\nu$-scaling for the ion transport coefficients such that the highest ion temperatures in W7-AS up to 1.7 keV have been achieved in this type of discharge. Again, transport is clearly anomalous at the boundary.

Although a radial electric field can considerably reduce neoclassical transport its formation cannot be well controlled experimentally. Therefore, the *a priori* reduction of $1/\nu$-transport already at the design stage of a stellarator is more promising or even mandatory. This can

be achieved for example by a quasi-symmetric field structure which is nearly 2D in magnetic coordinates (e.g. HSX) or by minimizing the effective helical ripple (e.g. W7-X). Fig. 13.9 left shows the calculated electron diffusivity as a function of density for different magnetic configurations that can be realized in HSX. At low density, i.e. low collisionality, D is strongly reduced in the standard QHS (quasi-helically-symmetric) configuration as compared to the so called mirror configuration where a toroidal mirror is introduced by additional coils which spoils the symmetry and leads to $1/\nu$-transport. Already the initial operation of HSX gave the first experimental evidence that in the collisionless regime transport can be strongly reduced by quasi-symmetry. Confinement in ECR-heated discharges is improved by a factor of six and, consistent with the predictions, the stored plasma energy decreases with density (collisionality) in the QHS-case and increases in the mirror case (see Fig. 13.9 right). There are further aspects which should improve with quasi-symmetry. For example, viscous damping of plasma rotation is strongly reduced in the quasi-symmetric direction. Since plasma rotation plays a key role in the reduction of anomalous transport and the formation of local transport barriers (see sec. 13.5.2), improvements in this area have to be expected for the future.

13.5.2 Anomalous transport

Neoclassical transport in stellarators prevails at low collisionality where the ripple induced losses can become large. At higher collisionality transport is anomalously enhanced compared to the neoclassical predictions, in particular for the electrons. This generally applies close to the boundary (see χ_e in Fig. 13.8 left and the fluxes in Fig. 13.8 right). It is common opinion that anomalous transport originates from plasma turbulence but its nature is not yet resolved. Therefore, empirical scaling laws are used to describe the dependencies of transport on the leading parameters. In case of energy transport the global energy confinement time, $\tau_E = W/(P - dW/dt)$ with plasma energy W and heating power P, is the figure of merit. The International Stellarator Scaling ISS-95 has been derived by a statistical analysis of confinement data from W7-AS, W7-A, Heliotron-E, CHS and ATF (Stroth et al. 1996)

$$\tau_E^{ISS-95} = 0.079 a^{2.21} R^{0.65} P^{-0.59} n^{0.51} B^{0.83} \iota^{0.4} \,. \tag{13.2}$$

The expression empirically relates the confinement time τ_E (in s) with the plasma dimensions a and R (in m), the heating power P (in MW), the average value of the plasma density n (in $10^{19}\,\mathrm{m}^{-3}$) and magnetic field properties in terms of the magnetic induction B (in T) and the rotational transform ι. Since ι has a radial variation in devices with magnetic shear, it is taken at $r/a = 2/3$ by convention. As in tokamaks confinement in stellarators exhibits a power degradation (τ_E decreases with power). In contrast to tokamaks a significant dependence of confinement on the ion mass (isotope effect) has not yet been observed. Fig. 13.10 left shows experimental τ_E-values from various stellarator and (L-mode) tokamak discharges versus the calculated ISS-95 values. Meanwhile, the best stellarator confinement has been achieved with $\tau_E = 0.3\,\mathrm{s}$ in LHD, having the largest dimensions, a and R. It is evident that

1. the smaller torsatrons and Heliotrons have a common scaling,
2. confinement in LHD and W7-AS exceeds this scaling by a factor of two,
3. confinement in stellarators scales similar as L-mode confinement in tokamaks.

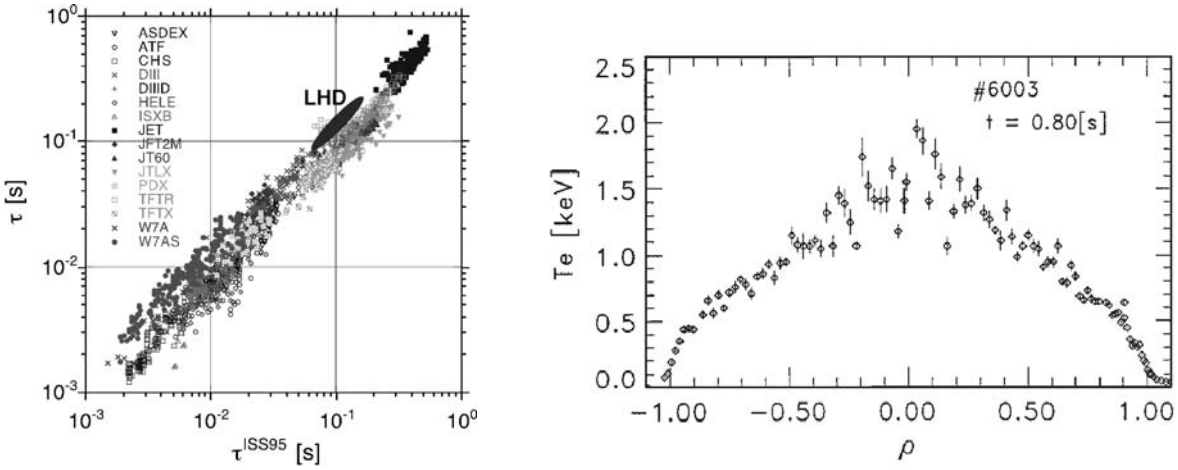

Figure 13.10: Left: Experimental energy confinement times from stellarator and L-mode tokamak discharges versus the ISS-95 values. The range of recent LHD confinement is indicated (Stroth et al. 1996, Yamada et al. 1996, Ohyabu et al. 1999).
Right: Typical electron temperature profile in a NBI discharge at LHD as a function of normalized effective radius r/a. A steep gradient at the edge forms a temperature pedestal (Ohyabu et al. 2000).

The better confinement in W7-AS may result from the low magnetic shear but possibly the W7-AS optimization also affects anomalous transport. The improved confinement in LHD is related to an edge transport barrier, i.e. a radially localized region of reduced transport. The barrier leads to a steep temperature gradient and to the formation of a temperature pedestal which is not observed in the smaller devices (see Fig. 13.10 right). The edge barrier is suspected not to be an H-mode due to the lack of key features as ELMs (= edge localized (MHD) modes) and a spontaneous transition but may be related to the existence of the $\iota = 1/1$ surface at the edge.

The H-mode is a high confinement regime with an edge transport barrier which is caused by a sheared (i.e. radially varying) poloidal $E \times B$ rotation in a radial electric field. It typically improves confinement by a factor of two. The H-mode was discovered in the ASDEX tokamak and has been observed in W7-AS as the first stellarator. The sheared rotation radially decorrelates turbulent structures which are assumed to be responsible for anomalous transport. Sheared rotation is also an essential ingredient in the formation of internal transport barriers (ITB) not being located at the edge. The rotation can for example be driven by the electric field resulting from the neoclassical particle fluxes.

High energy confinement in the H-mode is accompanied with improved particle and impurity confinement, causing a continuous rise of impurity radiation during a discharge. Therefore H-mode discharges are terminated by a radiative collapse (imbalance of heating and radiated power), unless the densities are not kept at a tolerable level by ELMs. In a certain sense, ELMs act like an overpressure valve, decreasing the pressure gradient, if it exceeds a limit. They intermittently enhance transport and remove particles and impurities but also part of the plasma energy. Very recently, a new ELM free high confinement regime has been discovered at W7-AS, which combines the desirable features of simultaneously high energy and low impurity confinement (see Fig. 13.11 left). It occurs above a threshold at very high density ($n_e > 10^{20}\,\mathrm{m}^{-3}$) and is therefore termed High Density H-mode (HDH). Basic features of the HDH-mode are compared to the normal confinement (NC) in Fig. 13.11 right. In contrast to

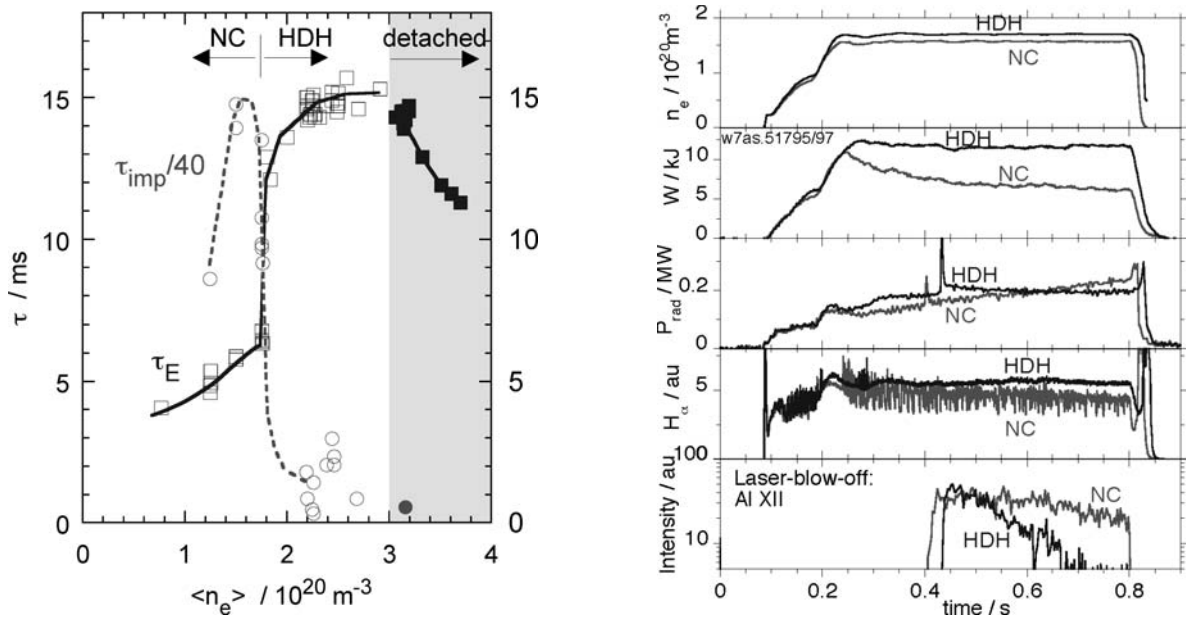

Figure 13.11: Left: Density dependence of energy and impurity confinement in W7-AS. At a threshold density τ_E doubles whereas τ_{imp} dramatically decreases. At the highest densities the plasma detaches from the targets ($P_{NBI} = 2$ MW) (McCormick et al. 2002).
Right: Time traces of plasma density, energy, radiation power and H_α-light for two NBI discharges below (NC = normal confinement) and above (HDH = high density H-mode) the HDH density threshold. The decay curves of aluminium injected as a tracer demonstrate the reduced impurity confinement in the HDH-regime ($P_{NBI} = 1$ MW) (Brakel et al. 2002).

transient NC-discharges with increasing impurity radiation and high fluctuation level HDH-mode discharges are quasi-stationary and very quiescent with respect to fluctuations (seen in the H_α-light). Energy confinement exceeds that of NC-discharges by a factor of two, whereas impurity confinement is lower by a factor of about ten.

The analysis of impurity tracer experiments has revealed that in the NC-regime an inward convection of impurities leads to impurity accumulation and a radiation distribution which is peaked at the centre. In contrast, the inward convection is strongly reduced in the HDH-mode and the radiation distribution is hollow and peaked at the edge. Radiation from the plasma core has to be avoided since it decreases the energy confinement, but radiation from the edge is desirable since it reduces the power flux into the divertor and decreases the heat load of the divertor targets. Thus the HDH-mode appears very promising with respect to both confinement and exhaust. The high density in the HDH-mode implies a rather low temperature (≈ 400 eV) and a high collisionality. Up to now it is an open question, if the HDH-mode can also be achieved at lower collisionality (higher temperature) as expected for larger devices.

In low shear stellarators there is strong evidence that the anomalous electron heat conductivity χ_e is increased at rational magnetic surfaces, i.e. at surfaces where $\iota(r) = n/m$ is a rational number. So Fig. 13.12 shows the sensitive dependence of confinement on the boundary value of ι observed in W7-AS. The best confinement is found right next to low order rational values $\iota = 1/2, 1/3$, etc. (only those have been used in the ISS95 data base). The ι dependence is reproduced by an empirical model which considers three contributions to the heat conductivity, $\chi_e = \chi_{neo} + \chi_0 + \sum \chi_{nm}$: Neoclassical transport, a term describing a basic level of anomalous

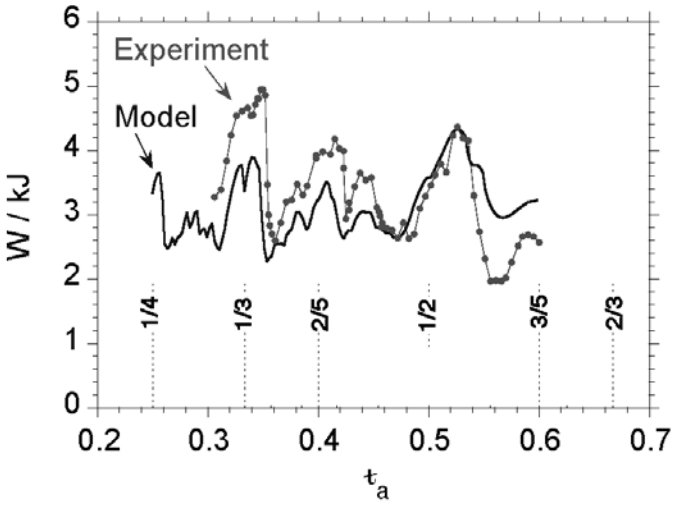

Figure 13.12: The dependence of confinement on the boundary value of the rotational transform for ECRH discharges in the low shear stellarator W7-AS ($P_{ECRH} = 0.34\,\mathrm{MW}$). The experimental plasma energy is compared with the kinetic energy of the plasma electrons as calculated from a transport model which assumes enhanced transport at rational magnetic surfaces (Brakel et al. 2002).

transport, and an additional term for enhanced turbulence at rational surfaces. The influence of the rational surfaces decreases with magnetic shear. Within this model, the confinement maxima are explained by the circumstance that in the close vicinity of low order rational numbers the density of rational numbers is generally smaller than elsewhere. It is very remarkable that local features in the T_e profile of various tokamaks, e.g. RTP, JET and TEXTOR-94, are also strictly correlated with the occurrence of low order rational $\iota(= 1/q)$ values. Close to these values a strong reduction of heat transport may give rise to local electron transport barriers. It may therefore be conjectured that the underlying processes are governed by the same physics in both stellarators and tokamaks.

13.6 Towards steady state

The steady state capability of stellarators has already been demonstrated in the ATF torsatron, although at low performance (see Fig. 13.13 left). A one hour and 17 minutes ECRH discharge has been run at reduced values of magnetic field ($B = 0.51\,\mathrm{T}$), heating power ($P = 70\,\mathrm{kW}$) and density ($n \leq 3 \cdot 10^{18}\,\mathrm{m}^{-3}$). The parameters had to be limited in order to prevent overheating of the copper coils and of the vessel wall, and to avoid the loss of density control. At the low level of heating power, the significant power loss due to atomic processes (ionization, excitation, etc.) kept the electron temperature at a low value of about 30 eV. The discharge was probably terminated by the build-up of impurities from outgassing of the vacuum vessel.

Steady state operation at high performance, i.e. at high field, power and density, requires superconducting coils and a divertor which can handle the power and particle exhaust. The divertor channels the power and particle fluxes emerging from the plasma to target plates where the particles can be pumped after being neutralized and the deposited energy can be removed by active cooling. The first superconducting stellarator, LHD, is not yet equipped with a full di-

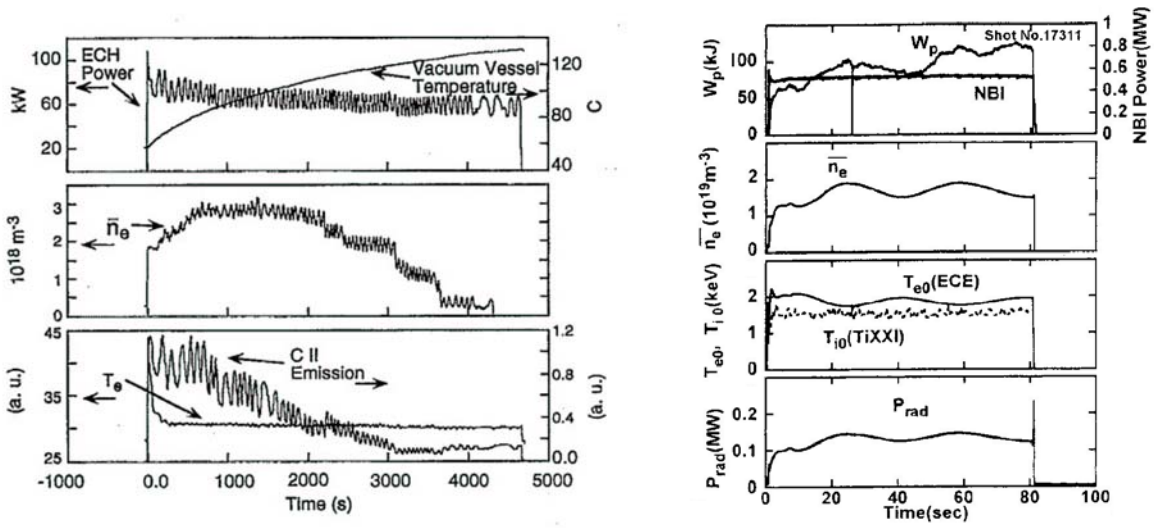

Figure 13.13: Left: Long pulse discharge in ATF with a pulse length of 4667 s at $B = 0.51$ T and 70 kW ECRH power (Jernigan et al. 1995).
Right: Long pulse discharge in LHD with a pulse length of 80 s at $B = 2.75$ T and 500 kW NBI power (Kawahata et al. 2000).

vertor and has achieved pulse lengths of 120 s with 400 kW ICRH and of 80 s with 500 kW NBI at $B = 2.75$ T and densities around 1.5×10^{19} m^{-3} (see Fig. 13.13 right). With proper divertor it is envisaged to operate LHD for one hour at 3 MW of heating power and W7-X for 30 min at 10 MW.

The different divertor concepts for stellarators are sketched in Fig. 13.14 left. As a common feature the confinement region with closed flux surfaces is surrounded by a region of open field lines which are *diverted* to target plates. Plasma particles diffuse across the last closed flux surface (LCFS) into the open field line region and follow the field lines to the targets where they are neutralized and deposit their energy.

The *helical divertor* makes use of the intrinsic field line diversion by the helical coils. Just outside the LCFS the field lines are nearly *confined* for many helical turns in a narrow ergodic layer close to the main plasma. After escaping from this layer they quickly move along the divertor legs to the targets. The divertor structure follows the pitch of the helical coils. The *island divertor* (ID) utilizes the field line diversion within magnetic islands, the islands being intersected by the target plates. The islands are induced either by external perturbation fields generated by additional control coils (e.g. in the *local island divertor*, LID) or they are intrinsic to the configuration (e.g. the island divertor in W7-AS, see also Fig. 13.2). In helical and local island divertors the target region and the main plasma are sufficiently separated, such that the divertor region can be closed except for a slit which allows the plasma flow to enter the divertor chamber. A *closed divertor* geometry allows for efficient pumping of neutrals and prevents their back-streaming into the core plasma. An island divertor of the W7-AS type has a rather small distance between target and core plasma. In this *open island divertor* geometry a high edge density is required to prevent the penetration of recycling neutrals into the core plasma and the neutrals have to be channelled into the pumping volume behind the targets by so called baffle plates (see Fig. 13.14 right).

The local island divertor concept has successfully been tested in CHS using an externally generated 1/1 magnetic island. Fig. 13.15 shows that with LID the plasma density is reduced as

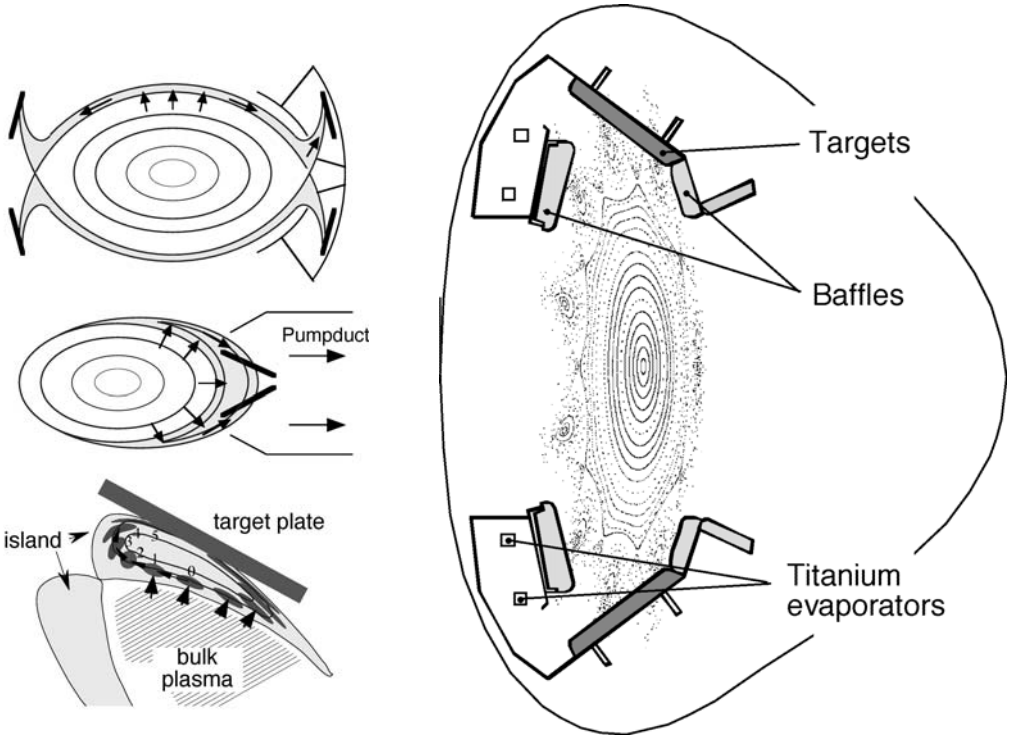

Figure 13.14: Left: Schematic view of the different divertor concepts for stellarators: The helical divertor with a closed divertor chamber indicated at the right (top), the local island divertor (middle), the target region in an open island divertor (bottom).
Right: The open island divertor in W7-AS. Poloidal cross section with flux surfaces, islands and divertor modules. Titanium can be evaporated in the sub-divertor chamber for pumping (top). Arrangement of the ten divertor modules (bottom). Targets and baffles are made from graphite (Grigull et al. 2001).

compared to a reference discharge without LID when the same gas puff rate is applied. In spite of lower density the LID discharge reaches the same plasma energy, i.e. the temperature increases because of a considerable reduction of impurity radiation, basically from oxygen. The local island divertor is now being implemented as a preliminary pumped divertor in LHD. Although plasma performance is expected to benefit from improved particle and impurity control, the LID is not suited to handle high power fluxes because of its small target area. Therefore, the final concept foreseen for LHD is a closed helical divertor.

The open island divertor has been realized at W7-AS. It uses the $5/m$ natural island chains ($m = 8, 9,$ or 10) in combination with ten discrete divertor modules (see Fig. 13.14 right) and serves to explore the general feasibility of the island divertor concept. With the island divertor a new quality of quasi-stationary high-power/high-density NBI discharges could be achieved. The reasons are twofold: Improved density and impurity control even at lower density (NC-regime) and, at higher density, the occurrence of the HDH-mode (see above) with simultaneously high energy and low impurity confinement. The edge density, about $5\times10^{19}\,\mathrm{m}^{-3}$, is sufficiently high for proper divertor action, the impurity radiation – basically from carbon – is concentrated at the plasma edge thus not affecting core confinement, and, at the highest densities stable detachment of the plasma from the targets occurs with a tolerable reduction of plasma energy (see Fig. 13.11). In case of detachment the convective energy and particle fluxes to the target plates nearly vanish since the edge plasma radiates the energy away and the

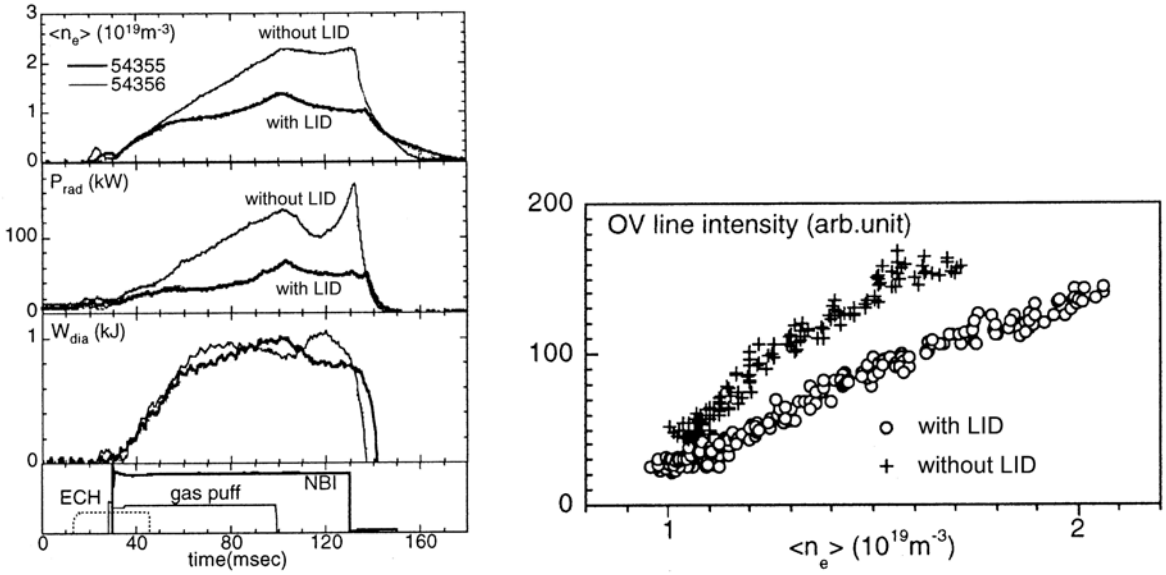

Figure 13.15: Left: Time evalution of plasma density, radiation power and plasma energy for NBI heated discharges in CHS with and without local island divertor.
Right: Radiation of O^{4+} impurity ions at 63 nm as a function of plasma density (Masuzaki et al. 1998).

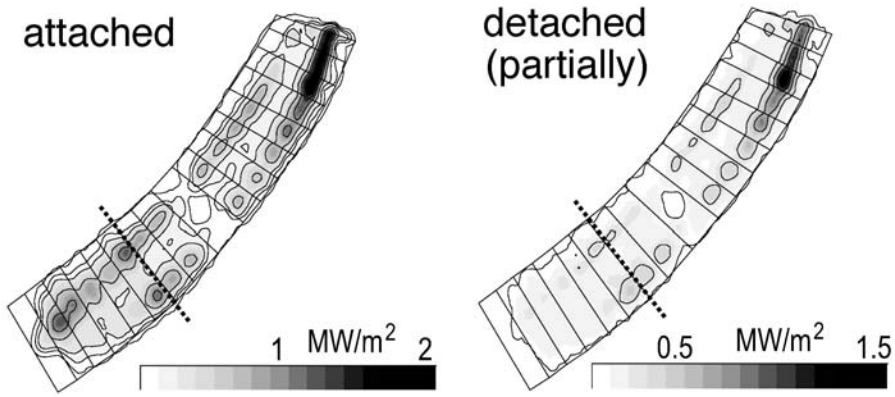

Figure 13.16: Power deposition pattern on a divertor target plate in W7-AS for attached and detached situations as observed by thermography (Feng et al. 2002).

temperature in front of the targets drops to values $< 5\,\mathrm{eV}$ such that ionization can no longer be sustained. The targets are thus protected by a cold radiating mantle. Fig. 13.16 shows the power deposition patterns on a target plate as observed by a thermography camera. In the attached case the dark areas reflect the energy deposition zone where the targets intersect the islands. In the detached case the power deposition vanishes except for a small area which remains attached, but with strongly reduced heat flux.

Table 13.2: The best plasma parameters in stellarators have been achieved in LHD and W7-AS so far. The values in a row have simultaneously been obtained in the same discharge. Ion temperatures in brackets have not been measured, but are assumed to equal the respective electron temperatures.

Best Values	$\langle\beta\rangle$ [%]	n [m^{-3}]	T_e [keV]	T_i [keV]	τ_E [s]	$nT_i\tau_E$ [m^{-3}keVs]	Device	Reference
$\langle\beta\rangle = 3.4\%$	3.4	2.5×10^{20}	0.2	(0.20)	0.004	2×10^{17}	W7-AS	PPCF **45**, A285(2003)
$\langle\beta\rangle \approx 4\%$	≈4	2.8×10^{20}					LHD	to be published
$n = 4\times10^{20}\,m^{-3}$	≈1	4×10^{20}	0.35	(0.35)			W7-AS	IAEA FEC 2002, OV/2-4
$T_e = 10.0\,keV$		5×10^{18}	10.0	2.0	0.04		LHD	PoP **10**, 1788(2003)
$T_i = 3.5\,keV$		1.3×10^{19}	3.3	3.5	0.09	2×10^{18}	LHD	NF **42**, 1179(2002)
$\tau_E = 0.3\,s$		6.5×10^{19}	1.1	(1.1)	0.3	2×10^{19}	LHD	PPCF **42**, B51(2000)
$nT_i\tau_E = 2\times10^{19}$		6.5×10^{19}	1.1	(1.1)	0.3	2×10^{19}	LHD	PPCF **42**, B51(2000)
$t_{pulse} = 120\,s$		9×10^{18}	1.3	1.3			LHD	IAEA FEC 2002, EX/P2-19

13.7 Summary

The recent progress in stellarator research has removed the earlier scepticism against the reactor potential of stellarators. The results have shown that the essential drawbacks of traditional stellarators, such as high neoclassical transport losses and low β-limit, can be overcome by optimized magnetic configurations. Plasma confinement is equivalent to that in tokamaks of comparable size and the island divertor has been shown to be a viable exhaust concept. The achievements in terms of the best plasma parameters are summarized in Tab. 13.2.

The first superconducting large scale device, LHD, has started operation and is continuously being upgraded with respect to heating and exhaust. W7-X is under construction. The mission of these large devices is to test the torsatron and Helias concepts, respectively, under reactor relevant conditions with particular emphasis on steady state operation. In parallel, various strategies of concept optimization are explored in small and medium scale devices, which are already operational (HSX, Heliotron-J) or under design (NCSX, QPS, CHS-qa).

Recommended literature

- L. Spitzer, The stellarator concept (Physics of Fluids, 1(4) 253-264 1958)
  "The basic concepts of the controlled thermonuclear program at Project Matterhorn are discussed." (The root of stellarator research. Lyman Spitzer has invented the stellarator and initiated the US fusion program with the Project Matterhorn in 1951.)
- A.H. Boozer, What is a stellarator? (Physics of Plasmas, 5(5) 1647-1655 1998)
  "The physics and mathematical concepts that are required to understand stellarators are reviewed."
- T.K. Chu, H.P. Furth, J.L. Johnson, C. Ludesher and K.E. Weimer, Modular coils - a promising toroidal coil system (IEEE Transactions on Plasma Science 9(4) 228-233 1981)
  "The concept of modular coils originated from a need to find reactor-relevant stellarator windings. Considerations of ... basic principles of modular coils ... are given"

- H. Wobig, Magnetic surfaces and localized perturbations in the W7-A stellarator (Zeitschrift für Naturforschung Section A - A Journal of Physical Sciences 42(10) 1054-1066 1987)
  "In order to study the structure of surfaces under the influence of perturbations, a mapping procedure is used ... '." (The mapping can easily be implemented in a simple computer program. It instructively shows the creation of magnetic islands by perturbations and their dependence on field parameters like rotational transform and magnetic shear).

- G. Grieger et al., Physics optimization of stellarators (Physics of Fluids B, 4(7) 2081-2091 1992)
  "This paper summarizes the status of advanced stellarators both from the conceptual point of view and also from the experimental side."

- R. König et al., The divertor program in stellarators (Plasma Physics and Controlled Fusion 44(11) 2365-2422 2002)
  "The helical and island divertor concepts ... are introduced and ... the ... experiments performed and planned for different devices are reviewed."

Chapter 14

Safety and environmental aspects of fusion

Hans-Werner Bartels

14.1 Introduction

Future fusion reactors will operate with radioactive materials: Tritium is radioactive and very mobile and the neutrons produced in the fusion reactions will activate the components near the plasma. To assess the radiological hazards of fusion, the inventories and possible release mechanisms are discussed. The behaviour of the plant during normal operation and accident situations is analyzed together with the waste management. The control of the mobile tritium is a key issue in reducing the effluents in normal operation. Associated with this is the design goal of minimizing the tritium inventories which can be released in accidents. The absence of chain reactions and the moderate decay heat densities in a fusion reactor are inherent safety-enhancing differences to fission plants. Since the neutron-induced radioactivity strongly depends on the materials used in a fusion-reactor, appropriate material selection offers the possibility of significantly influencing the amount of radioactivity produced. Generally, the decay times of fusion waste are much shorter than those of fission waste. Recycling of reactor materials after 50 to 100 years of cooling time is a potential waste management option instead of geological disposal.

14.2 Inventories

The safety implications of nuclear fusion can immediately be seen from the fundamental reaction equation

$$\mathrm{D} + \mathrm{T} \longrightarrow \mathrm{He} + \mathrm{n}\,.$$

Two distinct classes of radioactive inventories follow from this:

- Tritium as part of the fuel is radioactive.
- Neutrons leaving the plasma do not just produce tritium by nuclear reactions with lithium (breeding). They also perform nuclear reactions with other materials in the reactor, mainly those of structures near the plasma (first wall). Many of these reactions lead to radioactive end-products.

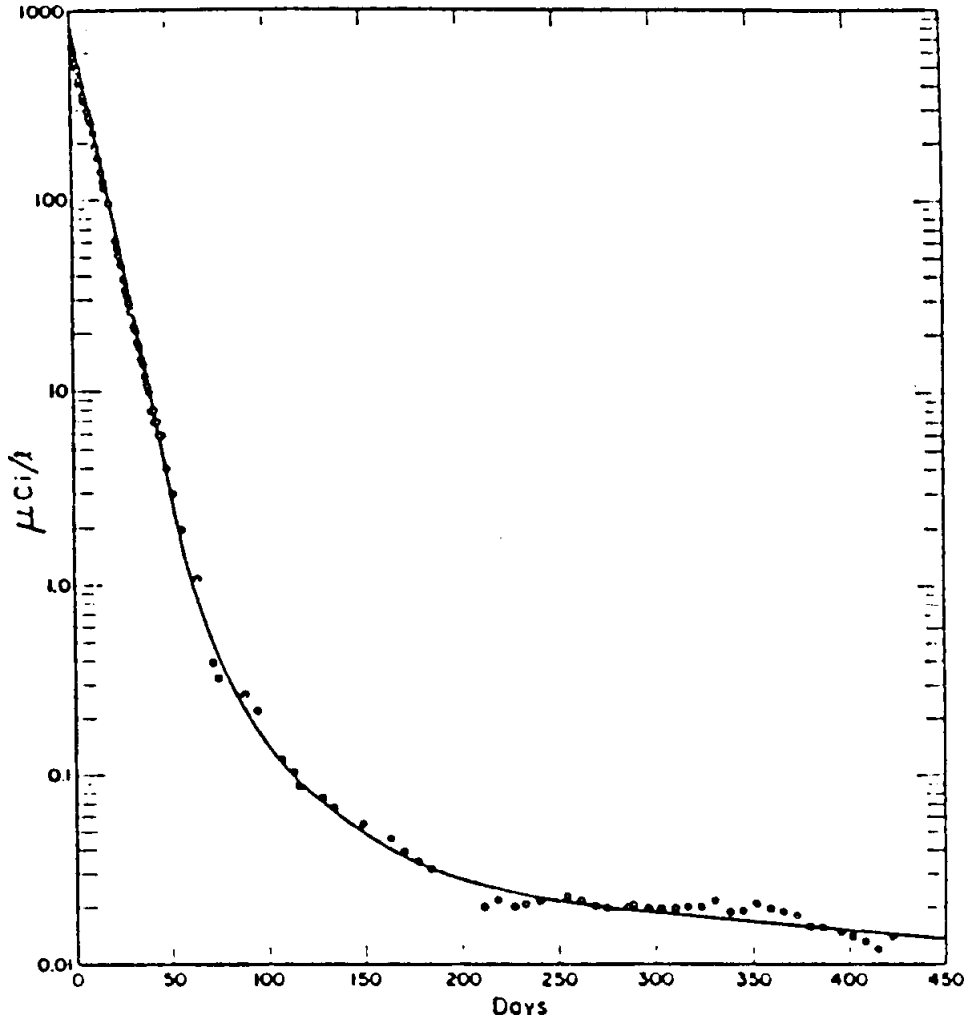

Figure 14.1: Time-dependent tritium concentration in a human after a single accidental incorporation of HTO.

Tritium

The expected tritium inventory of a fusion plant amounts to a few kg. Although just 0.5 g of tritium will be inside the hot plasma, much larger amounts will be present in other systems such as the blanket, pumping system, tritium processing plant and storage.

Tritium is a weak β^- emitter with a half-life of 12.3 years. Its mean β^- energy is 5.7 keV, its maximum energy 18.5 keV. Due to the rather low energy, its mean range in organic matter is below 6 μm, whereas the human skin is covered by a horny layer which is 70 μm thick. Thus tritium does not pose any hazard as an external radiator. The situation changes when tritium is incorporated into the body via ingestion, inhalation, or skin absorption. The most common chemical species of tritiated molecules are HTO (tritiated water) and HT (tritiated hydrogen gas). Boths forms are very mobile since their behaviour is similar to the non-tritiated species H_2O and H_2. Especially HTO can easily be absorbed into the human body. Once in the body it is rapidly dissolved in the human water cycle.

Fig. 14.1 shows the decrease of tritium in the body of a technician working in a tritium laboratory who accidentally inhaled a significant amount of HTO. The measurements show a decay with three time constants. The dominating decay time of about 10 days reflects the recycling in the water compartment of the human body. A reference person weighing 70 kg has a water

Table 14.1: Dose conversion factors for different isotopes.

Isotope	Dose Conversion Factor	Pathway	Relation to Tritium
Tritium	1.8×10^{-11} Sv/Bq	ingestion	1
	1.8×10^{-11} Sv/Bq	inhalation	1
Cs-137	1.4×10^{-8} Sv/Bq	ingestion	800
Pu-239	1.0×10^{-7} Sv/Bq	ingestion	5 500
	1.0×10^{-4} Sv/Bq	inhalation	5 500 000

compartment of 42 l and a daily water exchange of about 3 l leading to a biological half-life of ten days. The longer components of about 30 and 300 days in Fig. 14.1 pertain to the exchange between water and the organic compartment. On the average the slow component accounts for roughly 10% of the tritium dose. Thus the *effective* biological half-life of tritium in the human body is 11 days.

The intake of a certain amount of tritium measured in activity A (unit: Bq = decays per second) leads to the following energy deposition in the human body

$$\varepsilon = A \cdot \tau \cdot \langle E_{\beta^-} \rangle \cdot \, m^{-1}$$

with ε is the energy density [J/kg], A the activity [Bq], τ the effective biological lifetime [s], $\langle E_{\beta^-} \rangle$ the average β^- energy [J] and m the mass of reference person [kg].

Generally, the energy dose has to be multiplied with a quality factor to account for radiation forms more hazardous than γ-rays, e.g. α-radiation is assigned a quality factor of 20. The resultant quantity is the radiation *dose* measured in units of Sievert (Sv) and allows quantification of radioactive radiation hazards to humans. For tritium the international consensus is to use $Q = 1$, but some experiments tend in the direction of $Q = 2$–3 for tritium since the low β-energy leads to localized ionization.

With $Q = 1$, the intake of 1 Bq HTO leads to a dose of 1.8×10^{-11} Sv. Intake of tritium in organic form, e.g. by eating contaminated food, would increase the dose by a factor of 2.5. This is due to a larger fraction of tritium transfered into the body compartments with longer biological lifetimes. For a given air concentration, tritiated gas (HT) is 10 000 times less hazardous than HTO since the uptake and incorporation into the body is strongly reduced. Tab. 14.2 shows a comparison of doses for different radioisotopes. It can be clearly seen that the amount of radioactivity measured in units of activity (Bq) is not a good indicator of the associated hazard. Tritium produces smaller radiation doses per Bq because the average energy per release is much smaller than for other isotopes and the effective lifetime in the human body is also shorter.

The special concern with tritium is its high volatility and the associated problems in keeping it inside the fusion plant. Once released, tritium is still very volatile. In Fig. 14.2 the specific tritium activity in soil surface water is shown versus time after a controlled release experiment in Canada. In the first year the tritium concentration dropped by a factor of 1 000 and reached

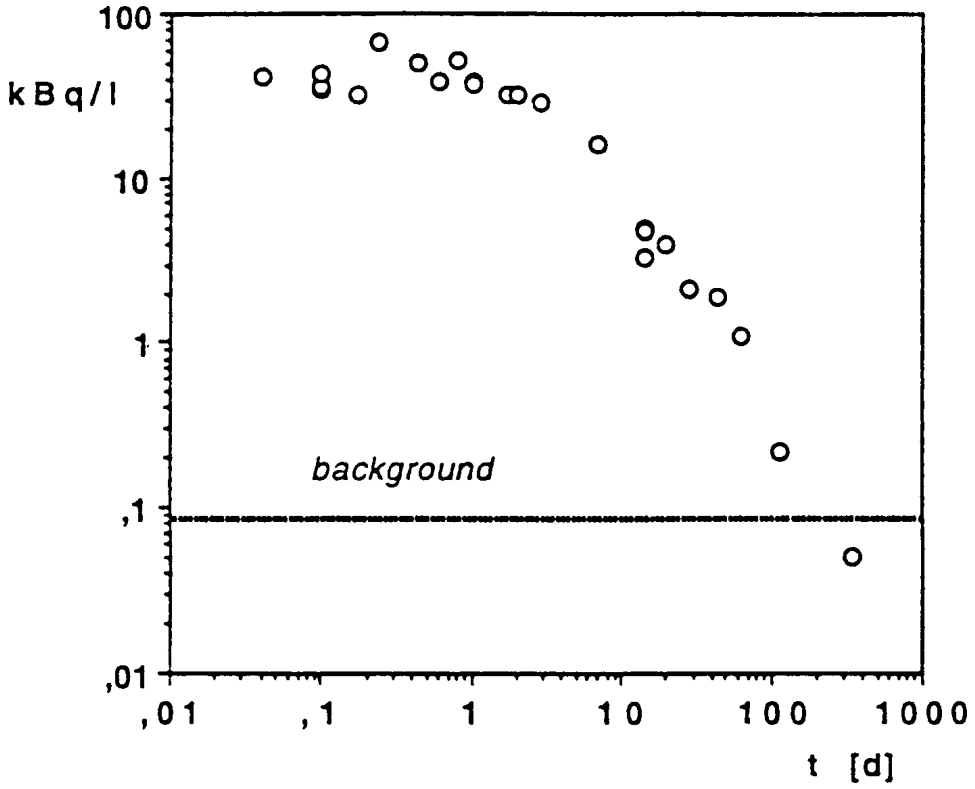

Figure 14.2: Time-dependent specific activity in the soil humidity of the top 20 cm after a controlled tritium release experiment (Canada 1987).

the background values which were measured before the experiment. Thus strong contamination of large areas which lasts for many decades is not expected in the event of a major tritium release. Instead, most tritium will end up in the oceans, which carry a natural tritium inventory of a few kg. This tritium is formed by nuclear reactions of cosmic rays entering the earth's atmosphere (e.g.: $n + {}^{14}N \rightarrow {}^{12}C + T$). During the period of extensive nuclear weapon testing in the fifties and sixties, the earth's inventory was increased to about 500 kg. Today the residual inventory has been reduced by decay of tritium to about 80 kg.

Activation products

The expected neutron wall loading is in the range between 2–5 MW/m^2, which will lead to considerable radiation damage of the components near the plasma. Thus a regular exchange of these components after 2.5–5 years of operation is envisaged. A target for fusion materials is a possible neutron fluence of about 12.5 MWa/m^2. The development of such materials is a very challenging task.

The amount of activation products in future fusion reactors strongly depends on the choice of materials. Fig. 14.3 shows the dose rates of some elements in the first wall. The total amount of radioactivity in a fusion plant will be governed by the activation products. If conventional steels are used, a level of about 50% of the radioactivity in fission plants is reached.

There is a clear distinction between the inventories of tritium and activation products, i.e. the volatility. The radioactivity inside the structural material is very hard to mobilize by definition since the structure has to withstand large forces during normal operation.

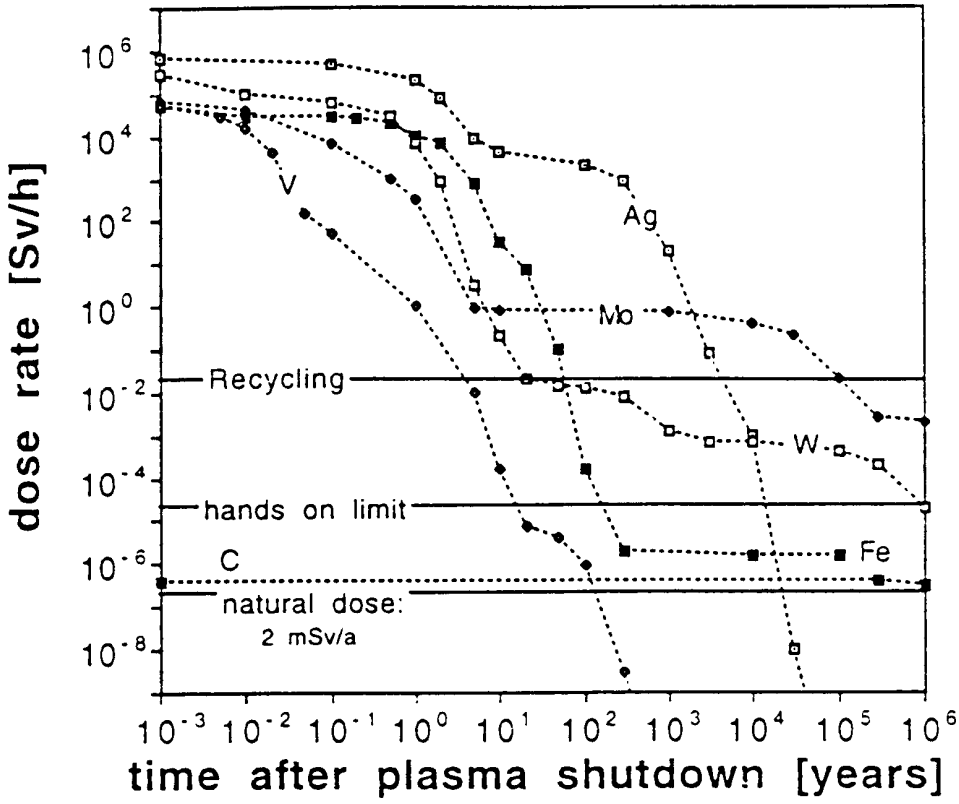

Figure 14.3: Dose rate of several elements after neutron irradiation of 12.5 MWa/m^2.

Special attention has to be given to the first-wall dust eroded by the plasma, because it can easily be mobilized. The use of very low activation materials such as carbon, beryllium, or boron would strongly reduce the hazard of this dust (see Fig. 14.3 for the dose rate of C). If high-Z materials have to be used in the plasma facing components (e.g. tungsten in the divertor), the dust inventory could pose problems similar to those of the tritium inventory. As indicated, a main issue of the activation products is waste management, which will be treated later. The environmentally most attractive elements for structural materials in a fusion plant are vanadium, chromium, and titanium.

14.3 Normal operation effluents

During normal operation, it is the volatile tritium which has to be properly controlled. Experience of tritium handling in large facilities is available from a special type of fission reactor working with natural uranium and heavy water as moderator, the Canadian CANDU reactors. In this type of fission reactor, inventories of a few hundred grams are produced from n-capture in D_2O. Experience with these CANDU reactors allows the extrapolation that with present technology tritium effluents can be limited to 2 g per year or 50 Ci/day (1 Ci = 3.4×10^{10} Bq). In Los Alamos, USA, the largest fusion-oriented tritium laboratory, with a maximum inventory of 200 g, is in operation. The experience from this laboratory (TSTA: Tritium Systems Test Assembly) has demonstrated that one might even do better than the extrapolation above. This laboratory was closed for three month after an unexpected release of 0.4 Ci HT, which demonstrates the high safety level of the plant.

If we assume a daily release of 50 Ci in the more hazardous form HTO from a 100 m high stack, the resultant dose to the most exposed individual (MEI) living at the fence has to be calculated. It is assumed that food and sometimes also water originate from the location of the MEI. A conservative estimation of the dose to the MEI is very simple: The source term S [Bq/s] will be diluted by atmospheric dispersion. For a 100 m high stack, the plume will reach the ground at about $R_{max} = 1\,000$ m, leading to a maximum ground level air concentration c_{air} of

$$c_{air} = S \cdot \frac{1}{v_{wind}} \cdot \frac{f}{2\pi R_{max}} \cdot \frac{1}{2h_{stack}}$$

with S being the source term in [Bq/s], v_{wind} the wind speed in [m/s], f a factor accounting for nonuniform wind rose, R_{max} the downwind distance from the source in [m], and h_{stack} the height of the source in [m].

A conservative assumption is $f = 3$ and a typical average wind speed is 6 m/s at a height of 100 m. Given the air concentration, one can transform this to a concentration in the air humidity

$$c_{H_2O,air} = c_{air}/\rho_{H_2O,air} \ ,$$

$\rho_{H_2O,air} = 10\,\mathrm{g/m^3}$ is a typical value for the Central European growing season.

Assuming complete equilibration of the specific tritium activity of the air humidity with that of soil water, plant water, animals, and humans, the average tritium concentration in the MEI is equal to $c_{H_2O,air}$ leading to a dose rate D of

$$D = c_{H_2O,air} \cdot \langle E_{\beta^-} \rangle \ .$$

For a source term of 50 Ci/d this simple approach results in an annual dose of 23 μSv/a, which is about 1% of the dose received from natural sources of radioactivity. More sophisticated models predict doses to the MEI which are 2–3 times smaller.

14.4 Accidents

With respect to safety in the event of accidents, the most important characteristic of fusion is self-termination of the fusion process under such conditions. So-called *passive safety* appears to be achievable in fusion power plants because of the absence of chain reactions. The energy sources that could drive accidents are low compared with those in fission, whereas the volumes and surface areas are large. Tab. 14.4 lists some relevant energy inventories together with typical time scales of release.

After shutdown of the reactor, the decay of radioactive nuclei constitutes a heat source, known as decay heat. Passive removal of the decay heat is a key safety feature. In the event of loss of coolant accidents (LOCA), the core of a fission reactor is prone to melting if no additional cooling can be applied. In the case of fusion, the decay heat is much smaller and is distributed over large surfaces. If all cooling media are lost, just thermal conduction and radiation are left as heat removal mechanisms. Fig. 14.4 shows a detailed analysis of such a situation for the

Table 14.2: Energy inventories and characteristic time scales for their release in a fusion reactor (water volume in the primary loop: $400\,m^3$, heat of evaporation at 1 bar: 900 GJ).

Source	Energy [GJ]	Time Scale
Plasma	2	< 1 s
DT in Plasma	250	1 min
Coils	100	1 min
Cooling Water	300	10 min
Decay Heat	80	1 hour
	550	1 day
	2 000	1 week

ITER device. This is a good example of passive safety since the removal of the decay heat is managed by physical mechanisms that do not rely on engineering systems, which can always fail with a certain probability. Thermal radiation will never fail. The maximum temperatures in the fusion device stay well below the melting point of the steel structures (1 400 °C).

The safety studies in fusion are prompted by the large radioactive inventories involved, but the fundamental difference between fusion and fission reactors is the fact that in the former major accidents are not driven by the nuclear system itself. Instead most safety studies focus on conventional hazards. The most important accident initiators are

- loss of vacuum accidents with air ingress into the plasma chamber;
  concerns: chemical reactions (fire), transport of tritium
- loss of coolant accidents;
  concerns: pressurization, formation of hydrogen (explosion hazard)
- loss of offsite electric power;
  concerns: loss of coolant flow, quench of magnets
- electric arcs in the coil system;
  concerns: melting of adjacent systems, tritium release to the building
- coil deformation and displacement;
  concerns: damage of adjacent components, loss of vacuum, missile generation
- volume change of cryogenic helium;
  concern: pressurization
- explosions in the hydrogen isotopic separation system;
  concerns: damage of building, tritium release
- fire in the long-term tritium storage beds;
  concern: tritium release

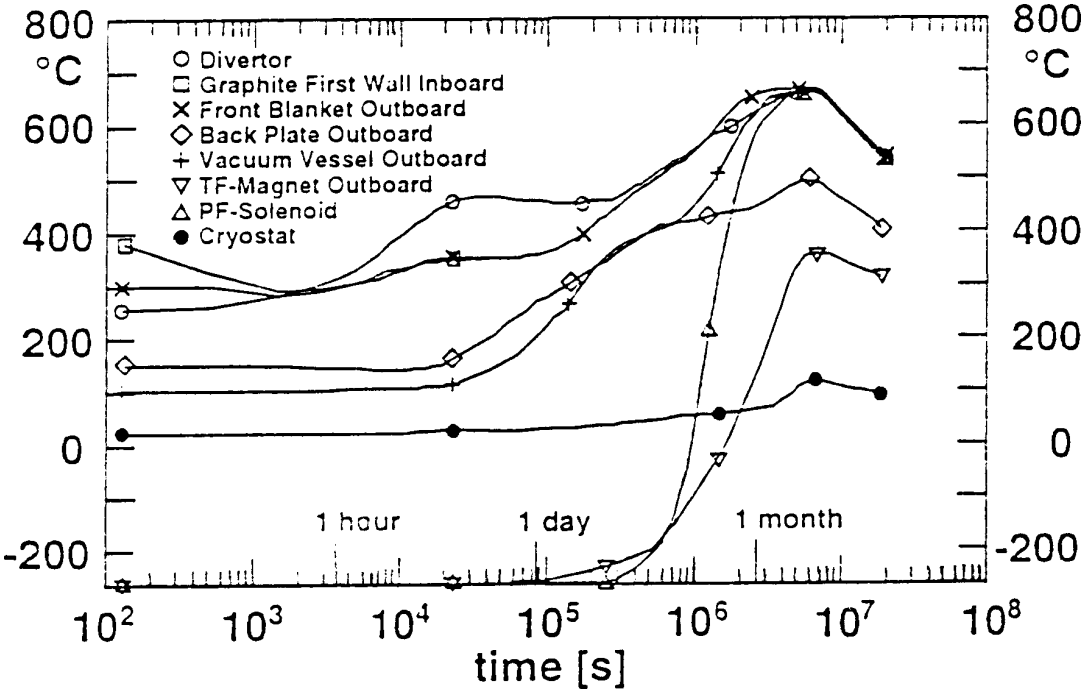

Figure 14.4: Temperature transient up to seven months for loss of all active cooling accident in ITER.

The most detailed analyses have been performed for the ITER conceptual design phase. One example is air ingress into the plasma chamber, which is of concern since then one major confining barrier is breached. For a design where the majority of the first wall is covered by carbon, chemical reactions of this material were investigated. No self-sustained fire can develop in such a case since the plasma would definitely extinguish and the first-all cooling would very effectively reduce the carbon temperatures. Even if the active cooling was simultaneously, the inertia of the cooling system would be sufficient to cool the carbon below its ignition temperature. The mobilized material, mainly tritium in the carbon dust and pumping system, would be released into the adjacent rooms. Here it would be confined in the second of three confinement barriers.

Generally, the aim of fusion safety studies is to ensure that future fusion plants are designed so that any internal accident and all conceivable external events should entail consequences confined inside the fusion plant by passive means. No internal accident should be able to destroy the buildings. The strategy is to provide a robust multi-confinement system, reduce all radioactive and energy inventories as far as possible, apply passive safety features and use high-quality nuclear components. Active systems can also play an important role to reduce any damage inside the plant.

In fusion reactors large amounts of lithium will be used to breed the necessary tritium. This could be done very efficiently by using liquid lithium. In this case the lithium could also serve as coolant since it has very good thermal properties which would simplify the design. Technical problems are still presented by the large pressure losses of liquid metals flowing in magnetic fields (MHD effect). Another serious drawback are safety concerns arising from violent chemical reactions of liquid lithium with air, water, nitrogen, and concrete. The potential energy release of the lithium inventory is about 7 000 GJ. Any contact with water produces large amounts of hydrogen with the unpleasant tendency to trigger detonations, which can seriously threaten the confinement buildings.

An alternative approach is the use of lithium ceramics such as Li_2O, Li_4SiO_4, Li_2ZrO_3, and other candidates which eliminate the chemical hazard caused by elemental lithium. Unfortunately, the need for a self-sufficient tritium breeding ratio calls for the neutron multiplier, beryllium (^{9}Be(n,2n)2He), in almost all ceramic breeder designs. Beryllium is a very toxic material which builds up significant tritium inventories during neutron irradiation. In addition, there are questions about the abundance of beryllium on earth. At temperatures above 600–700°C some violent chemical reactions can also occur with air and water. Consequently, attempts are being made to push the design of ceramic breeder blankets to the extreme so as to eliminate the beryllium. Li_2O is the best candidate for these studies since is has the highest lithium atom density of all lithium ceramics. The lithium density in Li_2O is even higher than in metallic lithium. In addition the neutron activation of Li_2O is extremely small.

Another option is to use $Li_{17}Pb_{83}$, which has a melting point of 235°C and is thus a suitable liquid metal. Its chemical reactivity is much smaller than that of liquid lithium, but the use of lead poses technical problems because of its weight and there are safety concerns because of the neutron activation of lead.

The final choice of the breeder material will strongly influence the safety and environmental properties of future fusion plants.

Accidental doses to the public

The early dose is defined as the dose received during the first week after an accident, excluding the ingestion pathway. This dose definition is the basis for considering evacuation. Above 100 mSv evacuation is triggered in many countries. The chronic accidental dose integrates over 50 years of exposure time and includes all pathways. In Germany 50 mSv is the legal upper limit for public exposure after *design basis accidents*, i.e. accidents which have to be controlled by design.

Detailed studies for atmospheric accidental tritium and activation product releases have been performed. Specific doses for the most exposed individual of the public (MEI) at a distance of 1 km from the release point are presented in Tab. 14.4. The dose due to inhalation and skin absorption is 0.5 mSv/g-T (early dose) for ground level releases in the chemical form of HTO. If ingestion is included, the dose values are about five times higher (chronic accidental doses). For gaseous releases (HT), doses are at least a factor of ten lower. The earlier mentioned difference in radiotoxicity of 10 000 between HTO and HT is levelled out by the fact that HT released to the environment will diffuse into the soil, where it is rapidly oxidized by microorganisms and subsequently re-emitted as HTO. Specific doses for steel dust envisaged during the conceptual design of ITER are about one order of magnitude below the tritium values, but for the chronic accidental doses similar values result.

Under the German licensing procedure, it has to be shown that in design basis accidents the releases stay below 20 g for tritium in the form of HTO for ground level releases. This is achievable as long as the confinement building remains intact. To avoid evacuation, tritium releases have to be kept below 200 g in all circumstances. This is the reason for setting up the safety target of keeping the tritium inventory below 150 g for all single components.

If we compare the potential hazard of the tritium and steel dust of a fusion plant with the hazard of the J-131 and Cs-137 inventories of a fission plant, fusion is 500 times more benign.

Table 14.3: Specific dose to the most exposed individual of the public (MEI) at a distance of 1 km from the release point.

Source	Specific Dose	Type of Dose
tritium as HTO	0.5 mSv/g-T	early
	2.5 mSv/g-T	chronic
tritium as HT	0.04 mSv/g-T	early
AISI-316 first-wall steel	0.03 mSv/g	early
ITER conditions	2 mSv/g	chronic

14.5 Waste management

The majority of the radioactive waste in a fusion reactor will arise from replacement of divertor, first wall, and blanket segments and decommissioning of the whole tokamak, including the vacuum vessel and the magnets. These components will be activated by the intense flux of 14 MeV neutrons. Due to the shielding effect of the materials involved, there will be a steep gradient in the activation when going away from the plasma.

The relatively short life of the majority of the radioisotopes produced and the absence of very toxic actinides (α-emitters) causes the ingestion hazard index of the fusion waste to be more than 1 000 times less than for fission waste after 100 years of cooling time. The basis of comparison is the total waste produced during the lifetime of the plants.

The volume of packed waste is estimated to add up to about 25 000 m^3 for a fusion reactor life. This is comparable to the amount of packed waste from a typical PWR plant life, including reprocessing. Without reprocessing the volume of packed fission waste will be 30–50% smaller. The fission waste still requires much more repository consumption due to the significantly larger heat production in the waste, which limits the packing density in geological repositories.

Fig. 14.4 shows the dose rates of some technologically important materials irradiated at the first wall. Given moderate progress in the development of fusion-optimized materials, the reuse of activated material in new reactors is a potential option of waste management. For reduced-activation steels, recycling of components is estimated to be feasible up to contact dose rates of 25 mSv/h by remote handling techniques. The most activated component, which is the first wall of the plasma chamber, would reach this level 50–100 years after being dismantled from the reactor.

If new classes of low-activation materials, such as vanadium alloys, could be used in fusion reactors, *hands-on recycling* might be feasible after a few decades of cooling time. The benefit will be strong simplification of recycling procedures and thus greater economic attractiveness. However, great care must be taken to keep undesirable impurities to a low level in order to retain the radiological attractiveness, e.g. below 0.1 ppm for silver (see Fig. 14.3).

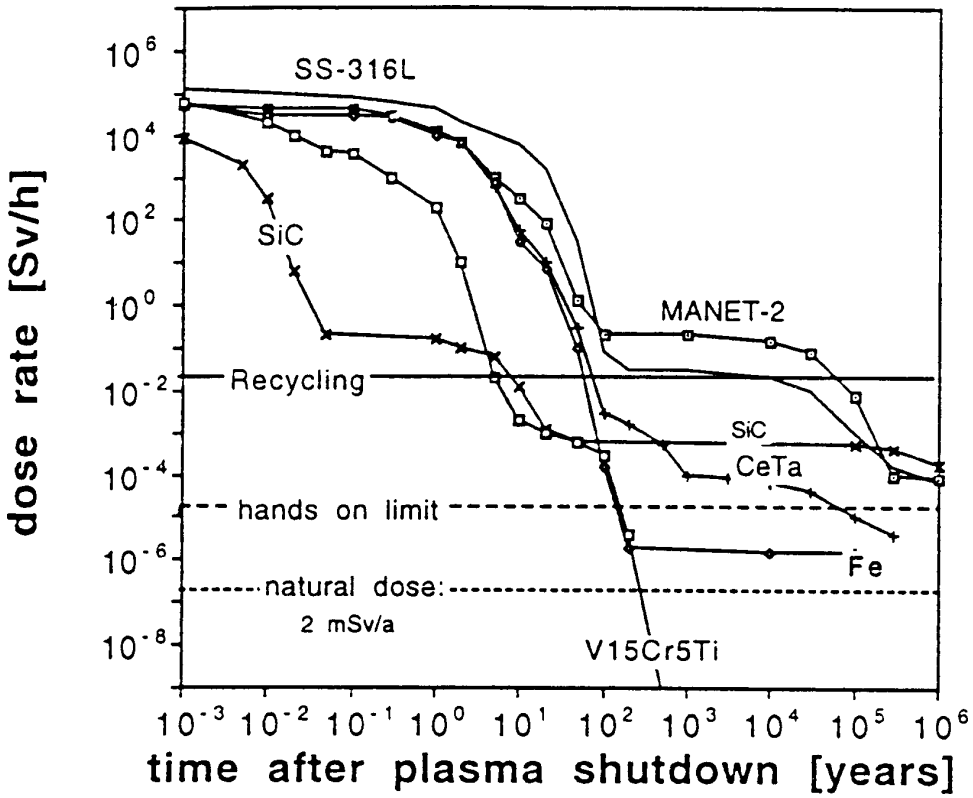

Figure 14.5: Time-dependent dose rates for technologically important materials irradiated by a neutron fluence of 12.5 MW/m^2; a standard steel (SS-316L), a fusion optimized steel (CeTa, KfK), the theoretical lower limit for iron based steels (Fe), a ceramic (SiC), and a vanadium alloy (V15Cr5Ti) are shown.

14.6 Conclusion

A board of independent scientists from different fields are regularly asked to review the European Fusion Programme. The following extract from the last *Fusion Programme Evaluation Board* (Colombo report, July 1990) is quoted to conclude this overview:

> It is essential to expand the effort on technology, not only on the Next Step, but also on longer term issues, particularly in relation to the new emphasis on environmental and economic constraints. Environmental and safety criteria should as of now be considered as essential elements in governing the evolution of the Fusion Programme. Problems concerning materials, the use of tritium, the maintainability of the reactor should all be faced in time avoiding freezing of design or engineering concepts which might lead to environmentally unacceptable fusion reactors or make their design excessively complex.
>
> Environment and safety must assume high priority in the European Fusion Programme and in its wider international extension...
>
> It would be particularly important for fusion to qualify in two respects:
>
> 1. It must be clearly shown that the worst possible fusion accident will constitute no major hazard to populations outside the plant perimeter that might result in evacuation.

2. Radioactive wastes from the operation of a fusion plant should not require isolation from the environment for a geological timespan and therefore should not constitute a burden for future generations.